HYDROGENISATION OF METALS

By

SENTSHO ZELDAH NGWANAKGAGANE

Submitted in partial fulfillment of the requirements of the

degree of

Magister Scientiae in the Department of Physics

University of the Western Cape

Supervisor: Dr. M. Topic, iThemba LABS

Co-Supervisor: Prof. C.J. Arendse, University of the Western

Cape

September 2013

This thesis is dedicated to my son *fulufhelo Maliaga*, born on 17 th May 2012

ACKNOWLEDGEMENTS

Blessed is the man who trusts in the Lord and has made the Lord his hope and confidence. I would like to thank all the people who contributed in some way to the work described in this thesis. I thank my supervisor, Dr. Miroslava Topic (iThemba LABS, Cape Town), who supported my attendance at various conferences, engaging me in new ideas and demanding a high quality of work in all my endeavors. This thesis would not have been possible without her help and patience. I'm grateful for the good advice, support and friendship which have been invaluable on both academic and personal level. I thank also my co-supervisor, Prof. Christopher Arendse (Physics department, UWC) for showing interest in my work and for the encouraging words that he was always ready to offer.

Every result described in this thesis was accomplished with the help and support of the following laboratory colleagues and collaborators:

The Center for materials engineering at UCT for allowing me access to their facilities for hydrogenation, sample polishing, microscopy studies and hardness measurements

Velile Vilane (Center for materials engineering, UCT) for her unselfish help and assistance in the experimental work throughout this thesis. She also assisted in the micro-hardness and microstructure investigations

Nasheeta Hanief (Center for materials engineering, UCT) for her assistance during the electron microscopy studies

The Ion beam team, Prof. Carlos Pineda and Mr. Phillip Sechoegela (Material research group, iThemba LABS) for the help and assistance during the analysis of hydrogen content by elastic recoil detection analysis technique.

Dr. Sylvain Halindintwali (Physics department, UWC) for the assistance with ERDA data analysis

Claire Van den Berg (Department of Physics, UCT) for the IGA measurements performed at Stellenbosch University

Dr. Remy Bucher (Material research group, iThemba LABS) for his assistance during the phase analysis using x-ray diffraction

The material research group (MRD) at iThemba LABS with whom I had the opportunity to work with at the most respected research institution in the Republic of South Africa.

I would like to acknowledge my family and friends who supported me in good and bad times:

My mother, Rosinah Lebeko Mmola, she respect my choices in life and always give me support in every way possible;

My sincere sister, Leah Sabinah Sentsho, for being a sister and a friend I could run to in bad times;

To my brothers, Zachariah Samuel and Kedibone Sentsho for their constant love

Samuel Maliaga for reminding me every day that I am able

I would also like to thank my student colleagues at iThemba LABS and UWC; Zebib Yenus Nuru, Aline Simo, Nametso Mongwaketsi and Ngwambe for the stimulation topics we shared as well as the staff at the Physics Department of UWC for their support.

DECLARATION:

I declare that

Hydrogenisation of metals

is my own work, that it has not been submitted for any degree or examination in any other university, and that all the sources I have used or quoted have been indicated and acknowledged by complete references.

UNIVERSITY *of the*
WESTERN CAPE

Sentsho Zeldah Ngwanakgagane   Date:.16 September 2013

Signed

Keywords

HYDROGENISATION OF METALS

SENTSHO ZELDAH NGWANAKGAGANE

Hydrogen storage systems

Palladium (Pd)

Palladium-Platinum (Pd-Pt) alloys

Palladium-Platinum (Pd-Pt) coating

Titanium (Ti)

Titanium alloy (Ti-6Al-4V)

Hydrogenation

System pressure

System temperature

Gravimetry

Elastic recoil detection analysis (ERDA)

Intelligent gravimetric analyser (IGA)

Microstructure

Hydrides

Microhardness

Sorption

desorption

Abstract

HYDROGENISATION OF METALS

SENTSHO ZELDAH NGWANAKGAGANE

MSc thesis, Department of Physics, University of the Western Cape

Transition metals are a group of metals which are light in weight and have high hydrogen solubility. Their interaction with hydrogen is exorthermic and this phenomenon makes them "ideal" candidates for various applications of hydrogen storage systems. This explains why the phenomenon of hydrogen storage in Pd is used as a model for hydrogen storage systems because of the nature of absorption associated with it (like a sponge even at low temperatures). The hydrogenation process can be conducted at either room or high temperatures in a furnace under low pressure-low hydrogen gas concentration-short hydrogenation time (LP-LC-ST) and in intelligent gravimetric analyser under high pressure-high hydrogen gas concentration-long hydrogenation time conditions.
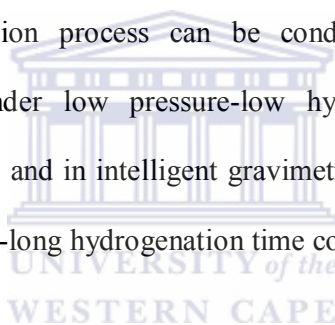
Most of the research on hydrogen storage sytems is based on gravimetric analysis of absorbed and desorbed hydrogen concentration. In this work, a comparison study of the hydrogen content in pure Pd, Pd-Pt coated systems, Pd-Pt alloys, commercially pure Ti and Ti-6Al-4V alloy determined by gravimetric methods and elastic recoil detection analysis (which is based on the detection of recoiled hydrogen after interaction with He^+ ions) technique was investigated. The changes in the structural properties and the hydrogen content of the materials when exposed to a hydrogen gas environment for different durations at various system temperatures and pressures will be reported. These changes have an effect on the microstructure of CP-Ti and Ti-6Al-4V alloy and structural properties of all the hydrogenated materials. The results obtained from optical microscopy, scanning electron microscopy, x-ray diffraction, intelligent gravimetric analyser, digital balance, elastic recoil detection analysis

and Vickers hardness test, show the following: it is found that hydrogenation of Pd at elevated temperatures (550 ˚C and 650 ˚C) does not yield hydrides under LP-LC-ST conditions. However, at room temperature the absorption of hydrogen occurred faster at the beginning of the process. Furthermore, the absorption of hydrogen increased with pressure where optimum absorption (0.67 wt. % hydrogen concentration) occurred under a system pressure of 2000 mbar. After pressure release, the remaining hydrogen content in the Pd sample was 0.6 wt. %. The Pd-Pt coated system provide hydrogen mobility at 550 and 650 ˚C where hydrides were formed under LP-LC-ST conditions. In addition to the decrease of hydrogen solubility in Pd-Pt alloys with an increase in Pt content, the probability of the alloys to achieve full saturation also decreases with an increase in Pt content under HP-HC-LT conditions. CP-Ti and Ti-6Al-4V alloy absorb substantial amount of hydrogen in the first hour of room temperature hydrogenation under LP-LC-ST conditions but hydrides were not formed. Therefore, under LP-LC-ST conditions at room temperature, Pd is able to store hydrogen in the form of hydrides whereas Ti and Ti-6Al-4V alloy could not. The 550 ˚C is the optimum temperature for hydrogenation of CP-Ti under LP-LC-ST conditions. The Ti-6Al-4V alloy absorb optimum hydrogen at 650 ˚C under LP-LC-ST conditions. Consequently, the change of microhardness of CP-Ti and Ti-6Al-4V alloy was found to depend on hydrogenation temperature.

TABLE OF CONTENTS

UNIVERSITY *of the*
WESTERN CAPE

Chapter 1: .   Introduction

1.1   Background

The problem of global warming has united countries to seek a solution of combating the growing emission of greenhouse gases that result mostly from the processing of coal into liquid fuels and electricity. Due to exponentially increasing energy demand globally, the depletion of the coal supply, fuel supply shortages and energy security, there is continuous need for energy to sustain old and grow new businesses. The use of vehicles increases as the global economy grows. An initiative was adopted in Kyoto in the year 1997 where countries were encouraged to reduce their greenhouse gas emissions by application of primary renewable energy technology such as wind, hydropower, solar and hydrogen. Wind energy uses wind as the source; hydropower uses water whereas solar uses sunlight. In this study, more attention is given to hydrogen as a clean energy carrier because it is lightweight, odourless, most abundant element in the universe and its oxidation product, water, is environmentally friendly. It also has the highest energy content per unit of weight of any other known element (1 kg of hydrogen has approximately the energy content of about 2.7 kg gasoline) [1.1].

Hydrogen was used in the 1920's to fuel the first self-sustained internal combustion engine [1.2]. The renewed interest of hydrogen as an internal combustion fuel was stimulated by the petrol crisis in the 1940's during World War II. Since then, hydrogen attracted a lot of attention as a potential engine fuel for vehicular use [1.2,1.3]. The other application includes its ability to improve the production of energy in fuel cells and also offers great potential in aircraft for supersonic and hypersonic operations [1.4]. Less than 1 % of hydrogen is available as molecular gas H_2. Most of it is chemically bound as H_2O in water and some is bound to liquid or gaseous hydrocarbons [1.5]. The hydrogen consumed today as a chemical

raw material (about 5×10^{10} kg per year worldwide) is to a large extent produced from fossil fuels and the reaction of hydrocarbon chains with water at high temperatures which produces large emissions of CO_2 [1.2]. Equations 1-1 and 1-2 illustrate the chemical reaction involved for the production of hydrogen from water and hydrocarbons:

$$H_2O \xrightleftharpoons[900°C/(Pt/Ru)]{} H_2 + O_2 \qquad (1\text{-}1)$$

$$(-CH_2-) + H_2O \xrightleftharpoons[high\ temperature]{} H_2 + CO_2 \qquad (1\text{-}2)$$
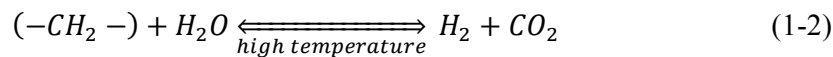
An efficient and controlled way to produce hydrogen can be achieved by application of primary energy sources discussed earlier.

The misconception related to the safety of hydrogen as a fuel was cleared by the recent analysis of the Hindenburg tragedy. It was found that the air ship caught fire because of a highly flammable skin material and static electricity [1.6]. Therefore, the safety of hydrogen relies on its high volatility and non-toxicity [1.5]. Its successful application in space technology led to the formation of national hydrogen associations and joint ventures such as the International Hydrogen Energy Association (IHEA) and solar hydrogen Research & Development programs globally [1.7]. It is expected that the hydrogen economy will require hydrogen storage systems for stationary and mobile applications including transportation. Each system has its own constraints and requirements [1.8].

The most challenging problem that faces the hydrogen economy is its storage. Different storage systems such as liquid, gas and solids were investigated in the past and certain conclusions were made [1.1,1.2]. One of the conclusions made was based on the temperatures and pressures required to maintain the systems. It was found that high pressure and very low temperature are needed to maintain the system in liquid storage systems, while very high temperatures and low pressures are needed to maintain the gas storage system [1.1,1.5].

Nevertheless the solid storage of hydrogen as hydride is the most stable and can be easily maintained under ambient pressures and temperatures. A serious damage to a hydride tank would not pose fire hazard because hydrogen would remain in tacked in the metal structure [1.1].

A comparison sketch of the storage systems under atmospheric pressure and room temperature is shown in Figure 1-1. Hydrogen forms metal hydrides with some metals and metal alloys. The hydrides have a critical temperature range 200 - 300 ˚C. Thus, their gravimetric, volumetric storage capacities and the safe operating pressures make them suitable hydrogen storage systems (solid-state hydrogen storage) [1.9]. The high hydrogen density in metal hydrides favours their application in energy storage systems as shown in Figure 1-2 [1.10].

| (a) Mg_2NiH_4 | (b) $LaNi_5H_6$ | (c) Liquid Hydrogen | (d) gas Hydrogen (200 bar) |
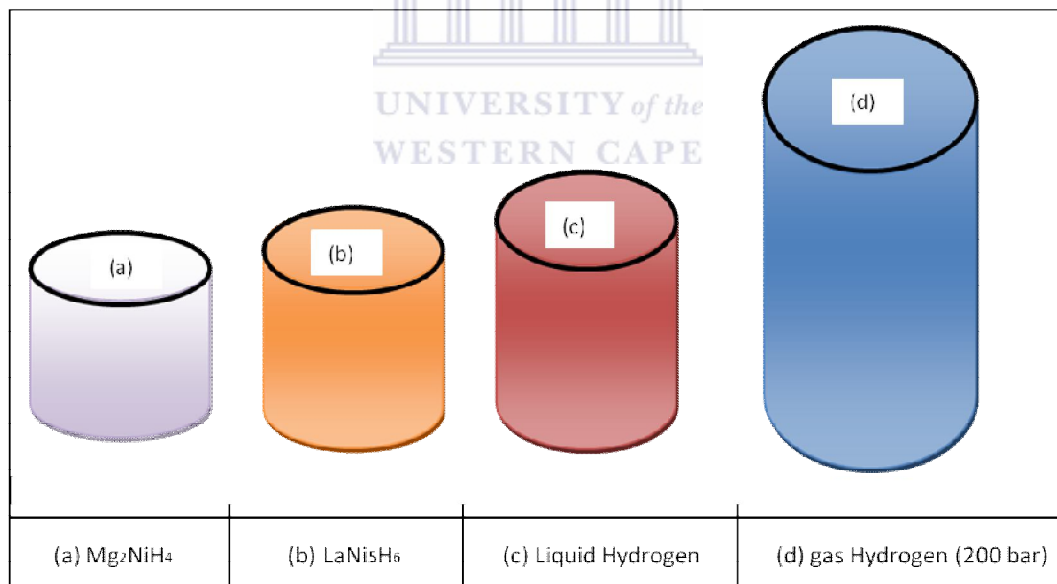
Figure 1-1: The same volume of hydrogen compacted in different ways (gas, liquid and solid storage systems).

A storage material that has high hydrogen absorbing capacity and also large hydrogen solubility is needed. A lot of research has been conducted on solid hydrogen storage materials, i.e. nano-structured graphitic carbon, carbon nanotubes [1.9] and metal hydrides [1.5,1.11]. In Figure 1-2, the volume density of hydrogen stored in metal alloys, carbon nanotubes, petrol and hydrocarbons is plotted against the corresponding hydrogen mass density for comparison.
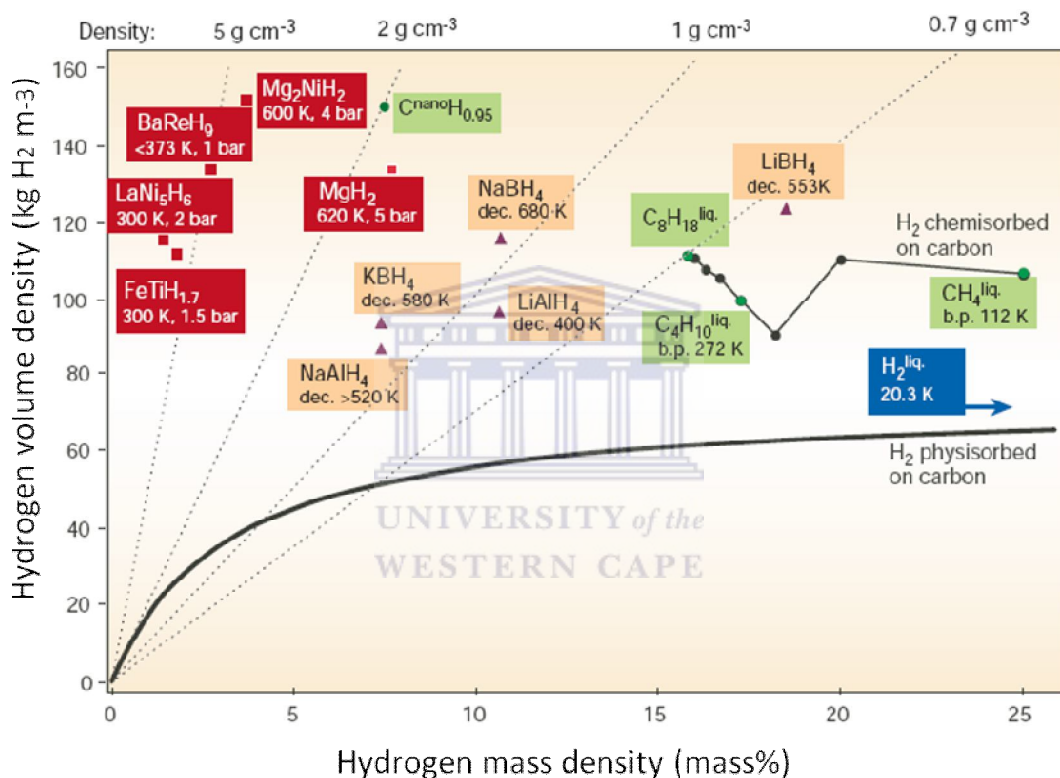
Figure 1-2: A schematic comparison of volumetric and gravimetric hydrogen density of bulk metal hydrides and carbon nanotubes hydrides with those of petrol and hydrocarbons [1.5].

The metal hydrides exhibit a higher gravimetric and volumetric density compared to the other storage systems. However, the slow hydriding/dehydriding kinetics, high release temperature, low storage efficiency due to the high enthalpy of formation, and thermal management during the hydriding reaction, are difficulties that are stumbling blocks for development of a feasible

hydrogen storage system. Nano-structured materials significantly improve the reaction kinetics, reduce the enthalpy of formation and lower the hydrogen release temperatures through destabilization of the metal hydride and multiple catalytic effects in the system. However, hydrogen adsorbed on high surface area carbons and nanotubes exhibits a low gravimetric density of less than 2 mass% and therefore also a low volumetric density [1.9]. The specific surface area increases together with the short diffusion paths and the lower stability of cluster as compared to bulk material [1.4].

For on-board energy storage, vehicles need compact, light, safe and affordable containment [1.12]. Figure 1-1 illustrates 4 kg hydrogen compacted in different ways [1.5]. The magnesium (Mg) alloy depicts the capacity of metal alloys as hydrogen storage materials. However the disadvantage of Mg is that 80 % of absorbed hydrogen desorbs at very high temperatures (above 330˚C), hence more research is now based on transition metals [1.5].
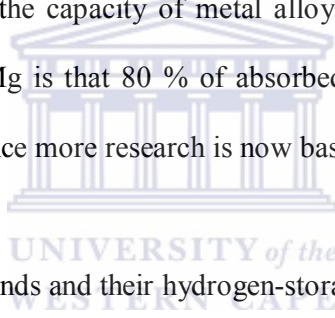
Table 1-1: Intermetallic compounds and their hydrogen-storage properties [1.5]

Type	Metal	Hydride	Structure	Mass%	$P_{eq,T}$
Elemental	Pd	$PdH_{0.6}$	Fm3m	0.56	0.02 bar,298 K
AB_5	$LaNi_5$	$LaNi_5H_6$	P6/mmm	1.37	2 bar,298 K
AB_2	ZrV_2	$ZrV_2H_{5.5}$	Fd3M	3.01	10^{-8}bar,323 K
AB	FeTi	$FeTiH_2$	Pm3m	1.89	5 bar,303 K
A_2B	Mg_2Ni	Mg_2NiH_4	P6222	3.59	1 bar,555K
BCC	TiV_2	TiV_2H_4	BCC	2.6	10 bar,313 K

The properties of transition metals satisfy the conditions of on-board hydrogen storage and they have high solubility to hydrogen. Most of them are capable of absorbing hydrogen at room temperature and very low pressures, for example, the characteristics displayed by Pd in Table 1-1 comply with these requirements. The interest in this study is based on pure

palladium (Pd), palladium-platinum (Pd-Pt) coated systems, palladium-platinum (Pd-Pt) alloys, commercially pure titanium (CP-Ti) and Ti-6Al-4V alloy. Hydrogen storage in these systems has been studied before by several researchers and the effects of hydrogen on the materials properties were determined [1.5,1.13,1.14].

1.2   Aims and outline

The storage of hydrogen in the form of solids (hydrides) in transition metals has been extensively studied due to their light-weight nature and their high solubility for hydrogen. In addition to that, the dissociation of hydrogen molecule on the metal surface is exothermic and therefore, no external form of energy is needed to enable adsorption. However, optimisation of parameters of hydrogenation can be done in order to increase the interaction of hydrogen molecules with the metal surface as well as increasing the energy of adsorbed hydrogen atoms in order to enable them to be absorbed. In spite of the good properties pointed above, less progress has been achieved in terms of quantifying the exact amount of hydrogen absorbed by transition metals. Gravimetric methods, which consider the weight difference as the weight of the hydrogen absorbed, and volumetric methods, which monitor the change in pressure during the charging, are mostly used. Furthermore, the change in electrical resistance of the metal can also be used as an indicator for absorption of hydrogen. These methods assume that the changes in the system occur as a result of the effect of hydrogen only.

The aim of this work is to study the effect of the following hydrogenation parameters on the resulting hydrogenated material in order to optimise the microstructure through various methods to improve the sorption process:

➢ Systematic-temperature

➢ Systematic-pressure

- ➢ Gas concentration

- ➢ Time

- ➢ Alloying

- ➢ Coating

A comparison will be made between the systems with regards to their hydrogen capacity, hydride formation and structural changes under the conditions mentioned above.

The outline of this thesis is as follows:

In *Chapter One*, a general background and physical theory involved in metals intended for hydrogen storage systems was given. The chapter highlighted the current state of hydrogen storage systems research around the world and the need for further research. The properties of the "ideal material" for hydrogen storage were also discussed.

Chapter Two will describe the mechanism of hydrogen absorption in transition metals. The factors that affect the solubility of metal hydrogen systems will be discussed in details as well as the transition metals and their alloys that will be used in this study. The permeation of hydrogen in the materials and the hydride formation mechanisms will also be highlighted.

Chapter Three will discuss all the analytical techniques that will be used in this study to investigate the effects of hydrogenation on Pd, Pd-Pt alloys, Pd-Pt coating, CP-Ti and Ti-6Al-4V alloy as well as the annealing effect on CP-Ti and Ti-6Al-4V alloy. Detailed theoretical background, upon which each technique is based, will be given. Moreover, the characterisation procedure and parameters used for each technique will be explained in detail.

Chapter Four will report and discusses the experimental parameters that enhance hydride formation in Pd, Pd-Pt coating and Pd-Pt alloys. Furthermore, sorption and desorption of

hydrogen in Pd and different compositions of Pd-Pt alloys studied over a wide range of systematic-pressures will also be discussed. The concentration of hydrogen in the charged materials will also be determined via various methods.

Chapter Five reports and discusses the effect of annealing, thermohydrogen treatment and room temperature hydrogenation on the microstructure and micro-hardness of CP-Ti and Ti-6Al-4V alloy. The hydrides formed during hydrogenation processes, the variation of the α- and β-phases volume fractions and the morphology evolution with temperature will be discussed in comparison to the amount of hydrogen absorbed.

Chapter Six will summarise the findings of *Chapters Four* and *Five* and provide details on possible future studies.
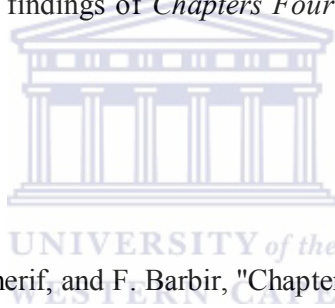
1.3   References

[1.1] T. Nejat Veziroglu, S.A. Sherif, and F. Barbir, "Chapter 7 - Hydrogen Energy Solutions", in: Franklin J. Agardy, Nelson Leonard Nemerow (Eds.), Environmental Solutions, Academic Press, Burlington, pp. 143-180 (2005).

[1.2] S.M.F. Valverde, Geofísica Internacional, 223-228 (2002).

[1.3] V.A. Goltsov, T.N. Veziroglu, and L.F. Goltsova, Int. J. Hydrogen En., 31, 153-159 (2006).

[1.4] A. Zuttel, P. Wenger, P. Sudan, P. Mauron, and S. Orimo, Mat. Sc. En., B, 108, 9-18 (2004).

[1.5] L. Schlapbach and A. Zuttel, Nature, 414, 353-358 (2001).

[1.6] A. Bain and W.D. Van Vorst, Int. J. Hydrogen En., 24, 399-403 (1999).

[1.7] V. Goltsov, T.N. Veziroglu, and L. Goltsova, Int. J. Hydrogen En., 31, 153-159 (2006).

[1.8] E.S. Kikkinides, Comput. Chem. Eng., 35, 1923-1936 (2011).

[1.9] V. Berube, G. Radtke, M. Dresselhaus, and G. Chen, Int. J. En. Res., 31, 637-663 (2007).

[1.10] R. Wiswall, Hydrogen in Metals II , 201-242 (1978).

[1.11] B. Sakintuna, F. Lamari-Darkrim, and M. Hirscher, Int. J. Hydrogen En., 32, 1121-1140 (2007).

[1.12] M. Conte, P.P. Prosini, and S. Passerini, Mat. Sc. En. B, 108, 2-8 (2004).

[1.13] T. Wu and J. Wu, Mater. Chem. Phys., 74, 5-12 (2002).

[1.14] F.A. Lewis, Platinum Met. Rev, 52, 120-122 (2008).

UNIVERSITY *of the*
WESTERN CAPE

Chapter 2: .   Literature review

2.1   Hydrogen storage in transition metals

The absorption of hydrogen by transition metals has been investigated over a wide range of operation temperatures, system pressures, and hydrogen gas concentrations [2.1,2.2]. The dissociation of hydrogen on transition metal surfaces occurs freely and results in the formation of strong atomic hydrogen bonds [2.3]. The charging of metals and metal alloys with hydrogen can be conducted in molecular hydrogen gas or by hydrogen atoms from an electrolyte; a process known as electrochemical hydrogenation, shown in Figure 2-1. Electrochemical charging occurs in an aqueous solution whereas gas charging occurs directly in a hydrogen gas environment. The similarity in both cases is that the interaction between hydrogen and the metal surface involves physical adsorption, chemisorptions, diffusion and hydride formation [2.4-2.6].
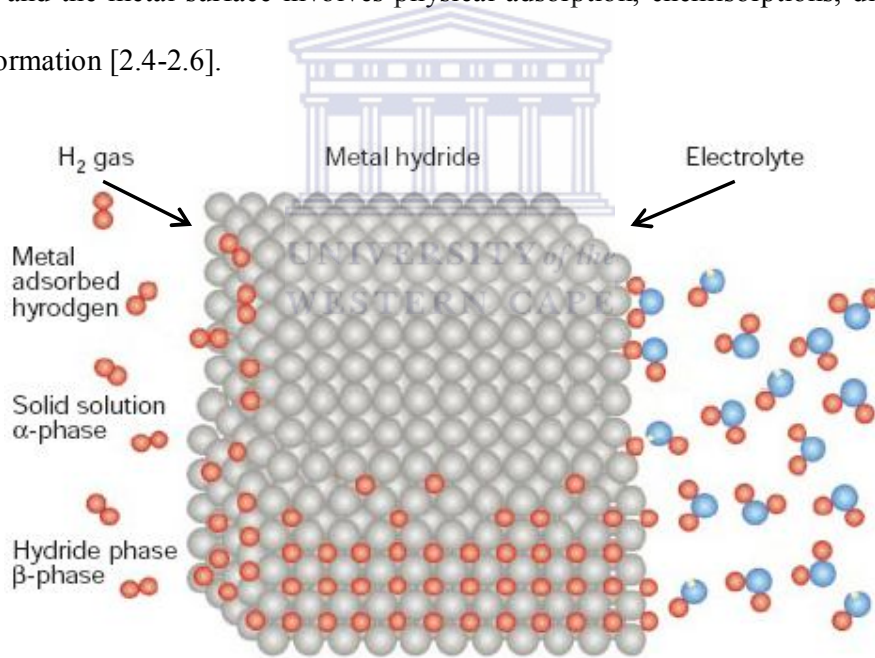
Figure 2-1: Direct gas and electrochemical hydrogenation of metals/metal alloys. The blue and brown spheres represent oxygen and hydrogen respectively [2.6].

During gas hydrogenation, diatomic hydrogen readily dissociates into monatomic form when it comes into contact with the metal surface as depicted in Figures 2-1 and 2-2. The reaction

process is exothermic, thus no external energy is needed to initiate the dissociation. In order for this absorption from the gas phase to occur, the surface of the metals should be sufficiently clean so that the $H_2 \rightarrow 2H$ reaction readily occurs during contact [2.5]. The mechanism of interaction between hydrogen and transition metals /metal alloys can be described by equation 2-1 [2.7].

$$H_2 \xleftrightarrow{(H_2{}^+)_{ad}} 2(H^+)_{ab} + 2e^-(metal) \tag{2-1}$$
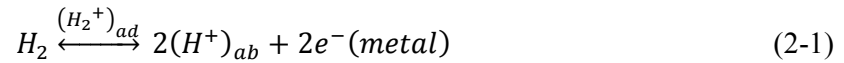
where $(H_2{}^+)_{ad}$ is the adsorption of hydrogen ion occurs near the surface regions and

$(H_2{}^+)_{ab}$ is the ionisation of $H_2{}^+$ ion within the bulk material.
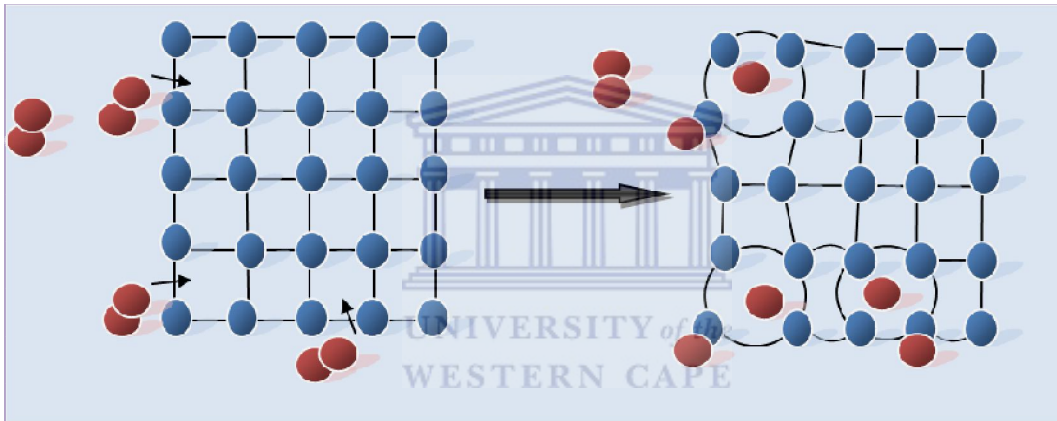
Figure 2-2: Illustration of the gas hydrogenation of a metal/metal alloy: $M + \frac{1}{2}H_2 \leftrightarrow MH_x$ where M represents the metal or metal alloy.

The chemical potential of H in the gas phase is given by:

$$\mu_H(g) = \frac{1}{2}\left(\mu_{H_2}{}^0 + RT\ ln\rho_{H_2}\right) \tag{2-2}$$

where $\mu_{H_2}{}^0$ standard chemical potential at infinite dilution of hydrogen, R the gas constant, T the absolute temperature in (K) and ρ_{H_2} the hydrogen partial pressure in the system [2.5].

Equilibrium between gaseous molecular hydrogen and hydrogen dissolved in the metals and metal alloys is rapidly established, provided that diffusion paths in the solid phase are not too long [2.5]. The hydrogen chemical potential within the solid will be governed by kinetic and not thermodynamic factors. Due to the high electron affinity of transition metals, hydrogen dissociates exothermally to occupy interstitial sites in the metal lattice. The neighbouring metal atoms are pulled further apart from each other as a result of the hydrogen ions insertion. The elastic strain exerted between the atoms increases the volume of nearest-neighbour shell of atoms, thus increasing the lattice parameter of the metal solution as well as reducing the cohesive forces between metal atoms [2.8,2.9]. Due to the increase of the unit cell's volume, the lattice of the metal/ metal alloy often loses its high symmetry, for example, from cubic system to hexagonal. The cohesive energy of the metal atoms is related to the extent to which the lattice expands [2.10]. After hydrogenation, some of the strain energy between the metal atoms is released, which is believed to be the driving force for the nucleation of a hydride phase. This nucleation process has been studied using statistical models by assuming that there is attractive interaction pair between hydrogen atoms in adjacent lattice sites [2.11].

The thermodynamic aspects of hydride formation from gaseous hydrogen are described by pressure-composition isotherms such as $LaNi_5$ in Figure 2-3 [2.6]. The amount of hydrogen absorbed as well as the volume fraction of the phases present in the $LaNi_5$ alloy depends on pressure and temperature of hydrogenation. It can be observed that the α-phase is stable at low hydrogen concentration while β-phase is stable at higher hydrogen concentration with the (α+β) dual phase co-existing in between. The length of plateau, also known as equilibrium pressure, determines how much of hydrogen can be stored reversibly with small pressure

variations. The plateau depends strongly on temperature and is related to the changes of enthalpy and entropy in the material [2.6].
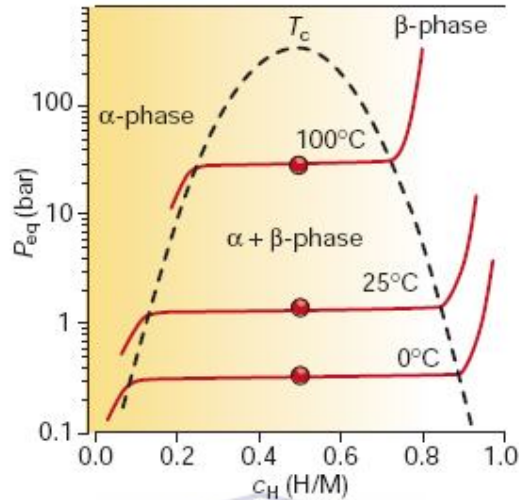
Figure 2-3: Phase diagram of metal hydrides [2.6]

The entropy change occurs when molecular hydrogen gas is dissolved into the material. The interaction between a hydrogen atom and transition metal is illustrated by the potential energy diagram shown in Figure 2-4. The surface bond is characterised by the heat of adsorption (E_{ads}) while the equivalent quantity for the bulk is the heat of solution ($\Delta \overline{H}^{\infty}$). In general, the heat of adsorption is larger than the heat of solution resulting in a higher concentration of hydrogen at the surface than into the bulk [2.12,2.13]. However, *Romanowski et al.* [2.14] studied the interaction between hydrogen and transition metals by density of functional theory (DFT). From this study, it was found that the interaction between hydrogen atoms is almost repulsive. Certain treatments for metals, such as ball milling, increase the adsorption of hydrogen atoms. Ball milling has the benefit of reducing the grain size whereby the concentration of defects increases and the diffusion path of hydrogen in the bulk of the material is shortened [2.6]. The lattice imperfections formed, such as edge dislocations, act as hydrogen traps in the material.
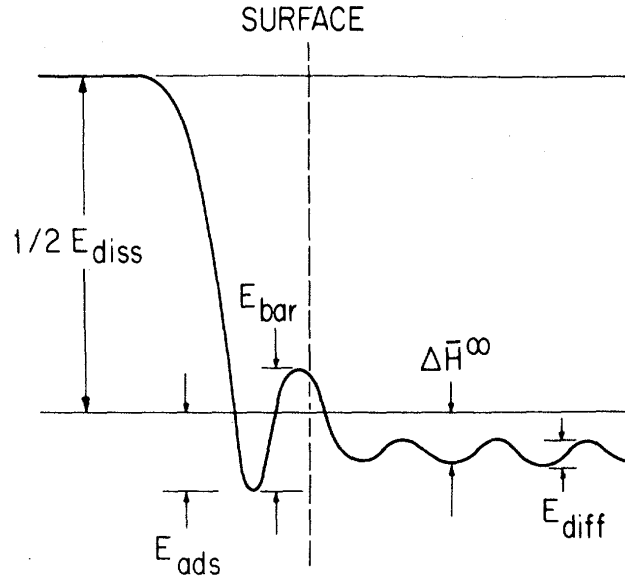
Figure 2-4: A schematic potential-energy diagram for a hydrogen atom between the gas phase on the left and the bulk of a transition metal on the right [2.12].

Savyak et al. [2.15] used differential scanning calorimetry (DSC) to study the thermal behaviour of hydrogen in transition metals and metal alloys at a constant heating rate. Another technique used was thermal desorption analysis (TDA) in an ultra-high vacuum chamber coupled with a quadruple mass spectrometer. However, the permeability of hydrogen in the material of interests has to be known and it can be described by an Arrhenius-type relation given in Equation 2-3:

$$k = k_0 exp\left(\frac{-E}{RT}\right)(mol/msPa^{1/2}) \tag{2-3}$$

where k_0 is the hydrogen permeability constant (mol/(m s Pa$^{1/2}$)), E is the activation energy (J/mol), R is the gas constant (8 .314 J/(mol K)) and T is the temperature in K.

The evaluation of the solubility of hydrogen in metals was conducted by applying Sieverts' law, described by Equation 2-4.

$$\sqrt{\frac{p}{p_o}} = K_s x \qquad\qquad (2\text{-}4)$$

$$ln\,K_s = -\frac{\Delta S_s}{R} + \frac{\Delta H_s}{RT} \qquad\qquad (2\text{-}5)$$

where p, p_0, K_s, ΔS_s, ΔH_s, and R are the hydrogen pressure, the standard pressure, the Sieverts' constant, the solution entropy of hydrogen, the solution enthalpy of hydrogen and the gas constant, respectively [2.16].

2.2 Factors affecting hydrogen solubility of metal-hydrogen systems

2.2.1 Operation temperature

The solubility of hydrogen varies in different metals and alloys. Some metals such as Pd have higher solubility at temperatures below 300 ˚C whereas others like titanium are more soluble at approximately 550 ˚C [2.5,2.17,2.18].
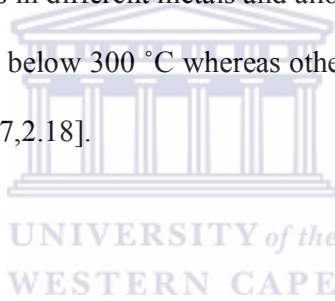
2.2.2 System pressure

High pressure systems increase the solubility of hydrogen in metals and metal alloys. The equilibrium between the metal environment and its inner surfaces is reached fast and therefore the adsorbed hydrogen ions diffuse into the bulk of the material [2.19,2.20].

2.2.3 Hydrogen gas concentration

The adsorption rate of hydrogen in transition metals and alloys depends on the concentration of the gas. The higher the gas concentration, the higher the probability for the reaction between hydrogen atoms and the metal surface, and therefore the larger will be the adsorption/ absorption [2.20,2.21].

2.2.4 Time

The saturation of hydrogen atoms in metals and metal alloys depends on the achievement of equilibrium between the metal and its surrounding. This depends also on the gas concentration, the state of the material and the alloy composition [2.5].

2.2.5 Alloying

Solubility of hydrogen in metal alloys depends on the alloy's composition [2.22,2.23]. Additional elements change the critical hydride phase formation temperature and affect the rate of absorption of hydrogen into the materials. The α→β phase transition temperature and the solubility of hydrogen can be increased or decreased by changing the content of alloying element. The additional elements act as hydrogen traps in the metal matrix [2.20,2.21].
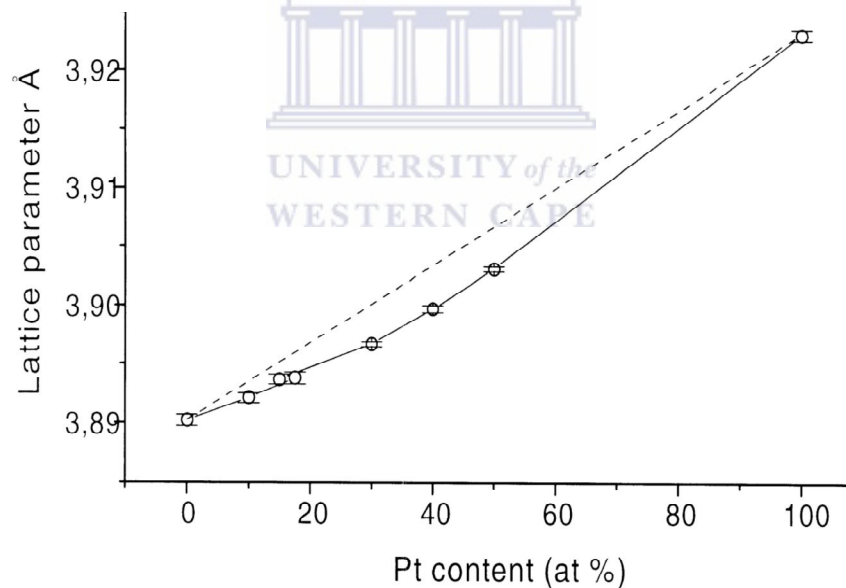
Figure 2-5: Lattice parameters of Pd-Pt alloys as a function of Pt content. The dashed line represents Vegard's law stated in equation 2-6 [2.27].

However, the experimental results obtained by several researchers including, *Moysan et al.* [2.24] show discrepancies in the Pd/Pt alloy lattice parameter as indicated in Figure 2-5. The

lattice parameter does not vary linearly with the Pt content. It is less expanded than expected with regard to Vergard's law which states that:

$$a_{alloy} = x_{Mpd}a_{Mpd} + x_{Mpt}a_{Mpt} \qquad (2\text{-}6)$$

where a_M denotes the lattice parameter of metal M and x_M the atomic fraction of M in the alloy [2.12,2.25,2.26].

2.2.6 Oxides

Oxide formation of the samples occurs during hydrogenation. The thin layer of oxide reduces the kinetics of diatomic hydrogen dissociation on the metal surface. The rate of penetration of the dissociated hydrogen atoms is slowed down and therefore affects the diffusion of atoms occupying interstitial sites in the metal [2.20].
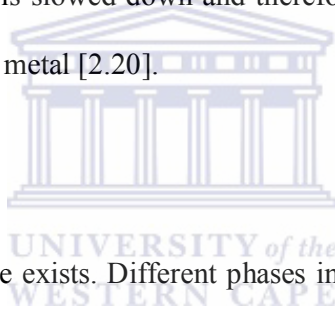
2.2.7 Microstructure

In pure metal only a single phase exists. Different phases in metal alloys respond differently when the material absorbs hydrogen, for example, the α-phase absorbs less hydrogen while β-phase absorbs more hydrogen. Therefore, hydrogen trapping characteristics of the microstructure will strongly influence the hydrogen concentration, particularly at lower temperatures [2.20]. For small-sized systems like thin films and nano-scaled microstructures, surface, grain/phase boundaries and interface-related sites change the overall solubility of hydrogen [2.28]. Hydride phases may accidentally be formed during sample preparation, rolling or polishing of samples [2.29,2.30].

2.3 Potential materials for hydrogen storage systems

Palladium (Pd), palladium-platinum (Pd-Pt) alloys and Pd-Pt coatings along with commercially pure titanium (CP-Ti) and Ti-6Al-4V alloy were considered as good candidates

for hydrogen storage systems. They absorb hydrogen in large amounts without the deterioration of their structure. There is a lot of research conducted on these materials which continues to be invaluable in solving the hydrogen storage challenge.

2.3.1 Pd and Pd-Pt alloy

Palladium and platinum are Group VIIIa metals and they are known as Platinum Group Metals (PGMs) that have a face-centered cubic (fcc) structure. Palladium and platinum atoms have 1.37 Å and 1.39 Å atomic radii, respectively, at room temperature.

Table 2-1: Properties of the platinum group metals [2.5]

	Ru	Rh	Pd	Os	Ir	Pt
Atomic weight (g/mol)	101.07	102.9	106.4	190.2	192.2	195.1
Crystal structure	h.c.p	f.c.c	f.c.c	h.c.p	f.c.c	f.c.c
Lattice constant at 20 ˚C- kx units 1 kx = 1.0022 Å	-	3.7963	3.8829	-	3.8317	3.9152
Density at 20 ˚C g/cm^3	12.45	12.41	12.02	22.61	22.65	21.45
Melting point (˚C)	2310	1960	1552	3050	2443	1769
Electrical resistivity at 0˚C μΩ/cm	6.8	4.33	9.93	8.12	4.71	9.85
Magnetic susceptibility at 18 ˚C (c.g.s. units x 10^6)	0.5	1.11	5.4	0.05	0.15	1.1

Table 2-1 gives the properties of PGMs. *Yu et al.* [2.31] has indicated that Pd has a critical temperature of 292 ˚C whereas *Yun et al.* [2.32] reported 298 ˚C. Furthermore, Pd is less

resistant to nitric and sulphuric acids. Since Pd cracks when it is charged with hydrogen, particularly when it is in its pure and annealed form, it must be strengthened and toughened by alloying [2.33]. Alloying Pd with another platinum group metal may exhibit various characteristics for hydrogen absorption with interest from both the fundamental and practical point of view. The alloying of Pd with PGMs will reduce the critical temperature of the hydride phase transformation and effectively modify the rate of absorption and desorption of hydrogen [2.34]. In this case, hydrogen absorption is more important since the objective of this project is hydrogen storage. Moreover, Pd alloys show very high selectivity for the hydrogen permeation [2.35]. The alloying of Pd with Pt forms substitutional face-centered-cubic (fcc) solid solutions with low transformation temperature from α- to ß-phase in order to avoid phase distortions [2.17,2.32, ,2.37]. The Pt atoms expand the lattice parameter of the Pd-Pt alloy slightly [2.24]. The increased atomic distance in the alloy enhances atomic diffusion. Some of Pd alloys, such as Pd-19 at. % Pt reported by *Moysan et al.* [2.24], exhibit a critical temperature for α→β transformation at room temperature. Pt has been chosen as a substitutional element in Pd, due to its low melting point and high electrical resistivity as compared to the other PGMs. Furthermore, platinum has a high oxidation resistance. These characteristics are responsible for the low critical temperatures needed for phase transformations with the possibility for the material to achieve superconductivity during hydrogenation [2.36]. Therefore, the Pd and Pd-Pt alloy systems are the favourites in the following applications: rechargeable batteries, cooling devices, transportation, and hydrogen storage systems for fuel cells. The high diffusivity of hydrogen also makes nano-scaled metal-hydrogen systems interesting candidates for sensor applications [2.38,2.39].

Hydrogen form hydride bonds with Pd even in Pd-Pt alloys due to the fact that Pt is insoluble to hydrogen [2.7]. Hydrogen occupies the fcc site in the Pd lattice and the equilibrium of

hydrogen in bulk palladium has been obtained down to -106 ˚C and to even lower temperatures, i.e. -153 ˚C in thin films of palladium [2.40,2.41]. Under atmospheric pressure of hydrogen and room temperature, Pd can absorb up to $\sim 10^3$ volumes of H_2, which corresponds to atomic ratio $PdH_{0.7}$ [2.7]. Its ductility property is not affected by the hydride formation [2.17]. The solubility of hydrogen in palladium is depicted in Figure 2-6 whereby the absorption decreases with an increase in hydrogenation temperature [2.5,2.25,2.26]. Because of the high absorption capacity of Pd at temperatures below 300 ˚C, the Pd-H system is often used as a model system to understand the process of hydrogen absorption in solid materials [2.43,2.44]. Hydrogen atoms are randomly distributed over the octahedral sites in the Pd lattice where there is 1 per Pd atom [2.4,2.45,2.46]. The incorporation of hydrogen in Pd lattice results in a decrease of electronic mobility and the formation of β-phase of PdH_x where $x \geq 0.6$ [2.47].
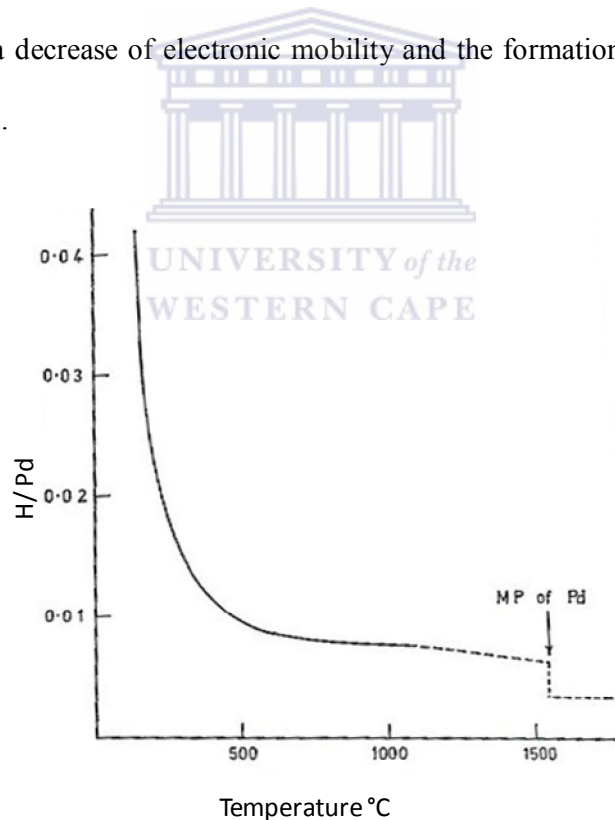
Figure 2-6: A curve of H/Pd vs temperature under normal pressure, showing an exponential decrease of solubility of hydrogen in Pd with increasing temperature. The solubility in Pd is higher at temperatures below 300 ˚C [2.5,2.42].

However, at high temperatures it is possible that both tetrahedral and octahedral sites are partially occupied [2.48-2.51]. High concentration of hydrogen transform Pd to a polymorphic material [2.6,2.11]. The hydrogen uptake in Pd depends on the initial grain size of the microstructure. The solubility of hydrogen is higher when the Pd grains are large. The average grain size of the sample decreases with an increase in hydrogen content following the large amount of dislocations formed. However, this occurs at longer charging time and high temperatures where grain recrystallisation occurs [2.28,2.52].

2.3.1.1 Permeation of hydrogen in Pd

The schematic energy level diagram for the Pd-H system presented in Figure 2-7 displays the steps and activation energies inherent in the model. The postulate of this model ignores external resistance of the gas to mass transfer in order to allow the effects of surface versus bulk processes in Pd to be observed without the complication of external mass transfer.
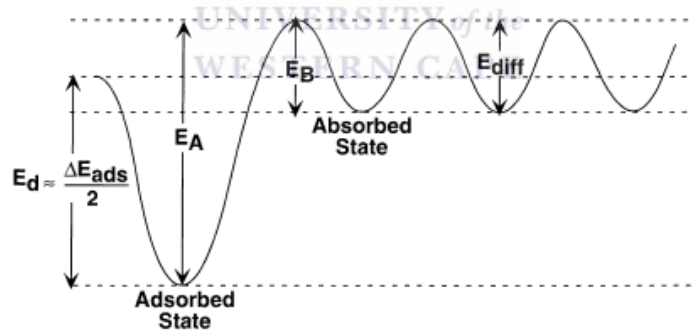
Figure 2-7: Energy level diagram used to model hydrogen permeation through Pd. E_A is activation energy for surface to bulk transition and E_B is the activation energy for the bulk metal to-surface transition all in (kcal/mol H) [2.53].

The transition rate of hydrogen from the adsorbed surface into the bulk metal is described by Equation 2-7:

$$surface\ to\ bulk\ rate = N_s N_b v_d \theta (1 - X_s) \qquad (2\text{-}7)$$

where N_s is the surface Pd atomic concentration, N_b is the bulk Pd atomic concentration , X_s the H/Pd ratio in the bulk metal adjacent to the surface, θ is surface coverage, and v_d is the activated rate constant for the surface-to bulk transition, given by:

$$v_d = v_0 exp\left(-E_A/RT\right) \tag{2-8}$$

where E_A is activation energy for surface to bulk transition and v_0 the activated rate constant for the bulk- to surface

The surface to bulk transition of hydrogen requires a vacant site in the bulk, which shows that the rate is dependent on the surface concentration and the vacant site concentration in the bulk. A value of E_A can be estimated based on the relationship described in Equation 2-9

$$E_A - E_B = (\Delta E_{ad} - \Delta E_{ab})/2 \tag{2-9}$$

where E_B is the activation energy for the bulk metal to-surface transition, ΔE_{ad} and E_{ab} are the heats of adsorption and absorption, respectively, in kcal/mol H_2.

Adsorption is only important at very low hydrogen partial pressures or in the presence of substantial surface contamination where desorption is the rate-limiting process particularly at low temperatures. The hydrogen permeability in palladium can be described by Equation 2-10:

$$k = \frac{1}{2}D_M K_S \tag{2-10}$$

where D_M is diffusion coefficient of hydrogen atom in metal (m^2/s) and K_S Sieverts constant (mol/(m^3 Pa$^{1/2}$)) [2.54].

The diffusion coefficient of hydrogen in palladium (D_H) is relatively large at 25 ˚C and is described by Equation 2-8:

$$D_H = 2.5 \times 10^{-7} exp \left[\frac{21.8 \ (kJ/mol\ )}{RT} \right] (m^2/s) \qquad (2-11)$$

2.3.1.2 Hydride formation in Pd

Subjection of palladium and its alloys to hydrogen increases the lattice volume while retaining the face centered-cubic structure [2.55-2.57]. The change in volume accompanying the phase transformation can give rise to strain and recrystallisation, which lead to formation of defects in bulk material and at the grain boundaries [2.32]. Hydrogen induces phase transformation and the process can be described by the phase diagram of Pd in Figure 2-8.
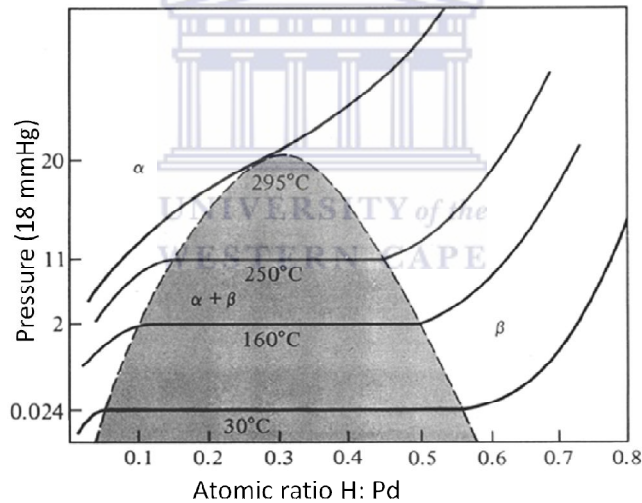
Figure 2-8: Phase diagram of Pd-H system at different temperatures, hydrogen content and pressures. The α- and β- phases co-exist in the shaded region [2.17,2.58].

At small concentrations of hydrogen, the dissolved hydrogen behaves ideally, and Sieverts' law as described in equation 2-3 is obeyed. The alpha-phase's non-ideal behaviour begins as the hydrogen concentration increases until the formation of a hydrogen-rich β- phase. Studies conducted by *Yu et al.* [2.31] at a temperature range from room temperature to 292 ˚C and

pressure range of 1×10^{-6} to 1.9×10^{-5} mbar showed that the α- to ß- phase hydride transition proceeds by a process of nucleation and growth. The kinetics of these transformations is similar to the C-shaped diagrams of austenite transformation in steels and of ß-phase in Ti alloys. The alpha phase (α) of Pd is maintained until a 0.025 c/a ratio is achieved. The (α+ß) co-exist between 0.025 and 0.6 atomic fraction in which the volume fraction of β- phase decreases with an increase of hydrogenation temperature. At concentrations greater than 0.6 atomic fraction, the alpha phase disappears completely and the beta phase remains [2.25,2.42].

The β phase has a considerably expanded lattice as compared to α-phase. Therefore the nucleation and growth of β-phase in the α matrix sets up severe strains in the material resulting in distortion, dislocation multiplication and hardening in order to accommodate the volume change [2.17,2.59]. Edge dislocations exhibit a strong interaction with hydrogen atoms because they act as traps for hydrogen. *Weissmuller and Lemier* pointed out that hydrogen accumulation at the grain boundaries does not result in an increase in lattice constant, but in stress contributions [2.59]. Diffusion of the hydrogen through the palladium is attributed to the jumping of hydrogen atoms through the octahedral interstitial sites of the face-centered cubic palladium lattice [2.54].

2.3.1.3   Hydride formation in Pd-Pt alloys

The isobars for the Pd-Pt-H system always show a decrease in hydrogen solubility at any given temperature as the platinum content in the Pd-Pt alloy increases due to volume effects caused by changes in the host lattice [2.6]. This occurs because the atomic radii of Pt are larger than that of Pd. The width of plateau region reduces sharply with an increase in Pt content [2.60]. Therefore, the presence of Pt reduces the solubility of the alloy and the

hydrogen capacity decreases with an increase in the Pt content. A comparison diagram of hydrogen absorption between different compositions of Pd-Pt alloys is shown in Figure 2-9. *Moysan et al.* [2.24] explained the solubility decrease of hydrogen in Pd-Pt alloys by the filling up the palladium conduction band by the valence electrons of platinum. Low-pressure studies by Lewis et al have shown that the range of hydrogen contents over which a phase transformation is occurring, decreases with increasing Pt content [2.5,2.61]. Therefore, the processes of absorption and desorption changes with alloying. Furthermore, *Lewis et al.* [2.62] reported that elastic effects in Pd-Pt alloys are responsible for the drastic modification of the diffusion behaviour of hydrogen in the alloy.
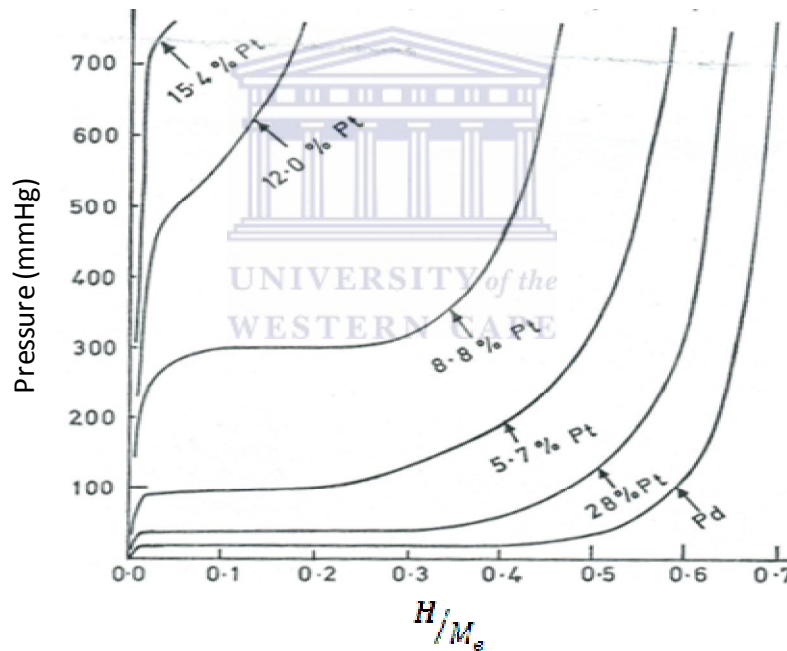
Figure 2-9: Pressure vs H/Me curve showing the solubility of Pd and Pd-Pt alloys to hydrogen at room temperature. Pd has the highest solubility at atmospheric pressure. Me represents Pd or Pd-Pt alloys.[2.5].

Hydrogen migration towards the opposite direction of the overall gradient in the chemical potential was observed. The β- hydride phase formation temperature in the alloy is lowered.

However, according to the curve in Figure 2-9, the capacity of the Pd-Pt alloys decreases with an increase in Pt content. It is shown that Pd-Pt alloys composed of 8.8 at. % Pt content and more need high pressures in order to absorb hydrogen. However, the plateaus indicate that although the hydrogenation takes place under high pressures, less hydrogen will be absorbed.

2.3.2 Thin films

Thin films deposited on Pd substrates improve the diffusion rate of the material [2.53]. They experience compressive stresses during hydrogen loading. The coatings provide high mobility to hydrogen atoms which occupy interstitial positions in the host metal lattice [2.45,2.63]. Interstitial diffusion exists inside the coatings, enabling easier achievement of thermodynamic equilibrium even at room temperature. Dislocations are always present in the coatings because they are introduced as a result of thermal stresses that appear during the solidification of the melt. Hydrogenation of the material also creates dislocations that results from the lattice mismatch between matrix and precipitate, as *Schober et al.* [2.64] has shown for Nb-H system using transmission electron microscopy. The lattice misfits between the film and substrate affect the film's microstructure and the built-in stress in the coating [2.65,2.66]. The lattice parameter increases with substitution of Pt but the stability of the corresponding hydride decreases [2.67].

2.3.3 CP-Ti and Ti-6Al-4V alloy

Titanium is a group IV transition metal with a density of 4.5g/cm^3 and a melting point temperature of 1670 ˚C. At room temperature and under atmospheric pressure, commercially pure titanium (CP-Ti) has hexagonal close-packed (hcp) structure called the α-phase with a low thermal conductivity. The α-phase transforms completely to a body-centered cubic (bcc)

crystal structure called the β-phase at a temperature of 920 ˚C [2.68,2.69]. However, *Kao et al.* [2.70] observed the commencement of this change at 883 ˚C whereas *Yuan et al.* [2.71] observed it at 890 ˚C, which is known as beta transus temperature. At this temperature, CP-Ti exhibits an allotropic phase transformation [2.72]. Titanium has a high hydrogen affinity [2.73] and according to theoretical calculations performed by *Xu et al.* [2.74] and *Tao et al.* [2.75], the hydrogen atoms prefer octahedral sites at low hydrogen concentrations and tetrahedral sites at high concentrations. Since high hydrogen concentrations will cause phase transformations, hydrogen atoms would therefore occupy octahedral sites in the α-phase and tetrahedral sites in β-phase. The sites are larger in β (bcc) phase than in α (hcp) phase and therefore *Senkov et al.* [2.76] assumed that hydrogen should be more soluble in ß-phase than in α-phase. Moreover, the introduction of hydrogen reduces the phase transformation temperature of α to β phase from 883 ˚C to temperatures just above 300 ˚C in Ti, depending on hydrogen concentration [2.77].
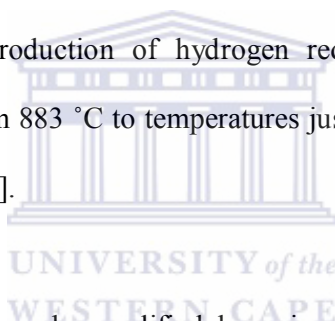
The solubility of pure metals can be modified by using metal alloys. For technological applications, a combination of α and ß phases is desired to strengthen the material. The ability of hydrogen to be added to or removed from titanium and its alloys makes it a unique temporary alloying element [2.74,2.75,2.77,2.78]. The high solubility of hydrogen in a wide range of titanium-based alloys is shown in Figure 2-9 [2.79]. The material for which the chemical activity is the lowest has the highest solubility for hydrogen.

Looking at the activity graph in Figure 2-10, CP-Ti and Ti-6Al-4V alloy have high solubility for hydrogen. Titanium is alloyed with α and ß stabiliser elements such as aluminium (Al) and vanadium (V) to form Ti-6Al-4V alloy. The Al in the alloy reduces the density, stabilises and strengthens the α- phase, while V provides a greater amount of the ß- phase. The amount

of α- phase or β- phase present in the Ti-6Al-4V alloy depends on the composition and preparation conditions. The alloyed transition metal always exhibits a higher beta transus temperature than the unalloyed transition metal. For example, Ti-6Al-4V alloy has a 990 ˚C beta transus temperature which is influenced by the presence of Al compared to CP-Ti that has a beta transus temperature of 883 ˚C [2.71,2.80,2.81].
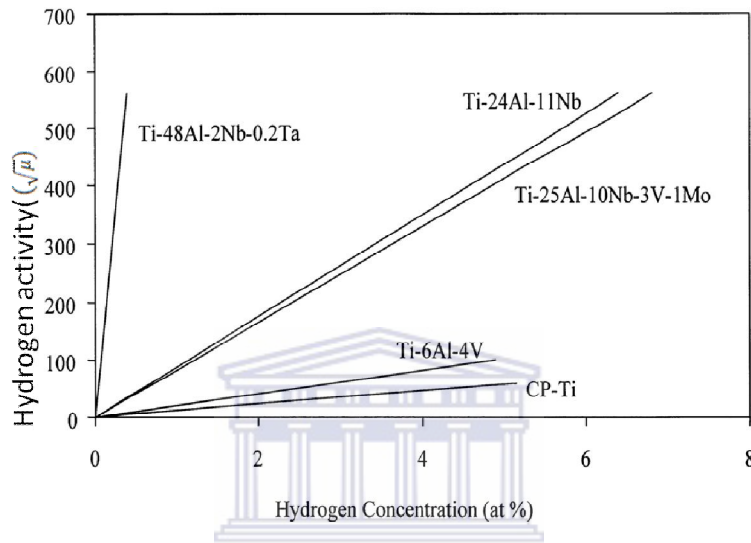
Figure 2-10: Hydrogen activity for selected titanium alloys at 800 ˚C [2.79]

Titanium alloys are widely used in many industries due to an abundant resource base, high chemical durability, good biocompatibility and corrosion resistance at 300 ˚C, castability and low density. [2.82,2.83].

Hydrogen improves the hot workability, machinability and refines the microstructure of titanium alloys [2.73,2.84-2.91]. It allows the titanium alloy to be processed at lower stresses and lower temperatures, since an absorbed hydrogen atom affects the strength of inter-atomic bonds between titanium atoms in the α-phase. Subsequently, the lattice volume of Ti increases following an increase of the hydrogen absorption c/a ratio [2.92]. Furthermore, significant changes in the structure, such as transformation of alpha to beta phase, formation

of hydrides and martensite, will occur [2.71]. It should be noted that the α-phase absorbs less hydrogen as compared to β-phase. Hydrogen can be easily introduced into titanium and titanium alloys by using controlled diffusion from a hydrogen environment at either room or high temperature. The interaction between hydrogen and Ti at high temperature is reversible and in Ti-based alloys, this heat treatment is known as thermo-hydrogen treatment (THT) process [2.79,2.80,2.85,2.93]. Thermo-hydrogen treatment is based on the effects of hydrogen-induced phase transformations.

2.3.3.1   Hydride formation in Ti

The α-phase in CP-Ti can absorb hydrogen at both room and high temperature. There are four homogeneous phase states which may be detected in the Ti-H system under equilibrium conditions, Figure 2-11, the hcp α- structure, bcc ß- structure, face-centered tetragonal (fct) γ- and fcc δ- hydride structures [2.36,2.72,2.73,2.107,2.108].
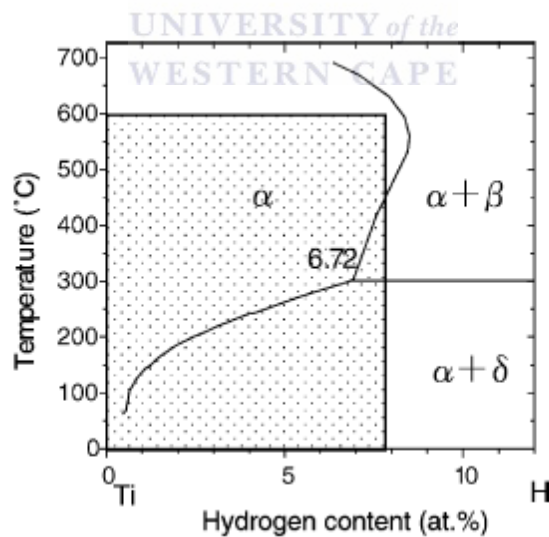
Figure 2-11: CP-Ti-H phase diagram [2.18].

The α-phase contains minor amounts of hydrogen, the ß-phase may contain up to 50 at. % of hydrogen, and γ-phase of fcc structure and γ-phase of fct structure 60 - 63 % and 66 - 66.7 at.

% of hydrogen, respectively. The formation of the phases depends on temperature, pressure and hydrogen concentration. At temperatures below 327 ˚C, a δ- hydride phase with CaF_2-type crystal structure can be formed and its growth depends on the hydrogen concentration [2.95]. The bcc ß- phase forms at temperatures just above the hydride formation temperature (327 ˚C). Additional hydrides can be formed from the β- phase [2.96]. Similar hydrides were observed at room temperature corresponding to various amounts of hydrogen, i.e. fct TiH, fct TiH_2 and fcc TiH_{2-x} with x ranging between 0 and 0.4 [2.97-2.99]. *Martin et al.* [2.100,2.101] observed TiH and TiH_{2-x} phases in the transition zone between pure α (hcp) region and (α+β) region. The formation of the TiH_{2-x} phase occurs by nucleation and growth of the TiH phase. The nucleation of the TiH phase is preceded by an ordering of the hcp phase containing a high density of solute hydrogen atoms. The transformation of TiH into TiH_{2-x} takes place with no significant change of orientation with respect to Ti but the density of dislocations increases. The rearrangement of hydrogen atoms in the Ti affects its electronic structure, which can be estimated by molecular orbital calculation [2.76]. The molecular orbital calculations suggested that the solute hydrogen atoms in interstitial sites drew off the 3d electrons from the metallic bond onto the Ti-H bond. The strength of the surrounding metallic bonds deteriorates with addition of hydrogen.

Gao et al. [2.77] studied the mechanism of diffusion of hydrogen in titanium by using a simulation code developed for one-dimensional diffusion controlled phase transformations in multi-component alloy systems (DICTRA). The model was based on thermodynamic and kinetics of hydrogen diffusion in Ti. Glow discharge optical emission spectroscopy was used to measure the depth profiles of hydrogen in the hydrogenated samples. Diffusion coefficient of hydrogen in α-Ti (D_α) and β-Ti (D_β) used were calculated by *Papazoglou et al.* at temperatures from 611 to 829 ˚C, while *Sevilla et al.* [2.102] determined the diffusion

coefficient at temperatures between 347 and 557 ˚C. Equations 2-11 and 2-12 describe the diffusion coefficient of hydrogen in alpha and beta - phase, respectively.

$$D_\alpha = 3 \times 10^{-6} exp \left[\frac{-14700 \pm 650}{RT}\right] (m^2/s) \tag{2-12}$$

$$D_\beta = 6.3 \times 10^{-8} exp \left[\frac{-14180 \pm 500}{RT}\right] (m^2/s) \tag{2-13}$$

where R is the universal gas constant in (J/(K mol)) and T is the absolute temperature in K. The diffusion in TiH_x (D_{TiH_x}) hydride described by equation 2-13 was determined by *Gao et al.* [2.77] by using the diffusion coefficient calculated by *Kaess et al* [2.103].

$$D_{TiH_x} = (2 - x)3.17 \times 10^{-7} exp \left[\frac{-11700}{RT}\right] (m^2/s) \tag{2-14}$$

where x ranges between 1.5 and 1.95 .

The diffusion study has revealed that at temperatures below 300 ˚C, δ-TiH_x is formed with a maximum hydrogen concentration of 0.38 wt. %. Given that the diffusion coefficient of this phase is low, and therefore its growth rate is slow. The β-phase was observed above 300 - 683 ˚C, which is formed from α-phase and then transforms to TiH_x at elevated temperatures. The β-phase forms at grain boundaries of α-phase while the δ-hydrides form within the β-phase. The transformation rate from β- to δ-TiH_x phase is slow even at higher temperatures because of the formation of the δ-TiH_x barrier layer with low hydrogen diffusion coefficient.

2.3.3.2 Hydride formation in Ti-6Al-4V alloy

Figure 2-12 shows the phase diagram of Ti-6Al-4V alloy. According to this diagram, the beta transus temperature ($T_\text{ß}$) decreases from about 1000 to 810 ˚C when the amount of hydrogen increases from 0 - 30 at. %. Below $T_\text{ß}$, the dual phase (α+ß) range is present at hydrogen concentrations less than 15 at. %. A hydride phase (δ), which is observed at higher hydrogen

concentration, is also present above the $T_ß$ where (ß+δ) dual phase coexists [2.105]. *Zhao et al.* [2.104] has studied the effects of hydrogenation on the Al and V alloying elements of Ti-6Al-4V alloy and reported that hydrogen facilitates the increase of V content in the α-phase while the contents of Ti and Al changes significantly. While the contents of Al and V change remarkably in β-phase, the content of Ti changes slightly. Therefore it can be concluded that the diffusion coefficient of alloying elements increases with hydrogen content, which enhance the self diffusion ability of metal atoms and diffusion ability of solute atoms after hydrogenation.
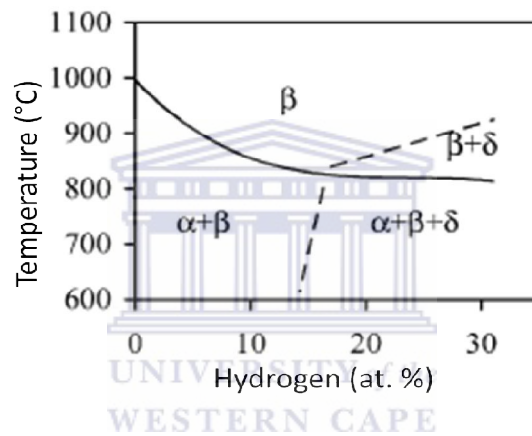
Figure 2-12: Phase diagram of Ti-6Al-4V-H system [2.105].

However, the diffusion coefficient of Al is lower than that of V as reported by *Hou et al* [2.73]. The beta phase starts softening when 0.5 wt. % of hydrogen is absorbed in the alloy. This means that at this region, the critical temperature for plastic deformation of the alloy is increased alloy is improved to higher stress.

Hydrogen improves the beta phase stability and reduces critical cooling rates and characteristic temperature of martensitic transformations. Titanium and its alloys have been extensively utilized in various fields such as chemical plants, nuclear materials and aerospace

components and more attention has been paid for application of Ti-based systems as hydrogen storage materials [2.18] .

2.4   References

[2.1] J.F. Lynch and T.B. Flanagan, J. Phys. Chem., **77**, 2628-2634 (1973).

[2.2] J. Zimbrick and L. Kevan, J. Chem. Phys., **47**, 2364 (1967).

[2.3] P. Ferrin, S. Kandoi, A.U. Nilekar, and M. Mavrikakis, Surf. Sc., **606**, 679-689 (2012).

[2.4] G. Alefeld and J. Völkl, Hydrogen in metals I-basic properties, Springer, **28** (1978).

[2.5] F.A. Lewis, ACADEMIC PRESS, INC., NEW YORK, 178, (1967).

[2.6] L. Schlapbach and A. Zuttel, Nature, **414**, 353-358 (2001).

[2.7] K. Juodkazis, J. Juodkazytė, A. Grigucevičienė, and S. Juodkazis, Appl. Surf. Sc., **258**, 743-747 (2011).

[2.8] R.A. Oriani, Fusion Technol., **26**, 235-266 (1994).

[2.9] A. Mallo and A. Krozer, J. Less-Common Met., **167**, 305-317 (1991).

[2.10] H. Smithson, C.A. Marianetti, D. Morgan, A. Van der Ven, A. Predith, and G. Ceder, Phys. Rev. B, **66**, 144107 (2002).

[2.11] S.B. Gesari, M.E. Pronsato, and A. Juan, Int. J. Hydrogen En, **34**, 3511-3518 (2009).

[2.12] W. Eberhardt, F. Greuter, and E.W. Plummer, Phys. Rev. Lett., **46**, 1085-1088 (1981).

[2.13] M.A. Pick, J.W. Davenport, M. Strongin, and G.J. Dienes, Phys. Rev. Lett., **43**, 286-289 (1979).

[2.14] S. Romanowski, W.M. Bartczak, and R. Wesolkowski, Langmuir, **15**, 5773-5780 (1999).

[2.15] M. Savyak, S. Hirnyj, H.-. Bauer, M. Uhlemann, J. Eckert, L. Schultz, and A. Gebert, J. Alloys Compounds, **364**, 229-237 (2004).

[2.16] O.M. Lovvik and R.A. Olsen, J. Chem. Phys., **118**, 3268 (2003).

[2.17] A.G. Knapton, Platinum Met. Rev., **21**, 44-50 (1977).

[2.18] D. Setoyama, J. Matsunaga, H. Muta, M. Uno, and S. Yamanaka, J. Alloys Compounds, **385**, 156-159 (2004).

[2.19] V. Antonov, I. Belash, V.Y. Malyshev, and E. Ponyatovsky, Platinum Met. Rev., **28**, 158-163 (1984).

[2.20] F. Lewis, Platinum Met. Rev., **26**, 20 (1982).

[2.21] F. Roa and J.D. Way, Fuel Chem. Division Preprints, **48**, 335-336 (2003).

[2.22] A. Carson, T.B. Flanagan, and F. Lewis, Trans.Faraday Soc., **56**, 1332-1339 (1960).

[2.23] A. Carson, T.B. Flanagan, and F. Lewis, Trans. Faraday Soc., **56**, 363-370 (1960).

[2.24] I. Moysan, V. Paul-Boncour, S. Thiebaut, E. Sciora, J.M. Fournier, R. Cortes, S. Bourgeois, and A. Percheron-Guegan, J. Alloys Compounds, **322**, 14-20 (2001).

[2.25] F. Vigier, R. Jurczakowski, and A. Lasia, J. Electroanal. Chem., **588**, 32-43 (2006).

[2.26] F.A. Lewis, K. Kandasamy, and X. Tong, Solid State Phenomena, **73**, 268-301 (2000).

[2.27] I. Moysan, V. Paul-Boncour, S. Thiébaut, E. Sciora, J.M. Fournier, R. Cortes, S. Bourgeois, and A. Percheron-Guégan, J. Alloys Compounds, **322**, 14-20 (2001).

[2.28] K. Sakaki, T. Yamada, M. Mizuno, H. Araki, and Y. Shirai, Mater. Trans.,JIM, **43**, 2652-2655 (2002).

[2.29] Z.H. Cheng, G. MacKay, D. Small, and R. Dunlap, J. Phys. D, **32**, 1934 (1999).

[2.30] R. Dunlap, Z. Cheng, G. MacKay, J. O'Brien, and D. Small, Hyperfine Interactions, **130**, 109-126 (2000).

[2.31] Y.A. Artemenko, M.V. Goltsova, and V.I. Zaitsev, Int. J. Hydrogen En., **22**, 343-345 (1997).

[2.32] S. Yun and S. Ted Oyama, J. Membr. Sc., **375**, 28-45 (2011).

[2.33] R. Oriani, COLD FUSION SOURCE BOOK, 155 (1994).

[2.34] F.A. Lewis, Platinum Met. Rev., **52**, 120-122 (2008).

[2.35] H. Kurokawa, Y. Makino, M. Takahasi, A. Endou, S. Takami, M. Kubo, N. Itoh, P. Selvam, and A. Miyamoto, Theoretical Study on the Hydrogen Absorption Behavior of Palladium and its Alloys.

[2.36] In, W.B.P., A Handbook of Lattice Spacings and Structures of Metals and Alloys, Pergamon Press, New York (1958).

[2.37] M. Hansen, K. Anderko, and H.W. Salzberg, J. Electrochem. Soc., **105**, 260C (1958).

[2.38] D.D. Macdonald, M.C.H. McKubre, A.C. Scott, and P.R. Wentrcek, Ind. Eng. Chem. Fundam., **20**, 290-297 (1981).

[2.39] M. Lischka and A. Groß, Recent Developments in Vacuum Science and Technology, edited by J.Dabrowski (Research Signpost, Kerala, 111–132, (2003).

[2.40] L.L. Jewell and B.H. Davis, Applied Catalysis A: General, **310**, 1-15 (2006).

[2.41] H. Hemmes, A. Driessen, R. Griessen, and M. Gupta, Phys. Rev., B, **39**, 4110 (1989).

[2.42] M.W. Roberts, J.M. Thomas, and R. Burch, The adsorption and absorption of hydrogen by metals, (2007).

[2.43] W.A. Oates and T.B. Flanagan, Prog. Solid State Chem., **13**, 193-272 (1981).

[2.44] T. Xu, M.P. Zach, Z.L. Xiao, D. Rosenmann, U. Welp, W.K. Kwok, and G.W. Crabtree, Appl. Phys. Lett., **86**, 203104 (2005).

[2.45] J. Völkl and G. Alefeld, Hydrogen in Metals I, 321-348 (1978).

[2.46] H. Kurokawa, T. Nakayama, Y. Kobayashi, K. Suzuki, M. Takahashi, S. Takami, M. Kubo, N. Itoh, P. Selvam, and A. Miyamoto, Catalysis today, **82**, 233-240 (2003).

[2.47] P. Agar, B.R. Mehta, D. Varandani, A.K. Prasad, M. Kamruddin, and A. Tyagi, Sensors Actuators B: Chem., **150**, 686-691 (2010).

[2.48] G. Boureau and O.J. Kleppa, J. Chem. Phys., **65**, 3915 (1976).

[2.49] G. Boureau, O.J. Kleppa, and P. Dantzer, J. Chem. Phys., **64**, 5247 (1976).

[2.50] C. Labes and R.B. McLellan, Acta Metal., **26**, 893-899 (1978).

[2.51] D.P. Broom, Int. J. Hydrogen En., **32**, 4871-4888 (2007).

[2.52] Y. Shirai, H. Araki, T. Mori, W. Nakamura, and K. Sakaki, J. Alloys Compounds, **330–332**, 125-131 (2002).

[2.53] T.L. Ward and T. Dao, J. Membr. Sc., **153**, 211-231 (1999).

[2.54] B.D. Morreale, M.V. Ciocco, R.M. Enick, B.I. Morsi, B.H. Howard, A.V. Cugini, and K.S. Rothenberger, J. Membr. Sc., **212**, 87-97 (2003).

[2.55] R.J. Wolf, M.W. Lee, R.C. Davis, P.J. Fay, and J.R. Ray, Phys. Rev., B: Condensed Matter;(United States), 48 (1993).

[2.56] Y. Fukai, The metal-hydrogen system: basic bulk properties, Springer Verlag (2005).

[2.57] T.B. Flanagan, R. Balasubramaniam, and R. Kirchheim, Platinum Met. Rev, **45**, 166-174 (2001).

[2.58] P. Tripodi, N. Armanet, V. Asarisi, A. Avveduto, A. Marmigi, J.D. Vinko, and J.P. Biberian, Phys. Lett. A, **373**, 3101-3108 (2009).

[2.59] J. Weissmüller and C. Lemier, Phys. Rev. Lett., **82**, 213-216 (1999).

[2.60] T. Flanagan, J. Clewley, H. Noh, J. Barker, and Y. Sakamoto, Acta mater., **46**, 2173-2183 (1998).

[2.61] F.A. Lewis, J.P. Magennis, S.G. McKee, and P.J.M. Ssebuwufu, J.Less-Common Met. (1983).

[2.62] A.W. Carson, T.B. Flanagan, and F.A. Lewis, Trans.Faraday Soc., **56**, 1311-1323 (1960).

[2.63] D. Richter, R. Hempelmann, and R. Bowman, Hydrogen in Intermetallic Compounds II, , 97-163 (1992).

[2.64] T. Schober, Scr.Met., **7**, 1119-1124, (1973).

[2.65] R. Koch, J. Phys.: Condensed Matter, **6**, 9519 (1994).

[2.66] R. Koch, The Chemical Physics of Solid Surfaces, **8**, 448-489 (1997).

[2.67] S.N.F. Mott and H. Jones, The theory of the properties of metals and alloys, Dover Pubns (1958).

[2.68] C. Schuh and D. Dunand, Scr. Mater., **40**, 1305-1312 (1999).

[2.69] I. Halevy, G. Zamir, M. Winterrose, G. Sanjit, C.R. Grandini, and A. Moreno-Gobbi, J.Phys: Conference Series, **215**, 012013 (2010).

[2.70] Y.L. Kao, G.C. Tu, C.A. Huang, and T.T. Liu, Mat. Sci. Eng.: A, **398**, 93-98 (2005).

[2.71] B. Yuan, C. Li, H. Yu, and D. Sun, Trans. Nonferrous Met. Soc. China, **19**, s423-s428 (2009).

[2.72] P. Danielson, R. Wilson, and D. Alman, Adv. Mater. Processes, **161**, 39 (2003).

[2.73] J. Lu, J. Qin, W. Lu, D. Zhang, H. Hou, and Z. Li, Mat. Sci. Eng.: A, **500**, 1-7 (2009).

[2.74] Q. Xu and A. Van der Ven, Phys. Rev. B, **76**, 064207 (2007).

[2.75] S. Tao, P. Notten, R. van Santen, and A. Jansen, Phys. Rev., B, **79**, 144121 (2009).

[2.76] R. Gruner, B. Streb, and E. Brauer, Titanium: Science and technology, 2571-2577 (1985).

[2.77] W. Gao, W. Li, J. Zhou, and P.D. Hodgson, J. Alloys Compounds, **509**, 2523-2529 (2011).

[2.78] H. Liu, J. Cao, P. He, and J. Feng, Int. J. Hydrogen En., **34**, 1108-1113 (2009).

[2.79] D. Eliezer, N. Eliaz, O. Senkov, and F. Froes, Mat. Sc. Eng.: A, **280**, 220-224 (2000).

[2.80] J. Zhao, H. Ding, Y. Zhong, and C.S. Lee, Int. J. Hydrogen En., **35**, 6448-6454 (2010).

[2.81] Y. Su, L. Wang, L. Luo, X. Jiang, J. Guo, and H. Fu, Int. J. Hydrogen En., **34**, 8958-8963 (2009).

[2.82] H. Dong and T. Bell, Wear, **238**, 131-137 (2000).

[2.83] H. Guleryuz and H. Cimenoglu, J. Alloys Compounds, **472**, 241-246 (2009).

[2.84] J. Qazi, J. Rahim, O. Senkov, and F. Froes, J. Minerals, Met. Mater. Soc., **54**, 68-71 (2002).

[2.85] F. Froes, O. Senkov, and J. Qazi, Int. Mater. Rev., **49, 3**, 227-245 (2004).

[2.86] Y. Zhang, S.Q. Zhang, and C. Tao, Int. J. Hydrogen En., **22**, 125-129 (1997).

[2.87] M.A. Murzinova, G.A. Salishchev, and D.D. Afonichev, Int. J. Hydrogen En., **27**, 775-782 (2002).

[2.88] O. Senkov and J. Jonas, Metall. Mater. Trans., A, **27**, 1877-1887 (1996).

[2.89] V.A. Goltsov, Int. J. Hydrogen En., **22**, 119-124 (1997).

[2.90] O.n. Senkov and F.H. Froes, Int. J. Hydrogen En., **24**, 565-576 (1999).

[2.91] O. Senkov, M. Dubois, and J. Jonas, Metall. Mater. Trans., A, **27**, 3963-3970 (1996).

[2.92] O. Senkov, B. Chakoumakos, J. Jonas, and F. Froes, Mater. Res. Bull., **36**, 1431-1440 (2001).

[2.93] J.C. Feng, H. Liu, P. He, and J. Cao, Int. J. Hydrogen En., **32**, 3054-3058 (2007).

[2.94] G.F. Kobzenko, A.P. Kobzenko, M.V. Chubenko, V.V. Pet'kov, and A.V. Polenur, Int. J. Hydrogen En., **20**, 383-386 (1995).

[2.95] H.R.Z. Sandim, B.V. Morante, and P.A. Suzuki, Mater. Res., **8**, 293-297 (2005).

[2.96] V.I. Trefilov, I.I. Timofeeva, L.I. Klochkov, I.A. Morozov, and R.A. Morozova, Int. J. Hydrogen En., **21**, 1101-1103 (1996).

[2.97] C.Q. Chen and S.X. Li, Mater. Sci. Eng., A, **387-389**, 470-475 (2004).

[2.98] C. Chen, S. Li, H. Zheng, L. Wang, and K. Lu, Acta Mater., **52**, 3697-3706 (2004).

[2.99] E. Conforto and D. Caillard, Acta Mater., **55**, 785-798 (2007).

[2.100] A. San-Martin and F. Manchester, J. Phase Equilib., **8**, 30-42 (1987).

[2.101] H. Numakura, M. Koiwa, H. Asano, H. Murata, and F. Izumi, Scr.Metall., **20**, 213-216 (1986).

[2.102] E.H. Sevilla and R.M. Cotts, J. Less-Common Met., **129**, 223-228 (1987).

[2.103] U. Kaess, G. Majer, M. Stoll, D. Peterson, and R. Barnes, J. Alloys Compounds, **259**, 74-82 (1997).

[2.104] J.W. Zhao, H. Ding, W.J. Zhao, X.F. Tian, H.L. Hou, and Y.Q. Wang, Trans. Nonferrous Met. Soc. China, **18**, 506-511 (2008).

[2.105] J. Qazi, J. Rahim, F. Fores, O. Senkov, and A. Genc, Metall. Mater. Trans., A, **32**, 2453-2463 (2001).

UNIVERSITY *of the*

WESTERN CAPE

Chapter 3: .   Experimental procedure and sample characterisation

3.1   Introduction

This chapter provides a description of the preparation methods for Palladium (Pd), Palladium-Platinum (Pd-Pt) alloys, the Pt coatings deposited onto Pd substrates, commercially pure Titanium (CP-Ti) and Ti-6Al-4V alloy investigated in this study. A description of the analytical techniques used to study the hydrogen (H) sorption/desorption effects, its storage capacity and the effects of hydrogen on the microstructure, microhardness and coating morphology is provided.

3.2   Materials and Sample preparation for hydrogenation

The Palladium with 99.96 % purity and Palladium-Platinum alloys used for hydrogenation were prepared by Mintek. The compositions of the Pd-Pt alloys were Pd-2 at. % Pt, Pd-6 at. % Pt, Pd-10 at. % Pt and Pd-12 at. % Pt. These alloys were prepared by melting pure Pd and Pt together until a homogeneous composition was achieved. Both the Pd and Pd-Pt alloys were prepared to a final solid ball finish. The balls were rolled and annealed at 1000 °C for 12 hours to achieve full homogenisation of the material and eliminate the hardening effects caused by rolling. Sheets of $10 \, mm \times 10 \, mm \times 0.5 \, mm$ and $5 \, mm \times 5 \, mm \times 0.5 \, mm$ dimensions were cut for hydrogenation under low pressure-low hydrogen concentration-short charging time (LP-LC-ST) and high pressure-high hydrogen concentration-long charging time (HP-HC-LT) conditions respectively. Further studies were also conducted on Pd-Pt coatings for comparison. A Pd substrate was coated with 0.5 μm Pt under a sputtering rate of 3.5 Å/s and power of 300 W. The grade 2 CP-Ti and Ti-6Al-4V alloy were supplied by Good Fellow Corporation. The CP-Ti metal was obtained in a form of annealed cold drawn rod and Ti-6Al-4V alloy in a form of annealed rod. The elemental composition of Ti-6Al-4V alloy is shown in Table 3-1.

Table 3-1: The elemental composition of Ti-6Al-4V alloy

Al	V	Fe	C	H	N	O	Ti
6 wt. %	4 wt. %	300 ppm	220 ppm	100 ppm	100 ppm	650ppm	balance

Samples of $16 \ mm \times 2 \ mm$ CP-Ti and $25 \ mm \times 2 \ mm$ Ti-6Al-4V alloy were cut. One set of each material was annealed at 550 ˚C, 650 ˚C, 750 ˚C and 850 ˚C for 3 hours to compare the effects of annealing and combined annealing-hydrogenation effects. The other set of samples was hydrogenated at room temperature in order to compare the effects of temperature and time on the absorption capacity of the material.

3.3   Hydrogenation

Hydrogenation of the materials was conducted under two different conditions:

1. LP-LC-ST conditions

The setup of the hydrogenation furnace used for these conditions is shown in Figure 3-1. A gas mixture of 15 % hydrogen (H) and 75 % argon (Ar) under 1013 mbar vacuum pressure was used for room and high temperature experiments. For high temperature hydrogenation, the gas flow was switched off during the cooling process. The Ar in the mixture prevents the occurrence of oxidation on the surface of samples. However, oxidation still occurs especially in CP-Ti and Ti-6Al-4V alloy because Ti reacts readily with oxygen. A precision bore flowmeter of FP1/16-16-G-5/84 was set to 13×10^6 mL/ min. For high temperature hydrogenation which lasted for 3 hours, the furnace was heated to 550 ˚C, 650 ˚C, 750 ˚C and 850 ˚C at a heating rate of 5 ˚C/ min for each experiment. After 3 hours of hydrogenation, the hydrogenated samples were cooled in vacuum with no gas in order to minimise oxidation. For room temperature hydrogenation, samples were held under vacuum in the furnace for a period of 1 hour, 2 hours, and 7 hours.
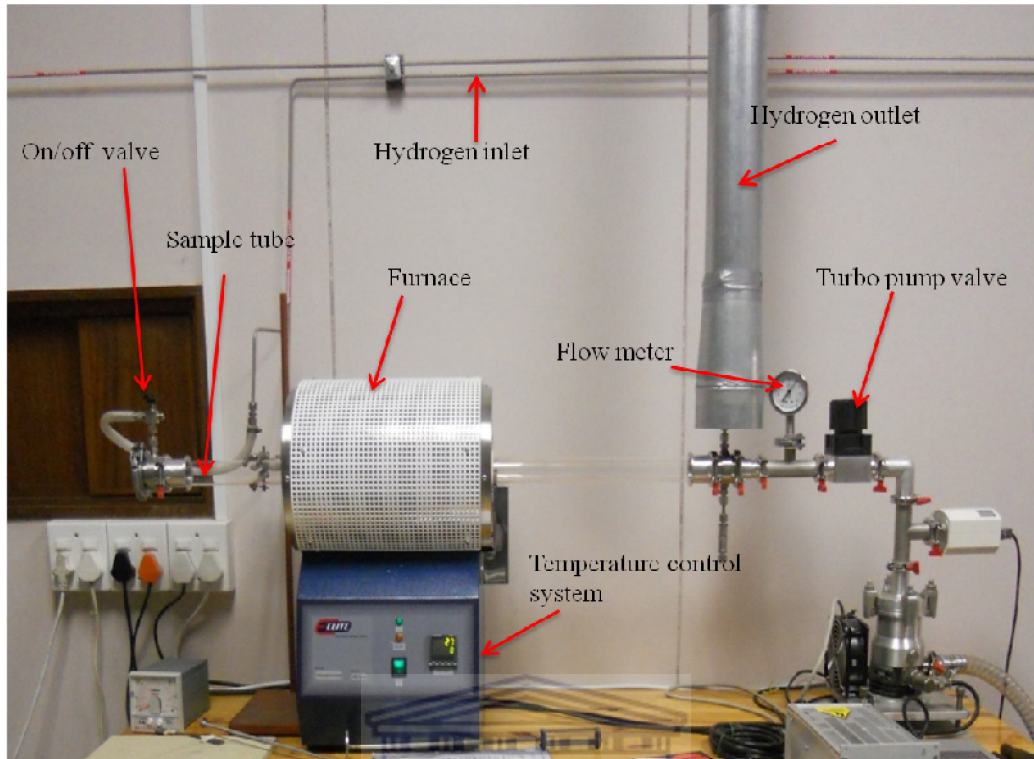
Figure 3-1: Setup of the hydrogenation furnace used for LP-LC-ST conditions.

2. HP-HC-LT conditions

The sorption of hydrogen in Intelligent Gravimetric Analyser (IGA-002) was conducted in a pure 99.99 % of hydrogen gas environment. The pressure was increased from 0.47 mbar to 2000 mbar during sorption and decreased from 2000 mbar to 0.47 mbar during desorption process. The gas flow rate is not important as it is an equilibrium pressure experiment. The IGA measurements were all run at room temperature.

Pd does not react significantly with oxygen at any temperature because it has low affinity for oxygen and therefore, no special precautions are needed for palladium and Pd-Pt alloys for hydrogen absorption. Sample preparation involves grinding and polishing of the samples before the hydrogenation process in order to examine the microstructure. However, CP-Ti and Ti-6Al-4V alloy surfaces are prone to oxidation which form an oxide film that act as a

protective layer against attack by hydrogen molecules. In order to minimise the reaction to oxygen, the material is treated with acetone in ultrasonic bath to remove the surface oxides before placing them in the charging furnace.

Table 3-2: Hydrogenation processes of Pd, Pd-Pt alloys, Pd-Pt coatings, CP-Ti and Ti-6Al-4V performed under different conditions (H-concentration, temperature, pressure, time).

Material	LP-LC-ST	HP-HC-LT	Temperature (˚C)	Time (hour)
Pd	✓	✓	Room temperature	1, 2, 7, 33
	✓	-	550, 650	3
Pd-2 at. %Pt	-	✓	Room temperature	33
Pd-6 at. %Pt	-	✓	Room temperature	33
Pd-10 at. %Pt	-	✓	Room temperature	33
Pd-12 at. %Pt	-	✓	Room temperature	33
Pd-Pt coating	✓	-	550, 650	3
CP-Ti	✓	-	Room temperature	1, 3, 7
	✓	-	550, 650, 750, 850	3
Ti-6Al-4V alloy	✓	-	Room temperature	1, 3, 7
	✓	-	550, 650, 750, 850	3

3.4   Analytic techniques

The study of hydrogen storage materials requires accurate techniques. Table 3-3 gives an overview of the experimental techniques used for the study of the hydrogen storage material's capacity, microstructure, phase transformation induced by hydrogen and temperature, and micro-hardness.

Table 3-3: Analytic techniques required for the study of hydrogen storage systems

Technique	Information
Optical microscopy (OM)	Microstructure
X-ray diffraction (XRD)	Phase analysis and the determination of lattice parameters
Digital balance	Mass difference
Intelligent gravimetric analyser (IGA)	Mass difference vs Pressure
Elastic recoil detection analysis (ERDA)	Hydrogen concentration and depth profiling
Vickers hardness test	Micro-hardness

3.4.1 Gravimetric methods

Gravimetric methods can be used to determine the change in mass of a material's sample before and after the hydrogenation process. Gravimetry is a quantitative analytical technique that can be applied for weight measurements [1]. For hydrogenated samples, an assumption was made that the mass difference is proportional to the amount of hydrogen absorbed in material during hydrogenation process performed in vacuum conditions. The conversion of the mass difference to hydrogen concentration in weight percent or atomic percent of the hydrogen in the metal-hydrogen system can be conducted. The two gravimetric techniques used in this study are digital balance and intelligent gravimetric analyser (IGA).

3.4.1.1 Digital balance

A digital balance is a measurement instrument for determining the mass of an object. The kind of digital balance used in this study, shown in Figure 3-2, is known as analytical balance which is a class of balance designed to measure small mass in the sub-milligram range to a very high degree of precision (0.01 mg or better).
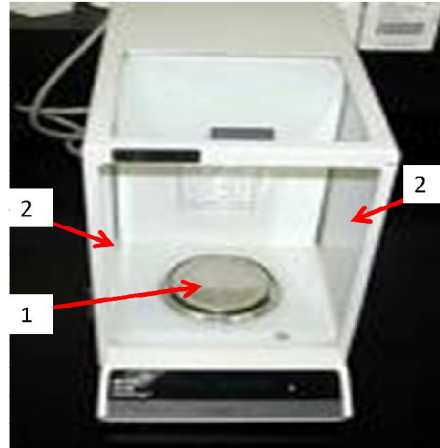
Figure 3-2: A digital balance.

The measuring pan of an analytical balance (1) is located inside a transparent enclosure with doors (2) to prevent dust to collect so that any air currents in the laboratory do not affect the balance's operation. The samples were washed in water bath using acetone before the hydrogenation process in order to remove contaminants on the sample surface. The zero value of the digital balance equipment was determined and each measured value is added or subtracted from the value if it is negative or positive respectively. A maximum of three measurements were repeatedly taken on each sample before and after the hydrogenation process. The difference of the average value of the measurements recorded before and after hydrogenation process is then considered the mass of hydrogen absorbed.

### 3.4.1.2 Intelligent gravimetric analyser (IGA)

The IGA system uses the gravimetric technique to measure accurately the magnitudes and dynamics of gas and vapour sorption on materials. The characterisation of sorption properties of materials can be calculated in real time. The Intelligent IGA design integrates precise computer-control and measurement of weight change, pressure, temperature, and gas flow.

The system can automatically and reproducibly measure sorption isotherms/isobars as well as investigating thermal desorption in diverse operating conditions.

(i)   Instrumentation

Figure 3-3 presents a schematic representation of the component features of an intelligent gravimetric analyser.
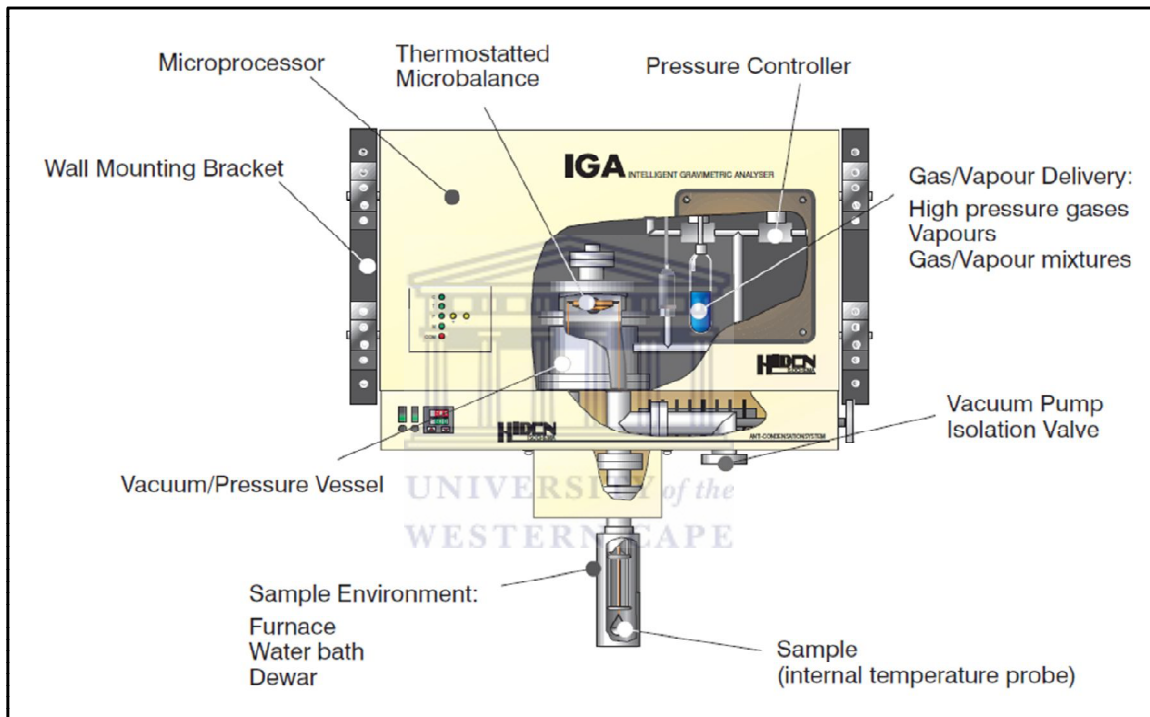
Figure 3-3: Schematic representation of IGA setup [3.16].

The microbalance incorporated in the gravimetric analyser used in this study is ultra sensitive to the weight change (mass) of material and it is mounted in thermostatted heat sink to provide high resolution and precise long-term stability. The design of the pressure vessel take into account all metal seals to UHV standards to allow measurements from high vacuum to high pressure. The pressure of the gases and vapours is accurately controlled by pressure control system. An internal temperature probe is embedded in the sample container for measuring the sample temperature. This probe is controlled by temperature control system

which operates from cryogenic to 1000 ˚C temperatures. Therefore, the whole design of IGA is controlled automatically by software package for experiment design, system control and data acquisition. Additional features such as vacuum pumping stations, furnaces, humidifier, water baths etc, enable a broad range of experiments to be performed.

The model used in this study is known as IGA-002 system which is specifically designed to study general vapour sorption processes from vacuum. An additional low range pressure sensor and an anti-condensation protection which is rated to 50 ˚C are incorporated. The IGA-002 model has a balance capacity of 5 mg which can weigh mass difference to approximately 200 mg. Its weight resolution of 0.2 μg provides high accuracy during the sorption measurements. The pressure vessel is assembled by UHV SS316/SS304 which can operate at 20000 mbar pressures. The embedded pressure sensors are sensitive from 1 mbar with approximately $\pm\,0.03$ % of accuracy. The temperature control system is equipped with sensors sensitive to temperature range from liquid nitrogen (-210 to -196 ˚C) to 1000 ˚C. The control system has a temperature accuracy range of ± 0.05 % to $\pm 1\,˚C$

(ii)   Sample preparation

The sorption and desorption measurements of hydrogen in Pd and Pd-Pt alloys with different Pt content were achieved by placing sample of $5\,mm\,\times\,5\,mm\,\times\,0.5\,mm$ dimensions in the sample holder which is connected to a sensitive microbalance. A holding time of 120 minutes was set between pressures steps from vacuum (0.47 mbar) to 2000 mbar during sorption and decreased in 9 step to vacuum pressure during desorption process. The increment of the pressure from one saturated point to the next poses no disturbance to the balance. A hydrogen environment was created around the sample by allowing 99.99 % of

pure hydrogen around the sample. However, a blank run of an inert gas is performed on the commencement of the experiment in order to correct buoyancy.

(iii)   Characterisation

The sorption kinetics and equilibrium isotherms can be determined by IGA method which is described in Figure 3-4. The pressure in the system is changed and then held constant during sorption and desorption at the set point P_n shown in Figure 3-4 (a). The weight data is acquired and analysed in realtime to determine kinetic parameters and predict the exact point of equilibrium uptake, E_n.
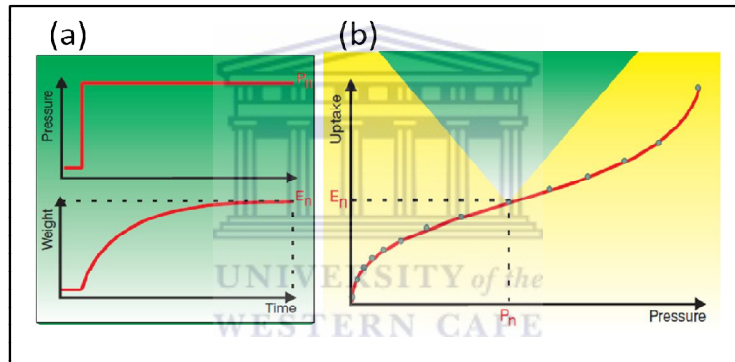
Figure 3-4: IGA method (a) and (b) isotherm showing the uptake with gas/ vapour pressure [3.16].

The kinetic response shown on the IGA method is used to determine equilibration which is useful in understanding the non-equilibrium sorption behaviour of materials in order to determine diffusion and transport parameters of adsorbates in materials. One of the most important advantages of using IGA method is that it provides a consistent reproducible analysis method from point to point on the isotherm whilst making the optimum use of laboratory time.

3.4.2 Elastic recoil detection analysis technique.

The concentration of hydrogen in Pd, Pd-Pt alloys, CP-Ti and Ti-6Al-4V alloy was determined before and after hydrogenation by ERDA technique. ERDA is able to detect light elements of low atomic number ($1 < Z < 8$) such as hydrogen, oxygen and nitrogen present in solids [3.2]. It uses an ion beam as a projectile to recoil atoms of light elements from the target sample. The ERDA method provides absolute concentration values and is not affected by matrix effects such as the energy or shape of the signal of an element in any environment as compared to this element in its pure form [3.3].

(i)   Theory

ERDA makes use of light ion beam such as He$^+$ with energies of 2 to 3 MeV to determine the content of hydrogen in targets. The stable, positive charged ions are used as projectiles to eject the target atoms kinematically. The elastic collision between the projectile and the atomic nucleus of the target is governed by Coulomb repulsive force. This collision is illustrated in Figure 3-5.
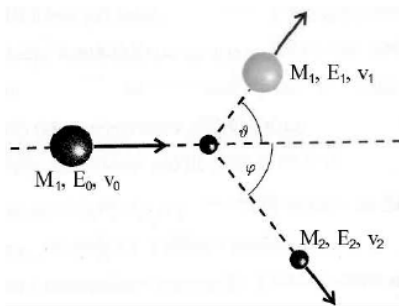
Figure 3-5: A schematic representation of elastic collision between incident ion and target atom [3.4].

Recoiled atoms with sufficient energy will reach the detector. When an incident particle of mass M_1 and energy E_0 moving with velocity v_0 hits a target of mass M_2 initially at rest, the

target atoms recoil with energy E_2 at an angle φ between 0 and 90 ° with velocity v_2. Since the collision is elastic, energy (E), and momentum (P) are conserved, and they can be described by equations 3-1 and 3-2 respectively [3.5].

$$E = \frac{1}{2}M_1 v_0{}^2 = \frac{1}{2}M_1 v_1{}^2 + \frac{1}{2}M_2 v_2{}^2 \tag{3-1}$$

$$P = M_1 v_0 = M_1 v_1 + M_2 v_2 \rightarrow \begin{bmatrix} M_1 v_0 = M_1 v_1 \cos\vartheta + M_2 v_2 \cos\varphi \\ = M_1 v_1 \sin\vartheta - M_2 v_2 \sin\varphi \end{bmatrix} \tag{3-2}$$

The energy of the recoiled atom is calculated by

$$E_{1,2} = K_{1,2} E_0 \tag{3-3}$$

where the energy ratio known also as the Rutherford kinematic factor K is given by conservation of both energy and momentum as

$$K_1 = \left[\frac{M_1 \cos\vartheta \pm \sqrt{M_2^2 - M_1^2 \sin^2\vartheta}}{M_1 + M_2} \right]^2 \tag{3-4}$$

$$K_2 = \frac{4M_2/M_1}{(1+M_2/M_1)^2} \cos^2\varphi \tag{3-5}$$

The kinematic factor corresponds to the peak in the ERDA spectrum. The geometry of the beam on the target surface can be described by Equation 3-1 [3.4].

$$a = \frac{d}{\cos 15°} \tag{3-6}$$

where a is the size of the beam spot on the sample surface and d is the diameter of incident beam.

The cross section of ion beam scattering on target atom at angle ξ is given by the well known Rutherford cross section

$$\left(\frac{d\sigma}{d\Omega} \right)_C = \left(\frac{z_i z_t}{4\pi\varepsilon_0 4E_c \sin^2(\xi/2)} \right)^2 \tag{3-7}$$

where $Z_t = \frac{e_t}{e_0}$ and $Z_i = \frac{e_i}{e_0}$ - the nuclear charge of target and projectile, respectively. E_c - the energy of projectile before scattering.

As the beam of alpha particles penetrate depth x of the target, they loose energy E_0 at the point of collision due to electronic and nuclear energy loss. The projectile beam spread as a result of straggling. The energy E_x after the collision of the incident projectile with the target can be approximated by Equation 3-8.

$$E_x = E_0 - \frac{x}{cos\theta_1} S_1 \ (keV) \tag{3-8}$$

where S_1 is the stopping power of the incident ion at mean energy $\bar{E}_1$:

$$\bar{E}_1 = \left[\frac{(E_x + E_0)}{2}\right] (keV) \tag{3-9}$$

The energy spread increases with depth until the lowest energy ions reach the energy of maximum stopping, shown in Figure 3-6.
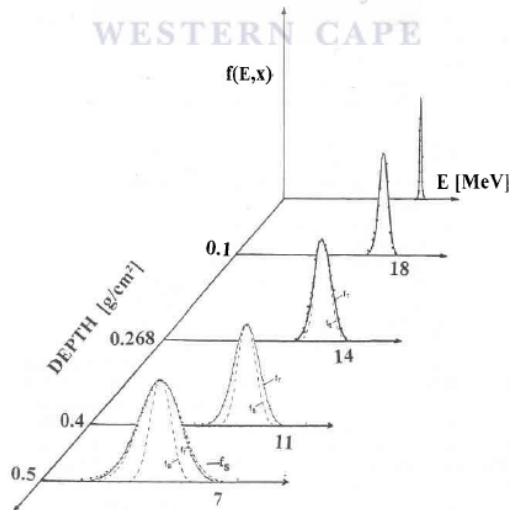
Figure 3-6: Energy straggling of a proton beam penetrating through thin Al absorber foil. The energy distribution is asymmetric because of large energy transfers [3.5].

Bohr made an assumption that energy transfer takes place between ion and free electrons of the target. This assumption predicts a Gaussian energy distribution with standard deviation given by Equation 3-10.

$$\sigma_B^2 = 4\pi e_i^2 Z_t n_t l \tag{3-10}$$

where e_i -charge of projectile, Z_t- atomic number of projectile and n_t- the atomic density of target.

It is important to know the stopping power and range of ions in the matter of interest. The ion ranges and the stopping of the targets were determined by using SRIM code. SRIM is a group of programs which calculate the stopping and range of ions between 10 eV and 2 GeV/amu into the matter using a full quantum mechanical treatment of ion-atom collision [3.5,3.6]. This calculation is made very efficient by the use of statistical algorithms which allow the ion to make jumps between calculated collisions and then averaging the collision results over the intervening gap. During the collisions, the ion and atom have a screened Coulomb collision, including exchange and correlation interactions between the overlapping electron shells. The ion has long range interactions creating electron excitations and plasmons within the target. The energy loss of the penetrating projectile in matter is described by the Bethe-Bloch, Equation 3-11, called the stopping power of the medium given as energy loss per unit path.

$$S = -\frac{dE}{dx} = 4\pi r_1^2 m_2 c^2 n_t \frac{e_i^2}{\beta^2} \left[\ln\left(\frac{2m_e c^2 \beta^2 \gamma^2}{\langle I \rangle}\right) - \beta^2 - \frac{\delta}{2} - \frac{C(v,\langle I \rangle)}{Z_t} \right] \tag{3-11}$$

where $\qquad r_1 = \frac{e_0^2}{4\pi\varepsilon_0 m_e c^2} = 2.817 \times 10^{-15} \, m \tag{3-12}$

$$n_t = \rho N_A \frac{e_t}{A_t}, \quad e_i = Z_i e_0, \quad \beta = \frac{v}{c}, \quad \gamma = (1 - \beta)^{-1/2}, \langle I \rangle, \; A_t, \; \rho$$ are the mean excitation potential energy of the target electrons, the atomic weight and the density respectively.

The stopping power and the ion range in the targets are given in Table 3-4. The higher the stopping power of the material, the shorter will be the He$^+$ ion range. This behaviour occurs as a result of the increasing energy loss of the ions per depth of penetration.

Table 3-4: The range of 3 MeV He ions in targets and the stopping power of the targets.

Target	Stopping power (MeV/ µm)	Ion range (µm)
Ti	7.63	1.99
Ti-6Al-4V	7.59	2.01
Pd	4.61	1.21
Pd-2 at. % Pt	4.61	1.20
Pd-6 at. % Pt	4.59	1.20
Pd-10 at. % Pt	4.57	1.19
Pd-12 at. % Pt	4.56	1.18

The recoiled energy is calculated relative to the energy of the incident projectile after collision with projectile.

$$E_2 = E_{20} - \frac{x}{\cos\theta_2} S_2 \; (keV) \tag{3-13}$$

where S_2 is the stopping power of the recoils at mean energy,

$$\bar{E}_1 = \left[\frac{(E_2 + E_{20})}{2}\right] (keV). \tag{3-14}$$

The difference between the detected energy of a recoil on the surface and that from depth x is determined by the energy loss factor, $\tilde{S}$, described by Equation 3-15.

$$\Delta E = K_2 E_0 - E_2 = \left[\frac{K_2}{\cos\theta_1} S_1 + \cos\theta_2 S_2\right] x = \tilde{S}x \tag{3-15}$$

The energy difference shows the depth at which the collision took place. Thus, the deeper the penetration of the projectile is the lower the energies detected. Therefore, energy resolution is connected with the depth resolution and is described as:

$$\delta x = \frac{\delta E}{\bar{S}}$$ (3-16)

Since the detected energies are a function of the depth of the scattering atom in the sample for a given element, the atoms extracted from the surface yield higher detected energies because they are not subjected to any stopping power. The knowledge of the yield as function of depth provides the information about the given element depth profile and of course the content of the scattering atoms in the sample. The link between the number of target atoms *Ns* and the detected particles or yield *Y* through a solid angle, Ω, is given by the scattering cross section σ (∅).

$$Y = \sigma(\emptyset).\Omega.Q.N_s$$ (3-17)

where ∅ is the scattering angle and *Q* is the total number of the beam incident particles.

(i)   Experimental set up

The ERDA instrumentation is located in the B-line at the single-ended 6.0 MeV Van de Graaff accelerator at iThemba LABs in Cape Town. The scattering chamber used at the ERDA system works at a pressure of $\times 10^6$ mbar. The chamber is equipped with a 360 ° protractor which allows the adjustment of the target - beam direction angle. This protractor is mounted on a turntable device which enables recoils detection angles in the angular range from 0 to 30 °. The target is tilted at 75 ° with the normal such that the incident beam strikes it at 15 °. A collimated beam of He$^+$ ions with energies ranging from 2 to 3 MeV were accelerated towards the targets loaded on a ladder in the chamber. The recoils are collected by a collimator tube with a built in $10\ mm \times 1\ mm$ slit. The collimator and Mylar stopping

foil are mounted in front of the surface barrier detector (SBD) to stop the primary He^+ beam and to allow the accurate setting of a fixed solid angle. The Mylar foil had a composition of $C_{10}H_8O_4$ with a 15 μm thickness. The SBD has an active area of 50 mm^2, a minimum sensitive depth of 100 μm and 15 keV full width at half maximum (FWHM) alpha resolution. The accuracy of the solid angle is normally determined by measuring the activity of an alpha-source with known activity as a function of the distance. The filtering of the primary ion beam by the slit and the foil reduces background noise [3.7]. The distance from the Surface Barrier Detector (SBD) to the sample surface position is ~15 cm. The schematic of the scattering geometry of recoils in ERDA is shown in Figure 3-7. The signal of charge recorded on the detector is further amplified and then converted to digital by ADC. The converted signal builds up a spectrum which relates the amount of recoils with the depth of their origin. In this research work, a circular He^+ beam of 0.7 mm diameter was used to irradiate the targets. The energy calibration data was obtained by irradiating a 125 μm polyimide foil called Kapton with $C_{22}H_{10}N_2O_5$ empirical formula at different ion beam energies (2 MeV to 3 MeV) increasing in 0.5 MeV step sizes. The targets of interest were irradiated with 3 MeV energy ions.
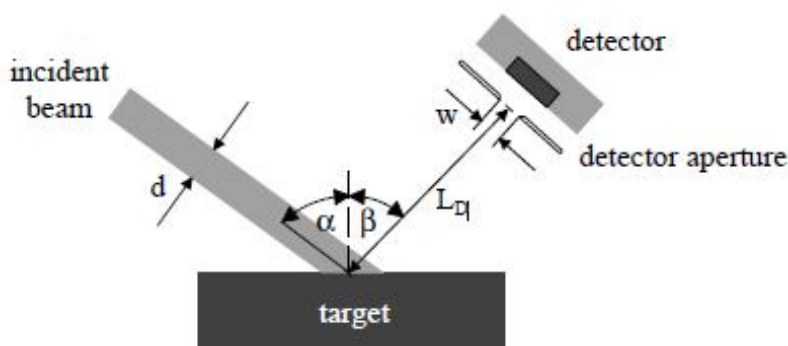

Figure 3-7: A schematic representation of the experimental setup of ERDA. The detector geometry presents the diameter d of the incident beam striking target at incident angle α. The recoils scatter at angle ß towards the detected with aperture width of w and L_D the distance between sample and the detector aperture [3.4].

The following parameters were used in the experiments performed in this study: Charge of 20000 nC, detector voltage of -100 V, amplifier fine gain of 0.47 and coarse gain of 1000. The beam currents were initially set to 20 nA but because of the small slits embedded in the collimators, the current values were unstable such that some of the irradiation were performed with less than 10 nA currents.

(ii)   Energy calibration and Data analysis

A concentration depth profile was calculated from the measured energy spectrum of the recoils. The precise depth profile is important especially in studying diffusion phenomenon [3.7]. The depth profile calculation was done by using spectrum simulation program called SIMNRA [3.2,3.8]. SIMNRA is a Microsoft Windows program for the simulation of back- or forward scattering spectra for ion beam analysis with MeV ions [3.4]. SIMNRA is mainly intended for the simulation of spectra with non-Rutherford backscattering cross-sections, nuclear reactions and elastic recoil detection analysis (ERDA). In simulation of ERDA spectra with SIMNRA, all the energy spread contributions are taken into account.
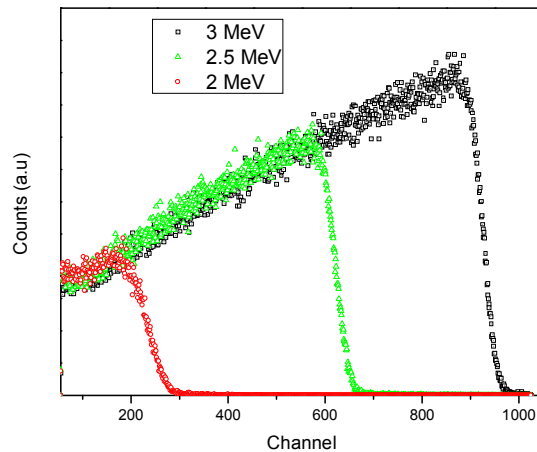
Figure 3-8: ERDA spectra showing the distribution of hydrogen in Kapton irradiated with ions of (a) 2 MeV, (b) 2.5 MeV and (c) 3 MeV energies.

The parameters that were used to calibrate the spectra of the references and hydrogenated samples were obtained by optimising the energy of the recoils from Kapton spectra irradiated with 2, 2.5 and 3 MeV ions. ERDA spectra of Kapton irradiated at 2, 2.5 and 3 MeV energies are illustrated in Figure 3-8. The statistical counts of the recoils depend on the charge of the projectiles. The channel corresponds to the energy and the depth from which the atom was recoiled. The energy of the recoils and their energy loss after passing through Mylar foil were determined by the kinematics of ions in the target. The full width at half maximum (FWHM) of each Kapton spectra was measured and a plot of final energy as a function of the channel of the recoils was made, Figure 3-9.
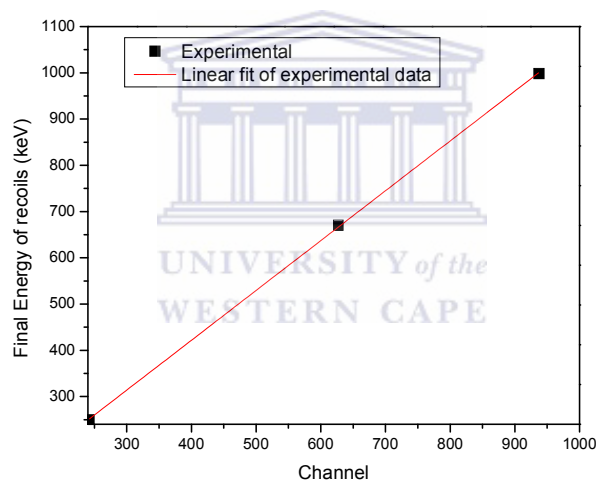
Figure 3-9: Linear fit graph of final energy of hydrogen atoms detected from the samples per channel.

The slope and the intercept found after a linear fit of the data points represent the energy per channel and calibration offset in the SIMNRA code. However, most of the time these calibration parameters do not give a satisfying fit. SIMNRA can use a non-linear energy calibration to account for the non-linearity of the detector. It makes use of a quadratic term of the form:

$$E = A + B \times channel + C \times channel^2 \tag{3-18}$$

where E-energy in keV, A-calibration offset in keV, B-energy per channel calculated in $keV/channel$ and C-quadratic correction term in $keV/channel^2$.

The quadratic term is incorporated in the automatic calibration tool found in the automatic fitting window. The number of recoiled particles is obtained from the collected charge. The number of particles is multiplied with the solid angle of the detector to get the steradians (sr) parameter which determines the height of the simulation spectra.

Fitting of the spectra is achieved by dividing the target into sublayers and therefore, a simulated spectrum is made of superimposed contributions of elemental compositions of sublayers of the sample target. The thickness of each sub layer is chosen in a way such that the energy loss of each sublayer is about the step width of the incoming particles. The profile of the layers portrays the hydrogen's depth of penetration in the material. The concentration of the hydrogen in each sublayer is given in atomic fractions. Equation 3-19 was used to convert hydrogen from atomic fractions to average atomic percent.

$$Average\ Hydrogen\ concentration = \frac{(C_{x1} \times B_{x1}) + (C_{x2} \times B_{x2}) + \cdots}{sum(B)} \times 100\ \% \tag{3-19}$$

where C is the concentration in atomic fractions, B is the thickness of the layer ($\times 10^{15} atoms/cm^2$) and the x represent sublayers.

Since the high energy beam of He$^+$ ions strikes the sample surface at high velocities, the ions will partially loose their energy with depth of penetration. The ions recoil hydrogen atoms on impact with the target or their energy is absorbed. The absorbed energy generates heat which, with time will give the hydrogen atoms sufficient kinetic energy to recoil. The fact that hydrogen diffusion occurs fast in Pd and Pd-Pt alloys as compared to CP-Ti and Ti-6Al-4V

alloy, three series of runs were conducted on each Pd and Pd-Pt samples hydrogenated under HP-HC-LT conditions. This was done to observe the effects of the beam on the hydrogen counts with time. Each consecutive run was concluded within a maximum period of 2 hours.

3.4.3 Polishing and etching of samples

In order to obtain a sample from the material, sectioning from the base material is required. Abrasive wet cutting is the most frequently used sectioning method. A diamond coated cutting wheel is used for cutting, shown in Figure 3-10 (a).
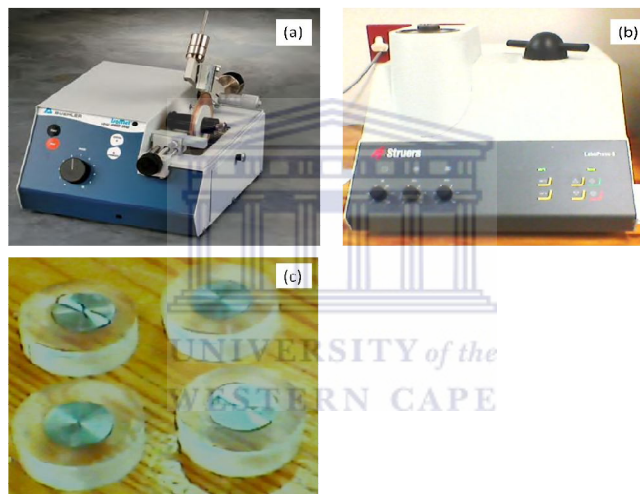
Figure 3-10: (a) Low speed precision saw for low volume applications, (b) electro-hydraulic programmable single cylinder mounting press , and (c) mounts of CP-Ti samples.

In some cases, the sample taken from the base material can be handled and treated directly as a specimen, but often a mount must be made to secure the handling and a satisfactory preparation. Therefore, mounting mainly takes place as hot compression in a resin. It can be observed in Figure 3-10 (c) that the hot mounting used in this work makes mounts with very precise dimensions. The sample is placed with an amount of resin in a cylinder in a electro-hydraulic programmable single cylinder mounting press shown in Figure 3-10 (b) and heated

at 180 ˚C under pressure for 7 minutes. All parameters such as pressure, temperature, cooling (cooling rate), and time, are microprocessor-controlled. The resin polymerises around the sample, and after cooling for 7 minutes the mount was removed from the press.

The sample preparation is completed through a number of mechanical steps which includes a plane grinding step, one or more fine grinding steps, and one or more polishing steps. The grinding removes damage introduced by sectioning and more importantly, it represents first step in sample preparation process to be able to be studied by microscopy. The morphology studies for Pd-Pt coated systems were performed without polishing in order to observe the effect of hydrogen at high temperatures on the coating. The polishing procedure for CP-Ti and Ti-6Al-4V alloy is given in Table 3-5.

Table 3-5: Polishing procedure for CP-Ti and Ti-6Al-4V alloy

Step	Grinding plate	Force (N)	Lubricant
1	800 Grit- SiC	20	Water
2	MD-DUR/MD DAC	20	9 μm diamond suspension
3	MD Nap	20	Op nap +H_2O_2 (attack)
4	MD Nap	20	Water (rinsing)

An automatic polisher was used for the polishing process. The surface needs to be etched to reveal the microstructure (grain structure: size and shape of grains, the presence of phases). Kroll's reagent was used as an etchant (100 mL distilled water, 6 mL 50 % Nitric acid and 3 mL 50 % Hydrofluoric acid). The Ti-6Al-4V alloy samples were etched with Keller's reagent which is a solution of 95 mL water, 2.5 mL Nitric acid, 1.5 mL Hydrochloric acid and 1 mL

Hydrofluoric acid. The samples were characterised using bright field mode of Reichert MeF3A optical microscope.

3.4.3.1   Optical microscope

A microscope is an optical system which transforms an object into an image. An optical image is formed by conventional lens systems. All parts of the optical image are formed simultaneously. The simplest optical microscope which has been used since the early seventeenth century is a single convex lens. The ray diagram of a convex lens system is shown in Figure 3-11 which illustrates the concepts of focal length, f, and magnification, M.
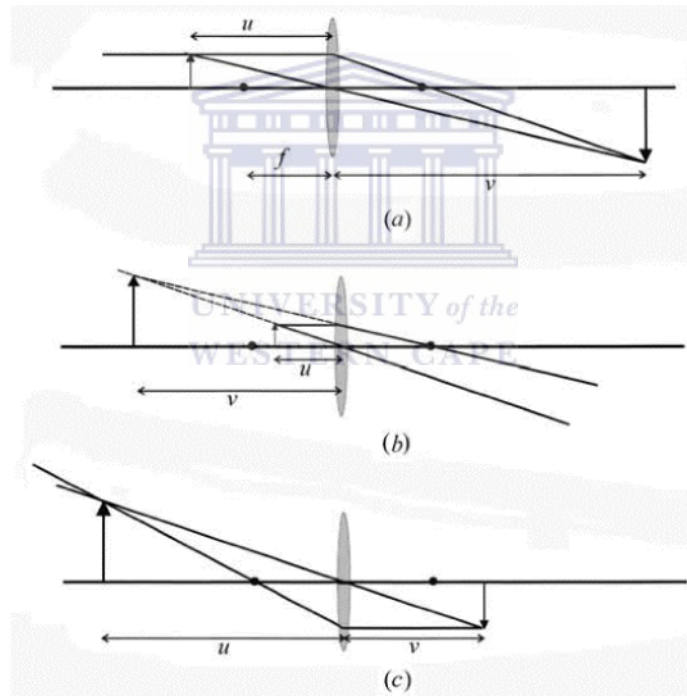
Figure 3-11: Ray diagram showing the formation of image by a single lens of focal length f [3.9].

If the object distance u (between lens and object) is between f and $2f$, as shown in Figure 3-11 (a), the real image will be magnified, and inverted. The image is erect but virtual if the object is within the focal distance (when the object is between zero and f in Figure 3-11 (b)).

However, if the object is further from the lens than $2f$, the image is demagnified as shown in Figure 3-11 (c). Therefore, the thin lens equation (Equation 3-20) summarises the behaviour of a convex lens with a focal distance f.

$$\frac{1}{f} = \frac{1}{u} + \frac{1}{v}$$

(3-20)

where u is the object's distance (the distance from the lens to the object) and v is the image distance. The magnification, M, produced by single lens is given by v/u. Substitution in the lens equation gives:

$$M = \frac{f}{u-f} = \frac{v-f}{f}$$

(3-21)

from which it can be deduced that for large magnification, $u - f$ must be small and positive. This can be achieved by placing the object outside the focal point of the lens.

Magnification of an object without severe distortion is very limited using a single lens. For high magnifications, combinations of lenses are used so that the total magnification is achieved in two or more stages. A simple two stage photomicroscope will have the ray diagram shown in Figure 3-12.
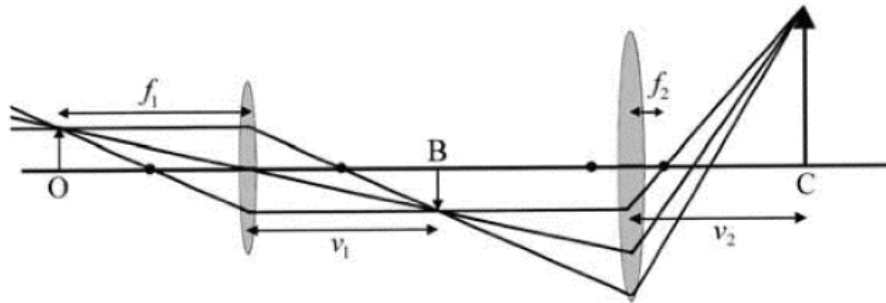
Figure 3-12: The ray diagram of a simple two stage projection microscope with the object placed at O and its final image at C, with an intermediate image at B [3.9].

The first lens, the objective, provides an inverted image at B with magnification $(v_1 - f_1)/f_1$ and the second lens, the projector, gives a final upright image at a further magnification of $(v_2 - f_2)/f_2$. The image is viewed in a screen at C with a total magnification of

$$M = \frac{(v_1 - f_1)(v_2 - f_2)}{f_1 f_2}$$

(3-22)

Therefore, a system of projector lenses can further be added in order to increase magnification. A sample is illuminated with light from a convenient source. Biologists work with mainly transparent tissues and therefore a transmission arrangement of optical microscope is suitable whereas a material scientists or geologists use a reflection arrangement of the optical microscope to study the surface structure of solid sample. Transmission and reflection arrangements of optical microscope are shown in Figure 3-13.
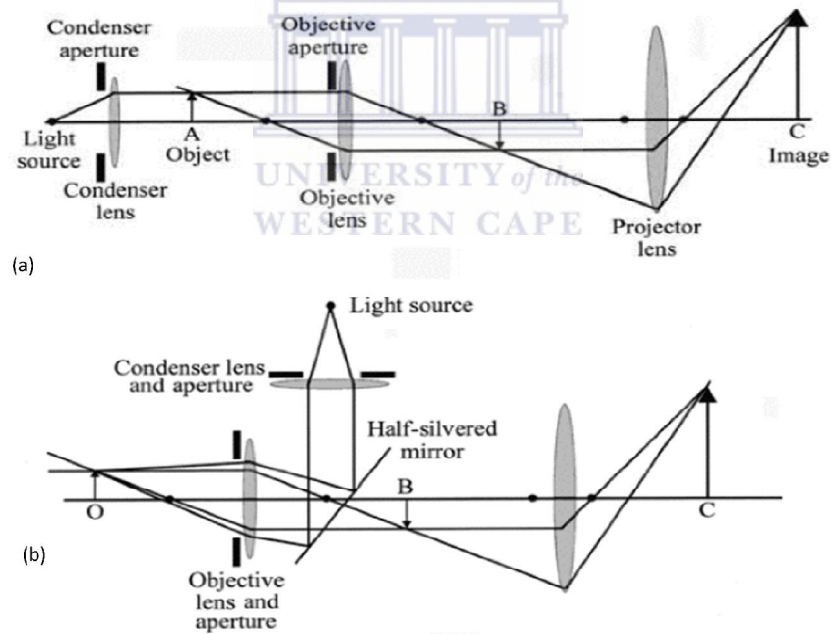

Figure 3-13: The optical systems of (a) transmission illumination, and (b) reflection illumination of microscope [3.9].

The essential parts of any illumination system are a light source and a condenser system. The condenser collects the light which is diverging from the source and directs it at the small area

of the sample which is to be examined. The main two purposes of this is that it makes the object appear brighter so that it can be seen more easily (by improving its contrast) and it also enables the microscopist to control the angle at which the illumination arrives at the sample. The beam can be made to converge or can illuminate the sample with parallel rays.

(i) Magnification

The f_1 and f_2 in Equation 3-22 can be altered rather than v_1 and v_2 by replacing one lens for another with a different focal length. The alternative is to alter the distances between all the components of the microscope. The smallest details which can be distinguished in a light microscope are about 200 nm in size. Thus any magnification greater than $1000 \times$ only makes the details bigger with a light microscope [9].
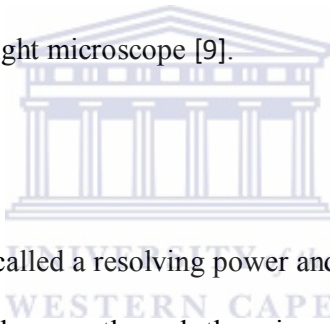
(ii) Resolution

The resolution of microscope is called a resolving power and is defined as the closest spacing of two points which can clearly be seen through the microscope to be separate entities. It is expected in any microscope that the light from the built in light source must pass through a series of lenses or apertures shown in Figure 3-14. Whenever light passes through an aperture, diffraction occurs so that a parallel beam of light (seen as a spot) is transformed into a series of cones, which are seen as circles and are known as airy rings. Figure 3-15 shows this effect with a laser beam and two small pinholes. For light of a given wavelength, the diameter of the central spot is inversely proportional to the diameter of the aperture from which the diffraction is occurring. The diffraction effect limits the resolution of a microscope because the light from every small point in the object suffers diffraction, particularly by the objective aperture, and even a small point becomes a small airy disc in the image.
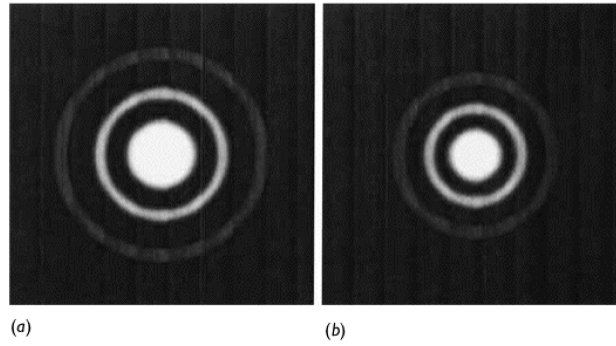
Figure 3-14: Diffraction of a laser beam by small pinholes (a) 75 µm diameter and (b) 100 µm diameter resulted in the formation of Airy rings [3.9].
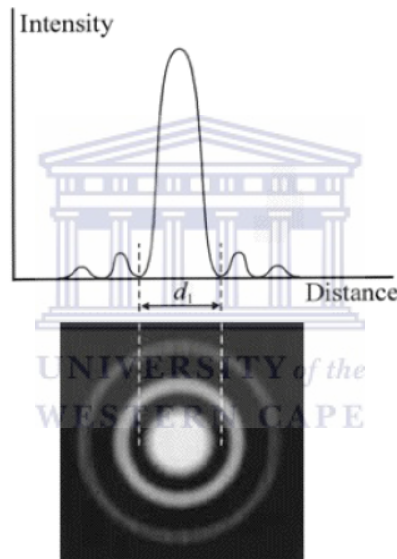
Figure 3-15: A 84% of light intensity across a set of airy rings lies within a spot of diameter d_1 in the first ring [3.9].

The size of the disc is related to the image of each point and therefore in order to make this disc as small as possible, the aperture must be as large as is practicable. Considering Figure 3-12, the variation of the light intensity across the series of rings makes up the disc. The central intense spot contains 84 % of all the light intensity. An assumption is made that all the light falls onto the spot of diameter d_1, where $d_1 \propto (1/aperture\ diameter)$. Thus the

resolution is the distance between the two spots in an image before they are distinguishable as two.

A proposition was made by Rayleigh that when a maximum of intensity of an airy disc coincides with the first minimum of the second, then the two points can be distinguished. This is illustrated in Figure 3-16 from which it can be seen that the resolution limit is $d_1/2$.
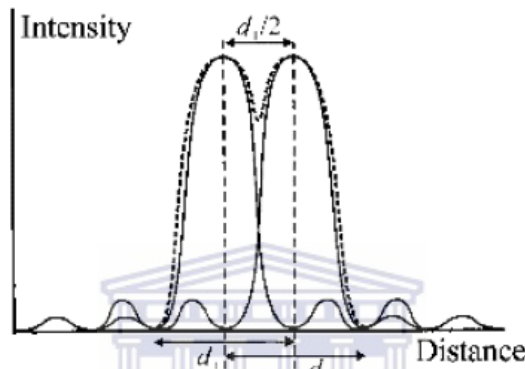
Figure 3-16: The intensity of the airy rings from two neighbouring pinholes [3.9].

Microscope apertures are normally referred to in terms of the semi angle, α, which they subtend at the sample. It is then possible to derive from the diffraction theory the relationship

$$r_1 = \frac{d_1}{2} = \frac{0.61\lambda}{\mu \sin \alpha} \tag{3-23}$$

where r_1 is the resolution limit, λ is the wavelength of the light and μ is the refractive index of the medium between the object and the objective lens. The product $\mu \sin \alpha$ is usually called the numerical aperture (NA). The best resolution can be obtained by achieving the smallest r_1, which can be done by decreasing the wavelength (λ) or by increasing μ or α. λ can be decreased to $400 \, nm$ by using green light or to about $200 \, nm$ by ultraviolet light. $\sin \alpha$ can be increased towards 1 by using as large an aperture as possible and μ can be increased by using oil immersion objective lens.

(iii) Depth of field and depth of focus

In any microscope, the image is only accurately in focus when the object lies in the appropriate plane. The part of the image will be out of focus if the equivalent part of the object being viewed lies above this plane. The range of positions for the object for which our eye can detect no change in the sharpness of the image is known as the depth of field. Since this distance is very small in most microscopes, the object must be flat in order to view its sharp images. The depth of field can be estimated from Figure 3-17 which shows rays converging at the sample. The diffraction effect will always limit the resolution at the sample to r_1 and therefore, there will not be any difference to the sharpness of the image if the object is anywhere within the range h. Simple geometry of the system gives:

$$h = \frac{0.61\lambda}{\mu \sin \alpha \tan \alpha} \qquad (3\text{-}24)$$

The only effective way to increase the depth of field is to decrease the convergence angle, which is controlled in most cases by the objective aperture, as shown in Figure 3-17.
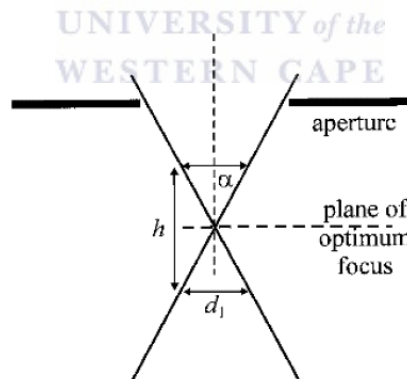
Figure 3-17: Depth of focus of an optical system showing the distance, h, from the plane of optimum focus within which the beam diverges by no more than the spot diameter d_1 [3.9].

Depth of field is often confused with depth of focus. Depth of focus refers to the range of positions at which the image can be viewed without appearing out of focus for a fixed position of the object. For a constant focal length, Equation 3-20 is differentiated to give

$$\frac{dv}{du} = \frac{-v^2}{u^2} = -M^2 \qquad (3\text{-}25)$$

This shows that dv, the effective shift in image position, is related to du, the change in position of the object via the square of the magnification. The negative sign arises as because the shifts are in opposite directions. If du is set to be the depth of field the equivalent depth of focus is a factor of M^2 bigger.

(iv) Instrumentation

Figure 3-18 shows the components of a modern inverted reflected-light type microscope. The illumination source and light path are important elements of a microscope. Halogen lamps are often used as light source. The illumination system produces images that are illuminated with evenly distributed light using three lenses placed between the light source (1) and the reflector (2) in Figure 3-18.
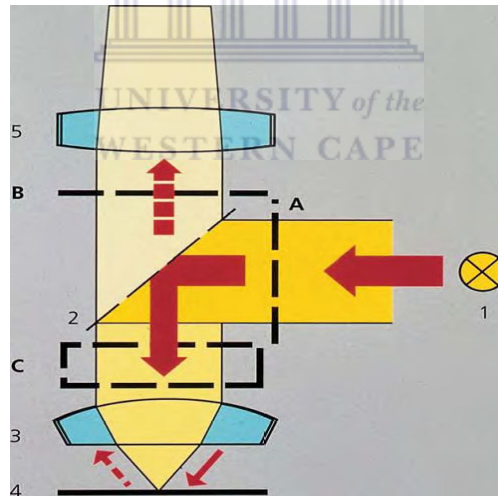
Figure 3-18: The process of bright field (BF) illumination in reflected light microscope and the optical path for establishing contrast: Light source (1), beamsplitter, color neutral (2), objective (3), object (4), lens (5) and contrast components on the side of the lamp (A), on the side of the eyepiece (B) and components for both light paths (C) [3.10].

Bright-field illumination of the reflected light is the most important method used in reflected-light microscopy and its components are shown in Figure 3-19.
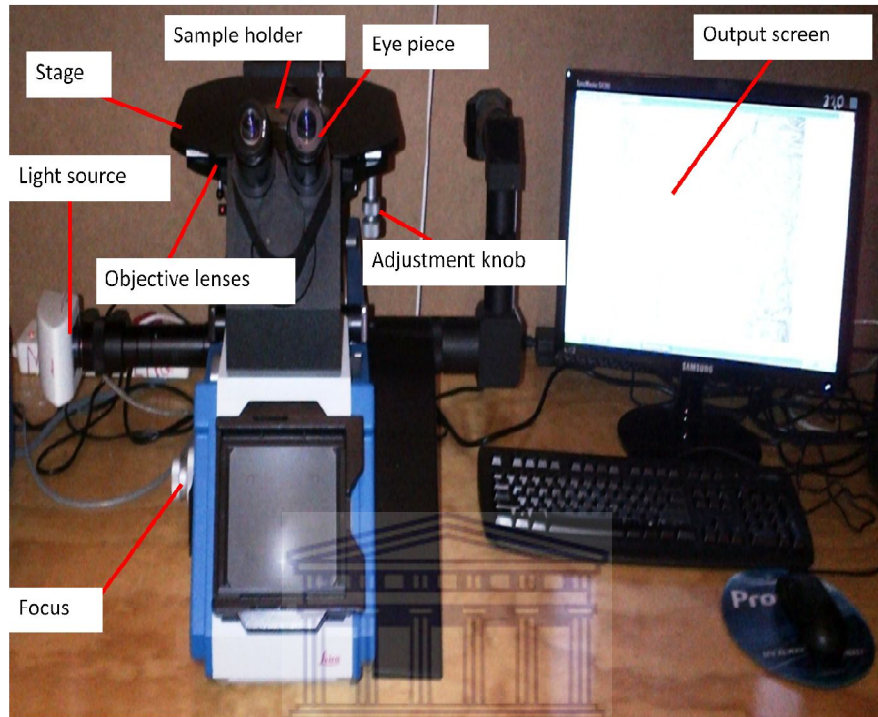
Figure 3-19: Inverted type of reflected-light microscope, Reichert MeF3A model.

This type of illumination contributes to the enhancement of the resolution power of equipment. In this process, the light that is reflected into the light path of the microscope passes through the objective directly onto the sample surface. The polished and etched sample is simply placed with the prepared surface facing down on a movable stage with a hole above the microscope column and the objective. The hole is located at the center of the stage through which the illumination light passes towards the sample. The three lenses of the Koehler system are part of the illumination elements shown in Figure 3-18 (A). The first lens in front of the light source (1), the collector lens, forms an image of the light source at the second lens, the first condenser lens. The third lens, the second condenser lens, reproduces

the image of the light source in the back focal plane of the objective (3) after passing the reflector (2). In this way the surface of the specimen is uniformly illuminated.

The movement of the stage is achieved via adjustment knobs that reposition the sample as desired. Focusing starts at lowest degree of magnification and proceed to higher magnification in order to check the quality of the sample preparation and also the details of the microstructure. Higher magnification requires the stage to be moved vertically higher for re-focus and which involves horizontal sample re-positioning adjustment. The image of the sample is captured on the computer screen.

(v) Characterisation

Grain size is a key determiner of materials properties. ASTM standards, both qualitative and quantitative exist that describe methods for determining grain sizes. Some of the shortfalls for these methods are that if the boundary between adjacent grains is incomplete when using a grain area method, the separate grain areas will be measured as one, resulting in erroneously high grain area data [3.10]. Similarly, missing boundaries will produce an inaccurately low measurement when employing a grain boundary length method of grain size determination. However in this study, the grain sizes in the microstructure were calculated by constructing at least five lines crossing over the grains, according to the basic principles of quantitative metallography. Their lengths were measured as well as the scale bar. Furthermore the number of grains crossed over by each line was counted. Using the formula

$$grain\ size = \frac{\left(length_x \times scale / scale\ length\right)}{number\ of\ grains\ crossed\ by\ length_x} \qquad (3\text{-}26)$$

where $length_x$ represent the length of specific line crossing over a certain number of grains.

3.4.4 Scanning electron microscopy

The scanning electron microscope (SEM) has been used for information on the structural properties and elemental composition of alloys. SEM makes use of electrons thermionically emitted from a heated filament of cathode or a field-emitter, within an electron gun situated at the top of its electron-optical column. It is capable of much better resolution than light microscopes because the wavelength of electrons is much smaller than that of the photons of visible light [3.9].

(i)   Instrumentation

Figure 3-20 is a schematic representation of the electron-optical column of a SEM. The emitted electrons form an electron cloud, which is then focused by electromagnetic lenses, coils and apertures into a fine probe that systematically scans over the specimen surface, to produce an image. The electrons are accelerated by high voltages towards the anode containing the sample. Two condenser lenses situated below the electron gun focuses the emerging beam into a much smaller diameter size, which is further aligned and focused by apertures and coils within the column until it reaches the final lens near the sample chamber.
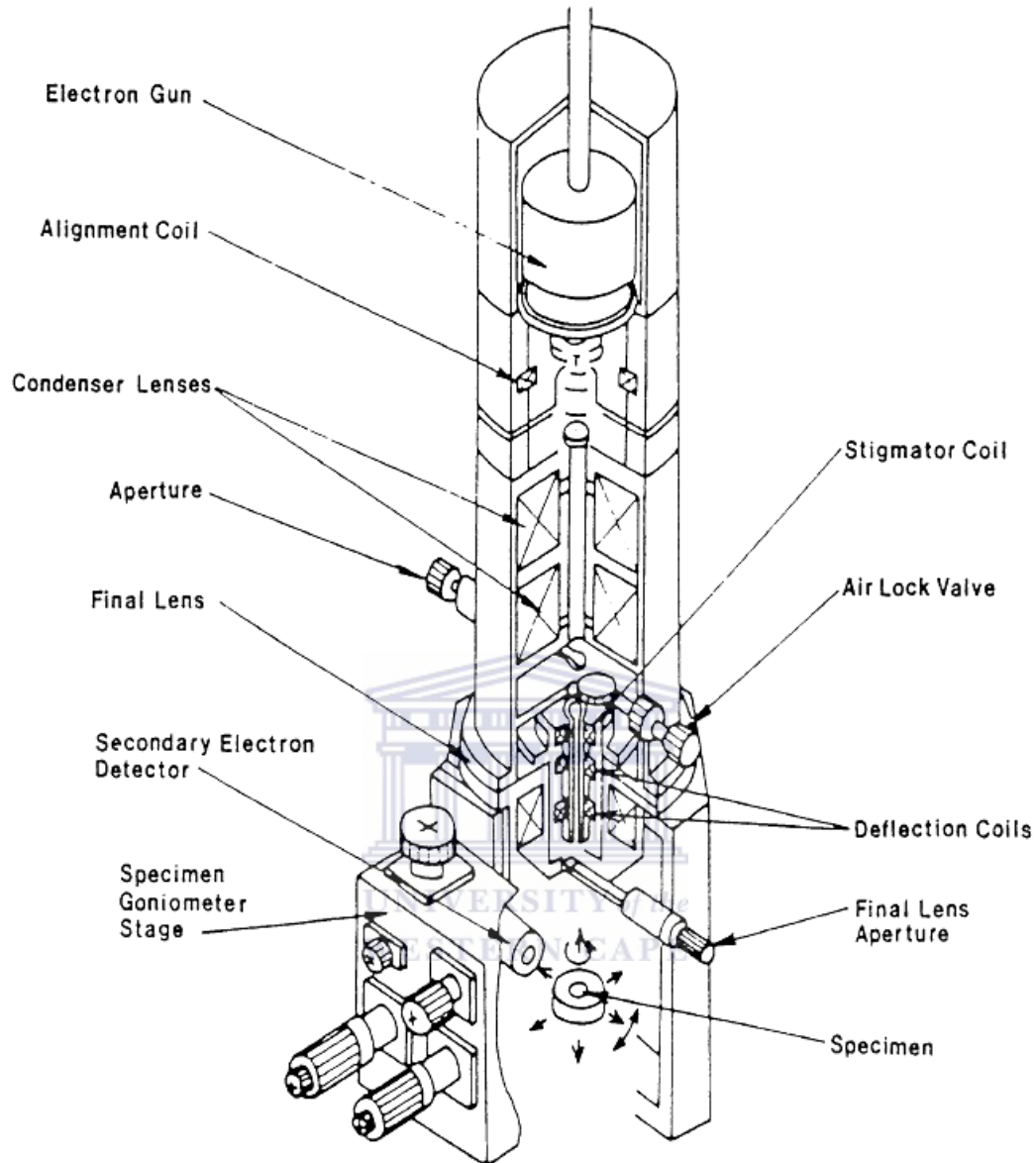
Figure 3-20: Schematic representation of SEM components [3.9].

The final lens further demagnifies the beam into a small spot, about 0.1-1 μm in diameter and moves it up and down in space until it reaches the sample surface. Despite its focusing capabilities, the objective lens also determines the intensity of the beam upon striking the sample and hence controls the image brightness.

(ii)   Resolution

The resolution of the equipment plays an important role in the imaging of samples. Resolution can be described as the distance at which two objects are observed as two separate entities. The limit of resolution which can be explained as the smallest separation distance, at which two objects are resolved, is described by Abbe's equation (3-27) [3.9]:

$$d = \frac{0.612\lambda}{n sin\alpha} \hspace{4cm} (3\text{-}27)$$

where d- resolution limit, λ- wavelength of the beam, n- refractive index of the medium through which the energy source travels and α- aperture angle.

(iii)   Influence of working distance on depth of field and resolution

Depth of field (DOF) refers to the depth for which the image is focused. The depth of field increases when the aperture angle, α, decreases.

Figure 3-21: The relationship between the working distance and the depth of field in SEM [3.9].

The working distance, which is defined as the distance between the final condenser lens pole piece and the uppermost part of the sample (see Figure 3-21), directly influences the depth of field observed for a particular sample. A short working distance results in the sample being scanned with electrons at a wider aperture angle (solid angle, α), thus resulting in an image with low depth of field, whereas when the sample is scanned at a longer working distance the aperture angle decreases, resulting in a greater DOF, as shown in Figure 3-21. A change in working distance will also influence the spherical aberration of the imaging system, thus affecting the resolution of the final image. Spherical aberration is a consequence of the geometry of the electromagnetic lenses; occurring when electrons which are closer to the beam axis will refract less than those passing through the edge of the electron beam, thus creating more than one focal point and therefore resulting in an enlarged, non-focused spot, as shown in Figure 3-22.
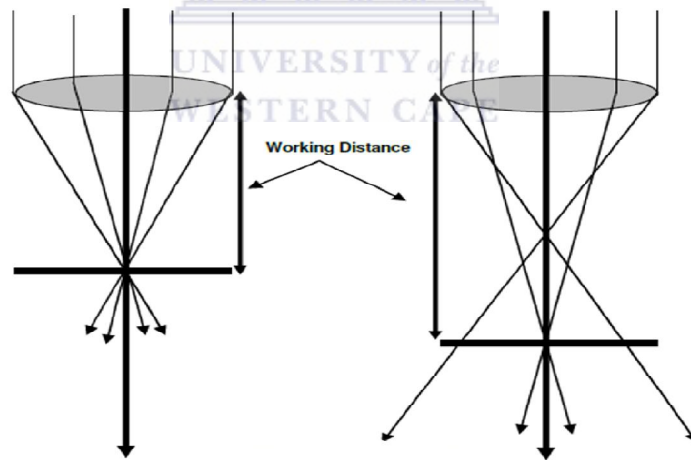
Figure 3-22: Effect of working distance on the amount of spherical aberration and resolution of the final image [3.9].

As the working distance decreases, however, the spherical aberration effects become less, resulting in a smaller, more focused beam spot; yielding a better resolved final image.

(iv)   Electron Beam

Upon interaction of the primary beam electrons with the specimen sample, several signals get detected within the SEM, providing valuable information about the sample's surface morphology and the specimen's composition. Signals including the secondary, backscattered and transmitted electrons as well as the specimen current all provide information about the surface features (morphology) of the sample whereas characteristic x-rays, cathodoluminescence and Auger electron signals give information regarding the composition of the specimen. Figure 3-23 gives a schematic illustration of the signals generated.
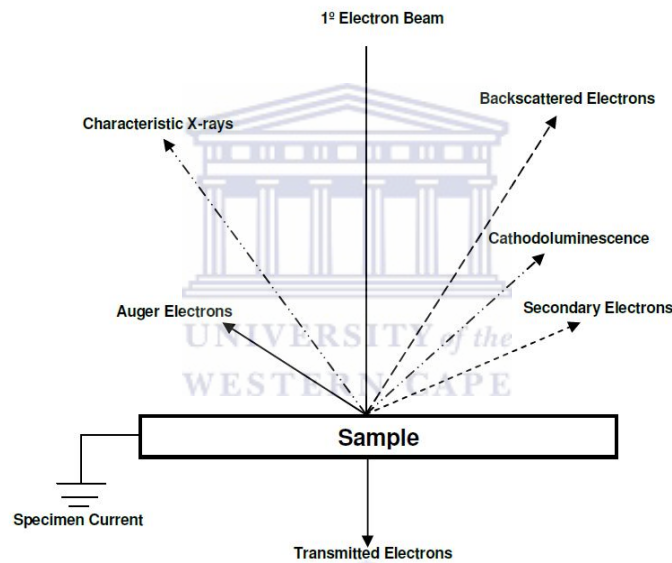
Figure 3-23: Schematic illustration of the signals generated during the primary electron beam - sample interaction [3.9].

(v)   Secondary electrons and image formation within the SEM

When the electron beam interacts with the sample an interaction volume is created in which the electrons undergo various scattering events. During these interactions secondary products such as secondary electrons, backscattered electrons, x-rays, heat and light forms. Image formation of the surface of a sample depends mainly on the production of secondary

electrons. Secondary electrons are low-energy electrons and thus will be absorbed by the sample when they are produced deep within the interaction volume; only those close to the surface usually have sufficient energy to escape as shown in Figure 3-24, therefore it is noted that the secondary electron image provides a surface profile of the sample.
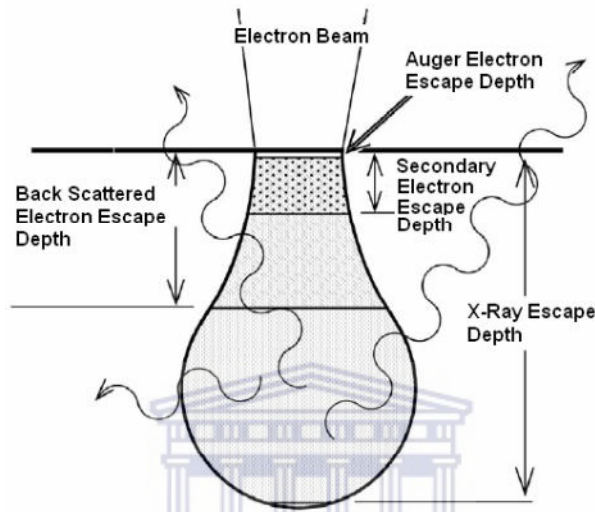
Figure 3-24: Interaction volume between the electron beam and the specimen [3.9].

The secondary electron image is the most common type of image used by modern SEMs and offers greater resolution compared to the other scanning signals. Structures down to 10 nm and better can be resolved by the secondary electron signal. The secondary electron detector, surrounded by a positively charged Faraday cup captures the electrons, whose energy is then converted into photons by means of a scintillator. These photons are then reflected down a light pipe where they are amplified into an electronic signal by a photocathode and photomultiplier. This signal is subsequently used to control the brightness of the image in proportion to the initial number of photons produced and allows for the distinction in contrast of the sample surface.

(vi)   Influence of accelerating voltage on the resolution

The accelerating voltage is the voltage that is applied to the filament. The applied voltage creates a current through the filament, causing it to emit electrons. Accelerating voltages often used in SEM work varies between 5 kV and 20 kV and in general, an increase in accelerating voltage will decrease the amount of spherical aberration of the system thereby enhancing its resolution. However, varying the accelerating voltage will also influence the electron beam–sample interaction. If a higher accelerating voltage is used the interaction volume between the beam and the sample will increase due to the more energetic electrons in the beam. The resolution of the system is also directly dependent on the area from which secondary electrons are emitted and normally this area is determined by the initial beam spot size. However, by increasing the accelerating voltage, backscattered electrons, which get emitted from a larger area of the sample, will interact on their way out, thus producing secondary electrons further away from the original beam spot size (Figure 3-24), which then also decrease the image resolution.
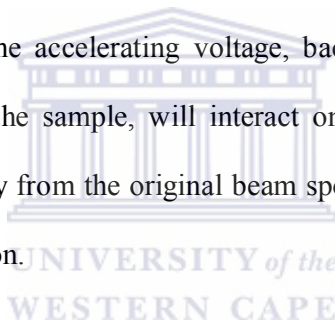
(vii)   Characteristic X-rays

The schematic representation of an atom is shown in Figure 3-25. The shells surrounding the nucleus of the atom, K, L, M, etc correspond to the principal quantum number, n = 1, 2, 3. A hole in an inner K shell of the sample atom is generated when an incident high-energy electron (E_0) that loses the corresponding energy (E) is transferred to the ejected electron. When this happens the atom is in an excited state. For the atom to return to its normal ground state, the hole in the K shell is subsequently filled by an electron from an outer shell, L or M. The superfluous energy is emitted as a characteristic X-ray quantum. When an electron from the L shell fills the K shell vacancy, the resulting x-ray is termed $K\alpha$, whereas when an M shell electron fills the vacancy K_β x-rays are emitted. The same nomenclature applies when

an electron from an outer shell (e.g. L) is knocked out. The difference in energy undertaken by the outer shell electron is a discrete amount, characteristic of the atom and is emitted as x-rays. The most probable transition that occurs when a K-shell vacancy is created is from the L to K shell because these are adjacent energy shells. Therefore K_α radiation will always be more intense than K_β radiation which originates from M shell. It also follows that K_β radiation will be of higher energy than K_α radiation, in as much as the energy difference between the M and K shells (K_β radiation) is greater than the energy difference between the L and K shells (Kα radiation).
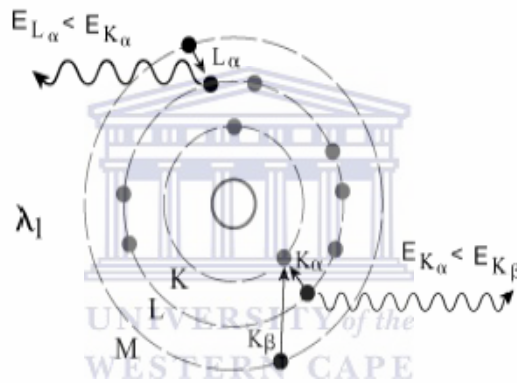
Figure 3-25: Characteristic x-ray emission by atom [3.9].

The energy difference between adjacent electron shells becomes less, progressing outward from the nucleus. The energy of the characteristic radiation within a given series of shells varies monotonically with atomic number. This is according to Moseley's Law which is described by Equation 3-28:

$$E = C_1(Z - C_2)^2 \qquad (3\text{-}28)$$

where E = energy of the emission line for a given X-ray series (e.g. K_α), Z = atomic number of the emitter, C_1 and C_2 are constants.

The K, L and M series X-rays increase in energy with increasing atomic number [3.1]. Characteristic X-rays reveal themselves as peaks imposed upon a background of Continuum X-rays.

(viii) Sample Preparation

In order to obtain an image of a non-conductive sample with the SEM, it must first be covered with an electrically conductive coating. This coating increases the sample's electrical conductivity, reduces the thermal damage caused by the beam to the sample and increases secondary and backscattered electron emission. Upon interaction of the primary beam with the sample there is a build up of charge, which must be dissipated in some way. For a conductive material, this is not a problem as the charge is conducted through the sample and eventually is grounded by contact with the sample stage. However, if the material is non-conductive, the charge builds up and causes charging. Charging results in the deflection of the electron beam and some secondary electrons, periodic bursts of secondary electrons and increased emission of secondary electrons from cracks and defects within the sample, which all serve to degrade the quality of the final image of the sample. Furthermore, because the coating helps to swiftly transfer the electrons of the beam away from the scanned region, it also avoids the build up of excessive heat, which can damage the sample. The coating of non-conductive specimen also serves to increase the number of secondary electrons produced. This is so since specimen of higher atomic number more readily produces secondary electrons, thereby contributing to an overall improved image. The conditions used for SEM in this study are: electron beam of 20 keV energy, secondary electron imaging mode, ETD/TLD or vCD detector.

3.4.5 X-ray diffraction (XRD) characterisation

X-rays are electromagnetic radiation of approximately the same nature as light but have shorter wavelengths ranging from 0.05 - 0.25 nm [3.11]. X-rays have wave-particle duality. This means that they can exhibit both wave and particle properties (dual nature) [3.11]. An X-ray beam carries energy and the rate of this energy per unit area is referred to as intensity *I*. The average value of the intensity is proportional to the square of the amplitude of the wave carrier (A^2). The energy carried by the X-rays radiation is proportional to the frequency, v of each photon's energy being equivalent to hv, where h is the Planck's constant.

(i)   Crystal structure and Bravais lattices

The atoms found in materials can be either randomly distributed, thus making the material amorphous or they can be arranged in a periodic pattern in three dimensions, resulting in a crystalline material. When thinking about the atomic arrangement within a crystal, it is best to imagine the atoms as a set of imaginary points with a fixed position in space. Figure 3-26 illustrates the above concept, referred to as a point lattice and is defined as an array of points in space, so arranged that each point have identical surroundings.
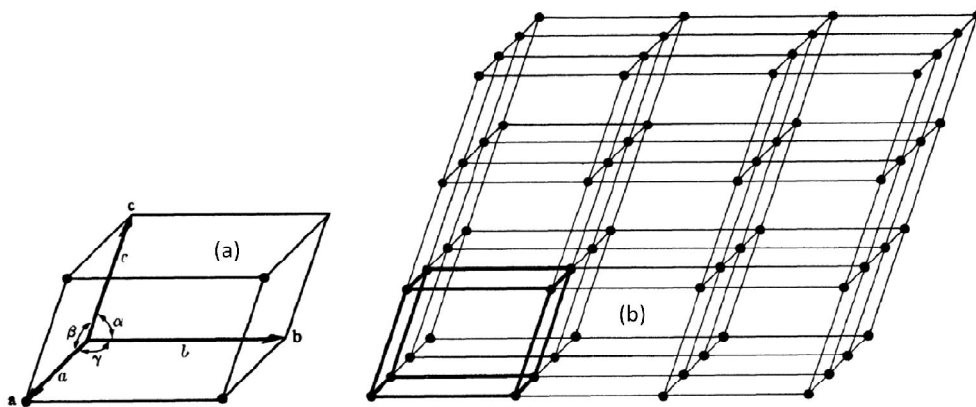
Figure 3-26: Schematic of (a) primitive cell and the angles between the translation vectors and (b) its point lattice [3.11].

By drawing three vectors $\vec{a}$, $\vec{b}$ and $\vec{c}$ from the corner of any lattice point, one generates a point lattice unit cell. These vectors, known as the crystallographic axes of the unit cell can also be described in terms of their lengths (a, b and c) and the angle between them (α, β and γ), known as the lattice constants or lattice parameters as shown in Figure 3-27.
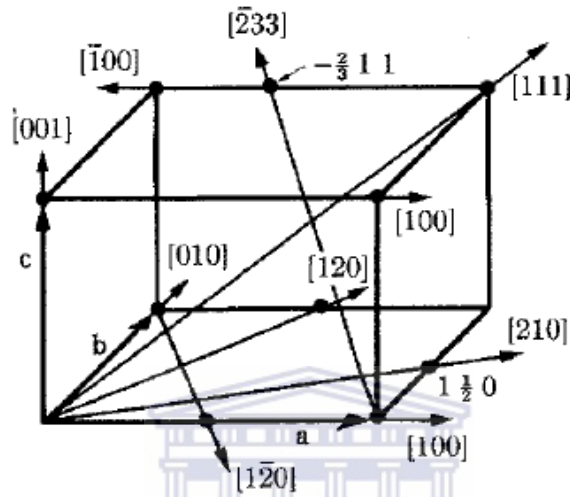
Figure 3-27: Indices for directions for a general unit cell [3.11].

Not only do the crystallographic axes define the unit cell, but it also defines the whole point lattice, which can be produced by repeated action of the vectors. Depending on the relationship between the lattice parameters (i.e. a, b, c, α, β and γ) one can distinguish fourteen lattices known as Bravais lattices, corresponding to seven crystal systems as shown in Table 3-6. The position of each atom in the crystal lattice is specified by the vector $\vec{R}$. The direction of any vector within the Bravais lattice is given as a linear combination of the three crystallographic axes as:

$$\vec{R} = u\vec{a} + v\vec{b} + w\vec{c} \qquad (3\text{-}29)$$

where $\vec{a}$, $\vec{b}$ and $\vec{c}$ - any vector in the Bravais lattice and u, v, w -coordinates of any point on the vector.

In conclusion, Equation 3-29 can be written as [u v w] as shown in Figure 3-27. Furthermore, directions related by symmetry are known as directions of a form, and are represented by angular brackets, e.g. the four body diagonals of a cube, [111], [$\bar{1}$11], [1$\bar{1}$1] and [11$\bar{1}$] are represented by ⟨111⟩ where the negative directions are indicated by a barred index. Furthermore, [u v w] are always converted to a set of smallest integers, e.g. [2 2 4] and $\left[\frac{1}{2}\frac{1}{2}1\right]$ represents the same direction, with [1 1 2] the preferred notation.

Table 3-6: Description of the fourteen Bravais lattices [3.11].

System	Axial lengths and angles	Bravais lattice	Lattice symbol
Cubic	Three equal axis at right angles $a = b = c$, $\alpha = \beta = \gamma = 90°$	Simple	P
		Body centered	I
		Face centered	F
Tetragonal	Three angles at right angles, two equal $a = b \neq c$, $\alpha = \beta = \gamma = 90°$	Simple	P
		Body centered	I
Orthorhombic	Three unequal axes at right angles $a \neq b \neq c$, $\alpha = \beta = \gamma = 90°$	Simple	P
		Body centered	I
		Base-centered	C
		Face centered	F
Rhombohedral	Three equal axis, equally inclined $a = b = c$, $\alpha = \beta = \gamma \neq 90°$	Simple	R
Hexagonal	Two equal co-planar axes at 120°, third axis at right angles $a = b \neq c$, $\alpha = \beta = 90°$, $\gamma = 120°$	Simple	P
Monoclinic	Three unequal axes, one pair not at right angles $a \neq b \neq c$, $\alpha = \gamma = 90 \neq \beta$	Simple	P
Triclinic	Three unequal axes, unequally inclined and none at right angles $a \neq b \neq c$, $\alpha \neq \beta \neq \gamma \neq 90°$	Simple	P

Collectively, all of these vectors form the reciprocal space of the lattice, or reciprocal lattice. Given any Bravais lattice, a lattice plane is defined as any plane containing at least three non-

collinear lattice points. A family of lattice planes is a set of parallel planes, which together contain all the points of the three-dimensional Bravais lattice.
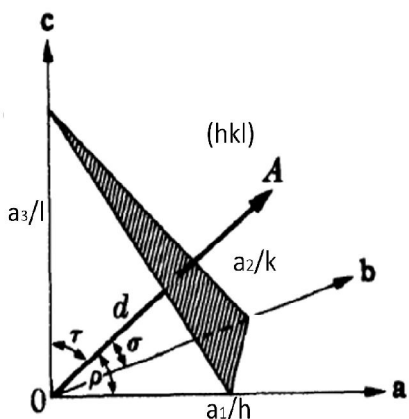
Figure 3-28: Relationship between the reciprocal lattice vector and the crystal plane (h k l) [3.11].

For cubic systems, there is an intrinsic relationship between the family of lattice planes and the vectors in the reciprocal lattice, which provides a convenient way of specifying the orientation of the lattice planes in space. Generally for cubic systems, the orientation of a plane is given by the vector normal to it and is denoted by Miller indices, h k l, contained in round brackets, e.g. (h k l). In Figure 3-28 the vector $\bar{n} = \frac{\bar{a}_1}{h} + \frac{\bar{a}_2}{k} + \frac{\bar{a}_3}{l}$ is normal to the plane (h k l) that intercepts the unit cell at $\frac{\bar{a}_1}{h}$, $\frac{\bar{a}_2}{k}$ and $\frac{\bar{a}_3}{l}$, where $\bar{a}_1$, $\bar{a}_2$ and $\bar{a}_3$ are the crystallographic axes. Similar to lattice vectors, planes related by symmetry are denoted by {h k l}.

(ii)   Bragg's Law for Diffraction

In Figure 3-29, a monochromatic beam of parallel x-rays, O and O', strikes a stack of hkl planes spaced a distance d apart at an angle θ. Each plane consists of a series of equally spaced atoms, each of which is capable of scattering the incident radiation.
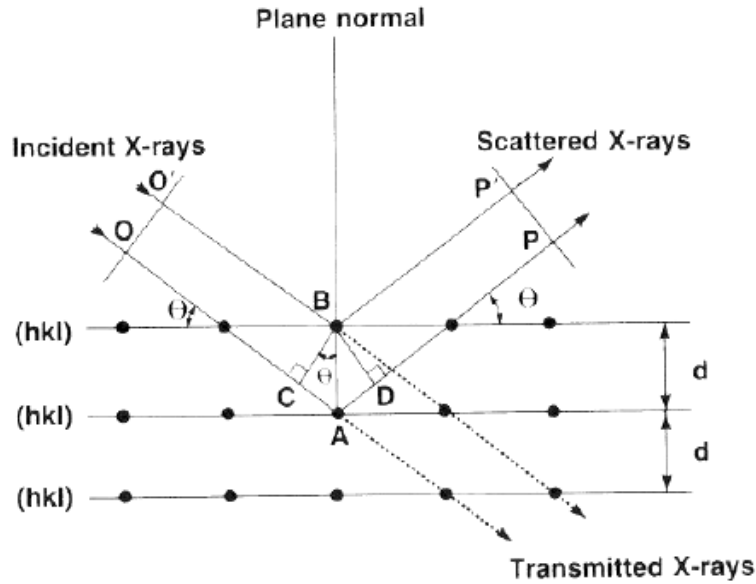
Figure 3-29: Derivation of the Bragg law $2d \, sin\theta = n\lambda$ [3.12].

The scattered rays P and P', resulting from the interaction of the incident beam with the atoms of the parallel planes, will recombine to form a diffracted beam if and only if their path difference is an integral multiple of wavelengths, i.e.

$$CA + AD = 2dsin\,\theta = n\lambda \qquad (3\text{-}30)$$

where n - integer multiple (order of diffraction), λ - wavelength of the radiation, d - interplanar spacing, θ - incident angle (Bragg angle), Equation (3-30) can be written simply as

$$2d \, sin\theta = n\lambda \qquad (3\text{-}31)$$

known as Bragg's law. X-rays will diffract constructively from a set of planes (hkl) only when this law is satisfied.

(iii)   Atomic and Structure Factors

A quantity f, called the atomic scattering (or form) factor, is used to describe the efficiency with which a given atom scatters an incident x-ray beam in a given direction and is defined by Equation 3-32 [3.11]:

$$f = \frac{amplitude\ of\ the\ wave\ scattered\ by\ an\ atom}{amplitude\ of\ the\ wave\ scattered\ by\ one\ electron} \qquad (3\text{-}32)$$

The scattering of the incident wave by an atom depends on the arrangement of the electrons within the atom. However, when scattering by the unit cell of the crystal is considered, the scattering process depends on the atomic arrangement within the unit cell. The wave diffracted by a unit cell containing 1, 2, 3,.., n atoms each with fractional coordinates $u_1v_2w_3..u_nv_nw_n$ and atomic factors $f_1f_2f_3,.., f_n$. f_n is called the structure factor, F_{hkl} and is defined by Equation 3-33 [11]:

$$F_{hkl} = \sum_{i=0}^{n} f_n e^{2\pi i(hu_n+kv_n+lw_n)} \qquad (3-33)$$

The absolute value of F_{hkl} gives the amplitude of the resultant wave in terms of the amplitude of the wave scattered by a single electron. The intensity of the beam diffracted by all the atoms within the unit cell is proportional to $|F_{hkl}|^2$ Furthermore, the structure factor is independent of the relationship between the lattice parameters and thus only depends on the number and position of the atoms within the unit cell of the Bravais lattice, i.e. only depends on whether the unit cell is primitive, body-centered, etc.

(iv)   Instrumentation and data collection

The apparatus with which x-ray diffraction is performed is called an x-ray diffractometer as shown in Figure 3-30 and consists of three basic parts; an x-ray source (S and T in Figure 3-30), diffractometer circle and a detector system (G and E). The detector (G) is placed on the circumference of a circle centered at the specimen stage, C. The specimen is supported on a Table H, which can rotate about an axis, O, perpendicular to this page. X-rays diverge from the source at S and are diffracted by the specimen at C to form a convergent diffracted beam, which focuses at the slit F before entering the detector at G, supported on a carriage, E. The carriage also rotates about the axis O and has an angular position 2θ. The supports H and E

are mechanically locked in a θ-2θ relationship. A filter is placed in the diffracted beam-path to suppress the K_β radiation and to decrease the background radiation originating in the specimen
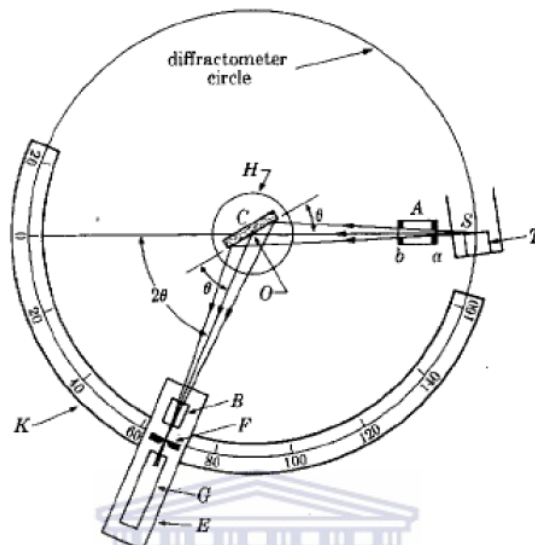
Figure 3-30: Schematic of an x-ray diffractometer. A and B are special slits that define and collimate the incident and diffracted beams [3.11].

The Bruker D8 ADVANCE X-ray diffractometer is set up in such a way that when the sample is placed in a sample holder at an angle between 0 ˚ and 180 ˚ with the direction of X-ray tube (goniometer) and the detector, has random distribution of all possible (h k l) planes. In this way, clearly defined planes can be evaluated. However, only crystallites having reflecting planes (h, k, l) parallel to the sample surface will contribute to the reflected intensities. For the θ: θ goniometer which was used in this study, the sample is stationary in the horizontal position while the X-ray tube and the detector both move simultaneously over the angular range θ. The Bruker D8 ADVANCE uses an X-ray tube with a copper (Cu) or molybdenum (Mo) anode as the primary X-ray beam source. In this component, X-rays are generated when a focused electron beam produced by heating the filament, is accelerated across a high voltage to bombard a stationary solid Cu or Mo target. The Cu target emit 8

keV x-rays with corresponding wavelengths of 1.54 Å and molybdenum (Mo) emits 14 keV x-rays of 0.8 Å wavelength. As electrons collide with atoms in the target, those electrons having sufficient energy to dislodge inner shell electrons of the target material produce characteristic X-ray spectra. These spectra consist of several components, the most common being K_α and K_β. K_α consists, in part, of $K_{\alpha 1}$ and $K_{\alpha 2}$. $K_{\alpha 1}$ has a slightly shorter wavelength and twice the intensity as $K_{\alpha 2}$. $K_{\alpha 1}$ and $K_{\alpha 2}$ are sufficiently close in wavelength such that a weighted average of the two is used. The specific wavelengths are characteristic of the target material.

The production of monochromatic X-rays needed for diffraction can be achieved by filtering using Nickel foil. These X-rays are collimated and directed onto the sample. When the geometry of the incident X-rays impinging the sample satisfies the Bragg Equation (3-31), constructive interference occurs. A detector records and processes this X-ray signal and converts the signal to a count rate which is then output to a device such as a printer or computer monitor. The following parameters were used: Cu $K\alpha$ target with a wavelength of 1.54 Å, 40 mA power and 40 kV voltage. The samples were run from a 2θ range 30 ˚ - 90 ˚ at a step size of 0.03 ˚.

3.4.6 Hardness Testing

Hardness is the resistance of a material to penetration by another (harder) material [3.10]. Hardness is an important property when judging the quality and possible applications of a material. It can also give information concerning the tensile strength, ductility, or wearing quality of the material. Furthermore, hardness is related to tensile strength of a metal and indicates its resistance to plastic deformation. The higher the hardness value of the material, the higher is its strength. The correlation of hardness with tensile strength is generally good

(difference usually less than ± 10 %). The determination of hardness of a metal is achieved by indenting the material with very hard objects of a specified size and shape. The most common techniques used for conducting this procedure are the Brinell, Rockwell, Knoop and Vickers hardness testing procedures which follow ASTM standards [17-19]. Figure 3-31 schematically shows the significant elements of indentation hardness testing.
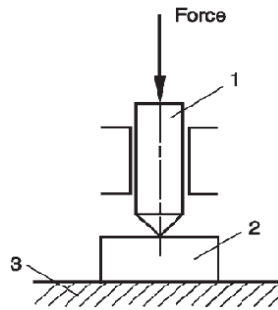
Figure 3-31: Schematic diagram of hardness tester indicating force, indenter (1) sample (2) and support (3) [3.10].

A particular indenter (1) attached to the lower end of a press, is pressed into the sample surface (2) with a particular test force measured in N or kgf and then pulled back. The indentation that is created can then be measured. Hardness is usually measured quantitatively according to the following general relationship:

$$hardness\ value = {Test\ force}/{indentation\ size} \qquad (3\text{-}33)$$

(i)   Indentation Hardness testing methods

Brinell hardness testing method makes use of a hardened steel ball or tungsten carbide ball with a diameter ranging from 1 - 10 mm. The sample of the material is pushed away sideways and downwards through plastic and elastic deformation as a result of the ball-shaped indenters. A spherically shaped indentation will be formed. A method was developed specifically for low load and micro-indentation hardness testing known as Knoop hardness

testing. In Knoop hardness testing, a rhombic-based pyramidal-shaped diamond indenter with edge angles of 172 ° and 130 ° is utilised. A diamond indenter is used for Rockwell C or a tungsten carbide/steel ball is used for Rockwell B. In this method, the hardness of a material is determined by means of measured indentation depth. With the Vickers test method, which was used in this study, several different loading settings give similar hardness values of material. The indenter used in this method is a regular four-sided diamond pyramid with an interfacial angle, α, of 136 °. The geometry of the pyramid produces a good correlation between the Vickers values HV and the Brinell hardness values HBS between 350 and 400 [3.10].

(ii)   Vickers hardness testing

The Vickers hardness is measured by vertically pressing the diamond-pyramid into the sample with a test force P (kgf) (2) shown schematically in Figure 3-32. Schematic (1) presents the face angle of the diamond (136 °) and, d_1 and d_2 (3) are the diagonals of the impression in (mm). The mean diagonal, *d,* of the indentation is used to calculate the Vickers hardness. The Vickers hardness is calculated from the mean indentation diagonal according to the following equation:

$$HV = 0.93 \frac{P}{A} = \frac{2P sin(136°/2)}{d^2} \approx 1.85 \times \frac{P}{d^2} (kg/mm^2) \quad (3\text{-}34)$$

where HV - Vickers hardness, P - test force in kgf, A- indentation surface area in mm^2 and d -arithmetical mean value of the measured indentation diagonals in mm. Because of the pyramidal geometry, the relationship between the indentation depth and the indentation diagonals is $h = {d}/{7}$.
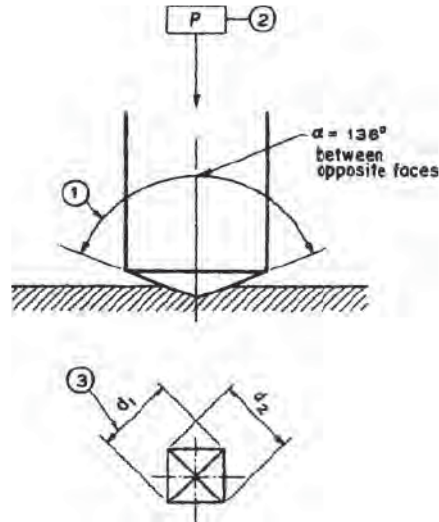
Figure 3-32: A schematic presentation of the indentation of material by the diamond shaped Vickers test indent [3.10].

Figure 3-33 shows the ideal indentation in *(a)* and possible undesirable indentations with sink-in *(b)*, pile-up *(c)* formation and kite shape *(d)*.
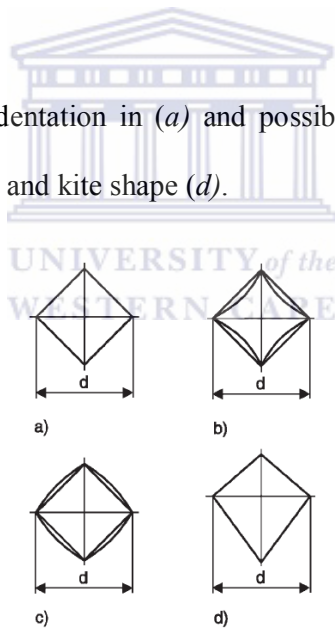
Figure 3-33: Vickers indentation shapes of (a) ideal indentation, (b) indentation with sink-in, (c) indentation with pile-up and, (d) kite-shaped indentation [3.10].

The undesirable indentations are disruptive in microhardness testing, where HV values that have been measured for the same specimen are no longer comparable. The reason for this can be due to plastic deformation induced when the Vickers pyramid is imposed or due to different respond of material during metallographic preparation [3.10].

In Vickers hardness testing, the distance between the center of the indentation and the sample edge, and between the center of two indentations should be greater than 2.5 d. For high-test forces, determination of Vickers hardness is independent of the test force. The phenomenon known as indentation size effect (ISE) occurs at test forces less than 5 N whereby the Vickers hardness becomes test force dependent. The influences of ISE are disruptive in micro-hardness testing where HV values that have been measured for the same sample with various test forces are no longer comparable. Due to this drawback, the micro-hardness value classification of Vickers test method is divided into test ranges which can be performed with test forces ranging between 1 and 1000 gf (9.8×10^{-3} and 9.8 N) according to the ASTM Standard (E384-11e1) [3.19]. This test extends testing to materials that are too thin or too small for macro-indentation hardness tests which are conducted with forces above 1000 gf. It allows specific phases or constituents and regions or gradients too small for macro-indentation hardness testing to be evaluated.
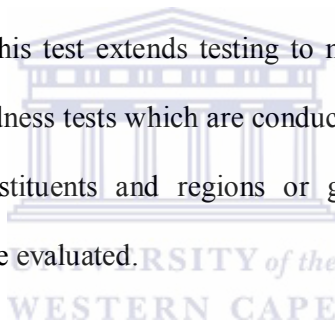
(iii)   Sample preparation

Vickers hardness tester is set up in such a way that the polished and cleaned surface of the sample should be placed perpendicular to the direction of indentation. In this way, clearly defined indentations can be evaluated microscopically. The smaller the test force and the indentation, the greater is the influence of sample preparation [3.10]. For example, excessive polishing can cause cold work of the surface material. Whenever possible, the surface should not be etched since the indentation otherwise becomes uneven due to the attacked surface and may be difficult to measure. Small unevenly shaped specimens must be mounted or fastened into specimen holders. It is important to ensure that the specimen cannot move under the effects of the force. In this study, the measurements were made with a Zwick Roell

ZHV Vickers hardness model. A loading force of 1 Kgf and a dwell time of 10 s were used.

A maximum series of eight test impressions were made on each sample.

3.5   References

[3.1] P.G. Laye, S. Warrington, G.R. Heal, and P. Haines, Principles of thermal analysis and calorimetry, Royal Soc. Chem., (2002).

[3.2] J.L. Ecuyer, C. Brassard, C. Cardinal, and J. Chabbal, J. Appl. Phys., **47**, 262 (1976).

[3.3] K.G. Malmqvist, Radiat. Phys. Chem., **71**, 817-827 (2004).

[3.4] M. Mayer, Max-Planck-Institut fur Plasmaphysik, Garching, Germany, (2006).

[3.5] J. Tirira, Y. Serruys, and P. Trocellier, Forward Recoil Spectrometry: Applications to Hydrogen Determination in Solids, Plenum Press (1996).

[3.6] J. Ziegler, J. Biersack, and U. Littmark, The stopping and range of ions in solids, Pergamon press, Inc., New York, (1985).

[3.7] E. Szilágyi, Nucl. Instr. Meth. Phys. Research Section B: Beam Interactions with Materials and Atoms, **161**, 37-47 (2000).

[3.8] N. Barradas, M. Mayer, and M. Thompson, Nucl. Instr. Meth. Phys. Research Section B: Beam Interactions with Materials and Atoms, **268**, 1824-1828 (2010).

[3.9] P.J. Goodhew, J. Humphreys, and R. Beanland, Electron microscopy and analysis, Taylor & Francis (2000).

[3.10] K. Geels, Metallographic and Materialographic Specimen Preparation, Light Microscopy, Image Analysis, and Hardness Testing, ASTM International (2007).

[3.11] B.D. Cullity and S.R. Stock, Elements of X-ray Diffraction, Prentice Hall Upper Saddle River, NJ (2001).

[3.12] H. Stanjek and W. Häusler, Hyperfine interactions, **154**, 107-119 (2004).

[3.13] T. Monecke, S. Köhler, R. Kleeberg, P.M. Herzig, and J.B. Gemmell, The Canadian Mineralogist, **39**, 1617-1633 (2001).

[3.14] E.H. Kisi and C.J. Howard, applications of neutron powder diffraction, Oxford series on neutron scattering in condensed matter, **15**, 486 (2008).

[3.15] D. Bish and S. Howard, J. Appl. Cryst., **21**, 86-91 (1988).

[3.16] HIDEN ISOCHEMA LTD. Technical data sheet 146, "Gravimetric Analysers for the Characterisation of the Sorption Properties http://www.hidenisochema.com/ of Materials". Accessed March 14, 2013. http:// www.hidenisochema.com

[3.17] ASTM Standard E10, 2012, "Standard Test Method for Brinell Hardness of Metallic Materials," ASTM International, West Conshohocken, PA, 2012, DOI: 10.1520/E0010-12, www.astm.org.

[3.18] ASTM Standard E18, 2012, "Standard Test Methods for Rockwell Hardness of Metallic Materials," ASTM International, West Conshohocken, PA, 2012, DOI: 10.1520/E0018-12, www.astm.org.

[3.19] ASTM Standard E384, 2011e1, "Standard Test Method for Knoop and Vickers Hardness of Materials," ASTM International, West Conshohocken, PA, 2011e1, DOI: 10.1520/E0384-11E01, www.astm.org.

Chapter 4: . Hydrogenation of Pd and Pd alloys

4.1 Introduction

The storage of hydrogen in the form of hydrides is safer as compared to its storage in the form of liquid or gas, due to the high pressures and cryogenic temperatures needed to maintain the systems [4.1,4.2]. The hydrogenation of Pd and its alloys can be used as a model for hydrogen storage systems because of the low diffusion path and their high solubility for hydrogen [4.3,4.4]. The absorption of hydrogen occurs even at room temperature and under low pressures. High pressures increase the dissociation of the hydrogen molecules on the Pd sample surface such that the adsorbed atoms diffuse easily (absorption) into the bulk material [4.5,4.6]. It is difficult to determine the phase transition from α- to β- phase because both phases have the same crystal structure (face centered cubic). The phase diagram of Pd has shown that the formation of β-phase hydride (PdH$_x$) occurs when $x \geq 0.6$ at low pressures while at high pressures the formation commence at lower hydrogen content [4.7,4.8]. However, the absorption capacity of Pd decreases with an increase in Pt content in the alloys at any given temperature as a result of volume effects caused by changes in the host lattice [4.2]. On the other hand, the substitution of Pd atoms with Pt strengthens the alloy and decreases the critical hydride phase formation temperature [4.9]. The Pd-Pt coating provide high mobility to hydrogen atoms which occupy interstitial positions in the host metal lattice [4.10,4.11]. Interstitial diffusion occurs inside the coatings and, as a result, thermodynamic equilibrium of hydrogen can be achieved even at room temperature. The presence of the dislocations due to the thermal stresses that appear during the coating deposition enhance the diffusion path of hydrogen. However, the probability of the hydrides formation depends on the coating thickness [4.12]. The gravimetric methods were used to determine the absorption of hydrogen in the material, in addition to elastic recoil detection analysis (ERDA) which was used to quantify the hydrogen content and to determine the depth of hydrogen penetration. The results presented in this chapter discuss the hydride formation and the determination of

absorbed hydrogen during hydrogenation of pure Pd, Pd-Pt coatings and Pd-Pt alloys under different hydrogenation conditions. The quantity of hydrogen determined by IGA measurements and ERDA experiment will be discussed for comparison.

4.2   Experiment

The Pd and Pd-Pt alloys used in this study were obtained from Mintek. The Pd has 99.96 % purity and the alloy compositions are Pd-2 at. % Pt, Pd-6 at. % Pt, Pd-10 at. % Pt and Pd-12 at. % Pt. The materials were cold rolled to a foil of about 1 mm thick and annealed at 1000 ˚C in vacuum for 12 hours. In addition, the Pd-Pt coated system with 0.5 μm of Pt layer deposited on a Pd substrate was studied. The coatings were deposited at a rate of 3.5 Å/s using sputtering method. The materials and the hydrogenation conditions used in this study are listed in Table 4-1.

Table 4-1: Hydrogenation processes of Pd and Pd-Pt alloys under different conditions.

Material	Temperature	LP-LC-ST (hours)	HP-HC-LT (hours)
Pd	Room temperature	1, 2, 7	14
	550 ˚C, 650 ˚C	3	-
Pd-2 at. % Pt	Room temperature	-	14
Pd-6 at. %Pt	Room temperature	-	14
Pd-10 at. % Pt	Room temperature	-	14
Pd-12 at. % Pt	Room temperature	-	14
Pd-Pt coating	550 ˚C, 650 ˚C	3	-

The experimental parameters used for low pressure-low hydrogen concentration-short charging time (LP-LC-ST) hydrogenation conditions are 1013 mbar pressure, 15 % of hydrogen concentration environment and 3 hours for high temperatures and a maximum of 7 hours for room temperature. High pressure-high concentration-long charging time (HP-HC-

LT) conditions were conducted up to a maximum of 2000 mbar in 99.99 % of hydrogen for 33 hours in total. These conditions were chosen in order to study the hydrogen absorption/desorption and storage capabilities of different Pd-based systems. Sorption of hydrogen under HP-HC-LT conditions was studied in 10 pressure steps by changing and holding the system pressure for 130 minutes or until full saturation.

The phase transformation occurring during hydrogenation was investigated using X-ray diffraction (XRD). The spectra were recorded with a D8-ADVANCE-Bruker X-ray powder diffractometer operating at 40 kV and 40 mA. Copper (Cu) K_α radiation with a wavelength of 1.54 Å was used as the X-ray source. The samples were run from 30 ˚ to 90 ˚ at a step size of 0.03 ˚. The hydrogenation of Pd-Pt alloys was only conducted in IGA under HP-HC-LT conditions
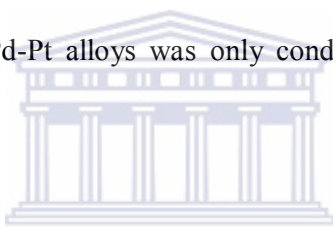
Gravimetric measurements of the samples hydrogenated at LP-LC-ST conditions were taken using a digital balance whereas gravimetric gas sorption analysis was conducted at high pressure systems in IGA. Both measurements determine the percentage of the mass difference of the material before and after hydrogenation processes. The pressure was increased in 10 steps from a pressure of 0 - 2000 mbar during sorption and decreased in 9 step to vacuum pressure during desorption. After the IGA processes, the hydrogen in the materials was quantified by employing an ion beam in elastic recoil detection analysis (ERDA) technique. The ERDA experiments make use of He^+ ion beam with 3 MeV energies which strike the sample surface at 75 ˚ with respect to the normal. The ions transfer part of their energies to hydrogen atoms which will recoil at a forward direction of 30 ˚ known as scattering angle directly towards the detector. The detector has $1.08 \times 10^{-3} \, sr$ solid angle with a minimum sensitive depth of 100 μm. The final energies of the recoils determine the

depth of their origin in the materials and therefore the energy is represented by a channel number on the ERDA spectra showing low energy recoils at high channels.

4.3   Results

4.3.1 Hydrogenation under LP-LC-ST conditions

4.3.1.1   Pure Pd

(i)   Phase analysis using X-ray diffraction

Figure 4-1 presents the XRD patterns of Pd samples treated at room and elevated temperatures under different periods of time and hydrogen content.
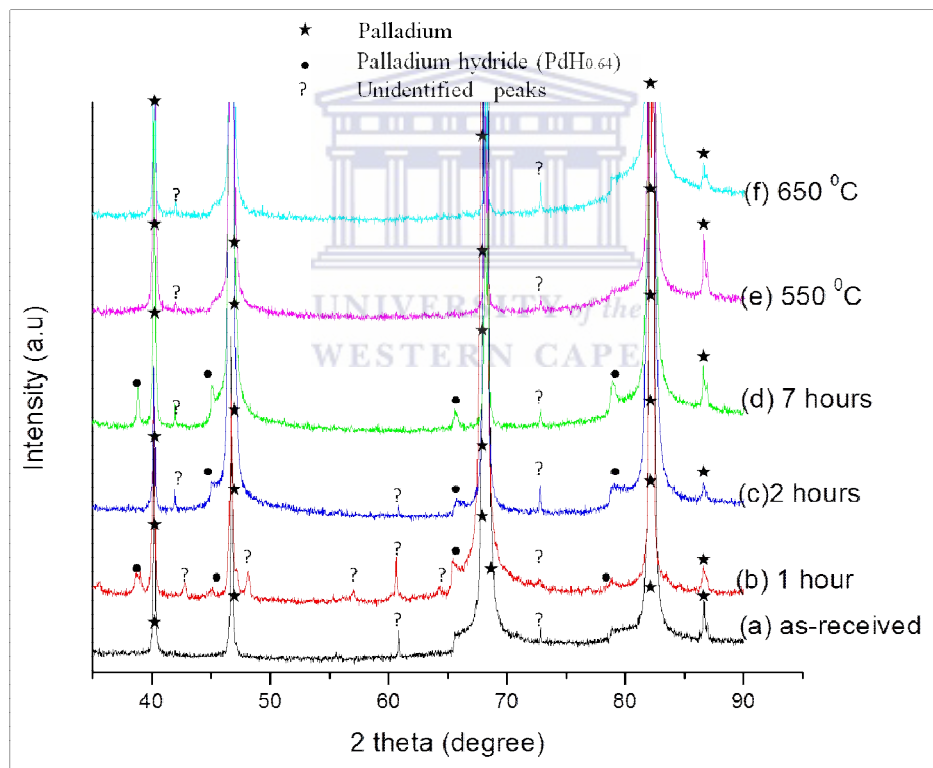
Figure 4-1: XRD patterns of Pd samples; (a) as-received, hydrogenated at room temperature for (b) 1 hour, (c) 2 hours, and (d) 7 hours, and hydrogenated for 3 hours at (e) 550 ˚C and (f) 650 ˚C temperatures.

X-ray diffraction pattern for as-received sample shows Pd diffraction peaks along with some

unidentified peaks which disappear at high temperatures. After the process of hydrogenation has occurred at room temperature, the peaks of ($PdH_{0.64}$) hydride with 4.03Å lattice parameter and face- centered- cubic (fcc) crystal structure appear. *Alefeld et al.* [4.10] has shown that the β- hydride phase of the Pd-H system start forming when the lattice parameter is above 3.89 Å and therefore, it is reasonable to assume that a β-phase formation has occurred. Considering the relationship between the lattice parameter and the interplanar spacings, the presence of hydrogen in Pd increases these spacings, thus increasing the lattice volume.

Introduction of hydrogen into pure Pd at elevated temperatures, 550 ˚C and 650 ˚C, does not yield hydrides. This was expected as reported in the work published by Antonov et al. [4.5] which indicated that at temperatures above 200 ˚C and hydrogen pressures up to $90 \times 10^6 \, mbar$, no transformations occur in the palladium-hydrogen system. The phase transformation in Pd can be described by the phase diagram of Pd-H system depicted in Figure 2-8 [4.7,4.8]. Because the influence of hydrogen in the unit cell of Pd atoms lowers the Pd states below the d-bands, these states are a manifestation of bonding between H and Pd and between H-H. However, for dilute hydrogen in the metal, H-H interaction is very weak such that there will be no significant lowering of the states [4.13]. Hence, it can be concluded that at 550 ˚C and 650 ˚C temperatures, the amount of hydrogen absorbed is not sufficient for the formation of hydrides whereas at room temperature, the solubility is so high that the quantity of hydrogen absorbed is high, resulting in a phase transition. The temperature dependency of the solubility of hydrogen in Pd which was also studied by *Lewis et al.* [4.14], as illustrated in Figure 2-6, has indicated that the absorption of hydrogen decreases with an increase in temperature.

Briefly, during the hydrogenation of Pd under low pressure- low gas concentration- short charging time (LP-LC-ST) conditions, the $PdH_{0.64}$ hydride was formed during the hydrogenation at room temperature for 1 hour. The equilibrium pressure for hydride formation at room temperature is less than 1013 mbar.

(ii)   Gravimetric measurements

Gravimetric measurements by a digital balance were taken before and after hydrogenation of Pd sample to determine the effect of hydrogen content on the mass of the sample. Hydrogenation of Pd at room temperature under LP-LC-ST hydrogenation conditions for 1 hour did yield the mass change of 0.22 mg which is equivalent to a hydrogen concentration of 0.04 wt. % (1.73 at. %).

(iii)   ERD analysis

The concentration of hydrogen in the Pd sample was determined before and after hydrogenation by ERDA.
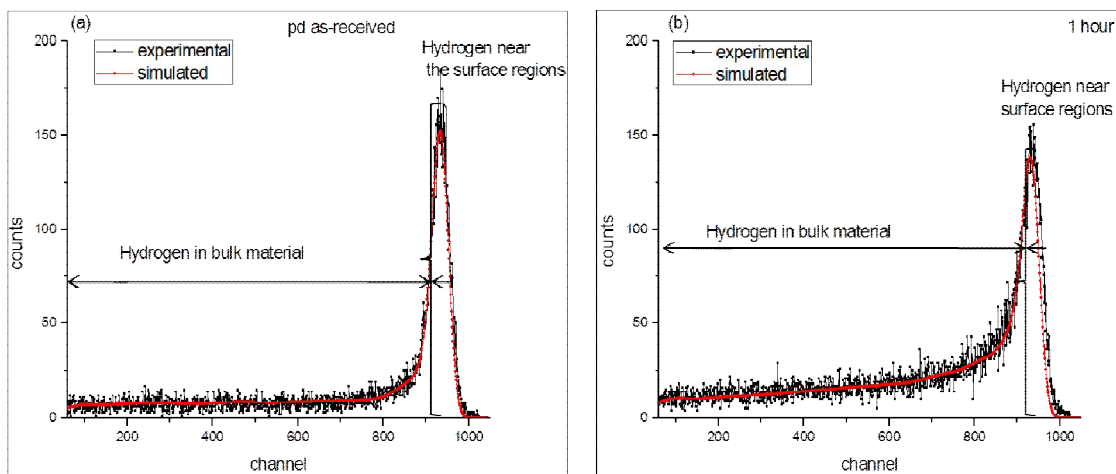
Figure 4-2: ERDA spectra of hydrogen distribution in (a) as received and (b) Pd sample hydrogenated at room temperature for 1 hour.

The ERDA spectra, Figure 4-2, show the distribution of hydrogen in the as-received and hydrogenated Pd sample for 1 hour. Both the as-received and hydrogenated Pd samples contain hydrogen at the surface and in the bulk of material. Generally, all the samples investigated in this study contain hydrogen at the surface and a homogeneous distribution in the bulk of the material. The origin of hydrogen in the as-received samples might be due to manufacturing processes or sample preparation treatments. The peak width of the spectrum increases after hydrogenation for 1 hour thereby increasing the peak area as shown in Figure 4-2 (b). Since the peak area correspond to the hydrogen content in the material and therefore, absorption of hydrogen has occurred. From the spectra, the concentration depth profile of hydrogen in Figure 4-3 was deduced.
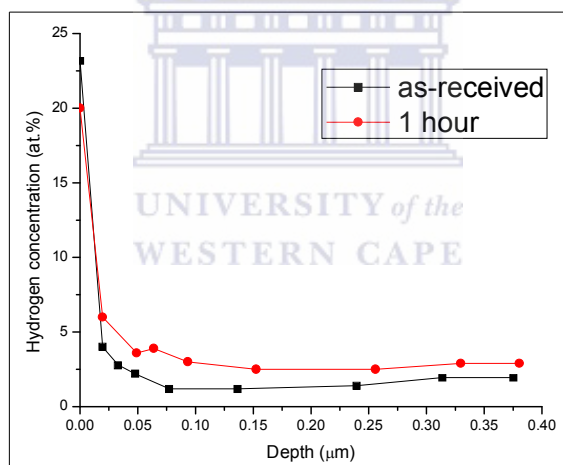
Figure 4-3: The depth profile of hydrogen in the Pd before and after hydrogenation for 1 hour performed under LP-LC-ST conditions at room temperature.

The depth profiles are plotted as hydrogen concentration (at. %) as a function of depth (µm). This preference applies to all the depth profiles discussed in this work. The average hydrogen concentration present in the sample before and after the hydrogenation process is given in Table 4-2. The average concentration of hydrogen decreased from 23.2 - 20 at. % on the

surface region after the hydrogenation process conducted under LP-LC-ST conditions. The depth of distribution of the hydrogen at the surface region of the hydrogenated sample is similar to that of as-received sample (0.02 μm). However, the concentration of the hydrogen in the bulk of the material after the hydrogenation process has increased from 1.63 - 3.08 at. %. It can be observed that the depth at which the hydrogen penetrates into as-received material is similar to that of hydrogenated sample (0.38 μm) shown in Figure 4-3.

Table 4-2: The average concentration of hydrogen in as-received and hydrogenated Pd sample under LP-LC-ST and room temperature conditions.

Pd	Average hydrogen concentration on the surface		Average hydrogen concentration in bulk material	
	(at. %)	(wt. %)	(at. %)	(wt. %)
As received	23.2	0.29	1.63	0.02
1 hour	20	0.24	3.08	0.03

In summary, the ERDA results show that pure Pd sample hydrogenated at room temperature under low pressure-low concentration-short time (LP-LC-ST) conditions has absorbed an average amount of 3.08 at. % of hydrogen in the bulk. It was also found that the hydrogen which was mainly concentrated on the surface region decreases to 20 at. % after hydrogenation. These results are in agreement with findings by *Lewis et al.* [4.14] and *Juodkazis et al.* [4.15] who stated that Pd is capable of absorbing a substantial amount of hydrogen at room temperature under atmospheric pressure. Therefore, the fact that Pd can absorb a great amount of hydrogen at room temperatures even at short charging times makes the Pd-H system an ideal model to be used in understanding the process of hydrogen absorption in solid materials [4.3,4.4]. Based on this model, the hydrogen interaction in different metallic systems can be predicted.

4.3.1.2 Pd-Pt Coating

(i) Phase analysis

The X-ray diffraction patterns of as-deposited Pd-Pt coatings and the coating samples hydrogenated at 550 ˚C and 650 ˚C temperatures for 3 hours are shown in Figure 4-4. Both the Pd and Pt were detected in the coatings.
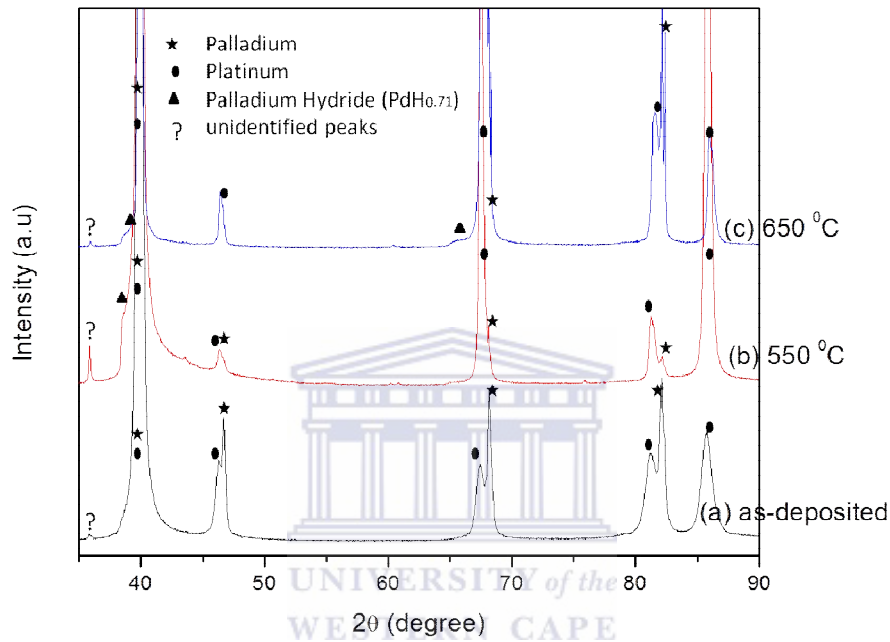
Figure 4-4: The diffraction patterns of Pd-Pt coating (a) as deposited and samples hydrogenated at (b) 550 ˚C and (c) 650 ˚C for 3 hrs**.**

Treating the coating at 550 ˚C and 650 ˚C in a hydrogen environment induce the face centred cubic (fcc) $PdH_{0.71}$ hydride with lattice parameter of 4.02 Å. Therefore, from this observation one can say that the coating provide higher mobility of hydrogen atoms in comparison with pure Pd (Figure 4-1). This findings are in agreement with the work reported by Richter et al. and *Alefeld et al.* [4.11,4.16]. The fact that the lattice parameter of the hydride ($PdH_{0.71}$) has increased above 3.89 Å, it is reasonable to assume that a β-hydride phase is present [4.13].

In summary, the hydrogenation of the Pd-Pt coated system performed at 550 ˚C and 650 ˚C temperatures was sufficient for the formation of hydrides. Peaks of $PdH_{0.71}$ hydride were identified.

(ii)   ERDA analysis

The hydrogen distribution in the as-deposited and hydrogenated coating samples is depicted in Figure 4-5 by fitted ERDA spectra.
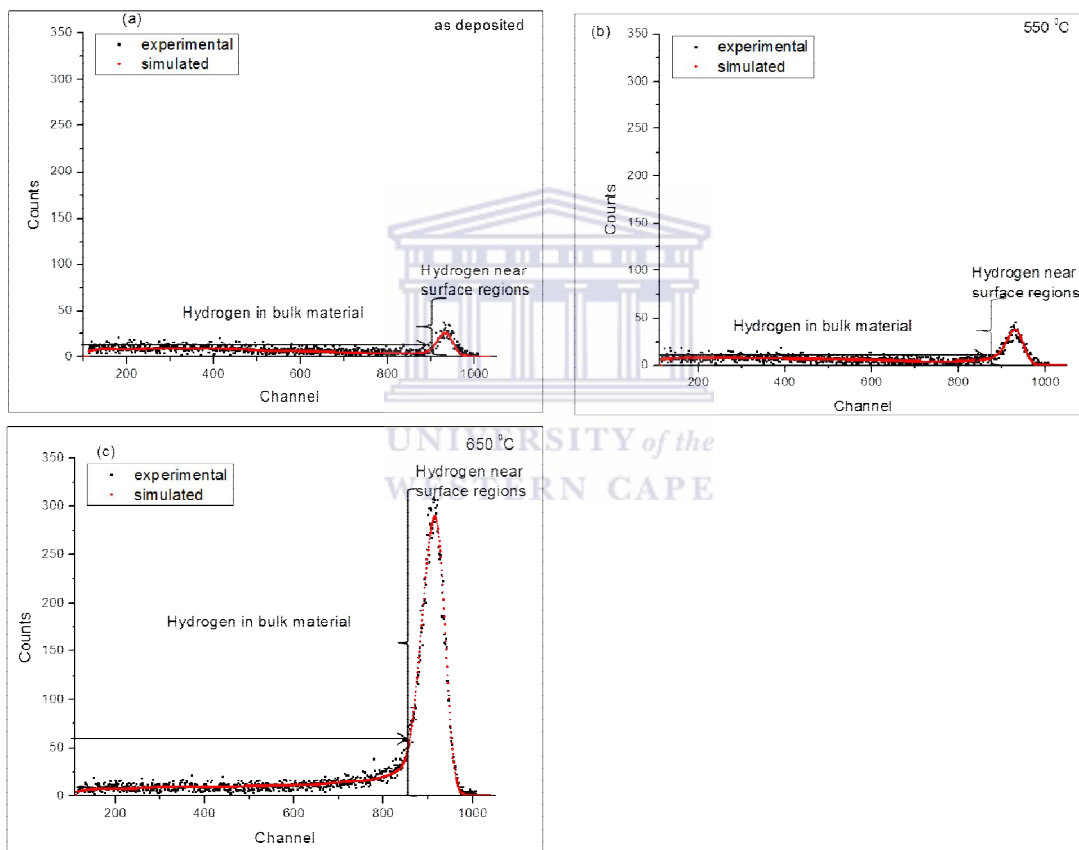
Figure 4-5: Spectra of hydrogen in the Pd-Pt (a) as-deposited sample and hydrogenated samples for 3 hours at (b) 550 ˚C and (c) 650 ˚C. Note: bulk material is considered as a region within coating (Pt coating thickness of 0.5 µm).

It is observed from the spectra that the amount of hydrogen recoiled from the surface region of the coating increases with the hydrogenation temperatures. Similarly, the concentration of

hydrogen within the material also increases during hydrogenation. The peak area also increases with hydrogenation temperature due to absorption of hydrogen in the coating. Figure 4-6 depicts the changes in hydrogen concentration with depth. It was determined that hydrogen distribution was higher on the surface regions than in bulk.
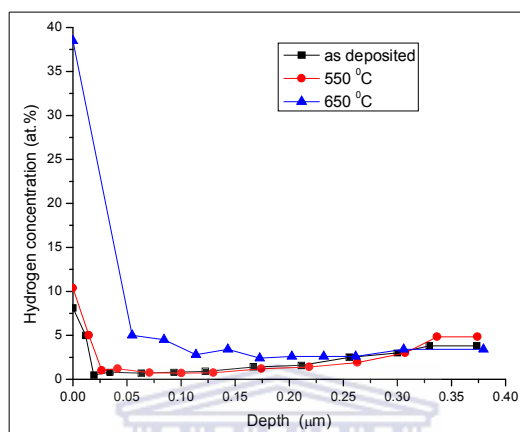
Figure 4-6: The depth profile of hydrogen in Pd-Pt coating samples of as-deposited and hydrogenated at 550 ˚C and 650 ˚C for 3 hours.

The average concentration of hydrogen in the as-deposited sample and the hydrogenated samples at 550 ˚C and 650 ˚C is given in Table 4-3.

Table 4-3: The average concentration of hydrogen in as-deposited and hydrogenated samples of Pd-Pt coating at 550 ˚C and 650 ˚C under atmospheric pressure.

Pd-Pt coating	Average hydrogen concentration at the surface regions		Average hydrogen concentration within the coating	
	(at. %)	(wt. %)	(at. %)	(wt. %)
As-deposited	8.1	0.08	1.53	0.01
550 ˚C	10.35	0.11	1.47	0.01
650 ˚C	38.5	0.59	3.25	0.03

The average concentration of hydrogen on the surface region of as-deposited Pd-Pt coating was found to be 0.08 wt. % (8 at. %) distributed over a depth of 0.01 μm. The concentration

increases to 0.11 wt. % (10.35 at. %) on the surface and 0.01 wt. % (1.47 at. %) within the coating when the coating is hydrogenated at 550 ˚C for 3 hours under 1013 mbar pressure. The difference in hydrogen concentration within the coating of the as-deposited and the coating hydrogenated at 550 ˚C is insignificant. Moreover, increasing the hydrogenation temperature to 650 ˚C under the same conditions increases the average hydrogen concentration on the surface region and within the coating to 0.59 wt. % (38.5 at. %) and 0.03 wt. % (3.25 at. %) respectively.

(i)   Scanning electron microscopy (SEM)

It was observed that the morphology of the Pd-Pt coatings, Figure 4-7, studied by SEM differs with temperature.
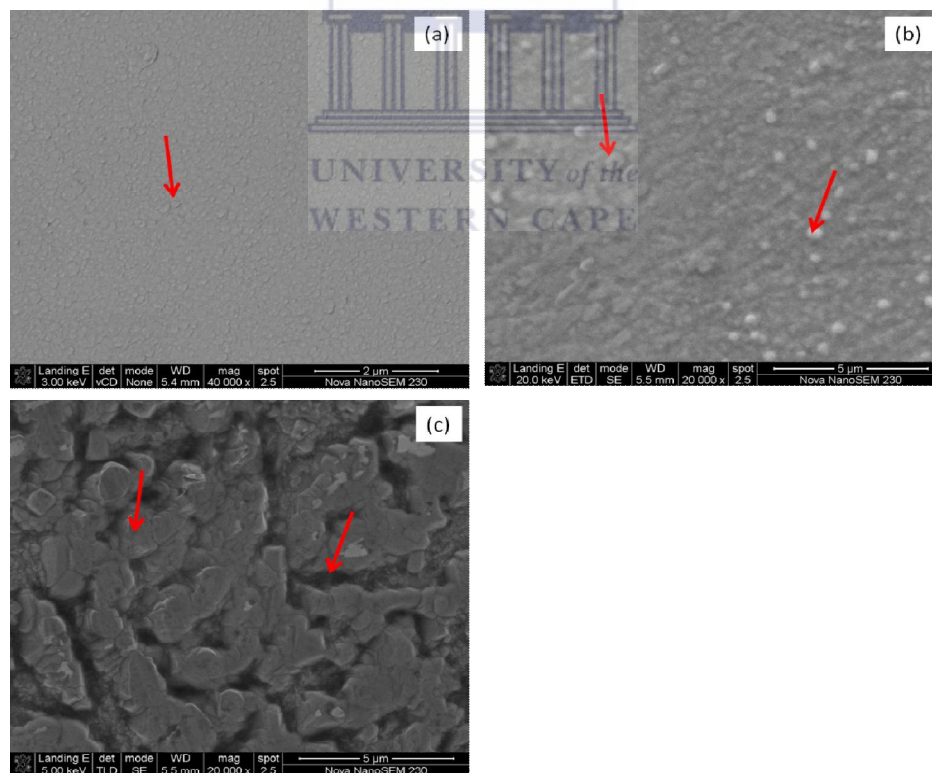
Figure 4-7*:* SEM micrographs showing the morphology of Pd-Pt coating (a) as-deposited, (b) subjected to hydrogen at 550 ˚C for 3 hours and (c) subjected to hydrogen at 650 ˚C for 3 hours.

The Pt splats (indicated by arrows in Figure 4-7 a,b) formed during coating deposition remained present after hydrogenation at 550 ˚C whilst the hydrogenation at 650 ˚C caused significant changes in the coating morphology; the surface roughness increased and the presence of distinct regions was observed (c).

In conclusion, absorption of hydrogen in Pd-Pt coating when hydrogenated under atmospheric pressure for 3 hours increases at high temperatures (550 ˚C and 650 ˚C). The formation of the $PdH_{0.71}$ hydride suggests that phase transformation from α- to ß- phase has occurred. The average concentration of hydrogen within the coating increases from 1.53 at. % in the as-deposited to 3.25 at. % in the sample hydrogenated at 650 ˚C. The formation of the hydrides is an indication that during deposition of Pt onto Pd substrate, dislocations are introduced which improve the hydrogen trapping effect of the coating [4.10,4.11]. Interstitial diffusion during hydrogen loading enables achievement of thermodynamic equilibrium. Furthermore, the temperature acts as a controlling factor for the diffusion of hydrogen into the coating [4.10,4.11,4.16]. The evolution of the coating morphology ranged from splats at 550 ˚C to the morphology with distinct regions formed due to higher hydrogenation temperature (650 ˚C).

4.3.2 Hydrogenation at room temperature under HP-HC-LT conditions

4.3.2.1 Pd

(i) Sorption and desorption analysis (IGA)

The effects of hydrogenation performed at high pressure-high concentration-long time (HP-HC-LT) conditions on the sorption in pure Pd are shown in Figure 4-8. The sorption rate of hydrogen in Pd sample depends on the system pressure. The slope between two consecutive saturation points (part of sorption curve) is greater at low pressures and therefore, the

sorption rate of hydrogen in Pd decreases with pressure towards maximum saturation. Therefore this suggests that the kinetic response corresponding to the sorption of hydrogen in the alpha phase is much faster in the dual phase region ($\alpha + \beta$). This behaviour was also observed in the study conducted by *Benham et al* [4.17].
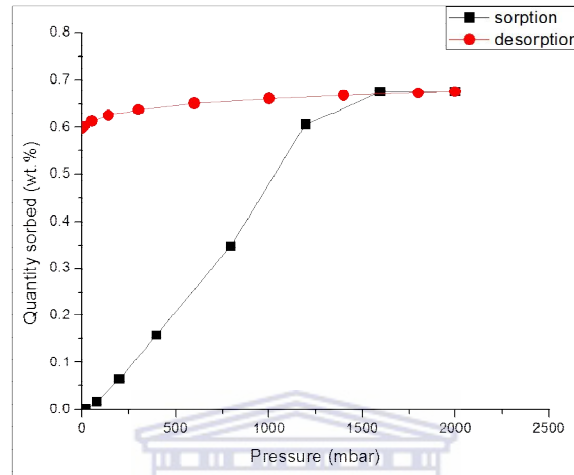
Figure 4-8: The absorption and desorption of hydrogen in Pd at room temperature and different system pressures. Each point represents saturation of sample at a particular pressure and time.

The experiments performed in this study show that pure Pd sample initially weighing 83.55 mg sorbed a maximum hydrogen concentration of 0.67 wt. % which is equivalent to 41.88 at. % under a pressure of 2000 mbar reaching a maximum mass of 84.12 mg. Decreasing the pressure in the system facilitates desorption of hydrogen from the Pd sample as it can be seen on the desorption curve depicted in red on Figure 4-8. The hydrogen content in the sample was reduced to 0.60 wt. % when the pressure was decreased from 2000 mbar to 0.47 mbar. The slope between consecutive saturation points on desorption curve decreases with a decrease in pressure from 2000 mbar to 0.47 mbar. It was also observed that the desorption rate of hydrogen in Pd is slow at low pressures. The desorption of hydrogen from the hydrides formed at high pressures is altered at low pressures. However, the slopes between

consecutive saturation points on sorption curve are steeper than on desorption curve, hence sorption of hydrogen occurs faster than desorption in Pd sample. Considering the time for sorption/ desorption of hydrogen in pure Pd under HP-HC-LT conditions, maximum sorption was achieved in 14 hours.

(ii)   Elastic recoil detection analysis

Figure 4-9 shows fitted ERDA spectra of a hydrogenated Pd sample irradiated in three consecutive cycles. The measurements were performed in three consecutive runs in order to investigate the effect of the He$^+$ ion beam with time of irradiation on the hydrogen content in the materials.
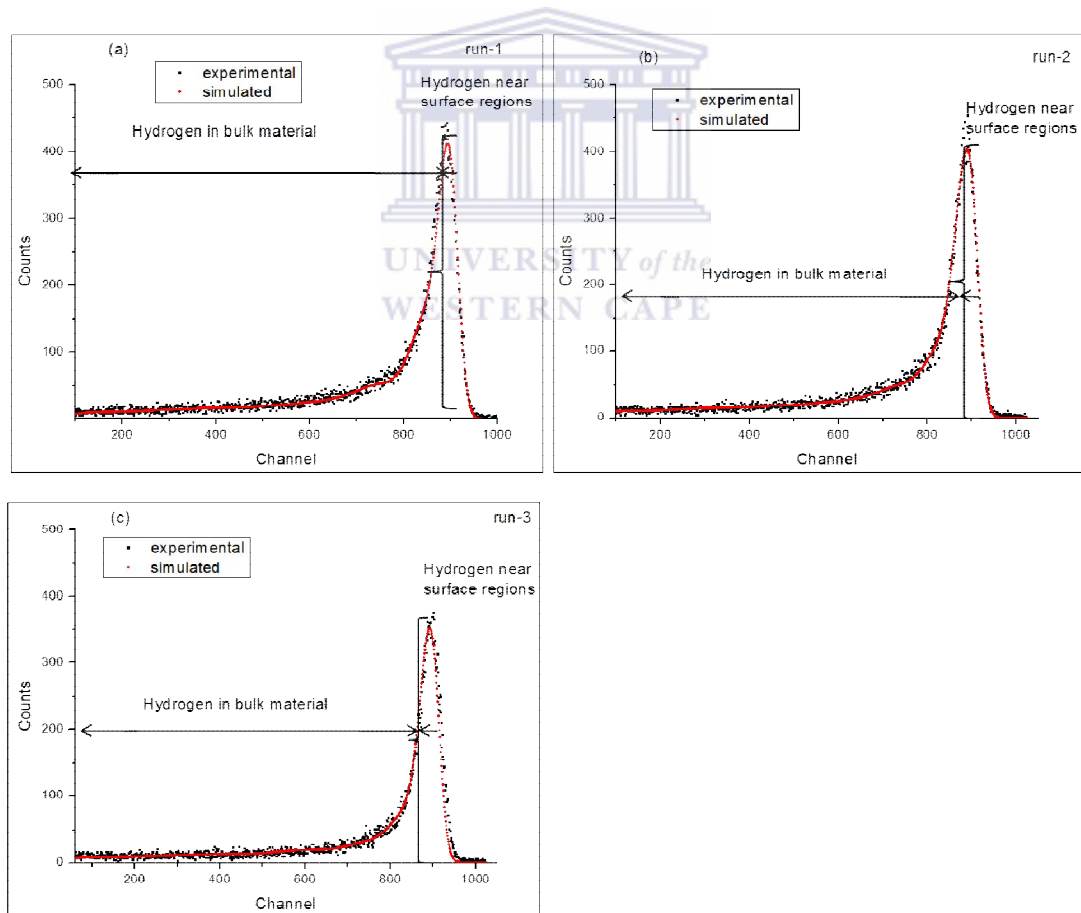
Figure 4-9: ERDA spectra of Pd hydrogenated at room temperature under HP-HC-LT conditions in IGA. Three irradiations of runs (a, b and c) were conducted.

The outputs of these consecutive runs help in checking the stability of the technique. The peak area corresponds to the content of hydrogen in the sample. The statistics of the recoils from the surface decreases with each run due to hydrogen desorption. The width of the peak is smaller for run-3 indicating that the amount of hydrogen in the Pd sample was reduced by irradiation. From spectra in Figure 4-9, the depth profile and calculations of hydrogen concentration in the samples can be determined. The diffusion behavior of hydrogen in the sample during all the three runs can best be described by depth profiling in Figure 4-10.
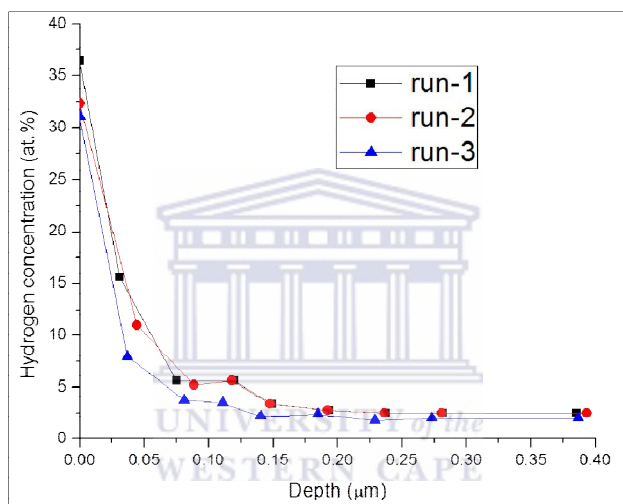
Figure 4-10: Depth profiles of hydrogen in Pd sample irradiated in three consecutive runs.

The hydrogen depth on the surface region is approximately 0.03 µm as determined in run-1. The distribution of the surface hydrogen has increased to a depth of approximately 0.04 µm in run-2. However, the average concentration of hydrogen remained quite similar in the bulk material. Desorption of hydrogen is prominent in run-3 whereby the concentration distribution has decreased on the surface regions and in the bulk material. The total depth of penetration of He$^+$ ions in Pd is similar in all three consecutive runs (run-1, run-2 and run-3).

The average concentration of hydrogen in the Pd sample is summarised in Table 4-4. It was found that the average hydrogen concentration on the surface region of Pd sample hydrogenated under HP-HC-LT conditions significantly changed after the first irradiation run from 36.5 - 32.4 at. % (run-1 to run-2). Similarly, the bulk concentration also decreases from 4.48 at. % (run-1) to 3.75 at. % in run-2. The Pd sample has lost 12 % of the total hydrogen detected in run-1 within a period of 1 hour which corresponds to the time between consecutive runs (run-1 to run-2). Furthermore, after the third irradiation cycle (run-3), 2.79 at. % of hydrogen was detected in the bulk material. Note that the concentration of the hydrogen on the surface region continues to decrease with each consecutive run (from 36.5 in run-1 to 31.05 at. % in run-3). The He$^+$ ions were capable of detecting the presence of hydrogen up to a depth of 0.38 μm. The rate of desorption was calculated taking into account the time elapsed between run-1 and run-3. A spontaneous desorption rate of hydrogen from the bulk material of the sample was found to be 1.13 at. % per hour.

Table 4-4: The average concentration of hydrogen in a Pd sample hydrogenated at room temperature determined by ERDA in three consecutive runs.

Pd	Average hydrogen concentration on the surface		Average concentration of hydrogen in bulk	
	(at. %)	(wt. %)	(at. %)	(wt. %)
run-1	36.5	0.54	4.48	0.04
run-2	32.4	0.45	3.75	0.04
run-3	31.05	0.42	2.79	0.03

There are two possibilities which might be responsible for desorption of hydrogen in the hydrogenated Pd sample:

➢ During the interaction between He$^+$ ions and the hydrogenated Pd sample, the energy of the ion beam is transferred to hydrogen in the form of heat. The increased temperatures give hydrogen atoms enough energy to vibrate in the matrix solution. If this energy is enough to break the bonds between the Pd and hydrogen atoms, hydrogen diffuses either into deeper regions or towards the surface of material.

➢ The movement of hydrogen atoms can also be affected by He$^+$ ions during the recoiling of hydrogen atoms from material. It is possible that some of the hydrogen atoms hit by the ions have insufficient energy to leave the material or they move towards greater depth or near surface regions.

In summary, a maximum of 0.67 wt. % hydrogen was sorbed by Pd sample using IGA up to a maximum pressure of 2000 mbar. Considering the amount of hydrogen present after desorption which was facilitated by decreasing the pressure in the system, desorption of hydrogen in Pd is slow. Out of the overall hydrogen content sorbed by the sample, only 0.07 wt. % hydrogen was lost after 19 hours by reducing the pressure from 2000 mbar to 0.47 mbar. The sorption rate of hydrogen in Pd sample was found to be faster than desorption rate by comparison of the slope between consecutive saturation points. Since ERDA measurements were performed 30 days after IGA experiments, further desorption of hydrogen was most likely to occur. The results of three consecutive ERDA runs show that the hydrogen concentration in the bulk material decreases from 0.04 wt. % determined in run-1 to 0.03 wt. % after the third measurement (run-3). This indicates that hydrogen is lost in the sample with each consecutive run because of the recoiling of hydrogen atoms from the sample. Similarly, the hydrogen occupying the surface region is lost with each consecutive run. Note that irradiations are conducted in vacuum and at room temperature and therefore all the hydrogen atoms detected are recoiled from the sample.

4.3.2.2 Comparison between Pd results conducted under LP-LC-ST and HP-HC-LT

In order to compare the results obtained by two different techniques (intelligent gravimetric analysis-IGA and elastic recoil detection analysis-ERDA) the following needs to be emphasised:

i. Pd samples were hydrogenated under different conditions in terms of system pressure, hydrogen environment concentration and time:

> ➢ LP-LC-ST

> ➢ HP-HC-LT

ii. Hydrogen concentration was determined by two techniques:

> ➢ IGA for HP-HC-LT conditions

> ➢ ERDA for LP-LC-ST and HP-HC-LT conditions

The summary of the findings is given in Table 4-5.

Table 4-5: Hydrogen concentration results in Pd samples hydrogenated at room temperature under LP-LC-ST and HP-HC-LT conditions.

Experimental parameters				IGA	ERDA
Pressure (mbar)	Hydrogenation Temperature (°C)	Hydrogenation Time (hours)	H concentration (wt. %)	H concentration (wt. %)	Average H concentration (wt. %)
1013	Room	1	15	n/a	0.04
2000	temperature	14	100	0.67	0.08

The concentration results determined by IGA and ERDA are different because the probing area on the sample is not the same. However they are both able to monitor the absorption of hydrogen by comparing with the as-received material. The geometry of the ion beam as it strikes the sample surface is shown in Figure 4-11.
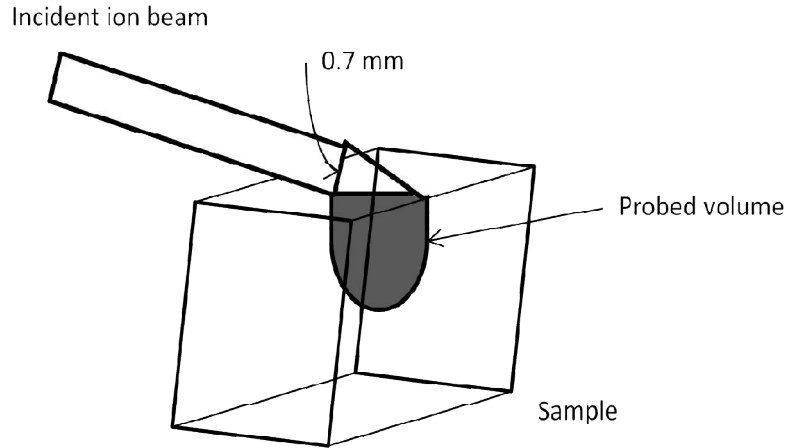
Figure 4-11: A schematic presentation showing the volume probed by He$^+$ ions during ERDA experiments.

An ion beam with 0.7 mm diameter strikes the sample at 75 ° with respect to the normal and spread over a length of 2.61 mm. The area and volume probed on the sample were calculated according to the geometry as follows:

$A = L \times B = 1.21 \times 10^{-3} \; mm \times 2.61 \; mm = 3.2 \times 10^{-3} \; mm^2$

$V = A \times 2.7 \; mm = 8.53 \times 10^{-3} \; mm^3$

where 1.21 μm ($1.21 \times 10^{-3} mm$) is the ion range in pure Pd.

Similarly, the absorption of hydrogen in a sample placed inside a cylinder for IGA measurements is illustrated in Figure 4-12 and the calculations of the area and volume probed are shown below:

$$A = L \times B = 5 \; mm \times 5 mm = 25 \; mm^2$$

$$V = (5 - 1.21 \times 10^{-3})^3 \; mm^3 = 124.91 \; mm^3$$

Note that the volume (V) was calculated based on the sample dimension and the depth of ion penetration in pure Pd obtained from SRIM programme.
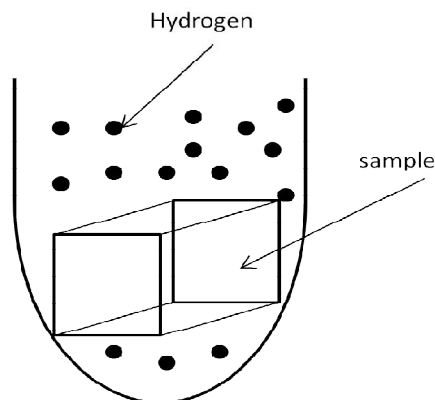
Figure 4-12: A sample in a cylinder during IGA measurements.

Therefore, ERDA probes a volume of $8.53 \times 10^{-3}\ mm^3$ whereas IGA probes $124.91\ mm^3$ which is significantly greater.
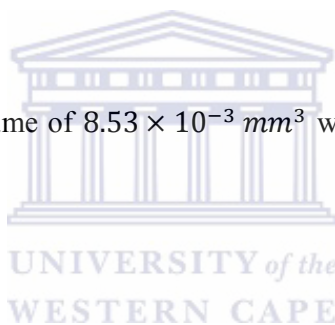
4.3.2.3 Pd-2 at. % Pt alloy

(i) Intelligent gravimetric Analysis (IGA)

The difference in mass of the Pd-2 at. % Pt sample due to hydrogen content was determined by IGA technique under high pressure-high concentration-long time (HP-HC-LT) conditions and the isotherm is shown in Figure 4-13. Considering the sorption and desorption parts of the curve, the change in weight of the sample was recorded at pressures where saturation was achieved. The sorption curve shows that absorption of hydrogen in Pd-2 at. % Pt sample increases from a pressure as low as 0.34 mbar to a maximum of 2000 mbar. The sample absorbed a maximum of 0.66 wt. % hydrogen at a pressure range from 0.34 to 2000 mbar. This maximum was achieved after 13 hours of charging.
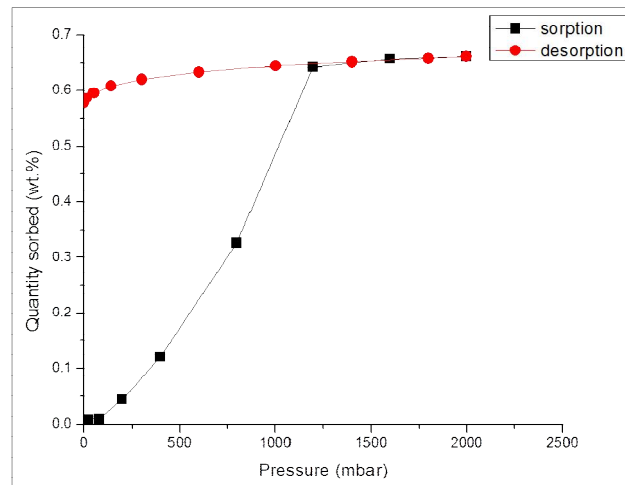
Figure 4-13: An absorption-desorption curve of Pd-2 at. % Pt sample hydrogenated in IGA under high pressure-high concentration-long time conditions at room temperature. Each point represents saturation at that pressure.

The slope between consecutive saturation points on the sorption curve decreases with an increase in pressure towards maximum pressure of 2000 mbar. Consequently, the rate of hydrogen sorption in Pd-2 at. % Pt sample is faster at low pressure and then decreases with an increase in pressure. This suggests that the diffusion path of hydrogen in the bulk material is enhanced at low pressures. Desorption process of hydrogen in the sample was investigated by decreasing the system pressure from 2000 mbar to 0.61 mbar for a period of 19 hours. During this process, 0.08 wt. % of hydrogen was lost and 0.58 wt. % remained in the sample after pressure release. The slope between the consecutive saturation points on desorption curve increases with a decrease in pressure indicating that desorption rate is higher at low pressures. A comparison between the rate of absorption and desorption determined by slopes between consecutive saturation points on the curves indicate that the sorption of hydrogen in Pd-2 at.% Pt is faster than its desorption rate.

(ii)   ERD analysis of hydrogen

The hydrogen distribution in Pd-2 at.% Pt sample after three consecutive runs of irradiation is presented in Figure 4-14.
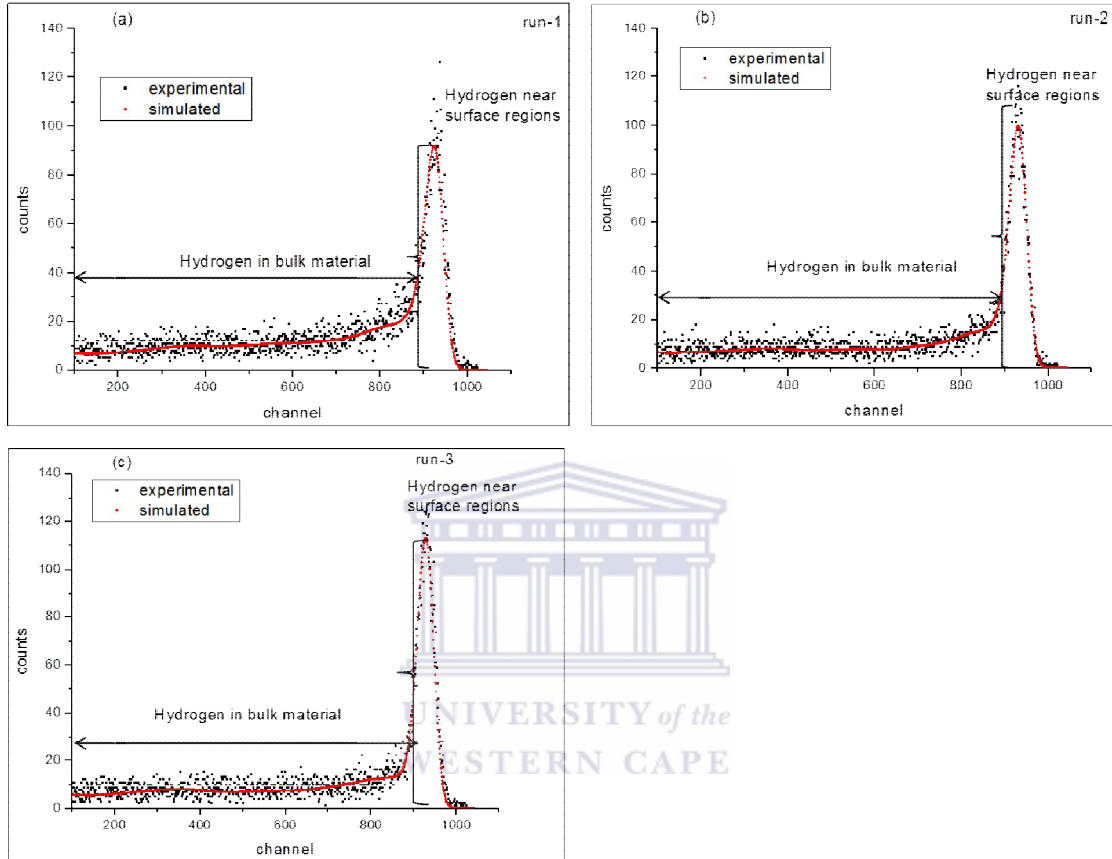
Figure 4-14: ERDA spectra of hydrogen distribution in (a) run-1, (b) run-2 and (c) run-3 of Pd-2 at. % Pt alloy hydrogenated under HP-HC-LT hydrogenation conditions at room temperature.

The count of recoils ejected from the surface region of the Pd-2 at. % Pt sample increases with each consecutive run as a result of migration of hydrogen from the bulk towards the surface. The migration of hydrogen from bulk towards surface regions might have occurred as a result of heating caused by the ions while the quantity of bulk hydrogen decreases. The possibility of desorption is confirmed by the decrement of hydrogen distribution in the bulk

material with each consecutive run. The peak widths as well as the area also decrease with each run. A depth profile of hydrogen in the Pd-2 at. % Pt alloy as a function of depth depicted in Figure 4-15 was deduced from the spectra. It is observed in run-1 that the hydrogen distribution on the surface extends to a depth of 0.02 μm and its distribution in the bulk material is homogeneous.
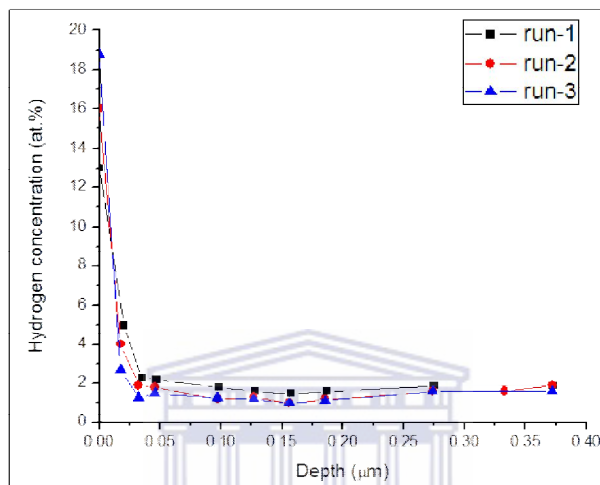
Figure 4-15: The hydrogen concentration as a function of its depth of penetration in Pd-2 at. % Pt sample hydrogenated at room temperature under HP-HC-LT conditions.

The depth at which the hydrogen occupies the surface region of the material is insignificantly reduced during run-2 and run-3. Nevertheless, it can be observed that the concentration distribution of hydrogen in deeper regions of bulk for both run-2 and run-3 is similar.

The calculated average concentration of hydrogen in the sample after each run is given in Table 4-6. It was observed in run-1 that the Pd-2 at. % Pt sample contains 12.99 at. % of hydrogen near the surface regions and an average of 1.94 at. % in the bulk material. However during run-2, it was found that the hydrogen in bulk material has decreased to 1.57 at. % while the surface hydrogen has increased to 16 at. % suggesting the occurrence of hydrogen

desorption. Similarly, the sample continued to lose the bulk hydrogen while at the other hand the surface hydrogen increased to 18.78 at. % in run-3.

Table 4-6: The average concentration of hydrogen in Pd-2 at. % Pt sample irradiated in three consecutive runs.

Pd-2 at. % Pt	Average hydrogen concentration near surface regions		Average hydrogen concentration in bulk material	
	(at. %)	(wt. %)	(at. %)	(wt. %)
run-1	12.99	0.14	1.94	0.02
run-2	16.00	0.18	1.57	0.01
run-3	18.78	0.21	1.39	0.01

For comparison, an overall of 33 % of the hydrogen escaped from the bulk material in 4 hrs. This implies that the diffusion of hydrogen has occurred from the bulk material towards the surface region with time in the chamber. The diffusion rate of hydrogen in Pd-2 at. % Pt sample using the data measured in this study was found to be 0.14 at. % per hour during desorption.

In summary, a Pd-2 at. % Pt sample has achieved saturation during IGA measurements under high pressure-high concentration-long time (HP-HC-LT) conditions at which a maximum of 0.66 wt. % hydrogen was sorbed. The sample then loses 0.05 wt. % of hydrogen during desorption process which was achieved by decreasing the pressure from the maximum saturation point, 2000 mbar, to 0.61 mbar. With ERDA experiments, a maximum of 0.14 wt. % of hydrogen was detected at the surface region and 0.02 wt. % present in bulk material of the same sample after 30 days of hydrogenation in IGA. Similar to Pd, the sorption rate is greater than desorption rate which allows more hydrogen to be stored in the sample than to

escape. The implication of these results is that hydrogen storage, which is the core of this study, is possible in these materials. Therefore, no special conditions (high pressure and low temperature) are required to retain the content of hydrogen in the Pd and Pd-2 at. % Pt alloy. A continuation of desorption has occurred in the sample during the ion beam irradiation which is caused by the heat generated by the He^+ ions. Because of the hydrogen migration towards the surface of the sample, the depth profile in Figure 4-14 has shown that the hydrogen concentration on the surface region increases with each run. As discussed on pg 134 and 135, the concentration of hydrogen in the Pd-2 at. % Pt sample found using IGA measurements and ERDA experiments are not comparable because of the different volume of the material probed. Elastic recoil detection analysis (ERDA) experiments use He^+ ions of 3 Mev energies which probe a $8.53 \times 10^{-3} \; mm^3$ volume of the sample to recoil hydrogen atoms while IGA measures the overall change in mass of the sample. More detailed discussion of the two techniques is found on pages 134 and 135.
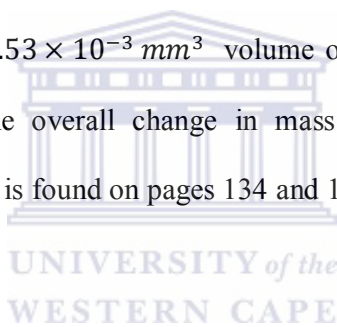
4.3.2.4   Pd-6 at. %Pt alloy

(i)   Intelligent gravimetric Analysis (IGA)

The sorption and desorption of hydrogen in Pd-6 at. % Pt sample, Figure 4-16, was determined by IGA measurements conducted at room temperature under high pressure-high concentration-long time (HP-HC-LT) hydrogenation conditions. Looking at the sorption part of the curve, it is observed that maximum saturation in this sample was not achieved in 13 hrs of charging as compared with pure Pd and Pd-2 at. %. The Pd-6 at. % Pt sample absorbs 0.45 wt. % of hydrogen in 13 hours when pressure is increasing from 0.47 to 2000 mbar. A further sorption of hydrogen by the Pd-6 at. % Pt sample occurred when the system pressure was reduced from 2000 mbar to 1000 mbar where a maximum of 0.56 wt. % hydrogen

concentration was sorbed. Desorption of hydrogen in the sample occurs at pressures below 1000 mbar until vacuum pressure.
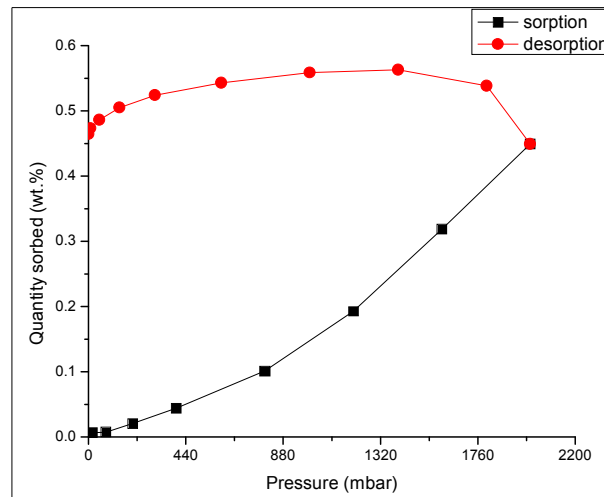
Figure 4-16: The absorption and desorption processes of hydrogen in Pd-6 at. % Pt sample hydrogenated under HP-HC-LT conditions. Each point represents the saturation of the sample at different pressures and time.
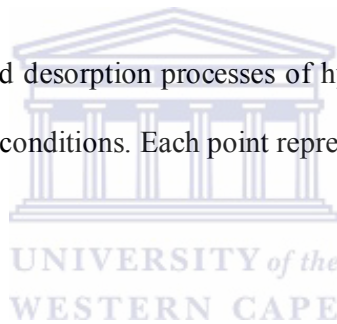
During the desorption process which occurred for 15 hours, a maximum of 0.1 wt. % hydrogen was lost from the Pd-6 at. % Pt sample. After the desorption process, 0.46 wt. % of hydrogen concentration was left in the sample. The slopes between consecutive saturation points on the sorption curve are steeper than those between consecutive saturation points on desorption curve. Since a steeper slope imply faster rate, and therefore, sorption of hydrogen in Pd-6 at. % Pt sample occurs faster than desorption when it is hydrogenated at room temperature under HP-HC-LT conditions. Therefore, the desorption rate of hydrogen in Pd-6 at. % Pt sample is slower than sorption rate.

(ii)   ERD Analysis

Three consecutive ERDA cycles were run to quantify the amount of hydrogen in the Pd-6 at. % Pt sample. The ERDA spectra of the Pd-6 at. % Pt sample irradiated in three consecutive cycles is shown in Figure 4-17.
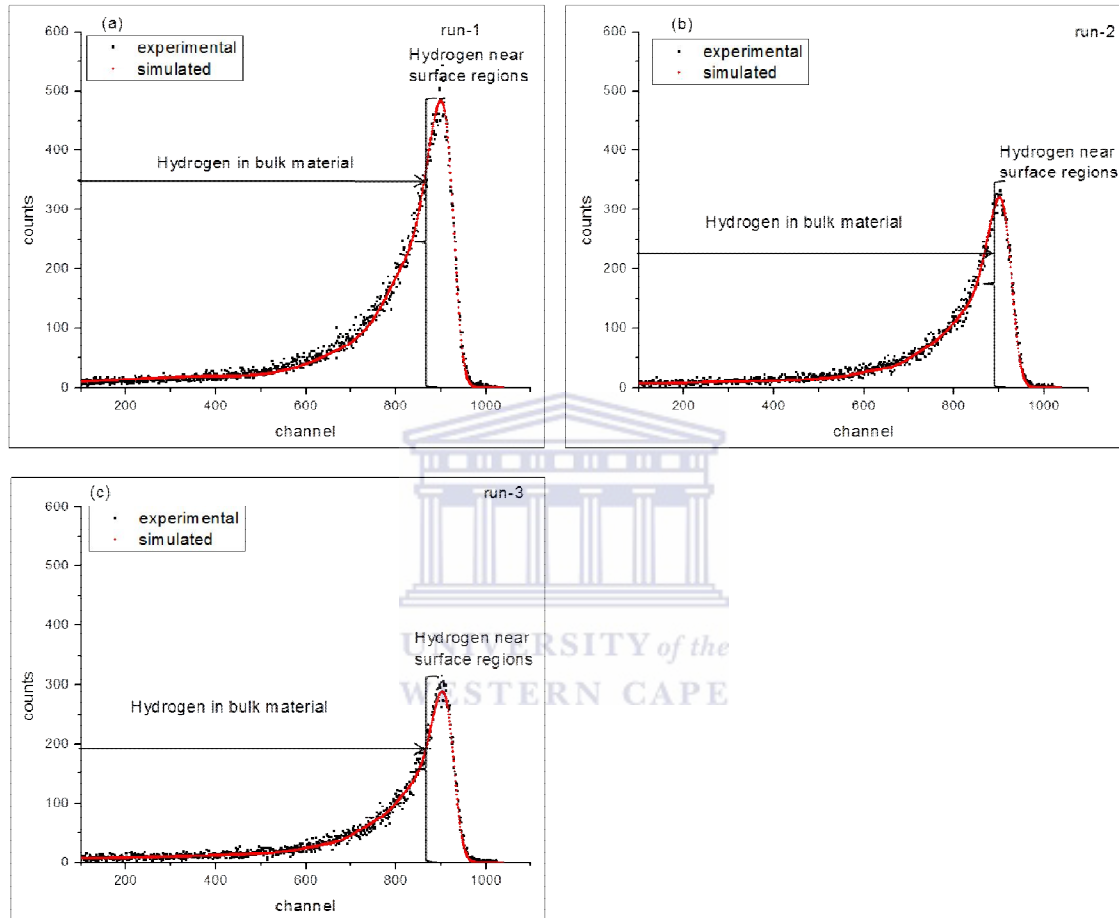
Figure 4-17: ERDA spectra of hydrogen distribution in Pd-6 at. % Pt sample hydrogenated in IGA at room temperature under HP-HC-LT conditions. Three consecutive irradiation runs (a, b, c) were conducted on the sample.

The statistical counts of recoiled hydrogen atoms from the surface region of the sample decreases with each run, i.e. approximately 484 in run-1, 320 in run-2 and 289 counts in run-3. Similarly, the width and the area of the peak decrease with each run. Note that the peak

area corresponds to the overall hydrogen content in the probed volume. The decrease of both the peak width and area suggest that desorption occurred in the sample with time. Figure 4-18 gives the depth profile of the hydrogen content in the material. The run-1 profile indicates that the hydrogen is distributed over a depth of 0.06 µm on the surface of Pd-6 at. % Pt sample. The distribution of hydrogen concentration in the bulk decreases with depth. Looking at run-2, the sample loses hydrogen on surface region reducing the depth of distribution to 0.04 µm. It is observed that desorption has been altered after run-2 where the concentration distribution of hydrogen in the bulk and on the surface region has insignificantly changed.
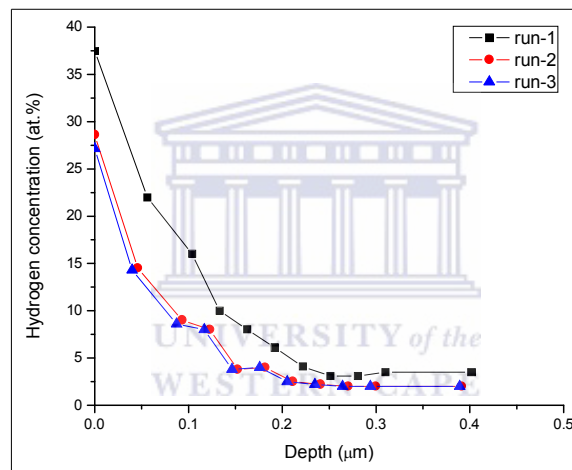
Figure 4-18: Depth profile of hydrogen in Pd-6 at. % Pt sample hydrogenated at room temperature in IGA under HP-HC-LT conditions.

The average concentration of hydrogen in the Pd-6 at. % Pt sample after each consecutive irradiation run is given in Table 4-7. The sample has 37.5 at. % of hydrogen on the surface region and an average concentration of 8.25 at. % in bulk at run-1. It loses 3.04 at. % of the hydrogen in the bulk material at run-2 and a further 0.1 at. % at run-3. Similarly, the surface hydrogen concentration is decreased with each consecutive run (from 37.5 at. % in run-1 to 27.15 at. % in run-3). Therefore, desorption occurs with time in the Pd-6 at. % Pt sample.

Most of the hydrogen in the sample is lost within the first 2 hours after run-1 while a total loss of 50 % occurred within 4 hours. The rapid loss of hydrogen may be due to the presence of oxygen in air [4.18]. Therefore, it is believed that the occurrence of the loss started before the ERDA experiments and continued during the irradiations. It was observed in run-2 that the loss of absorbed hydrogen from the hydrided Pd-6 at. % Pt alloy is minimised with longer periods in vacuum which is similar to the conduct of hydrided Pd near the surface regions. An overall diffusion rate of hydrogen was found to be 1.24 at. % per hour.

Table 4-7: The average concentration of hydrogen in the Pd-6 at. % Pt sample hydrogenated at room temperature under HP-HC-LT conditions.

Pd-6 at. % Pt	Average hydrogen concentration near surface regions		Average hydrogen concentration in bulk material	
	(at. %)	(wt. %)	(at. %)	(wt. %)
run-1	37.5	0.52	8.25	0.08
run-2	28.6	0.35	5.21	0.05
run-3	27.15	0.33	5.11	0.05

The total depth of penetration of He^+ ions has decreased from 0.4 μm to 0.39 μm as a result of the change in physical, chemical and mechanical properties of the alloy by hydrogen absorption [4.18,4.19]. For instance, the findings of the study of magnetic properties of Pd-Pt alloys of different hydrogen and Pt content by Hara et al. [4.19] revealed that the magnetic susceptibility of the different Pd-Pt alloys decreased with increasing hydrogen and Pt content. These results were attributed to a change in the electronic structure of the valence band which occurs when hydrogen content is increased. The Fermi level rises and the density of states at the Fermi level decreases [4.19].

In summary, the absorption of hydrogen in Pd-6 at. % Pt sample conducted in IGA under high pressure-high concentration-long time (HP-HC-LT) conditions increases with pressure as shown in Figure 4-16. Using IGA measurements, hydrogen concentration of 0.45 wt. % was calculated in Pd-6 at. % Pt sample at 2000 mbar. Maximum saturation point was not reached during the charging of the Pd-6 at. % Pt sample due to the following possible factors:

(i) The maximum system pressure used was low for the sample to achieve full saturation.

(ii) The holding time at each pressure step was short for saturation to occur at this particular pressure.

Since the slopes between consecutive points on sorption part of the curve is greater than those between points on the desorption parts of curve, therefore sorption rate of hydrogen in Pd-6 at. % Pt sample is greater than desorption rate. An average hydrogen concentration of 0.52 wt. % was detected on the surface region and 0.08 wt. % in the bulk material using ERDA experiments. The distribution of hydrogen into the bulk of the material is profoundly illustrated by the depth profiles in Figure 4-16. The profiles show that during desorption process, hydrogen moves from the bulk of the sample towards the surface region while some of the hydrogen atoms are lost in the process. However, the rate of desorption decreases with time.

4.3.2.5   Pd-10 at. % Pt alloy

(i)   Phase study using X-ray diffraction

Figure 4-19 presents the diffraction patterns of Pd-10 at. % Pt before and after hydrogenation under LP-LC-ST conditions. Only Pd peaks appeared in the diffraction patterns of as-received sample. As reported by Cullity et al. [20], the detection limit of a phase by XRD is 0.2 wt. %. In addition, the solubility of Pt in Pd is high and therefore, the presence of Pt in Pd solid solution will be impossible to detect by XRD. Therefore, the results do not imply that Pt

phase is not present in the composition of the Pd-Pt alloy. Also, the Pt peaks are not resolved fully due to their low intensity. The signal of the diffracted beam to noise ratio determines whether a peak will protrude. If the volume fraction of the phase present is small, the signal will be diminished and broadened over a 2-theta range 30 - 90 °. Hydride peaks can be observed at longer exposure time, for example above 1 hour. A face- centred cubic $PdH_{0.71}$ hydride with a lattice parameter of 4.02 Å was detected in the samples hydrogenated for 2 hours and 7 hours. Looking at the lattice parameter, it is evident that phase transformation from α- to β- hydride has occurred.
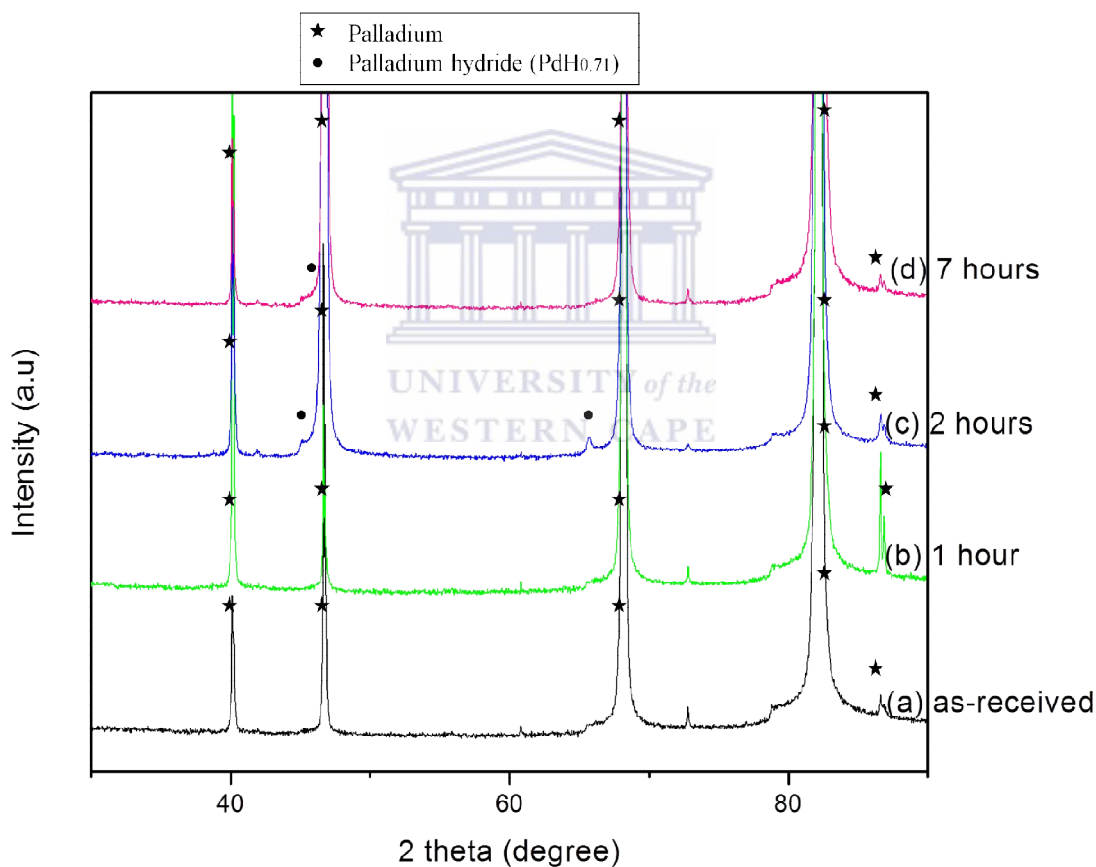
Figure 4-19: X-ray diffraction patterns of Pd-10 at. % Pt samples; (a) as-received, hydrogenated at room temperature for (b) 1 hour, (c) 2 hours and (d) 7 hours (LP-LC-ST). Note: unidentified peaks.

In summary, the hydrogenation of Pd-10 at. % Pt alloy at room temperature form hydrides after 1 hour of exposure to gaseous hydrogen, i.e. the $PdH_{0.71}$, when the process is conducted under LP-LC-ST conditions.

(ii)   Intelligent gravimetric Analysis (IGA)

Figure 4-20 shows the difference in mass of Pd-10 at. % Pt sample as a result of the induced hydrogen determined by IGA measurements conducted at room temperature under high pressure-high concentration-long time (HP-HC-LT) conditions.
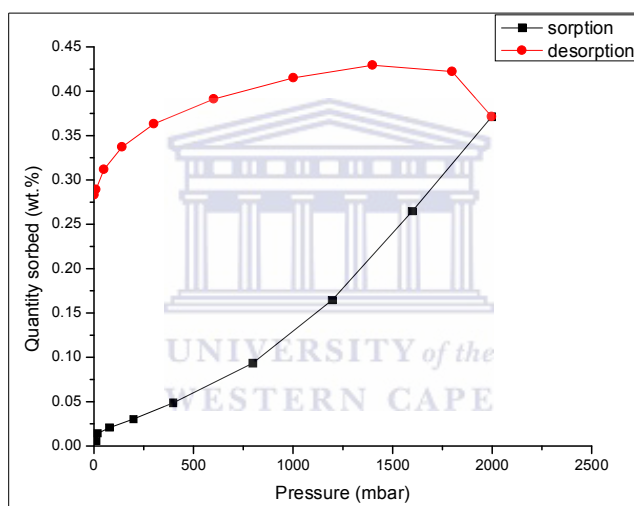
Figure 4-20: The relationship between the absorption and desorption of hydrogen in Pd-10 at. % Pt sample hydrogenated in IGA under HP-HC-LT conditions. Each point represents saturation of sample at different pressures and time.

The introduction of hydrogen into Pd-10 at. % Pt sample initially weighing 71.90 mg increased the sample's mass to 72.21 mg at 2000 mbar acquiring hydrogen concentration of 0.37 wt. % in 15 hrs. Looking at the sorption/desorption parts of the curve, full saturation was not achieved in the sample. The slope between two consecutive saturation points on the absorption part of the curve decreases from 11 mbar to 78 mbar and then increases with

pressure until 2000 mbar. Therefore, sorption rate of hydrogen in Pd-10 at. % Pt sample is slower at low pressures (e.g. at 11 mbar) but faster at higher pressures (2000 mbar). As the pressure was decreased in the system, sorption of hydrogen continued to occur in the sample until the pressure was reduced to 1399 mbar where a maximum of 0.43 wt. % of hydrogen was acquired. Desorption of hydrogen in the sample started occurring at pressures below 1399 mbar until vacuum pressure at which the amount of hydrogen contained in the sample was 0.28 wt. %. It is observed that the slopes between consecutive saturation points on the desorption part of the curve become steeper with a decrease in pressure. This means that desorption rate of hydrogen in the sample is faster at low pressures. A comparison of the slopes between consecutive points on sorption and desorption parts of the curve suggest that Pd-10 at. % Pt sample sorbs hydrogen faster than it desorbs.

(iii) ERD analysis

Figure 4-21 shows the ERDA spectra of hydrogen in Pd-10 at. % Pt irradiated in three consecutive cycles. It is observed that the spectrum taken from Pd-10 at. % Pt sample during run-1 has the highest amount of recoils ejected from the surface region which decreases with time as observed in run-2 and run-3 (314 counts for run-2 and 302 counts for run-3). The peak width and area of spectra get smaller with time. The depth profiles in Figure 4-22 show the distribution of hydrogen in the sample. The hydrogen concentration on the surface of the Pd-10 at. % Pt sample hydrogenated at room temperature under high pressure-high concentration-long time (HP-HC-LT) conditions was distributed over 0.05 μm depth in run-1. Irradiation of the sample for the second time (run-2) revealed that some of the hydrogen atoms initially on the surface region have escaped reducing the depth of distribution to 0.04 μm.
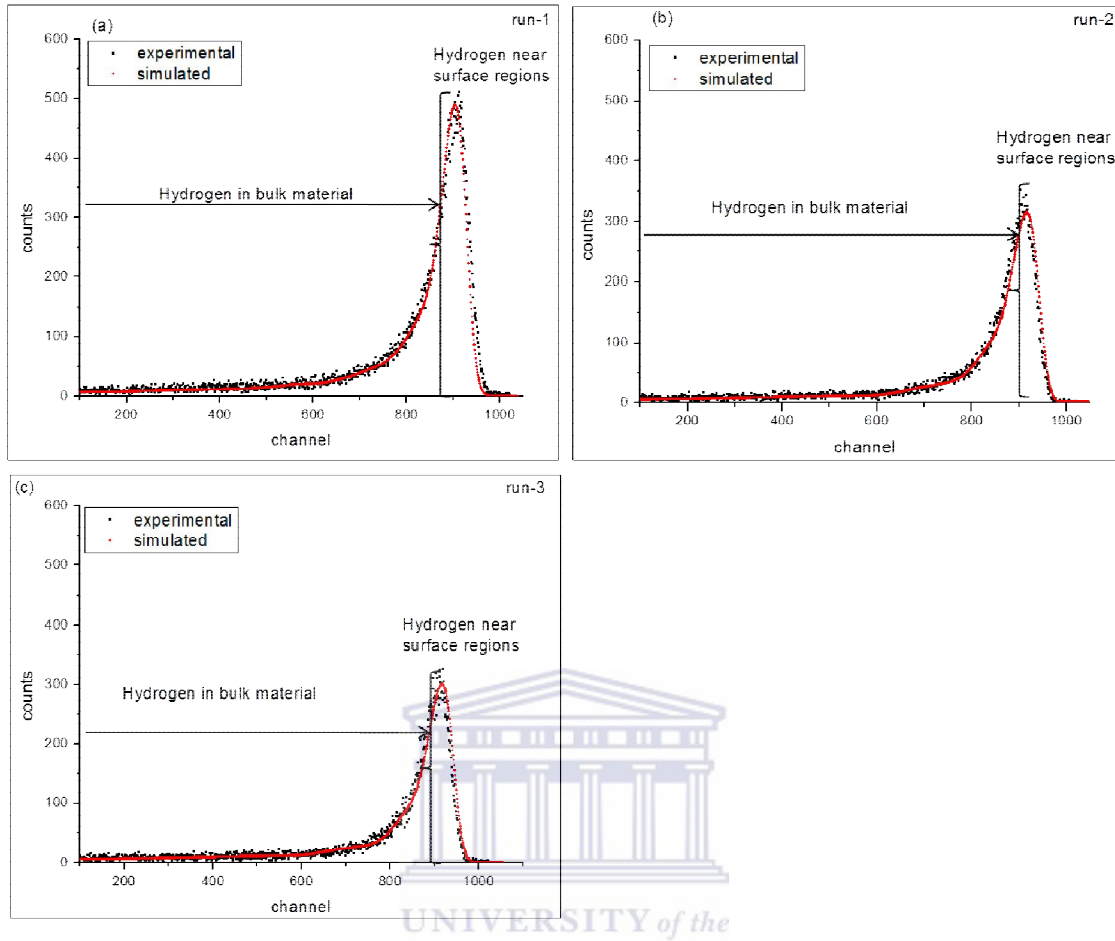
Figure 4-21: Fitted ERDA spectra of Pd-10 at. % Pt sample hydrogenated in TGA at room temperature under HP-HC-LT conditions.

The insignificant changes of concentration distribution of the hydrogen on the surface region of the sample indicate that the impact of the beam on the sample after run-2 is negligible. Therefore, one can say that desorption rate of hydrogen in Pd-10 at. % Pt sample enhanced by the heat generated by He$^+$ ions is slow after the second irradiation (run-2). This occurs because most of the hydrogen atoms are excited during run-1 and move towards the surface region where some of the hydrogen is desorbed.
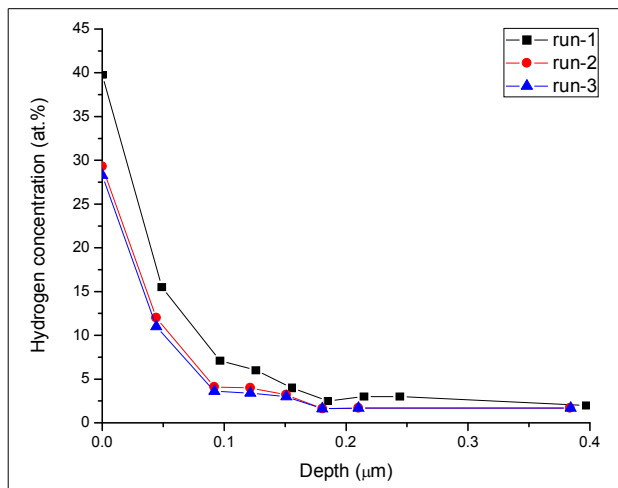
Figure 4-22: The depth profile of hydrogen in Pd-10 at. % Pt sample hydrogenated in IGA under HP-HC-LT conditions at room temperature.

The average hydrogen content in the sample at each run is given in Table 4-8. A sample of Pd-10 at. % Pt alloy hydrogenated at room temperature under HP-HC-LT conditions has absorbed 4.9 at. % of hydrogen in the bulk as detected in run-1.

Table 4-8: The average hydrogen concentration in Pd-10 at. % Pt sample hydrogenated in IGA at room temperature under HP-HC-LT conditions.

Pd-10 at. % Pt	Average hydrogen concentration on surface region		Average hydrogen concentration in bulk material	
	(at. %)	(wt. %)	(at. %)	(wt. %)
run-1	39.78	0.55	4.91	0.05
run-2	29.30	0.35	3.67	0.03
run-3	28.30	0.33	3.42	0.03

Most of the hydrogen is adsorbed on the surface region. During run-2, the average hydrogen concentration in the bulk material was reduced to 3.67 at. % as a result of desorption. A 7 %

of the hydrogen determined in run-2 was lost leaving the sample with 3.42 at. % of hydrogen in bulk material (average concentration) after run-3. The rate of desorption of hydrogen in bulk material of Pd-10 at. % Pt sample is 0.37 at. % per hour. The overall amount of hydrogen atoms diffusing out of the bulk material of the sample in 4 hours was found to be 36 %. Using the He^+ ions with 3 MeV energies, the distribution of hydrogen atoms were detected over a depth of 0.38 µm into bulk material.

In summary, it was found that a sample of Pd-10 at. % Pt alloy hydrogenated in intelligent gravimetric analyser (IGA) at room temperature under high pressure-high concentration-long time (HP-HC-LT) conditions sorbed 0.37 wt. % at 2000 mbar over a period 15 hours. The sorption/desorption parts of the curve in Figure 4-18 has shown that maximum saturation does not occur in the sample. The sample has sorbed its maximum hydrogen, 0.43 wt. % concentration, at 1399 mbar during the pressure release. Hydrogen desorption has started occurring below 1399 mbar until vacuum pressure of 0.61 mbar was reached where only 0.28 wt. % of hydrogen remained in the sample. The slope between consecutive points in both sorption and desorption part of the curve indicated that the rate of hydrogen sorption is greater than desorption in Pd-10 at. % Pt. Elastic recoil detection analysis (ERDA) experiments detected a maximum average of 4.91 at. % (0.05 wt. %) of hydrogen in the bulk of sample and 39.78 at. % near the surface regions 30 days after the hydrogenation in IGA. It was observed that after 4 hrs of irradiation, 3.42 at. % (0.03 wt. %) in bulk and 28.3 at. % (0.33 wt. %) near the surface regions of hydrogen concentration were contained in the sample indicating that desorption has taken place.

4.3.2.6   Pd-12 at. % Pt alloy

(i)   Intelligent gravimetric Analysis (IGA)

IGA measurements were conducted on a sample of Pd-12 at. % Pt alloy under high pressure-high concentration-long time (HP-HC-LT) conditions at room temperature in order to determine the mass difference due to hydrogen sorption and desorption. The curve shown in Figure 4-23 depicts the sorption and desorption processes of hydrogen in Pd-12 at. % Pt sample at different pressures.
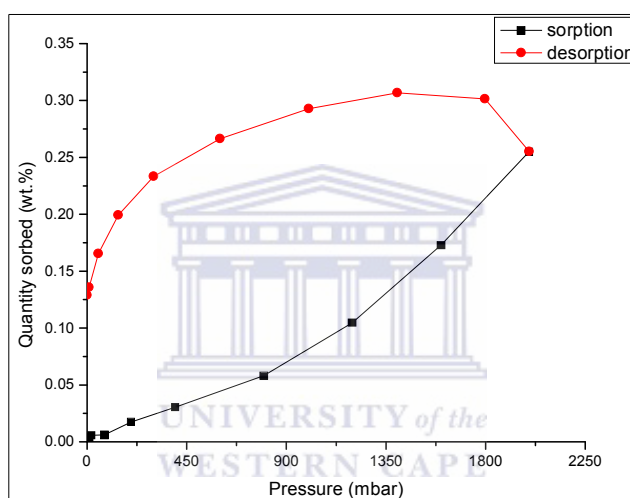
Figure 4-23: The sorption/desorption curve of hydrogen in Pd-12 at. % Pt sample hydrogenated in IGA under HP-HC-LT conditions.

As the system pressure is increased from 0.47 mbar to 2000 mbar, the mass of Pd-12 at. % Pt sample which initially weighs 80.74 mg increases to 80.95 mg. At this pressure, the sample has sorbed 0.26 wt. % of hydrogen. It is further observed that full saturation is not achieved by sample. However, decreasing the system pressure causes a further hydrogen sorption in the sample where a maximum concentration of 0.31 wt. % was recorded at 1400 mbar pressure. The slopes between consecutive saturation points on the absorption part of the curve become steeper at high pressures. The sorption of hydrogen in the sample is faster at high

pressures as shown in Figure 4-23. Desorption process occurs at pressures below 1400 mbar

at which a maximum hydrogen concentration of 0.13 wt. % remained in the sample at 0.47

mbar. This maximum value of hydrogen content was achieved in 15 hours of desorption. The

slope between the consecutive saturation points on the desorption part of the curve increases

with a decrease in pressure.

(ii)   ERD analysis

The hydrogen distribution in the Pd-12 at. % Pt sample was determined 30 days after the

hydrogenation process conducted in IGA and the fitted ERDA spectra is shown in Figure 4-

24.
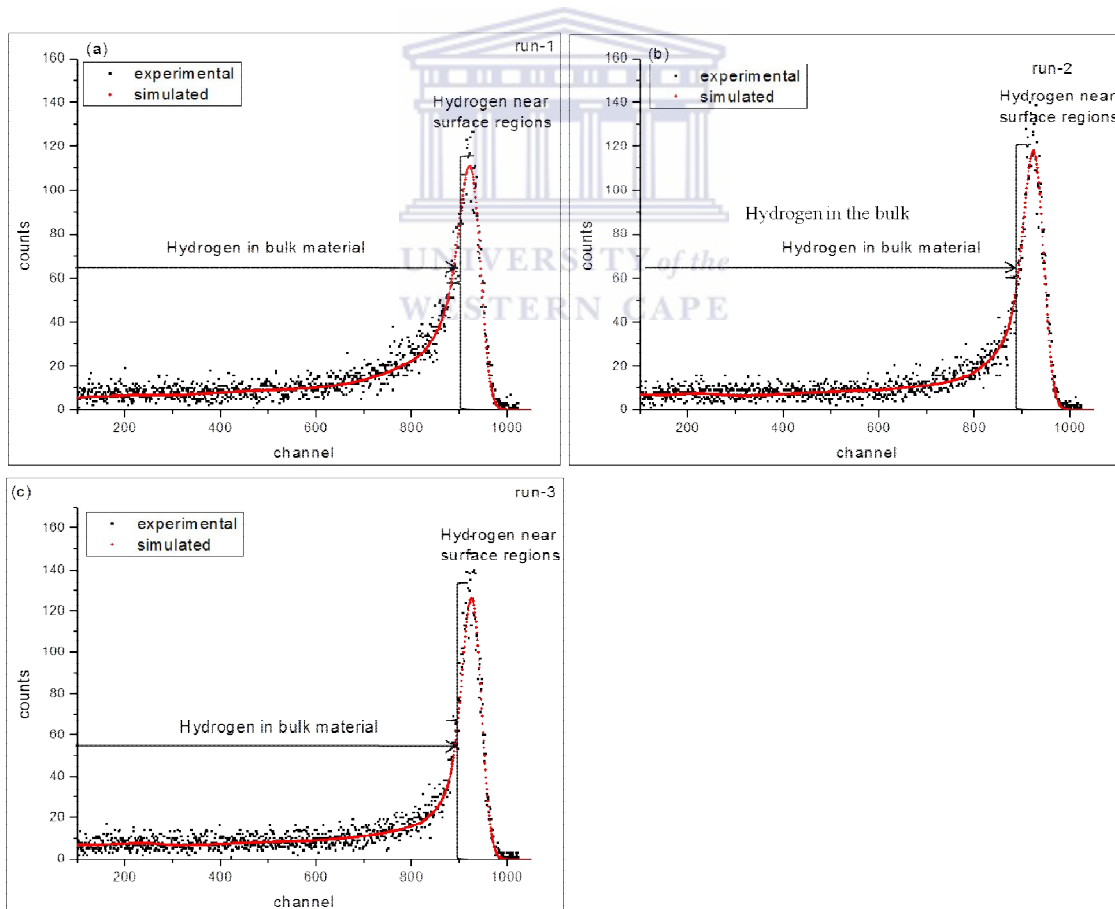
Figure 4-24: The distribution of hydrogen in a sample of Pd-12 at. % Pt alloy hydrogenated

in IGA under high pressure-high concentration-long time (HP-HC-LT) conditions.

The maximum recoils of hydrogen ejected from the surface region of Pd-12 at. % Pt sample during the irradiations increases from run-1 to run-3 as a result of diffusion of hydrogen from bulk material towards the surface. The reduction of the width and area of the peak in run-2 and run-3 occurs as a result of desorption. The depth profiles of hydrogen in Pd-12 at. % Pt sample shown in Figure 4-25 depicts the concentration distribution in each run. It was observed that the concentration of hydrogen distributed on the surface region increases with each consecutive run whereas it decreases with each run in the bulk material.
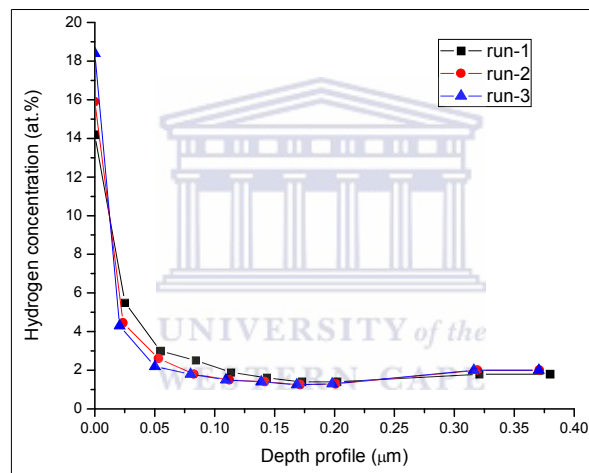
Figure 4-25: The depth profile of hydrogen in a sample of Pd-12 at. % Pt alloy hydrogenated in IGA under HP-HC-LT conditions.

The hydrogen is distributed over a depth of 0.03 μm on the surface region of the sample in run-1. During run-2 and run-3, the distribution of hydrogen occupying the near surface regions decreased to a depth of 0.02 μm which indicate that a shift of hydrogen has occurred towards a confined space near the surface.

The average concentrations of hydrogen in the Pd-12 at. % Pt sample after each run are given in Table 4-9. It was found that a sample of Pd-12 at. % Pt alloy hydrogenated in IGA under high pressure-high concentration-long time (HP-HC-LT) conditions contain an average hydrogen concentration of 2.09 at. % in bulk material during run-1. The average hydrogen concentration decreases to 1.85 at. % in run-2 and 1.8 at.% in run-3. The movement of hydrogen from the bulk material towards the surface increases the hydrogen concentration on the surface region. There is 14.2 at. % of hydrogen in run-1 which increases to 15.9 at. % in run-2 and 18.4 at. % in run-3. The diffusion rate of hydrogen in Pd-12 at. % Pt sample was found to be 0.07 at. % per hour from the bulk towards the surface regions. The maximum depth at which the He^+ ions have penetrated the hydrogenated Pd-12 at. % Pt sample was found to be 0.38 μm.

Table 4-9: The average concentration of hydrogen in Pd-12 at. % Pt sample hydrogenated in IGA under HP-HC-LT conditions.

Pd-12 at. % Pt	Average hydrogen concentration on surface region		Average hydrogen concentration in bulk material	
	(at. %)	(wt. %)	(at. %)	(wt. %)
run-1	14.2	0.14	2.09	0.02
run-2	15.9	0.16	1.85	0.02
run-3	18.4	0.19	1.8	0.02

In summary, a sample of Pd-12 at. % Pt alloy hydrogenated in IGA at room temperature under high pressure-high concentration-long time (HP-HC-LT) conditions sorbed 0.26 wt. % of hydrogen at a pressure range 0.47 - 2000 mbar. Sorption of hydrogen continued to occur even when the pressure was decreased from 2000 mbar to 1400 mbar. At this pressure, hydrogen concentration in the sample increased to 0.31 wt. %. Desorption was possible

below 1400 mbar. A minimum of 0.13 wt. % of hydrogen in the sample was recorded at 0.47 mbar. In this study, the sorption of hydrogen in Pd-12 at. % Pt sample was found to be faster than desorption. This suggests that the storage of hydrogen in this alloy can be effective however, the content of hydrogen stored in this alloy is less than in Pd. The average concentration of hydrogen in the bulk material of Pd-12 at. % Pt sample was detected by ERDA experiments to be 2.09 at. % (0.02 wt. %). The depth profile revealed that the He^+ ions have only penetrated 0.38 μm of the sample. It has also indicated that the hydrogen diffuses from the bulk material towards the surface of sample in the chamber at a rate of 0.07 at. % per hour leaving the sample with 1.8 at. % of hydrogen concentration in the bulk material in 4 hours.

4.3.2.7 Comparison between the hydrogen capacity of Pd and Pd-Pt alloys

The comparison between the hydrogen capacity of Pd and Pd-Pt alloys hydrogenated in intelligent gravimetric analyser (IGA) under high pressure-high concentration-long charging time (HP-HC-LT) conditions emphasise the difference with regards to the Pt content in the Pd alloys. There are two processes investigated with IGA which are sorption and desorption. The sorption and desorption of hydrogen in Pd and in the different Pd-Pt alloys is given in Table 4-10 in an increasing order.

Table 4-10: The absorption and desorption of hydrogen in Pd and Pd-Pt alloys listed in an increasing order (IGA measurements).

Trend (ascending order)	Sorption	Desorption
1	Pd-12 at. % Pt	Pd-2 at. % Pt
2	Pd-10 at. % Pt	Pd
3	Pd-6 at. % Pt	Pd-6 at. % Pt
4	Pd-2 at. % Pt	Pd-10 at. % Pt
5	Pd	Pd-12 at. % Pt

The experimental results show that sorption of hydrogen is high in Pd and decreases with an increase in Pt content. These findings are consistent with the research reported by *Lewis et al* [4.15]. As opposed to sorption process, desorption of hydrogen increases with Pt content. Desorption of hydrogen at low pressures was also studied by ERDA experiments conducted at $1 \times 10^{-6}\ mbar$ pressure.

The desorption of hydrogen in the materials is summarised in Table 4-11 in an ascending order and these results are inconclusive due to several possible reasons. The desorption rate in Pd and Pd alloys determined by IGA and ERDA are different because the process is conducted at high pressures in IGA with samples containing large amount of hydrogen whereas the samples have already lost part of the hydrogen by the time ERDA experiments were performed. In addition, the volume of probe investigated on similar samples was different for each technique, i.e. $124.91\ mm^3$ for IGA and $8.53 \times 10^{-3}\ mm^3$ in ERDA. Furthermore, desorption was enhanced by the heat generated over time when the He$^+$ ions strike the sample surfaces.

Table 4-11: The absorption and desorption rate of hydrogen in Pd and Pd-Pt alloy determined by ERDA experiments in an increasing order.

Trend	Desorption rate
1	Pd-2 at. % Pt
2	Pd-12 at. % Pt
3	Pd-10 at. % Pt
4	Pd
5	Pd-6 at. % Pt

Therefore, temperature and pressure are the driving force behind desorption of hydrogen in Pd and Pd-Pt alloys.

4.4 Discussions

This study investigated the hydrogen capacity of Pd, Pd-Pt coated systems and Pd-Pt alloys at room temperature and high temperatures using either intelligent gravimetric analyser (IGA) where the experiments were performed at high pressure-high hydrogen concentration-long lime (HP-HC-LT) conditions and furnace which operated under low pressure -low hydrogen concentration-short time (LP-LC-ST) environment. The parameters that were investigated include the system pressure, the hydrogen concentration of the environment and the charging time. It was found that under low pressure-low concentration-short charging time (LP-LC-ST) conditions, hydride formation does not occur in Pd when the hydrogenation is conducted at high temperatures. This finding is consistent with the studies conducted by *Lewis et al.* [4.14,4.21] and *Vigier et al.* [4.22], which revealed that hydrogen sorption decreases with an increase in hydrogenation temperature. The redistribution of atoms and the formation of vacancies occurring at elevated temperatures decrease the time for interstitial diffusion of hydrogen atoms whereby desorption of hydrogen is increased [4.23-4.26]. The concentration of vacancies formed by hydrogenation of Pd is of the order of 10^{-3} to 10^{-2}, which is much higher compared to the vacancy concentration in thermal equilibrium at the melting point of metals, 10^{-4} to 10^{-3} [4.27]. The formation of hydrides in the samples hydrogenated at room temperature in 1 hour has demonstrated the great absorption capacity of Pd which is consistent with the investigation by *Oates et al.* [4.3] and *Xu et al.* [4.4] at temperatures below 300 ˚C. Similarly, the absorption of hydrogen in Pd and Pd-Pt alloys occurs at a higher rate at room temperature. Hydrogen atoms are randomly distributed over the octahedral sites in the Pd lattice at room temperature [4.10,4.13,4.28]. The incorporation of hydrogen atoms in octahedral sites of Pd lattice cause a strain to metallic atoms and as a result increasing the unit cell volume which alternatively weaken the inter-atomic bonds [4.10,4.11]. However, when the hydrogenation is conducted under LP-LC-ST conditions, saturation is not fully

achieved due to low pressure and low concentration of hydrogen in gas atmosphere. The amount of hydrogen sorbed in Pd under LP-LC-ST conditions is equivalent to the quantity desorbed after pressure was released. High hydrogen concentration was detected by ERDA in the Pd sample hydrogenated at room temperature for 1 hour.

As indicated by the isotherms in Figure 2-9, the sorption of hydrogen conducted under HP-HC-LT conditions increase the chemical potential of hydrogen [4.14]. The rate at which hydrogen is absorbed in Pd was increased as compared to LP-LC-ST conditions. High pressures of gaseous hydrogen increase the intermolecular interactions by increasing the density of the molecules. The rate at which the hydrogen molecules dissociate on the surface of the Pd sample increases, and as a result, adsorption of hydrogen occurs rapidly. High pressure of gaseous hydrogen and high hydrogen concentration lead to the absorption of hydrogen till saturation. High pressures of gaseous hydrogen and high hydrogen concentration lead to the formation of hydrides. The hydrides formed were $PdH_{0.64}$ in Pd at room temperature, $PdH_{0.71}$ in the coating at high temperatures (550 ˚C and 650 ˚C) and $PdH_{0.71}$ in Pd- 10 at. % Pt under HP-HC-LT conditions.

Substitution of Pd with Pt (alloying) leads towards formation of Pd-Pt alloys which exhibit low α- to- ß phase transformation temperature. In this study, the hydrogen solubility in Pd-Pt alloys was found to decrease with Pt increment. According to the study by *Schlapbach et al.* [4.2] and *Moysan et al.* [4.29], the solubility of hydrogen is lowered by the volume effects which cause changes in the host lattice (Pd) as the Pd conduction band is filled up by the valence electrons of Pt. The elastic effects are responsible for drastic modification of the diffusion phenomenon of hydrogen in Pd-Pt alloys [4.30]. Figure 2-9 illustrate the solubility of hydrogen in Pd-Pt alloys at high pressures [4.14]. Furthermore, the trapping effect is

decreased with increased Pt content as illustrated by desorption data in Table 4-11. On the other hand, desorption of hydrogen from the alloys increases with Pt content [4.14,4.31]. Note that full saturation was not achieved in samples with 6 %, 10 % and 12 % of Pt content under these conditions (HP-HC-LT). Therefore, for these alloys to attain full saturation, higher pressures of hydrogen gas and longer holding times during the IGA measurements should be applied. Nevertheless, it is evident from the IGA results that the capacity of the Pd-Pt alloys investigated in this study decreases with an increase in Pt content. These results are in agreement with those reported by *Flanagan et al* [4.32]. The highest absorption rate and the lowest desorption rate in both Pd and Pd-2 at. % Pt makes these materials good hydrogen storage systems when the hydrogen charging is conducted under HP-HC-LT conditions at room temperature. The presence of 2 at. % Pt in the Pd matrix has improved the hydrogen trapping effect of Pd while a large presence of Pt (e.g. 12 at. % Pt) decreased the solubility of Pd for hydrogen [4.8,4.33,4.34].
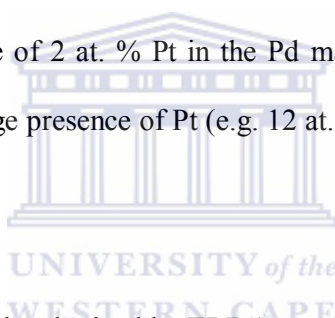
The hydrogen concentration results obtained by ERDA experiments have shown that after the hydrogenation of Pd and Pd-Pt samples in IGA, desorption process has occurred even further. The trend of desorption studied with ERDA technique, summarised in Table 4-11, is different from that found from IGA measurements. These results are inconclusive since the ERDA experiments were performed after some time following IGA measurements. In addition to the different volume probed on the samples in both techniques, IGA and ERDA, the pressure under which the measurements were taken were also different. ERDA experiments were conducted under a pressure of 1×10^{-6} $mbar$ whereas IGA measurements were taken up to a maximum pressure of 2000 mbar. A general conclusion can be made that absorption and desorption rate of hydrogen in Pd and Pd-Pt alloys is pressure, time, temperature and alloy composition dependent.

In Pd-Pt coated systems where 0.5 µm Pt was deposited on Pd substrate, absorption increases with temperature (550 ˚C, 650 ˚C), under LP-LC-ST conditions. *Mott et al.* [4.12] reported that the coating thickness affects the absorption and desorption processes of hydrogen. The hydrogen absorption decreases with increased coating thickness.

4.5 Conclusion

Hydride formation occurs during the hydrogenation of Pd at room temperature due to the incorporation of hydrogen into the octahedral site of Pd under low pressure-low concentration-short time (LP-LC-ST) conditions. Face-centered cubic ($PdH_{0.64}$) hydride with 4.03Å lattice appeared in an hour. This was expected according to the Pd-H phase diagram in Figure 2-9, because the dissociation of hydrogen atoms on the Pd surface does not need activation energy. The formation of a fcc $PdH_{0.71}$ hydride with lattice parameter of 4.02 Å, occurs in Pd-Pt coating when it is hydrogenated at high temperatures under LP-LC-ST conditions. However, most of the hydrogen occupies the surface regions of the coating than in the Pd sample hydrogenated for 1 hour with most of its hydrogen in the bulk of the material. The sorption and desorption study of Pd and Pd-Pt alloys using intelligent gravimetric analyser (IGA-002) conducted under HP-HC-LT conditions, show that pressure and time are critical parameters for the study of hydrogen storage systems at room temperature. The mass difference increases significantly when the hydrogen absorption is conducted up to a maximum pressure of 2000 mbar in a 99.99 % hydrogen environment. Under HP-HC-LT conditions, the probability of the material to achieve full saturation decreases with the increment of Pt content which indicated that the hydrogen diffusion rate in the alloys decreased with high Pt content. It was also found that the effects of irradiation on the sample during ERDA experiments contribute to desorption process. However the results of the two different hydrogenation conditions under LP-LC-ST and HP-HC-LT conditions

have shown that the dissociation of hydrogen atoms on Pd and Pd-Pt surfaces is exothermic. The kinetics of hydrogen during sorption was found to be faster at low pressures in the alpha region and slows down towards the two phase region as depicted in Figure 4-8). Therefore, the continuation of hydrogenation of Pd and Pd-Pt alloys decreases the solubility of the material due to the presence of hydrides formed at lower pressures (1013 mbar).

4.3   References

[4.1] T. Nejat Veziroglu, S.A. Sherif, and F. Barbir, "Chapter 7 - Hydrogen Energy Solutions", in: Franklin J. Agardy, Nelson Leonard Nemerow (Eds.), *Environmental Solutions,* Academic Press, Burlington, pp. 143-180 (2005).

[4.2] L. Schlapbach and A. Zuttel, *Nature,* **414**, 353-358 (2001).

[4.3] W.A. Oates and T.B. Flanagan, *Prog. Solid State Chem.,* **13**, 193-272 (1981).

[4.4] T. Xu, M.P. Zach, Z.L. Xiao, D. Rosenmann, U. Welp, W.K. Kwok, and G.W. Crabtree, *Appl. Phys. Lett.,* **86**, 203104 (2005).

[4.5] V. Antonov, I. Belash, V.Y. Malyshev, and E. Ponyatovsky, *Platinum Met. Rev.,* **28**, 158-163 (1984).

[4.6] F. Lewis, *Platinum Met. Rev.,* **26**, 20 (1982).

[4.7] P. Tripodi, N. Armanet, V. Asarisi, A. Avveduto, A. Marmigi, J.D. Vinko, and J.P. Biberian, *Phys. Lett. A,* **373**, 3101-3108 (2009).

[4.8] A.G. Knapton, *Platinum Met. Rev.,* **21**, 44-50 (1977).

[4.9] F.A. Lewis, *Platinum Met. Rev.,* **52**, 120-122 (2008).

[4.10] J. Völkl and G. Alefeld, *Hydrogen in Metals I*, 321-348 (1978).

[4.11] D. Richter, R. Hempelmann, and R. Bowman, *Hydrogen in Intermetallic Compunds II*, 97-163 (1992).

[4.12] S.N.F. Mott and H. Jones, *The theory of the properties of metals and alloys,* Dover Pubns (1958).

[4.13] G. Alefeld and J. Völkl, Hydrogen in metals I- basic properties, **28** (1978).

[4.14] F.A. Lewis, *ACADEMIC PRESS, INC., NEW YORK, N.Y.1967, 178 P,* (1967).

[4.15] L.L. Jewell and B.H. Davis, *Applied Catalysis A: General,* **310**, 1-15 (2006).

[4.16] G. Alefeld and J. Völkl, Hydrogen in metals I, (1978).

[4.17] M. Benham and D. Ross, *Zeitschrift für Physikalische Chemie,* **163**, 25-32 (1989).

[4.18] F. Lewis, *Platinum Met. Rev.,* **4**, 132 (1960).

[4.19] M. Hara, J. Sakurai, S. Akamaru, K. Watanabe, K. Nishimura, K. Mori, and M. Matsuyama, *Mater. Trans.,* **47**, 2373 (2006).

[4.20] B.D. Cullity and S.R. Stock, *Elements of X-ray Diffraction,* Prentice hall Upper Saddle River, NJ (2001).

[4.21] F.A. Lewis, K. Kandasamy, and X. Tong, *Solid State Phenomena,* **73**, 268-301 (2000).

[4.22] F. Vigier, R. Jurczakowski, and A. Lasia, *J. Electroanal. Chem.,* **588**, 32-43 (2006).

[4.23] G. Boureau and O.J. Kleppa, *J. Chem. Phys.,* **65**, 3915 (1976).

[4.24] G. Boureau, O.J. Kleppa, and P. Dantzer, *J. Chem. Phys.,* **64**, 5247 (1976).

[4.25] C. Labes and R.B. McLellan, *Acta Metall.,* **26**, 893-899 (1978).

[4.26] D.P. Broom, *Int. J. Hydrogen En.,* **32**, 4871-4888 (2007).

[4.27] K. Sakaki, T. Yamada, M. Mizuno, H. Araki, and Y. Shirai, *Mater. Trans.-JIM,* **43**, 2652-2655 (2002).

[4.28] H. Kurokawa, T. Nakayama, Y. Kobayashi, K. Suzuki, M. Takahashi, S. Takami, M. Kubo, N. Itoh, P. Selvam, and A. Miyamoto, *Catalysis today,* **82**, 233-240 (2003).

[4.29] I. Moysan, V. Paul-Boncour, S. Thiebaut, E. Sciora, J.M. Fournier, R. Cortes, S. Bourgeois, and A. Percheron-Guegan, *J. Alloys Compounds,* **322**, 14-20 (2001).

[4.30] A. Carson, T.B. Flanagan, and F. Lewis, *Trans. Faraday Soc.,* **56**, 1332-1339 (1960).

[4.31] F.A. Lewis, I. Lewis, and S.G. McKee, *J. Less-Common Met.,* **101**, 503-521 (1984).

[4.32] T. Flanagan, J. Clewley, H. Noh, J. Barker, and Y. Sakamoto, *Acta mater.,* **46**, 2173-2183 (1998).

[4.33] J. Weissmüller and C. Lemier, *Phys. Rev. Lett.,* **82**, 213-216 (1999).

[4.34] M. Yoshihara and R.B. McLellan, *J. Less- Common Met.,* **107**, 267-279 (1985).

Chapter 5: .   Hydrogenation of CP-Ti and Ti-6Al-4V alloy

5.1 Introduction

There has been a growing research interest in the interaction between titanium (Ti) and hydrogen due to the fact that this metal, Ti, is regarded as one of the promising materials for hydrogen storage [5.1,5.2]. Ti has high affinity for hydrogen, which can be easily added and removed through vacuum annealing [5.3]. Alloying Ti with aluminium (Al) and vanadium (V) is significant because Al reduces the metal density, stabilises and strengthens the α- phase while V provides a greater amount of the ß- phase. The alloyed transition metal always exhibits a higher beta transus temperature than unalloyed transition metal [5.4-5.6]. Materials with high beta transus temperature are useful for the components subjected to high temperature operational conditions such as aircraft engines [5.4-5.6]. However, hydrogen also serves as a beta-stabilising element in titanium alloys. Hydrogen, as a unique alloying element for titanium and titanium alloys can be easily introduced into these materials using controlled diffusion from a hydrogen environment at both room and elevated temperatures. Studies have shown that hydrogen improves the properties of titanium and titanium alloys by modifying the microstructure and this has attracted much interest of materials scientists [5.3,5.7]. Theoretical calculations performed by *Xu et al.* [5.1] and other researchers revealed that the hydrogen atoms prefer octahedral sites at low hydrogen concentrations and tetrahedral sites at high concentrations [5.1,5.8-5.10]. Due to an excellent combination of a high strength-to-weight ratio and good corrosion resistance, Ti and its alloys have been widely used as one of the most important structural materials in various areas such as aerospace, marine, chemical plants and automobiles [5.2]. An extensive research has been conducted on Ti and its alloys whereby the effect of hydrogen on phase transformation, the effect on the microstructure and the formation mechanism of titanium hydrides were

studied, whereas relatively little work has been reported with regard to the quantity of the absorbed hydrogen [5.2,5.5,5.8,5.11-5.13]. This chapter will report and discuss the microstructure evolution, phase transformations and the effect of hydrogen absorbed in commercially pure titanium (CP-Ti) and Ti-6Al-4V alloy as a function of hydrogen content, temperature and material condition.

5.2   Experiment

The materials used in this study are grade 2 CP-Ti and a two - phase ($\alpha + \beta$) Ti-6Al-4V alloy supplied by Good Fellows. The CP-Ti was obtained in a form of annealed cold drawn rod and Ti-6Al-4V alloy in a form of annealed hot drawn rod. Samples of $16\,mm \times 2\,mm$ CP-Ti and $25\,mm \times 2\,mm$ Ti-6Al-4V alloy were cut. Annealing and hydrogenation were performed at separate sets of samples. One set of each material was annealed at 550 ˚C, 650 ˚C, 750 ˚C and 850 ˚C for 3 hours and the mass difference was determined as the mass of the absorbed oxygen (and possible formation of oxide layer). The hydrogenation was performed by holding the second set of material at 550 ˚C, 650 ˚C, 750 ˚C and 850 ˚C in a gas mixture (15 % hydrogen and 75 % Ar) environment for 3 hours under low pressure-low concentration-short charging time (LP-LC-ST) conditions. A gas flow rate of 223 L/sec was used under a system pressure of 1013 mbar. Another set of samples was hydrogenated at room temperature in durations of 1, 3 and 7 hours under the same gas concentration and pressure conditions.

The microstructural changes of CP-Ti samples as a result of annealing temperatures and hydrogen were studied using Reichert optical microscope. A bright field mode was used to obtain information about microstructure of investigated samples. Phase identification was investigated using a D8-Bruker X-ray powder diffractometer. The system was operated in a θ

- 2θ geometry at 40 kV and 40 mA using Cu Kα radiation as an X-ray source with a wavelength of 1.54 Å. X-ray diffraction (XRD) spectra were collected from 2θ = 30 ˚ to 90 ˚. The step size was 0.03 ˚. The hydrogen content in the samples was determined by weighing the samples before and after hydrogenation treatment and by probing with He$^+$ ions using elastic recoil detection analysis (ERDA) technique. As a result of the annealing temperatures and the hydrogen content in CP-Ti and Ti-6Al-4V alloy samples, the hardness of the materials is affected which was determined using a Vickers hardness test. Hardness generally represents the strength and wear resistance of a material [5.14]. The higher the hardness value of material, the higher the strength and wear resistance. The measurements were conducted in a Zwick Roell Vickers hardness tester with a force of 1 Kgf at a dwell time of 10 s. The tests were performed using a diamond indenter in the form of pyramid with a square base and an angle of 136 ˚ between opposite faces. A maximum series of eight test impressions were made on each sample.
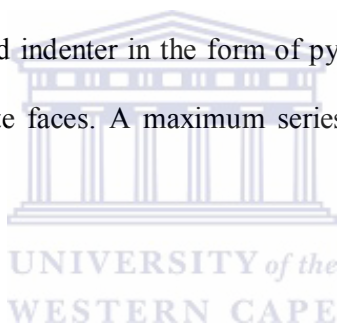
5.3   CP-Ti

5.3.1 Results

5.3.1.1   Room temperature hydrogenation

(i)   Optical images (Microstructure analysis)

The microstructure of CP-Ti samples hydrogenated at room temperature for different times are shown in Figure 5-1. The optical micrograph in Figure 5-1 (a) shows the microstructure of CP-Ti before hydrogenation whereby the arrows show the plastic deformation lines caused by manufacturing process. The microstructure of as-received CP-Ti consists of α-phase. The grain boundaries of the α-phase become distinct as the hydrogen is absorbed at room temperature and a fully recrystalised grain structure was observed.
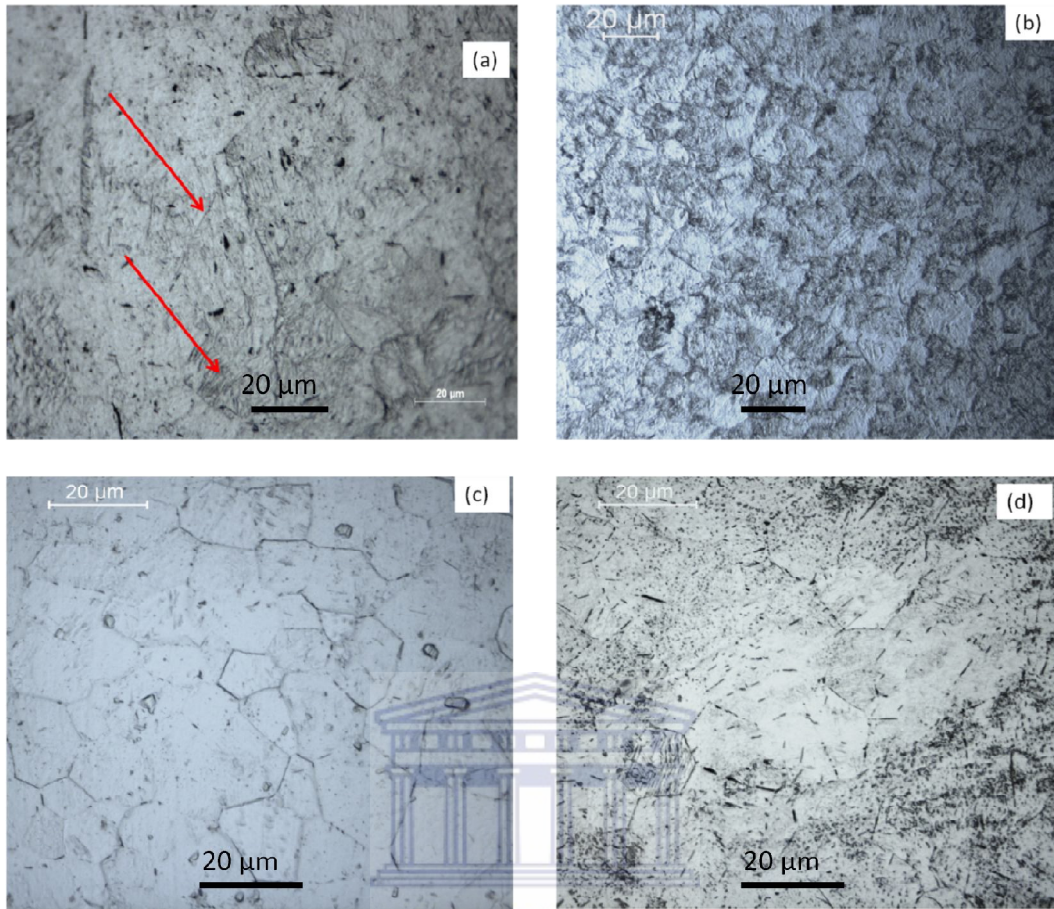
Figure 5-1: Optical images of CP-Ti: (a) as received and, hydrogenated at room temperature for (b) 1 hour, (c) 3 hours and (d) 7 hours.

The average size of the grains in hydrogenated samples is approximately 10 μm. Therefore, hydrogen induction in CP-Ti eliminates the plastic deformation of material caused by manufacturing process and promotes the formation of equiaxed grains during hydrogenation at room temperature for different periods of time.

(ii) Phase identification using XRD technique

Figure 5-2 shows the X-ray diffraction patterns of the as - received and hydrogenated CP-Ti samples at room temperature. The X-ray diffraction pattern of the as-received sample shows

that the starting material consists of α-phase. Similarly, the XRD patterns of the samples hydrogenated at room temperature for different times show no significant changes; the hydrogenation at room temperature did not induce phase transformation.
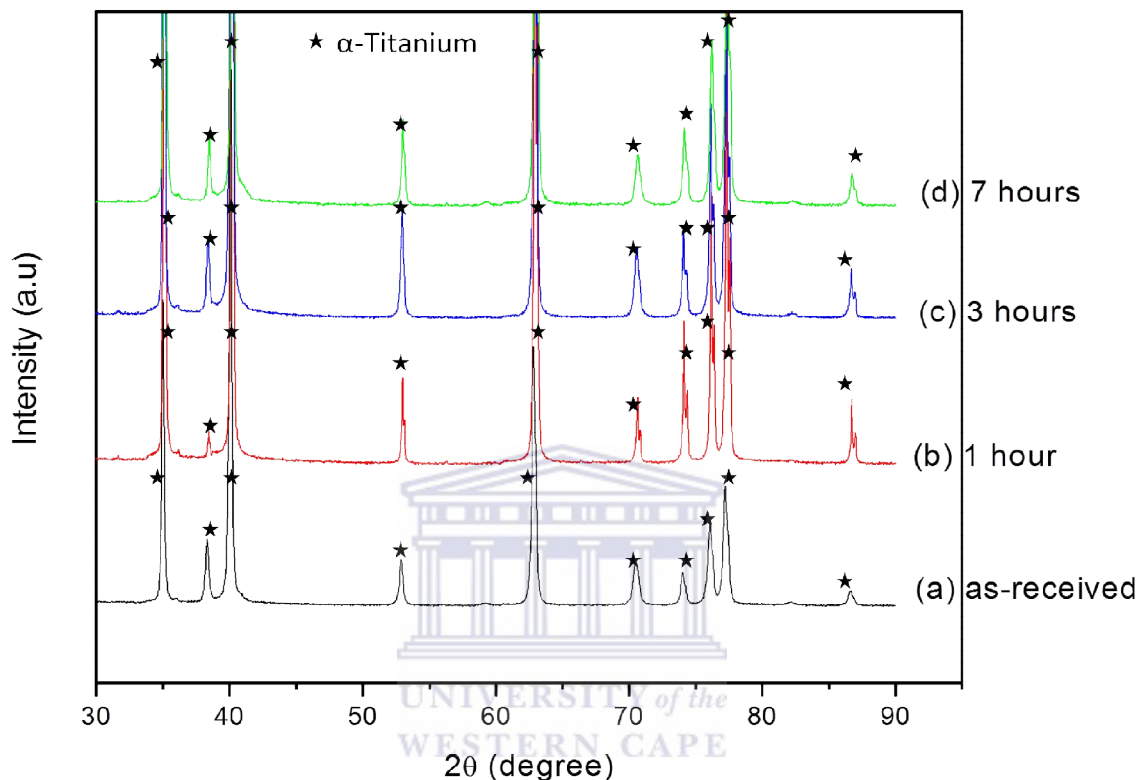
Figure 5-2: XRD diffraction patterns of CP-Ti before (a) and after hydrogenation at room temperature for (b) 1 hour, (c) 3 hours and (d) 7 hours.

In conclusion, hydrogenation of CP-Ti at room temperature under LP-LC-ST conditions is insufficient for hydride formation as well as phase transition from α → β.

(iii)   ERD analysis

The analysis of the hydrogen concentration in CP-Ti before and after the hydrogenation process conducted at room temperature was determined by the use of ERDA technique.

Figure 5-3 shows the distribution of hydrogen in the samples prior to and after hydrogenation for different periods of time.
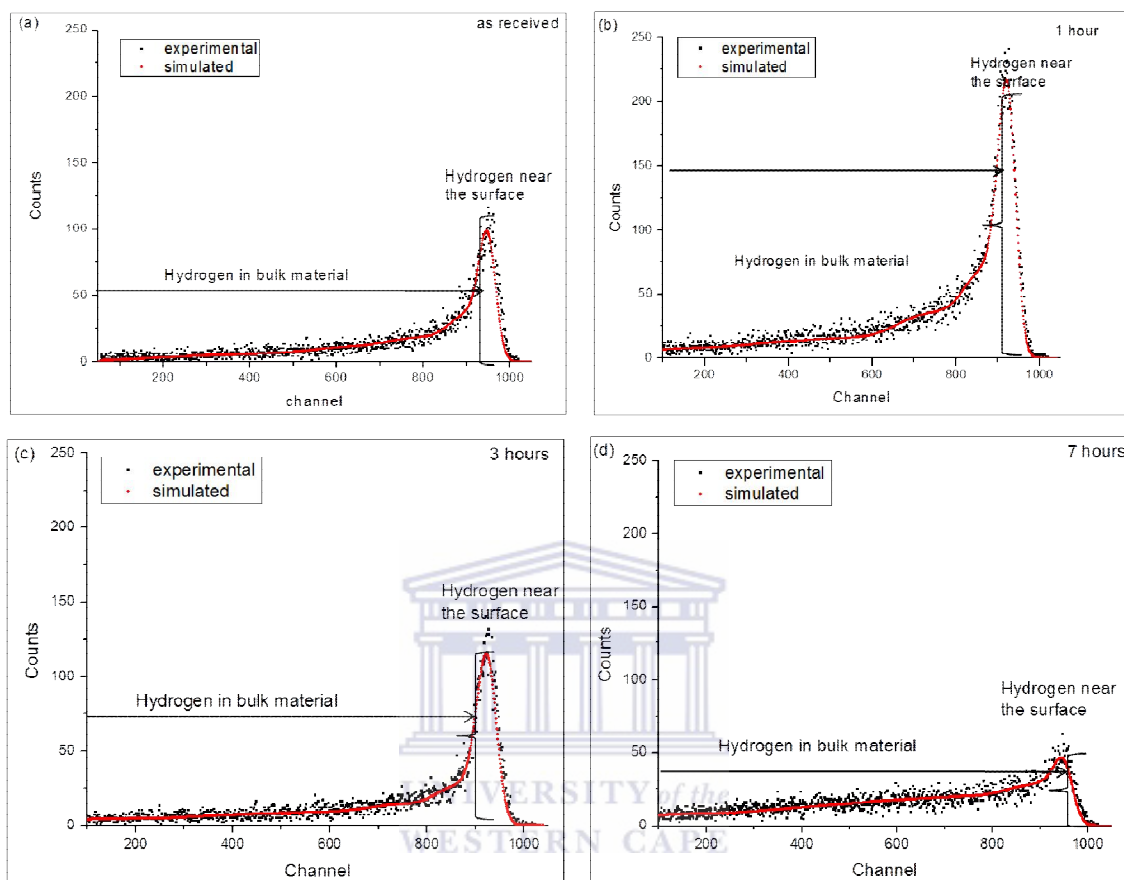
***Figure 5-3:*** The spectra of hydrogen distribution in CP-Ti samples prior (a) and after hydrogenation at room temperature for (b) 1 hour, (c) 3 hours and (d) 7 hours.

Hydrogen was detected in the as-received CP-Ti sample. It can be observed that hydrogenation process increases the depth of hydrogen present on the surface region for the samples treated for 1 and 3 hours. For the sample hydrogenated for 7 hours, less hydrogen was detected. The degree at which the peak area and the width increase is high at 1 hour, which indicates that more hydrogen has been absorbed during this time, and it becomes less with time. A conclusion can be made that the depth of hydrogen absorption on the sample

surface of CP-Ti decreases at long hydrogenation periods. The depth profile of hydrogen for the samples used in this study is shown in Figure 5-4.
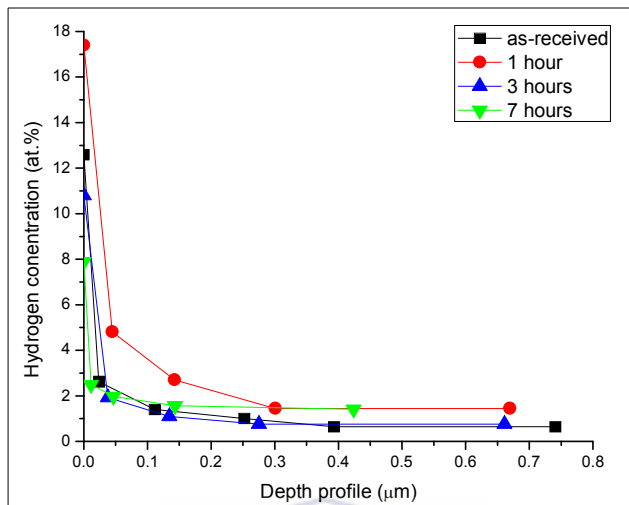
Figure5-4: Depth profile of hydrogen in CP-Ti samples before and after room temperature hydrogenation for different periods of time.
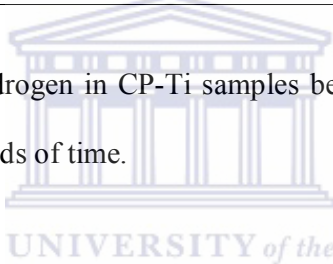
The profile of hydrogen present in as-received CP-Ti decreases with the depth of penetration of the He^+ ions. The distribution of hydrogen concentration increases towards the bulk of the material after the hydrogenation process has been conducted for 1 and 7 hours. There is no significant change to the hydrogen distribution when the hydrogenation is conducted for 3 hours. The average concentrations of hydrogen on the surface region and in the bulk of the CP-Ti material are given in Table 5-1. The as-received sample of CP-Ti has an average hydrogen concentration of 12.6 at. % distributed at a depth of 0.02 µm near the surface regions and 1.11 at. % in the bulk of the material. The concentration of the hydrogen on the surface increases to 17.39 at. % when the hydrogenation process is conducted for 1 hour and then decreases with further time increment. The depth of hydrogen distribution also increases from 0.02 - 0.04 µm in the 1 hour and 3 hours treated samples while it decreases to 0.01 µm in the samples hydrogenated for 7 hours. The average hydrogen concentration is increased in

the bulk of the material where there is more hydrogen absorbed for 1 hour treatment as compared to the samples treated for 3 and 7 hours. The depth of penetration for He^+ ions is approximately 0.74 µm in as-received material and it decreases with hydrogenation to approximately 0.67 µm.

Table 5-1: The average concentration of hydrogen in CP-Ti samples before and after hydrogenation at room temperature.

CP-Ti samples	Hydrogen concentration near surface		Average hydrogen concentration in bulk	
	at. %	(wt. %)	at. %	(wt. %)
As-received	12.6	0.30	1.11	0.02
1 hour	17.39	0.44	2.29	0.05
3 hours	10.8	0.25	1.02	0.02
7 hours	7.9	0.18	1.62	0.03

In conclusion, it was established that absorption of hydrogen occurs in CP-Ti at room temperature. The micrographs have shown that equiaxed grains are formed in CP-Ti when it is exposed to hydrogen gas for long periods of time. It was also observed that the plastic deformation lines disappeared with hydrogenation. However, hydrides were not identified by XRD which indicate that the amount of hydrogen absorbed by each sample was insufficient for the formation of detectable hydrides. The concentration values determined from ERDA data have shown that hydrogenation of CP-Ti sample at room temperature occurs faster in 1 hour than in 3 and 7 hours which indicate that the diffusion of hydrogen in CP-Ti decreases with time of exposure at room temperature. Furthermore, the He^+ ions' depth of penetration decreased with an increase of hydrogen content in CP-Ti samples because hydrogen changes
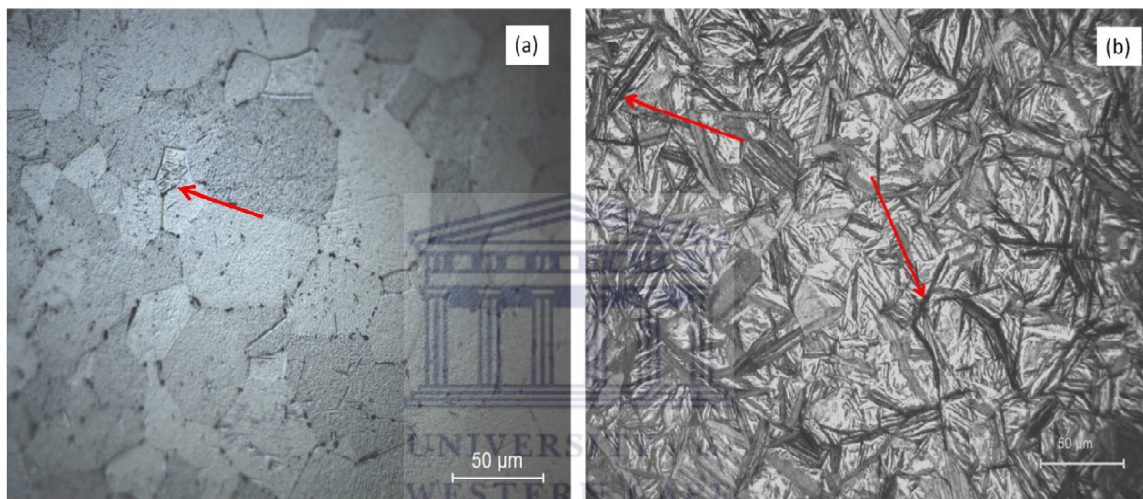
the properties of the metal [5.2,5.15,5.16]. The presence of hydrogen in α-Ti improves the mechanical properties of Ti [5.2].

5.3.1.2   Temperature and hydrogen effect

(i)   Microstructure analysis

The optical images in Figure 5-5 to 5-8 show the effects of temperature and hydrogen in CP-Ti.

Figure 5-5: Optical micrographs of CP-Ti (a) annealed at 550 ˚C and (b) hydrogenated at 550 ˚C for 3 hours.

The micrograph in Figure 5-5(a) shows the presence of equiaxed fully recrystalised α-grains with annealing twins. The average grain size of the annealed CP-Ti sample is approximately 30 μm.

The presence of hydrides is observed in the 550 ˚C hydrogenated sample as shown by arrows in Figure 5-5(b). The micrograph shown in Figure 5-6 (a) shows the fully recrystalised microstructure of CP-Ti sample hydrogenated at 650 ˚C for 3 hours. The microstructure has an average α-grain size of approximately 37 μm. The microstructure of the hydrogenated CP-

Ti sample, Figure 5-6(b), consists of α- phase with hydrides and needle-like structures called

martensite.
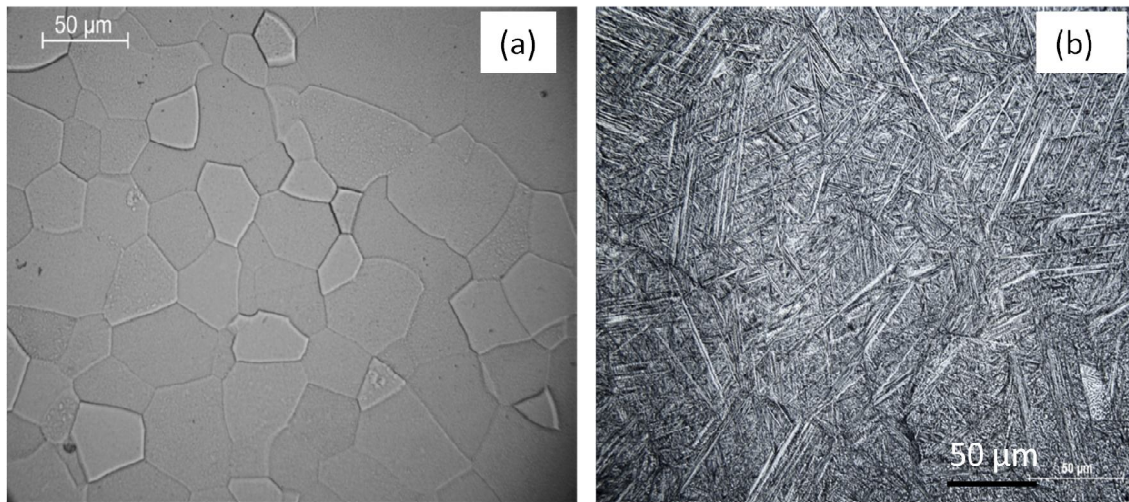
Figure 5-6: Microstructures of (a) annealed and (b) hydrogenated CP-Ti samples at 650 ˚C

for 3 hours.

A higher annealing temperature of 750 ˚C causes grain growth of approximately 70 μm as

shown in Figure 5-7 (a). The hydrogen has facilitated the formation of hydrides in Figure 5-7

(b) when introduced at 750 ˚C. Long needles (martensite) in specific crystallographic

orientations are pointed by arrows.

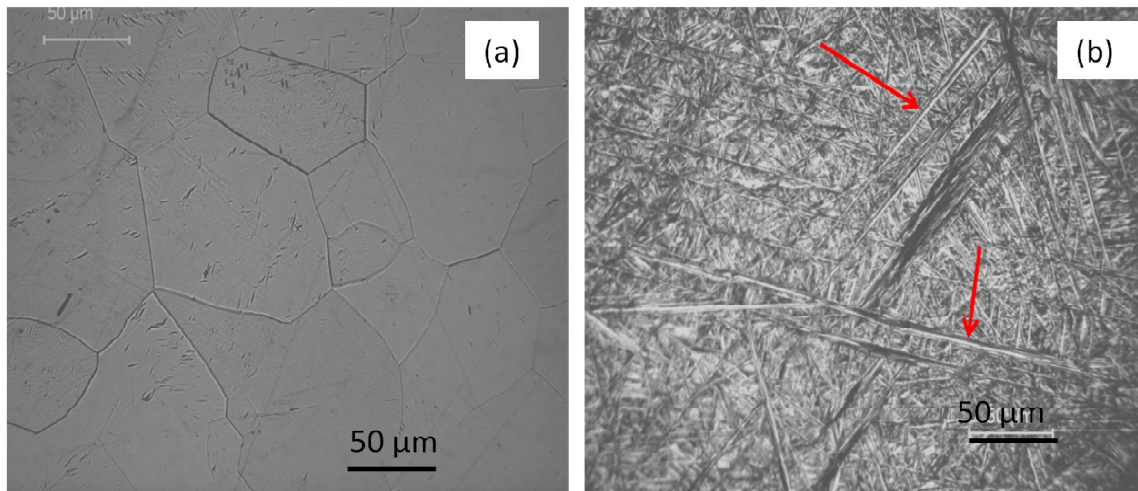***Figure 5-7:*** Micrographs of CP-Ti (a) annealed and (b) hydrogenated at 750 ˚C for 3 hours.

The grain size increased at 850 ˚C annealing temperature to approximately 204 µm in Figure 5-8 (a). Introduction of hydrogen at this temperature has formed hydrides and coarse martensite as observed in Figure 5-8 (b).
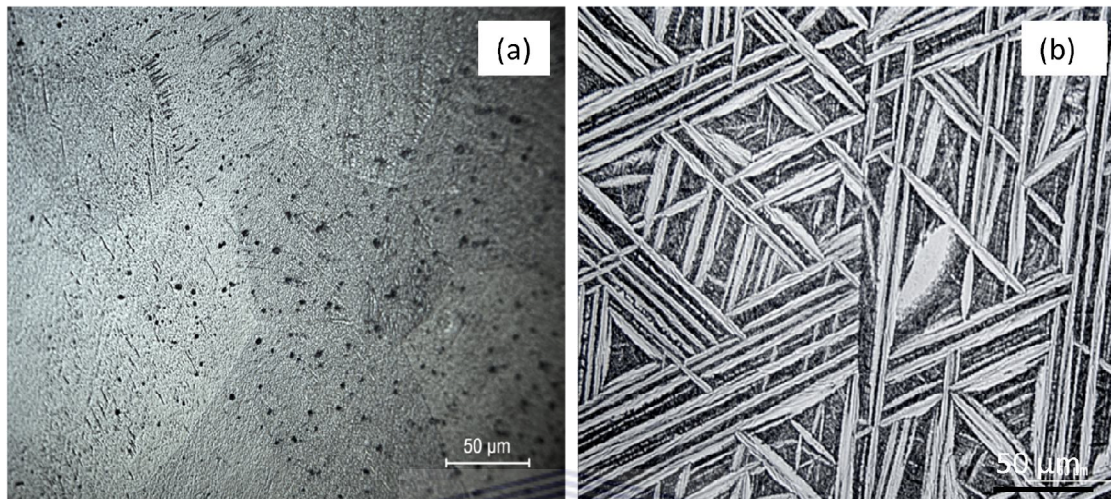
Figure 5-8: Microstructures of (a) annealed and (b) hydrogenated CP-Ti samples at 850 ˚C.

In summary, the high annealing temperatures have affected the microstructure of CP-Ti; the grain size increases from 30 µm to 204 µm. It was observed in this work that the grains grow with an increase in temperature and these findings are in agreement with the work by *Bozzolo et al* [5.17]. The mechanism of grain growth in this material occurs as follows: the grain size increases rapidly at the beginning of annealing and subsequently more slowly because of the weakening in the driving force associated with the reduction in grain boundary surface. The free enthalpy of the material decreases during grain growth by reducing the total surface of the grain boundary. This decrease is more effective at high temperatures when high energy grain boundaries are eliminated. Therefore, the grain boundaries remaining after grain growth are the less thermodynamically unfavourable ones, i.e. the ones with lowest energy [5.17]. High annealing temperature and hydrogen contributed towards the formation of martensitic structure; higher temperature caused formation of coarse martensite needles.

(ii)   Phase transition

The diffraction patterns of CP-Ti samples hydrogenated at high temperatures are shown in Figure 5-9. Hydrogenation of CP-Ti at different temperatures has facilitated phase transformation and the formation of Ti-hydrides was observed. The fcc hydrides, TiH_{2-x}, with stochiometry ranging from $TiH_{1.97}$ to TiH_2, were formed at 550 ˚C and 650 ˚C. The lattice parameter of TiH_{2-x} ranges from 4.42 - 4.44 Å. In both temperatures, the presence of a hexagonal close packed α-phase (hcp) was detected. An additional tetragonal γ-TiH hydride was detected in the 750 ˚C hydrogenated sample with a = 4.21 Å and c = 4.59 Å lattice parameters. However, the γ-TiH hydride does not form during the hydrogenation at 850 ˚C. This is an indication that this phase might be metastable. The phases present are the α-phase and TiH_{2-x} hydrides.
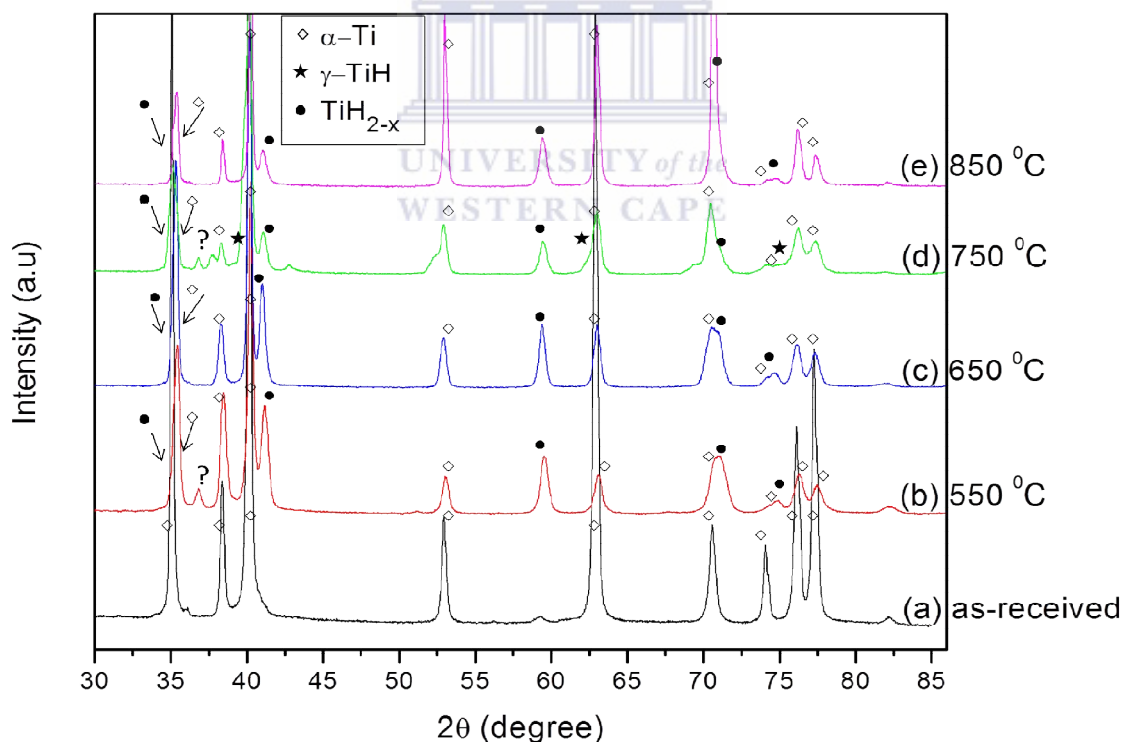
Figure 5-9: X-ray diffraction patterns of CP-Ti (a) as received and hydrogenated at (b) 550 ˚C, (c) 650 ˚C, (d) 750 ˚C and (e) 850 ˚C for 3 hours.

At the temperatures under which the study was conducted, phase transformation from α(hcp) to β(bcc) did not occur as a result of low hydrogen gas concentration and system pressure. Therefore, it was assumed that the kinetics of hydrogen sorption was too low to reach a minimum hydrogen content of 8 at. % in order to enable the formation of a β-phase [5.18].

In summary, the introduction of hydrogen in CP-Ti at high temperatures causes the formation of hydrides. The hydrides detected are TiH_{2-x} present in all hydrogenation temperatures and γ-TiH which only appeared at 750 ˚C.

(iii) Gravimetric measurements

The difference in mass of CP-Ti samples before and after annealing at different temperatures was measured using a digital balance in order to determine the effects of temperature on the mass of the samples due to possible oxidation. It was found that the difference in mass of CP-Ti samples before and after annealing is similar for the temperatures ranging from 550 ˚C - 850 ˚C. This implies that the change in mass of CP-Ti samples is similar for all temperatures when annealed for equal periods under the same pressure of 1013 mbar. Since CP-Ti is prone to oxidation, the change in mass might have been caused by the formation of oxide layer on the surface of samples given that the accuracy of the digital balance used in this experimental procedure is 0.01 mg [5.19]. However, significant mass changes are observed when annealing is conducted in a mixture of 15 % hydrogen and 75 % Ar environment.

The average concentrations of hydrogen in CP-Ti samples hydrogenated at temperatures ranging from 550 ˚C to 850 ˚C are given in Table 5-2. An assumption was made that the change in the mass of the samples occurred as a result of absorbed hydrogen only because the argon (Ar) gas in the gas mixture is responsible for minimising oxidation.

Table 5-2: The average concentration of hydrogen in CP-Ti determined by gravimetric method.

Hydrogenation temperature (˚C)	Mass before hydrogenation (g)	Mass after hydrogenation (g)	Mass difference (g)	Hydrogen concentration (wt. %)	Hydrogen concentration (at. %)
550	1.61	1.65	0.03	1.88	47.70
650	0.88	0.89	0.01	1.35	39.36
750	0.88	0.88	0.01	0.84	28.64
850	0.92	0.92	0.004*	0.43	17.13

*no significant change in terms of mass

The sample hydrogenated at 550 ˚C has the highest mass change as compared to the other samples hydrogenated at different temperatures. The concentration values show that the sample hydrogenated at 550 ˚C absorbs more hydrogen as compared to the ones hydrogenated at 650 ˚C, 750 ˚C and 850 ˚C temperatures. A trend can be observed whereby the absorption of hydrogen in samples decreases with an increase in temperature. This means that the absorption of hydrogen into the samples is altered at high temperatures (above 550 ˚C).

In summary, it was found that the change in mass of CP-Ti samples after annealing at different temperatures for 3 hours is similar. Therefore, the rate at which oxidation occurs in CP-Ti is independent of the temperature but however, depends on the annealing time. Annealing the samples under the same LP-LC-ST conditions in a hydrogen environment has a different effect on the mass of the samples. Comparison of the effect of temperature on the mass observed after annealing with that observed after thermohydrogen treatment indicate that hydrogen is the contributor to the mass increase of the CP-Ti samples. The absorption of hydrogen in CP-Ti has occurred mostly at 550 ˚C whereby a maximum of 47 at. % of

hydrogen was calculated using the difference in mass of the sample before and after hydrogenation as the hydrogen mass. By referring to the phase diagram of Ti-H system determined by *Setoyama et al.* [5.18], the absorption of hydrogen in α-Ti increases from room temperature to 550 ˚C and then decreases with increased temperature.

(iv)   ERD analysis

ERDA was performed on the samples before and after the hydrogenation process at 550 ˚C, 650 ˚C, 750 ˚C and 850 ˚C temperatures in order to quantify the hydrogen concentration and to profile its distribution with depth of penetration. The output spectra of the profiled hydrogen in the samples are shown in Figure 5-10 and 5-11.
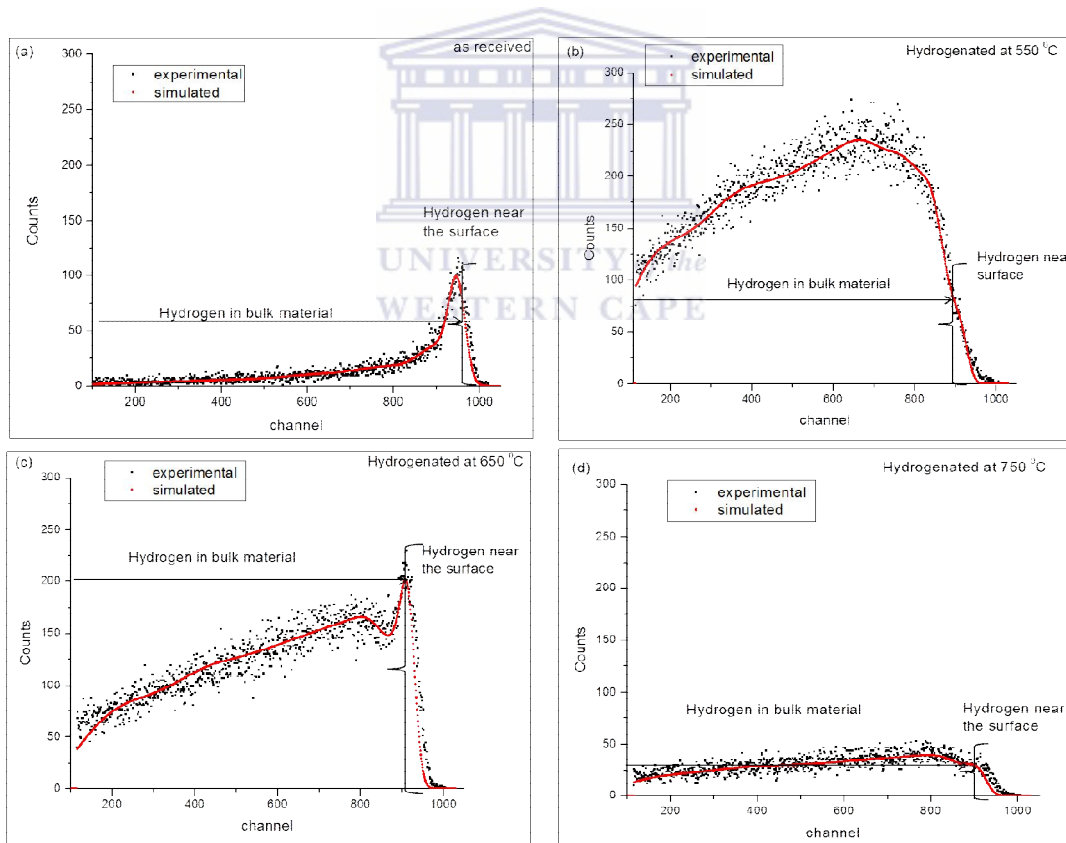
Figure 5-10: Simulated ERDA spectra of CP-Ti samples (a) before and after hydrogenation for 3 hours at (b) 550 ˚C, (c) 650 ˚C and (d) 750 ˚C temperatures.

Figures 5-10 and 5-11 show that the hydrogen that recoils from the surface region of the hydrogenated CP-Ti samples increases by a degree which is higher at 550 ˚C and lower at elevated temperatures of up to 750 ˚C. An exception is found at 850 ˚C in which the recoils measured are less than those found in the as-received material. It can be observed that when the hydrogenation process is conducted at 550 ˚C temperature, there is more hydrogen distributed in the bulk of the material (width of the peak is broader). The amount of hydrogen distribution into bulk material decreases with depth whereby less hydrogen is found in the deeper regions of all samples (left part of all spectra). This phenomenon is related to the energy loss of the He$^+$ ions as they penetrate deeper into the bulk of the CP-Ti samples.
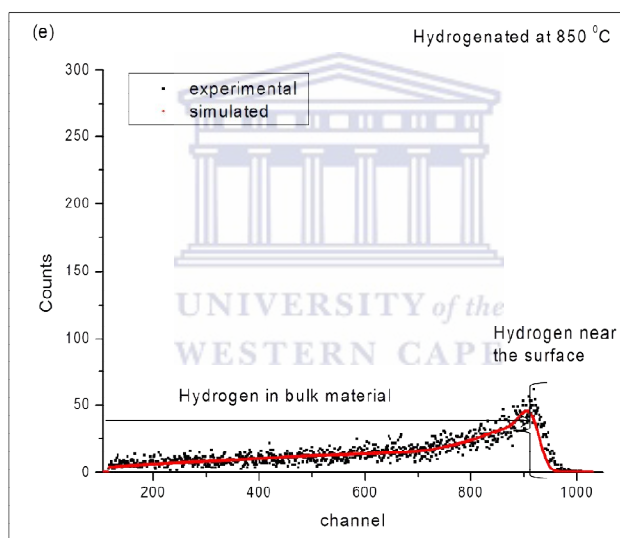
Figure 5-11: A simulated ERDA spectrum of hydrogen in a sample of CP-Ti which was hydrogenated at 850 ˚C.

Therefore, more hydrogen was absorbed during the hydrogenation at 550 ˚C temperature. The hydrogen in the samples was calculated and plotted to determine the concentration distribution with depth as shown in Figure 5-12 and the average concentrations are given in Table 5-3. The hydrogen profile of as-received CP-Ti indicates that there is 12.6 at. % average concentration of hydrogen distributed over 0.02 μm depth and 1.11 at. % in bulk of

material. Therefore, the as-received samples of CP-Ti initially have 12.6 at. % of hydrogen near their surface regions and less in the bulk of the material. The overall concentration of hydrogen detected was distributed over a depth of 0.74 µm. The depth profiles of the hydrogenated samples show that absorption of hydrogen has occurred whereby the bulk concentration has increased particularly at 550 ˚C. The hydrogen concentration on the surface has decreased to 8.07 at. % in comparison to 12.6 at. % of as-received, while its depth of distribution increased to 0.07 µm in 3 hours. The increment of the depth of distribution confirms that the diffusion of hydrogen has occurred towards the bulk of material. Similarly, the concentration of hydrogen into bulk material increased with depth reaching an average maximum of 27.78 at. %. The total depth of penetration probed in this sample was 0.85 µm.
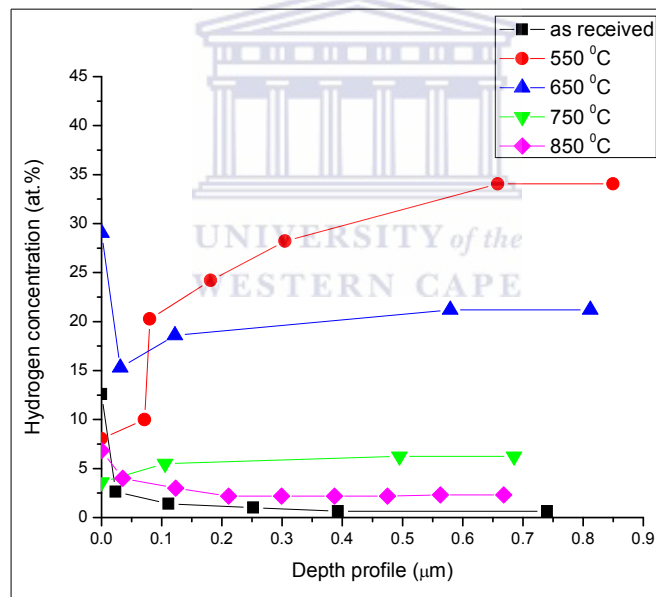
Figure 5-12: The profile of hydrogen in CP-Ti samples before and after hydrogenation for 3 hours at 550 ˚C, 650 ˚C, 750 ˚C and 850 ˚C.

Further increment of the hydrogenation temperature decreases the degree at which the hydrogen concentration increases in bulk material. At 650 ˚C, the depth of hydrogen distribution near the surface regions has increased to 0.03 µm while 18.98 at. % of

concentration was detected in bulk of material. The distribution has increased to a depth of 0.81 µm. When the hydrogenation is performed at 750 ˚C, the 5.76 at. % of hydrogen distribution on the surface region increases to 0.11 µm. The overall depth of penetration was found to be 0.69 µm. The hydrogenation at 850 ˚C increases the distribution depth to 0.04 µm (2.58 at. % surface hydrogen) while the overall distribution has decreased to 0.67 µm.

Table 5-3: The average concentration of hydrogen in CP-Ti samples before and after hydrogenation at different temperatures for 3 hours.

CP-Ti samples	Hydrogen concentration at the surface regions		Average hydrogen concentration in bulk material	
	(at. %)	(wt. %)	(at. %)	(wt. %)
As-received	12.60	0.3	1.11	0.02
550 ˚C	8.07	0.18	27.78	0.8
650 ˚C	29.03	0.85	18.98	0.49
750 ˚C	3.62	0.08	5.76	0.13
850 ˚C	6.83	0.15	2.58	0.06

In summary, CP-Ti has absorbed hydrogen at high temperatures where a maximum hydrogen concentration of 27.78 at. % was detected in the bulk material of the sample hydrogenated at 550 ˚C in 3 hours. Concerning the average values detected on the surface region and in the bulk of the CP-Ti, it is important to have higher concentration of the hydrogen in the bulk of the material for hydrogen storage systems. In this region, the movement of hydrogen towards the surface is slower than on the surface region and therefore, limiting the occurrence of desorption. Therefore, under low pressure-low concentration-short time (LP-LC-ST) conditions studied in this work, the 550 ˚C was found to be the suitable temperature to store hydrogen in the form of hydrides when the introduction of hydrogen into the CP-Ti is conducted for a period of 3 hours.

(v)   Hardness measurements

Figure 5-13 show the change of hardness in CP-Ti with annealing and hydrogenation at room and elevated temperatures. The surface hardness of the CP-Ti decreased from 166 HV in the as-received sample to 151, 149 and 142 HV after it is heat treated at 550, 650 and 750, and 850 ˚C for 3 hours. The hydrogenation occurring at room temperature decreased the surface hardness from 166 HV in as-received sample to approximately 154, 144 and 156 HV in a period of 1, 3 and 7 hours.
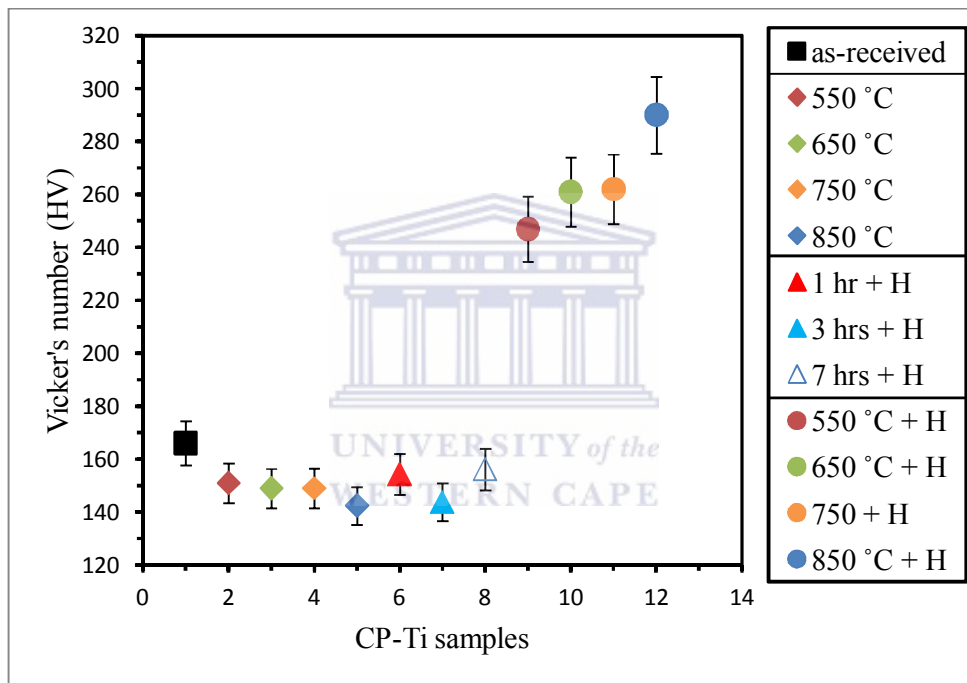
Figure 5-13: Vickers hardness of as received, annealed and hydrogenated CP-Ti samples at different temperatures.

The mutual effect of temperature and hydrogen on the micro-hardness of CP-Ti samples contributes to a hardness increase. Hydrogen and temperature increase the micro-hardness of as-received CP-Ti sample to 247, 261, 262 and 290 HV at 550, 650, 750 and 850 ˚C respectively. The difference in the change of micro-hardness of CP-Ti when hydrogenated at room and high temperatures can be explained as follows: the decrease of hardness for the

samples hydrogenated at room temperature occurred due to decreasing dislocation density and annihilation of dislocations causing recrystallisation of the material. Hardness of CP-Ti increases when hydrogen is induced at high temperatures due to the formation of hydrides, the phase transition of α-phase to β and the formation of martensite. It should be underlined that the hardness increase depends on volume fractions of the phases formed during hydrogenation process. High density of dislocations is associated with the formation of the above mentioned phases. It should be mentioned that the hardness decrease with annealing is due to grain growth phenomenon.

In summary, the absorption of hydrogen in CP-Ti at room temperature is low as compared to the hydrogen uptakes at high temperatures. It is known that grain refinement is the main strengthening mechanism in CP-Ti, Ti alloys and alloys in general [5.20]. The micro-hardness values of α-Ti found in this study significantly increased with hydrogenation temperature. Therefore, the hydrogen serves as a temporary induced alloying element responsible for strengthening. The presence of high dislocation density martensite in samples hydrogenated at temperatures above 550 ˚C also contributes to the strengthening of this material [5.14]. The grain growth observed in annealed samples ranging from 30 - 204 μm indicates that grain boundaries initially present in as-received CP-Ti have migrated, thereby decreasing the volume of defects in the sample. Considering the micro-hardness of annealed samples, the decrease of hardness values with temperature can be observed. This is an indication that dislocations initially present in the as-received material have been eliminated with the increase in temperature. For example, the sample hydrogenated at 850 ˚C with 204 μm grains has the lowest hardness value. These results correlate with those found by *Kao et al* [5.14] where the hardness value of α-Ti with larger grains was relatively lower than that

with smaller grains (in this case at 550 ˚C). Therefore, the main strengthening mechanism in the α-Ti sample is the grain refinement caused rather by hydrogen than by temperature.

5.3.2 Comparison between room and high temperature hydrogenation of CP-Ti

The absorption of hydrogen in CP-Ti was studied under 1013 mbar in a mixture of 15 % of hydrogen and 75 % of Ar environment. The comparison emphasises the following:

i.   The hydrogenation of CP-Ti samples was conducted at different temperature conditions:

➢ At room temperature for 1, 3 and 7 hours

➢ At temperatures of 550 ˚C, 650 ˚C, 750 ˚C and 850 ˚C for 3 hours

ii.   The hydrides present in the samples after hydrogenation are summarised in Table 5-4. Note that the samples hydrogenated at room temperature are not included because no hydrides were detected.
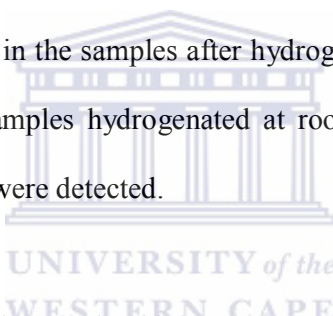
Table 5-4: The hydrides formed in CP-Ti at high temperatures of hydrogenation.

Temperature (˚C)	$TiH_{1.97}$	TiH_2	γ-TiH
550	✓	✓	-
650	✓	✓	-
750	✓	✓	✓
850	✓	✓	-

iii. The average hydrogen concentration in the bulk material of high temperature hydrogenated samples was determined by two techniques, as given in Table 5-8:

➢ Gravimetric

➢ ERDA

Table 5-5: Hydrogen concentration in CP-Ti as determined by gravimetry and ERDA.

Temperature (˚C)	Gravimetric measurements		ERDA experiments	
	Mass difference (g)	Hydrogen concentration (at. %)	Hydrogen at the surface regions (at. %)	Average hydrogen concentration in bulk (at. %)
550	0.03	47.7	8.07	27.78
650	0.01	36.36	29.03	18.98
750	0.01	28.64	3.62	5.76
850	0.00	17.13	6.83	2.58

There is a similar trend between the concentration of hydrogen in CP-Ti samples determined by ERDA and gravimetry. However, as explained in Chapter 4, the volume of probed matter of samples examined by gravimetric and ERDA techniques is incomparable.

5.3.3 Discussions

The study of the effects of hydrogen and temperature on the microstructure of CP-Ti was conducted under low pressure-low concentration-short charging times (LP-LC-ST) conditions. It was found that hydrogen and temperature change the microstructure. When the introduction of hydrogen into CP-Ti samples is conducted at room temperature, equiaxed grains of approximately 10 μm are formed. The formation of recrystalised grains and the elimination of plastic deformation induced by manufacturing of Ti rod decrease the micro-hardness of the material. However, according to XRD results, there are no hydrides in the microstructure. These results are in disagreement with the study conducted by *Shih et al.* [5.21] and *Numakura et al.* [5.22] on the formation of hydrides in CP-Ti at room hydrogenation temperature. The average concentration values of hydrogen in all the hydrogenated samples as determined by ERDA are over 5 at. % and according to *Shih et al.* [5.21] and *Numakura et al.* [5.22], face-centered cubic δ-TiH$_x$ and the metastable face-

centered tetragonal γ-TiH are expected to form at low hydrogen concentrations (1-3 at. %). *Gao et al*. [5.12] also observed TiH_x hydride formation at temperatures below 300 ˚C but the absorption rate was low and therefore this could be one of the possible explanations why hydrides are absent. The concentration of hydrogen in CP-Ti was found to be greater when the process is conducted for 1 hour than 3 and 7 hours. Due to the low kinetics of hydrogen at room temperature and low pressures, a thin hydride layer is formed on the sample surface with less permeability for hydrogen. The hydride layer decreases the diffusion of hydrogen into the bulk of the material as hydrogenation time increases which result in a slower hydride phase growth rate [5.19]. This is an indication that the diffusion coefficient of hydrogen in Ti-H is lower than in α-Ti. Note that the diffusion mechanism of hydrogen atoms in α-Ti is interstitial [5.12]. Furthermore, comparison between the activation energy for Ti self-diffusion in alpha Ti-H (2.51 eV) with that in pure α-Ti (2.76 eV) indicate that hydrogen atoms reduce the potential barrier for Ti self-diffusion, and thereby enhance the self-diffusivity of titanium in the alpha Ti-H system [5.23]. In conclusion, the rate of hydrogen absorption in CP-Ti occurs fast within the first hour when the process is conducted at room temperature.

Annealing temperatures in CP-Ti form equiaxed grains with sizes ranging between 30 μm at 550 ˚C and 204 μm at 850 ˚C. The grain sizes in CP-Ti increases with temperature and these results correlate with those found by *Kao et al* [5.14]. The gravimetric measurements taken before and after annealing suggests that at elevated temperatures (maximum of 850 ˚C), the mass of CP-Ti samples increase as a result of possible oxidation. The hardness value of the samples was determined before and after the annealing process and it was found that it decreases with an increase in annealing temperature due to grain growth. The difference in

hardness of the samples was caused by the different sizes of grains present in the microstructure at different temperatures.

High temperatures enhanced the formation of hydrides when hydrogen is introduced into CP-Ti samples. The hydrides summarised in Table 5-4 were also observed in studies conducted by *Xu et al* [5.1]. The lattice constants of the δ-TiH$_{2-x}$ hydride vary with the hydrogen concentrations in Ti as reported by *Wu et al* [5.24]. The various compositions of this hydride form constantly between 300 ˚C and 683 ˚C [5.12]. The γ-Ti-H formed at 750 ˚C has c/a < 1 as opposed to c/a > 1 reported at room temperature studies by *Wu et al* [5.21]. The Monte Carlo simulation performed by *Xu et al.* [5.1] has shown that the stability of γ-TiH hydride depends on temperature. This indicates that this hydride decreases with increasing hydrogen concentration until it disappears completely between TiH$_{1.5}$ and TiH$_{1.99}$ as determined by *Numakura et al* [5.22]. Therefore, it is expected that the concentration of hydrogen absorbed at 750 ˚C temperature is low. Martensite formation at temperatures above 550 ˚C was observed in Figures from 5-6 (b), 5-7 (b) and 5-8 (b). Therefore it can be concluded that hydrogen has lowered the maternsite formation temperature in CP-Ti which was initially above 850˚C. The morphology of the martensite needless formed at 750 ˚C and 850 ˚C temperatures are coarse. According to the hardness values studied in this work, the formation of hydrides and martensite increases the hardness of CP-Ti.

Gao et al. [5.12] has shown that it is possible to lower the beta transus temperature of CP-Ti from 882 ˚C to just above 300 ˚C. However, under the temperatures, pressure and hydrogen gas concentration used in this study, the presence of a β-phase was not detected by XRD. Therefore, the β-transus temperature might not have been achieved or because the volume fraction of the β-phase is less than 0.2 wt. % in the composition detected [5.25]. However, a

significant difference in mass of CP-Ti samples before and after hydrogenation was observed. A maximum hydrogen concentration of 47.7 at. % of hydrogen was determined in the sample hydrogenated at 550 °C using the gravimetric measurements. Therefore, the results show that the diffusion coefficient of hydrogen in α-Ti is temperature dependent and that the desorption rate of hydrogen is higher at elevated temperatures. The ERDA experiments conducted on the same set of samples also showed that the CP-Ti sample hydrogenated at 550 °C has a higher hydrogen concentration, 27.78 at. %, as compared to the other samples hydrogenated at 650, 750 and 850 °C that have displayed percentages of 18.98, 5.76 and 2.58 at. % respectively. Different volume was considered on the samples when the experimental data was collected by ERDA and digital balance and therefore, the hydrogen content is not directly comparable. The hardness of hydrogenated CP-Ti samples increased with temperature which is in disagreement with the study conducted by *Setoyama et al.* [5.18], which showed that the Vickers hardness of hydrogenated CP-Ti decreases with temperature. The solubility of the CP-Ti decreases with an increase in hydrogen content as hydrogen atoms reduce the formation energy for a vacancy in α-phase of Ti [5.23].

5.3.4 Conclusions

When CP-Ti is exposed to hydrogen at room temperature under low pressure-low concentration of hydrogen-short charging time (LP-LC-ST) conditions, equiaxed grains are formed. The effect of annealing on the CP-Ti was investigated in vacuum and also in a hydrogen environment under a pressure of 1013 mbar. These effects were investigated from temperature range between 550 °C - 850 °C because hydrides are expected to form at temperatures above 500 °C. It was found that the formation of fully recrystalised equiaxed grains is promoted by annealing at this temperature. The hydrogenation process conducted at similar annealing temperatures resulted in the formation of hydrides whereas room

temperature did not yield any formation of hydrides. The dissociation rate of hydrogen molecules as they come into contact with the surface of the CP-Ti samples is increased at elevated temperatures making the absorption faster. The quantity of hydrogen detected in the samples hydrogenated at high temperatures is greater than in those hydrogenated room temperature as determined by ERDA and gravimetry. The formation of the hydrides during thermohydrogen treatment is the main factor influencing the increase of hardness. Therefore, it is efficient to form hydrides in CP-Ti when the process is conducted at elevated temperatures such as 550 - 850 ˚C. Furthermore, in order for the material to absorb more hydrogen under atmospheric pressure, the process should be conducted at 550 ˚C temperature.
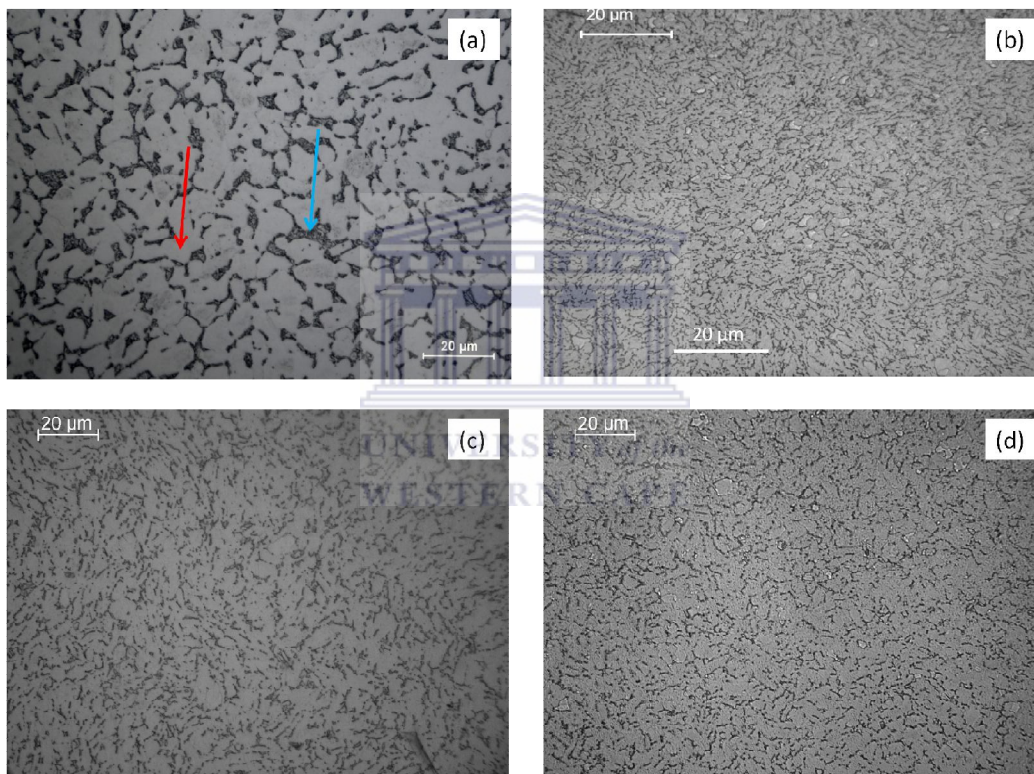
5.4   Ti-6Al-4V alloy

5.4.1 Results

5.4.1.1   Hydrogenation of Ti-6Al-4V alloy at room temperature under LP-LC-ST

(i)   Optical microscopy observations

The effects of room temperature hydrogenation on the microstructure of Ti-6Al-4V alloy were studied by optical microscopy. The microstructure evolution is shown in Figure 5-14. The bright and grey regions in the images represent α and ß phases respectively.

Figure 5-14: Microstructure of Ti-6Al-4V alloy samples (a) as-received, hydrogenated at room temperature for (b) 1 hour (c) 3 hours and (d) 7 hours. The red and blue arrows show the α-phase and the β-phase in as-received Ti-6Al-4V sample.

Looking at the microstructure of as received Ti-6Al-4V alloy in Figure 5-14 (a), it is observed that the sample has (α + ß) dual phase structure. The average size of the α-grains is approximately 8 μm. It is observed in Figure 5-14 (b), (c) and (d) that room temperature

hydrogenation of Ti-6Al-4V alloy change the shape of the grains. The microstructure is composed of elongated primary α-and differently distributed ß-phase.

(ii)   XRD analysis

The X-ray diffraction patterns of Ti-6Al-4V alloy hydrogenated at different periods of time are presented in Figure 5-15.
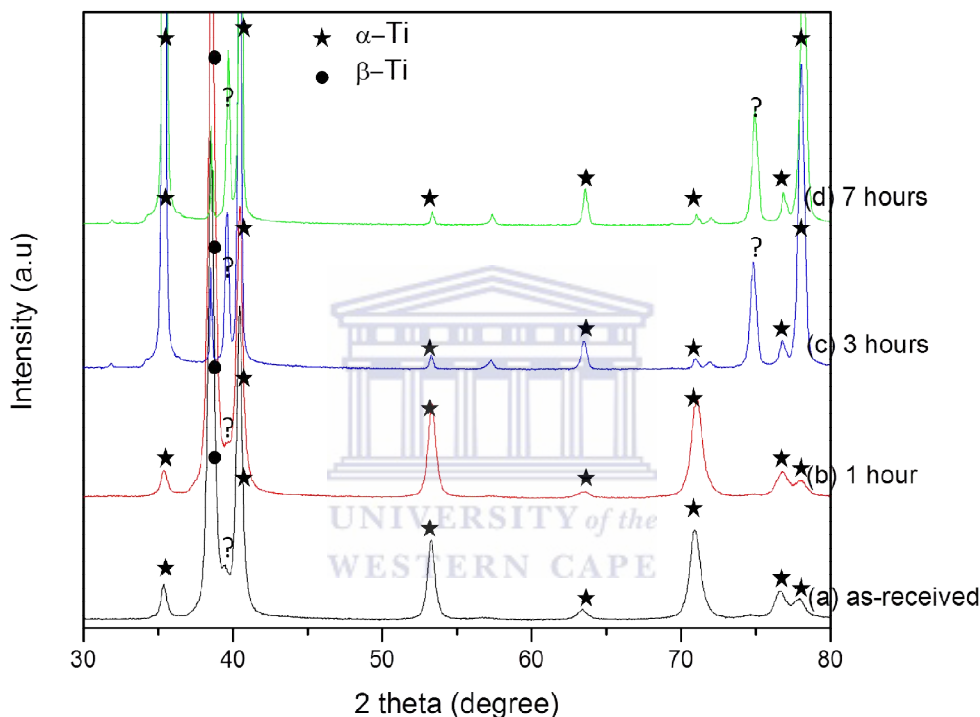
Figure 5-15: XRD patterns of the Ti-6Al-4V samples in (a) as-received state, hydrogenated at room temperature for (b) 1 hour, (c) 3 hours and (d) 7 hours.

The diffraction pattern of as-received sample shown in Figure 5-15 (a) depicts the presence of α and ß-phases in the alloy. The XRD has confirmed that the α-Ti has hexagonal closed packed (hcp) crystal structure with $a = b = 2.92\,Å$ and $c = 4.67\,Å$ lattice parameters and body centered cubic (bcc) ß-Ti has $a = b = c = 3.31\,Å$ lattice parameters. Figure 5-15 shows only one peak associated with ß-phase. The rest of the peaks are associated with α-phase and are diffracting at higher angles than β- phase. This is an indication that the volume

fraction of the α- phase in the alloy is greater than β- phase. Hydrogenation of this alloy at room temperature for different periods of time does not yield hydrides. It was observed that the unidentified peaks became more pronounced with hydrogenation time.

In conclusion, hydrogenation of Ti-6Al-4V alloy at room temperature between 1 and 7 hours does not yield hydrides. However, the significant effect of hydrogen is observed in the microstructure; formation of elongated primary α-grains and re-distributed β-phase.

(iii)   ERD analysis

Elastic recoil detection analysis (ERDA) was performed on Ti-6Al-4V samples before and after the hydrogenation process conducted at room temperature in order to determine the hydrogen's distribution and the average concentration in the samples.
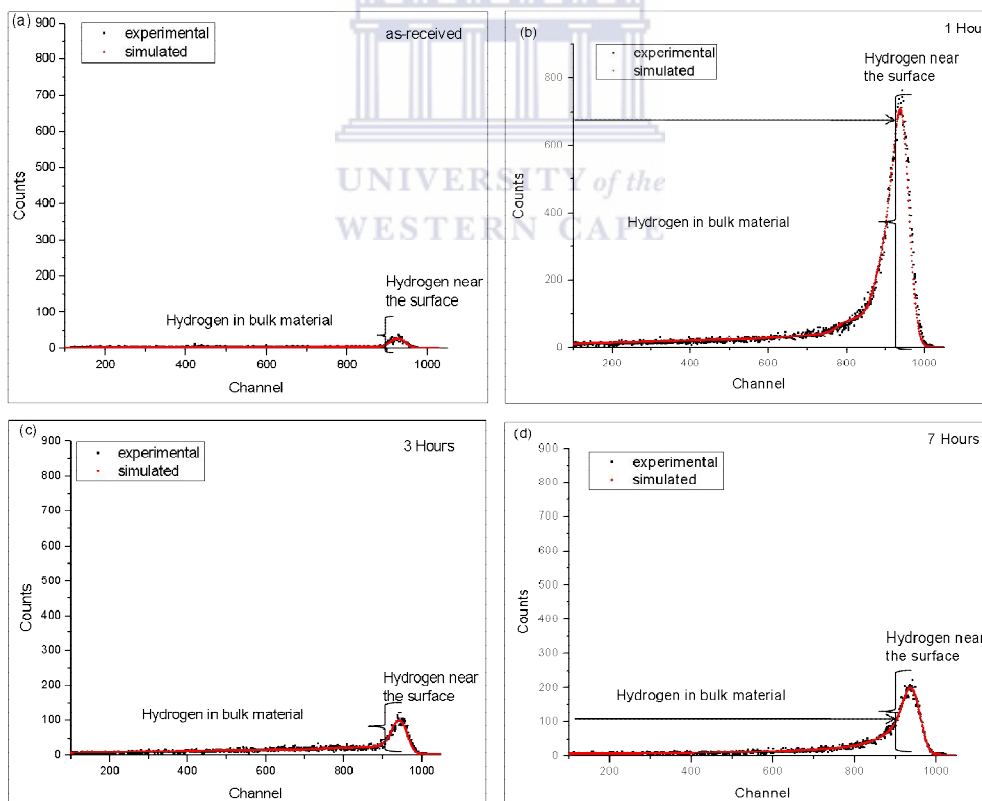
Figure 5-16: The ERDA spectra of hydrogen in Ti-6Al-4V samples before and after hydrogenation at room temperature.

The spectra in Figure 5-16 show the distribution of hydrogen from the surface region into bulk material of the as-received and hydrogenated samples of Ti-6Al-4V alloy for 1, 3 and 7 hours. From this fitted spectra, the hydrogen profile in the sample was determined and plotted in Figure 5-17. Furthermore, the hydrogen concentration on the surface region and in the bulk material was calculated as given in Table 5-10.
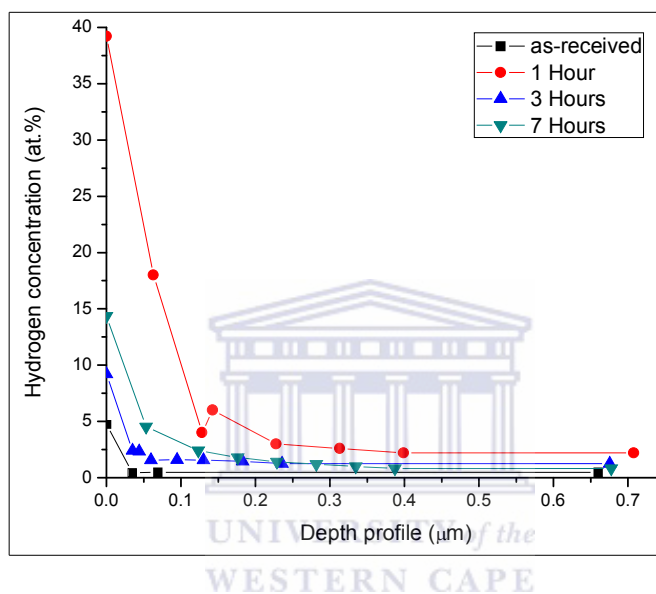
Figure 5-17: The profile of hydrogen in Ti-6Al-4V samples before and after hydrogenation.

The depth profile shows that the as-received sample of Ti-6Al-4V alloy has less hydrogen distributed on the surface region. An average hydrogen concentration of 4.75 at. % hydrogen on the surface and 0.47 at. % in bulk of the material was found. The hydrogen atoms occupy 0.03 μm depth on the surface region. The He^+ ions have penetrated a depth of 0.66 μm in the sample. The profiles show an increase of hydrogen concentration on the surface region and into the bulk of the material during room temperature hydrogenation. The depth of distribution on the surface region has increased to 0.06 μm in the sample hydrogenated for 1 hour which has 39.2 at. % near the surface and 4.5 at. % in bulk of the material. The overall depth of penetration of the He^+ ions increases to 0.71 μm in this sample.

Table 5-6: The average concentration of hydrogen in Ti-6Al-4V samples hydrogenated at room temperature.

| Ti-6Al-4V samples	Hydrogen concentration on surface region		Average hydrogen concentration in bulk material	
	(at. %)	(wt. %)	(at. %)	(wt. %)
as-received	4.75	0.11	0.47	0.01
1 hour	39.20	1.44	4.50	0.10
3 hours	9.20	0.22	1.38	0.03
7 hours	14.34	0.37	1.55	0.03

The concentration of hydrogen on the surface region of the samples hydrogenated for 3 hours is 9.2 at. % is distributed over a depth of 0.04 μm with an average of 1.38 at. % in the bulk of the material. The depth of penetration of the He$^+$ ions in this sample is 0.68 μm which is similar to that hydrogenated for 7 hours. There is 14.34 at. % of hydrogen distributed at 0.05 μm depth on the surface region and 1.55 at. % in the bulk material when the hydrogenation time is increased to 7 hours. However, the distribution of hydrogen is homogeneous in the bulk material of all samples. Therefore, hydrogen absorption in Ti-6Al-4V is faster at short periods of time when the process is conducted at room temperature.

In summary, the hydrogenation of Ti-6Al-4V alloy at room temperature under LP-LC-ST conditions has shown that the absorption process occurs faster at short periods than at longer exposure times. The presence of hydrogen in the as-received sample was detected (4.75 at. % on the surface region). This layer of hydrogen already acts as a barrier for the penetration of hydrogen at room temperature. The amount of hydrogen in Ti-6Al-4V alloy induced for 1 hour has increased the depth of penetration of the He$^+$ ions from 0.66 to 0.71 μm. Therefore, hydrogen increases the depth of He$^+$ ion's penetration in the alloy.

5.4.1.2 The effects of annealing temperatures and thermohydrogen treatment

**(i) Microstructure analysis**

The optical micrographs of annealed and high temperature hydrogenated samples of Ti-6Al-4V alloy are shown in Figure 5-18. The 550 ˚C annealing temperature used in the heat treatment of the alloy for 3 hours reduces the grain size of the α -phase to approximately 3 μm while growing the β-phase (Figure 5-18 (a)). The micrograph in Figure 5-18 (b) depicts the effects of both hydrogen and the annealing temperature on the microstructure of the alloy. It can be observed that the introduction of hydrogen into the alloy at 550 ˚C temperature facilitates the formation of hydrides. Grain distortions occurred during the hydride formation and cause re-distribution of α- and β- phases.
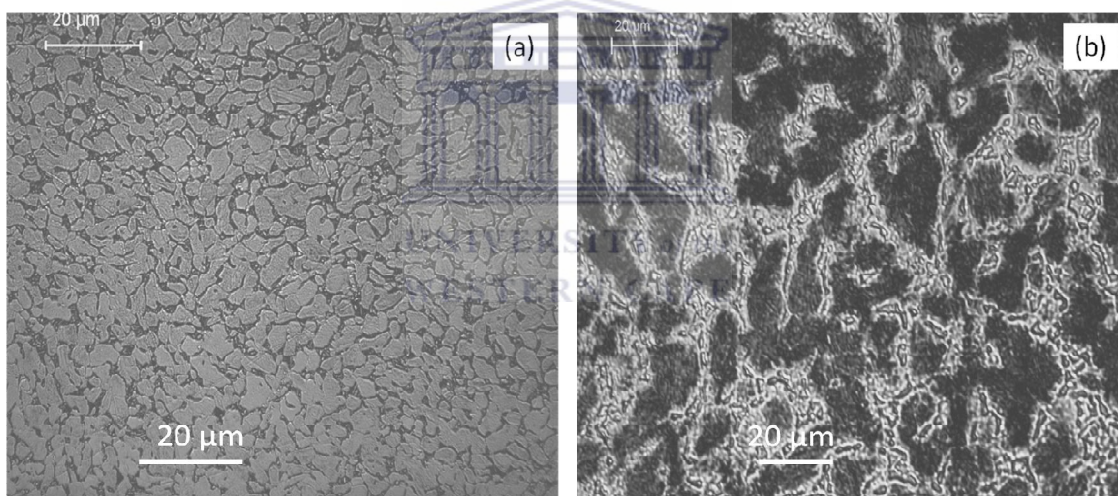
Figure 5-18: Micrographs of Ti-6Al-4V samples, (a) annealed at 550 ˚C and (b) hydrogenated at 550 ˚C for 3 hours.

Micrographs in Figure 5-19 show the effect of annealing temperatures and thermohydrogen process on the alloy when the temperature is 650 ˚C. Figure 5-19 (a) show the distortion of the α-grains during annealing at 650 ˚C. Hydrogenation of the alloy at the same temperature forms islands of ß-phase within the matrix of the α-phase (b).
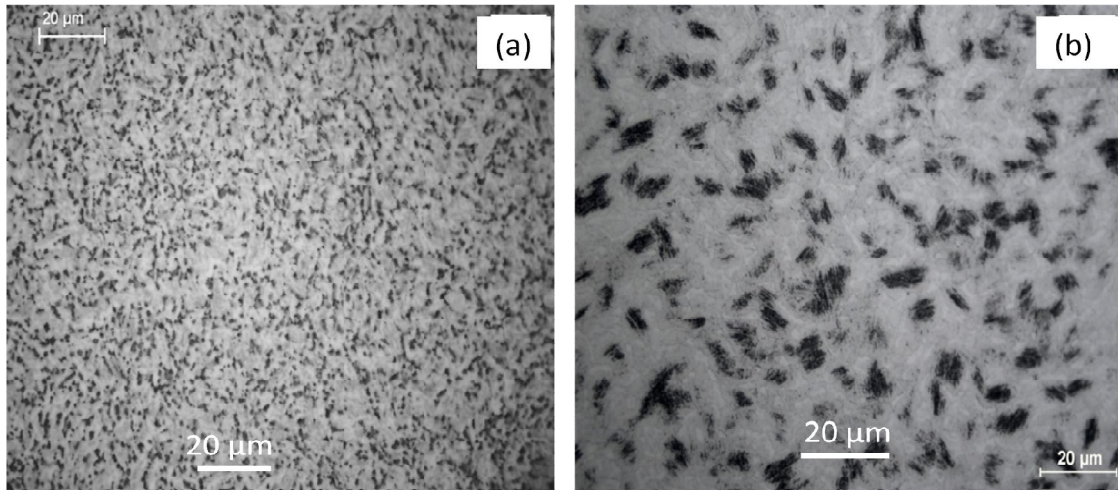
Figure 5-19: Microstructure of Ti-6Al-4V samples (a) annealed at 650 ˚C and (b) hydrogenated at 650 ˚C for 3 hours.

Elongated α- grains of approximately 4 µm can be observed in Figure 5-20 (a) after a heat treatment was performed on Ti-6Al-4V alloy at 750 ˚C. The volume fraction of the ß- phase has been reduced by annealing (ß→α, nucleation of α-phase). The hydrogenation process occurring at 750 ˚C temperatures formed hydrides and martensite phase, Figure 5-20 (b).
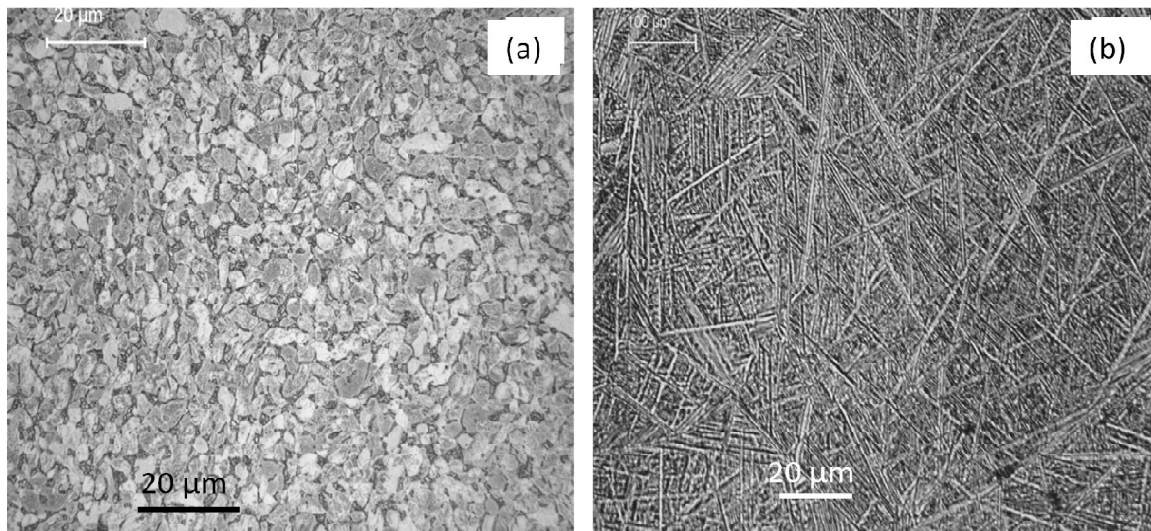
Figure 5-20: Annealed (a) and hydrogenated (b) micrographs of Ti-6Al-4V alloy conducted at 750 ˚C.

The α- grains shown in Figure 5-21 (g) are approximately 6 μm when annealing is conducted at 850 ˚C. Nevertheless, hydrogenation of the alloy at this temperature forms hydrides and needles of different sizes, Figure 5-21 (h).
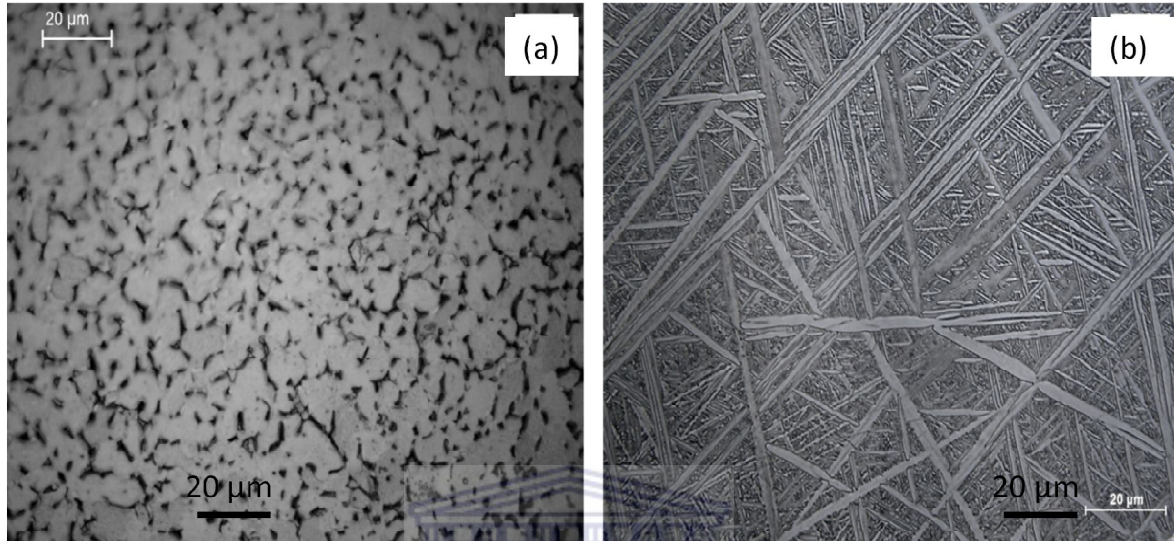
Figure 5-21: Microstructure images of (a) annealed and (b) hydrogenated Ti-6Al-4V samples at 850 ˚C for 3 hours.

According to the study of Qazi et al.[5.26] and Lu et al.[5.27], the formation of martensite is related to the reduction of critical cooling rate for martensite transformation in Ti-6Al-4V due to hydrogen addition. The morphology of the α structure is dependent on its formation temperature, alloying composition and hydrogen content [5.10]. Since the alloying composition was the same in this study and thus the hydrogenation temperature was important in determining the martensite structure. An increase in the hydrogenation temperature lowered the martensite start temperature of the Ti6Al4V alloy in which the cooling rate increased with increasing hydrogenation temperature and, in turn, fine martensite needles are formed.

(ii)   Phase transition

The diffraction patterns shown in Figures 5-22 and 5-23 show the effects of thermohydrogenation process in Ti-6Al-4V alloy. Hydrogenation of the alloy at different temperatures resulted in the formation of hydrides which were detected by XRD. However, the intensity of the peaks diffracted by the sample hydrogenated at 550 ˚C cannot be resolved in comparison with that of other patterns when stacked together and therefore, its XRD pattern is presented at a single graph, Figure 2-22.
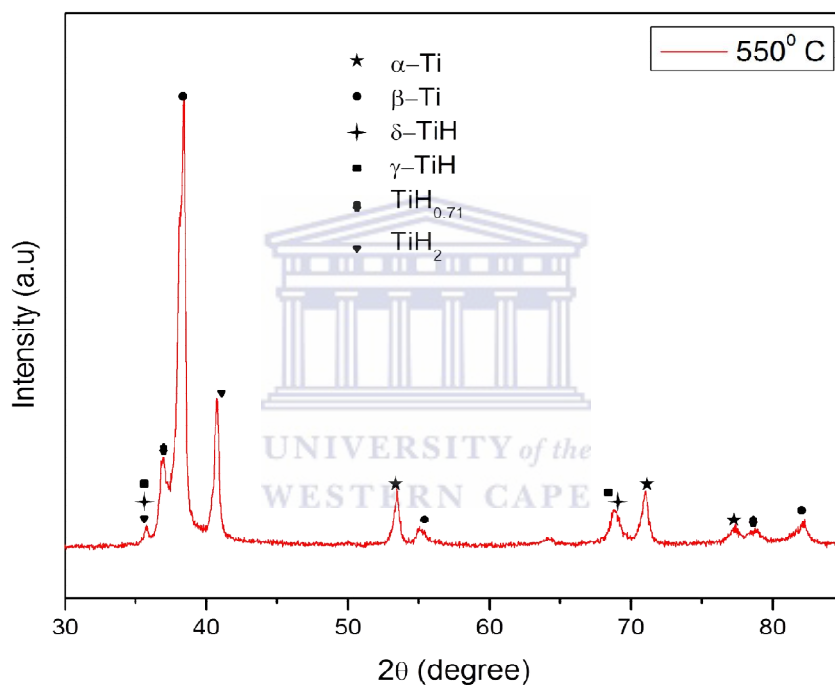
Figure 5-22: XRD spectra of Ti-6Al-4V alloy as a function of hydrogenation temperature for 3 hours at 550 ˚C.

According to Cullity et al. [5.25], the redistribution of atoms in the sample due to thermal agitation during the hydrogenation process affects the Bragg law which in turn decreases the intensity of the diffracted beam. In addition, a sample with large absorption coefficient diffracts a beam of low intensity [5.25]. Hence, the pattern of the sample hydrogenated at 550 ˚C is plotted in Figure 5-22 to enable the identification of the diffracted peaks. The hydrides

formed in the 550 ˚C hydrogenated sample are body-centered tetragonal (bct) TiH_2, delta δ-TiH and orthorhombic $TiH_{0.71}$. From the patterns, it can be observed that the TiH_2 hydride grows from the α-phase while the γ-TiH and δ-TiH grow from the ß-phase. Therefore, both the α-and ß- phases contribute to the formation of hydrides.
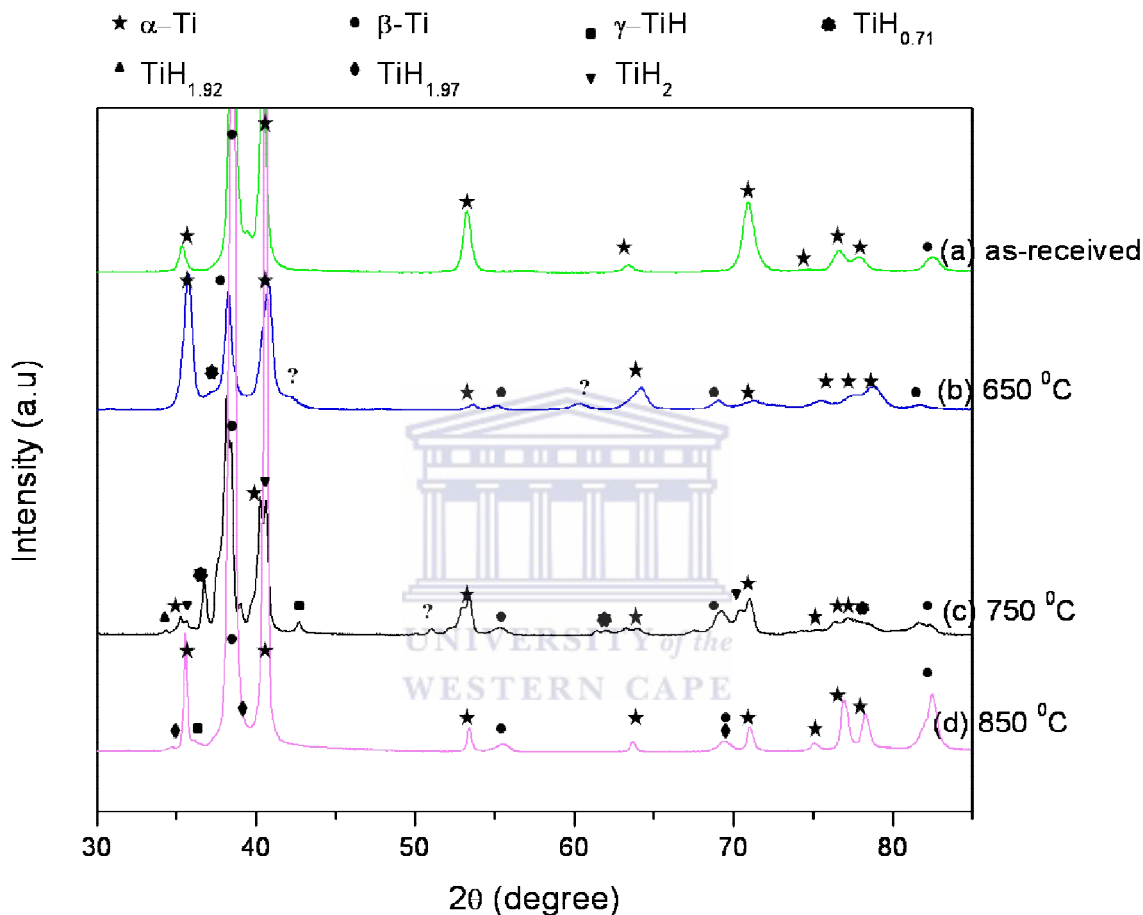
Figure 5-23: XRD spectra showing the phase transition of the Ti-6Al-4V alloy as a function of hydrogenation temperature for 3 hours.

The α- and ß- phase peaks in Figure 5-23 also lose their intensity at 650 ˚C. In other words, the redistribution of the Ti atoms due to the temperature and the hydrogen content is decreasing their periodicity which hinders Bragg's law. However, a $TiH_{0.71}$ hydride was identified while several unidentified peaks were detected. The TiH_2 hydride is still present

when the hydrogenation temperature is increased to 750 ˚C together with face-centred cubic $TiH_{1.92}$, orthorhombic $TiH_{0.71}$ and tetragonal γ-TiH hydrides. The ß-phase, γ-TiH and TiH_2 hydrides were grown from the α-phase which diffracted at lower 2θ angles. Further increase of the hydrogenation temperature to 850 ˚C yields a $TiH_{1.97}$ hydride which might be growing from the $TiH_{1.92}$ hydride. In general, the $TiH_{1.92}$, $TiH_{1.97}$ and TiH_2 are called δ- TiH hydride.

In summary, it was observed that 550 ˚C and 650 ˚C hydrogenation temperatures reduces the periodicity of the α- and ß- titanium atoms present in the Ti-6Al-4V alloy. Several hydrides were identified in these samples using powder diffraction file (PDF) search. Hydrogenation at 750 ˚C and 850 ˚C increases the intensity of α- and ß-Ti peaks indicating that Bragg's law is enhanced. In other words, the peaks of α- and ß-phase are strengthened, which means that the elevated temperatures improve the periodicity of both the α- and ß-Ti atoms. The lattice parameters of the hydrides detected in hydrogenated Ti-6Al-4V samples is given in Table 5-7:
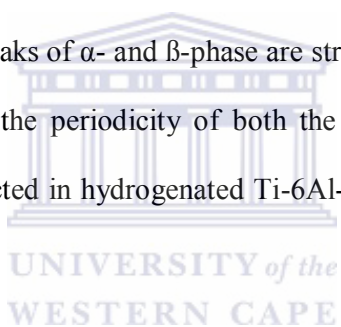
Table 5-7: Summary of the hydrides present in hydrogenated samples of Ti-6Al-4V alloy.

Hydride	Crystal structure	Lattice parameters (Å)
TiH_2	Body-centered tetragonal	a = b = 3.12 c = 4.18
γ-TiH	Tetragonal	$a = b = 4.21$ $c = 4.59$
$TiH_{0.71}$	Orthorhombic	$a = 4.34$ $b = 4.18$ $c = 4.02$
$TiH_{1.92}$	Face-centered cubic	a = b = c = 4.448
δ-TiH:	Base centered orthorhombic	a = 4.18 b = 4.22 c = 4.59

(iii) Gravimetric measurements

The change in mass of Ti-6Al-4V samples annealed and hydrogenated at temperatures ranging from 550 ˚C and 850 ˚C for 3 hours was measured using digital balance. There was no significant change in mass of samples annealed at 550 ˚C, 650 ˚C, 750 ˚C and 850 ˚C. This suggests that the annealing experiments performed on these temperatures and annealing time of 3 hours have no significant effect on the Ti-6Al-4V alloy oxidation. The difference in mass of Ti-6Al-4V alloy as a result of the introduction of hydrogen at high temperatures is given in Table 5-8. The change in mass corresponds to the concentration of hydrogen in the hydrogenated samples. The hydrogen content introduced at 550 ˚C for 3 hours increased the mass of the Ti-6Al-4V sample by 0.04 g. The difference in mass is equivalent to 1.9 wt. % of hydrogen concentration. When the hydrogenation temperature is increased to 650 ˚C, the mass of the sample increases by 0.16 g which is equivalent to a hydrogen concentration of 7.65 wt. %.
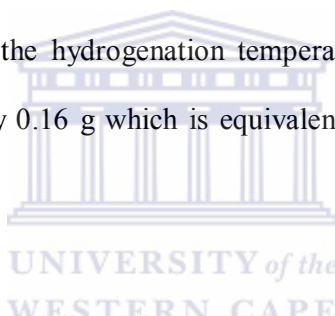
Table 5-8: The effects of both hydrogen and temperature on Ti-6Al-4V samples in 3 hours.

Hydrogenation temperatures (˚C)	Mass before hydrogenation (g)	Mass after hydrogenation (g)	Mass difference (g)	Hydrogen concentration (wt. %)	Hydrogen concentration (at. %)
550	2.09	2.13	0.04	1.90	46.75
650	1.97	2.14	0.16	7.65	78.56
750	2.12	2.13	0.01	0.50	17.84
850	2.05	2.06	0.01	0.53	18.55

A further increase of hydrogenation temperature to 750 ˚C increases the sample's mass by 0.01 g which is equal to 0.5 wt. % of hydrogen concentration. The mass change of Ti-6Al-4V sample hydrogenated at 850 ˚C is 0.01 g and is equivalent to 0.53 wt. % of hydrogen.

In summary, the gravimetric measurements show that more absorption of hydrogen has taken place at 650 ˚C where a maximum hydrogen concentration of 7.65 wt. % was achieved. This suggests that the solubility of the alloy to hydrogen has been enhanced at 650 ˚C temperature. Therefore, hydrogen and temperature enhances the diffusion of hydrogen into the bulk material of Ti-6Al-4V alloy.

(iv)   ERD analysis

The ERDA spectra shown in Figure 5-24 illustrate the distribution of hydrogen in samples of Ti-6Al-4V alloy before and after hydrogenation at 550 ˚C, 650 ˚C, 750 ˚C and 850 ˚C for 3 hours. The depth profile of the hydrogen in the samples is depicted in Figure 5-25 and the concentrations are given in Table 5-9. From the spectra, it can be observed that the ion beam has recoiled hydrogen on the surface region and in the bulk material of the as-received and hydrogenated samples. It can be observed on the depth profile of as-received Ti-6Al-4V sample that 4.75 at. % of hydrogen occupies a depth of 0.03 μm on the surface region whereas 0.47 at. % was detected in the bulk material. The overall depth of penetration of the ions was found to be 0.66 μm. The counts of hydrogen recoiled from the sample hydrogenated at 650 ˚C is greater than from the other samples hydrogenated at 550, 750 and 850 ˚C. The area under the peak has increased significantly at 650 ˚C which indicate that the absorption of hydrogen by the alloy has reached its maximum capacity at this temperature as compared to the other temperatures under the same pressure and time conditions.
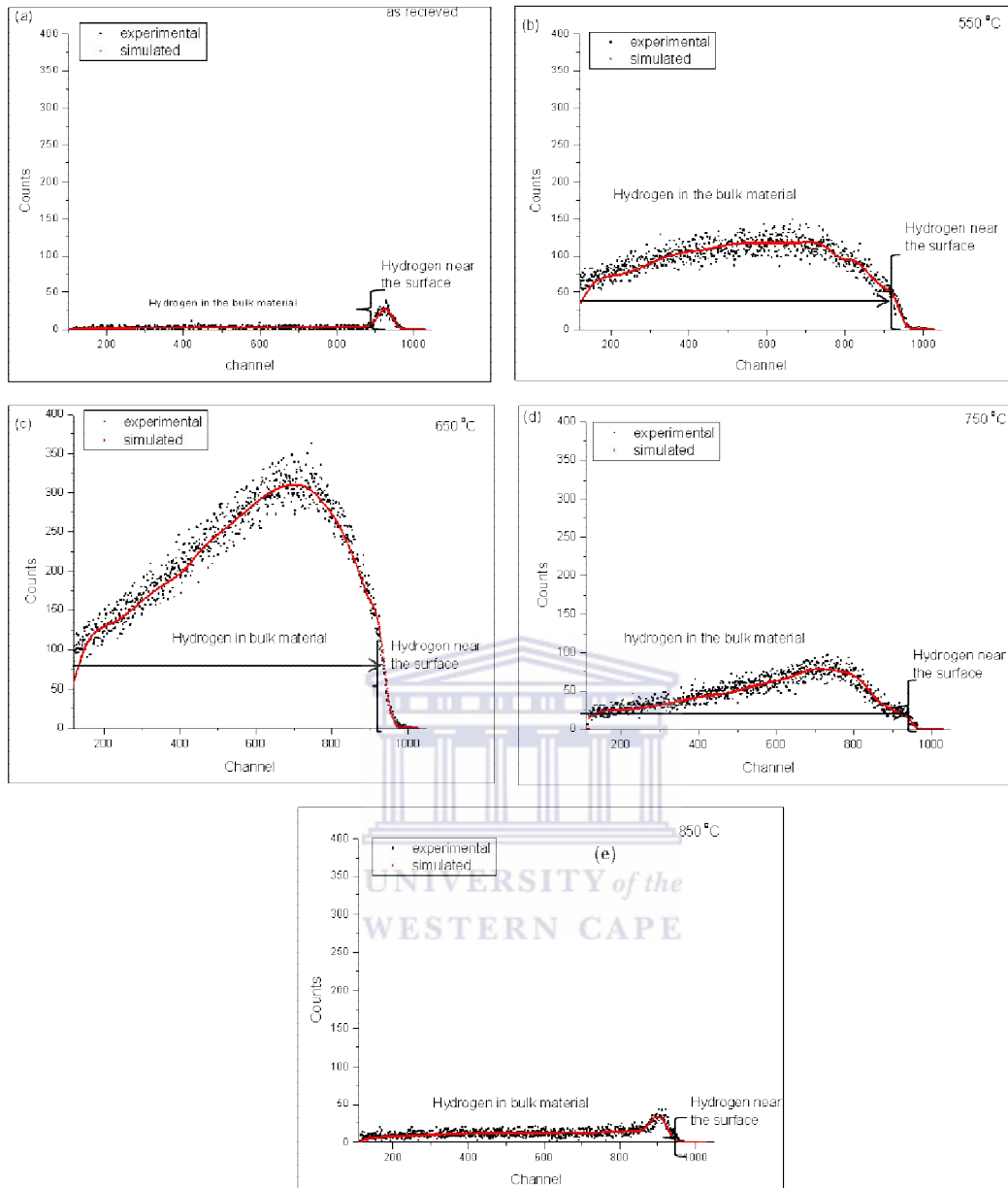
Figure 5-24: The spectra of Ti-6Al-4V samples as-received, hydrogenated at 550 ˚C, 650 ˚C, 750 ˚C and 850 ˚C for 3 hours.

Hydrogen concentration of 15.8 at. % was detected on the surface region of the sample hydrogenated at 650˚C and an average of 28.78 at. % was found in the bulk material. The depth of penetration of hydrogen on the surface region (0.03 μm) does not change during the hydrogenation at 550 ˚C and 650 ˚C. However, the He^+ ions' depth of penetration was

increased from 0.66 µm to 0.88 µm in the sample hydrogenated at 650 ˚C and therefore, the hydrogen content has improved the penetration of He$^+$ ions in the Ti-6Al-4V alloy. Using the hydrogenation temperatures above the 650 ˚C, it was found that the amount of counts recoiled from the surface region decreases with an increase in temperature, 850 ˚C as maximum.
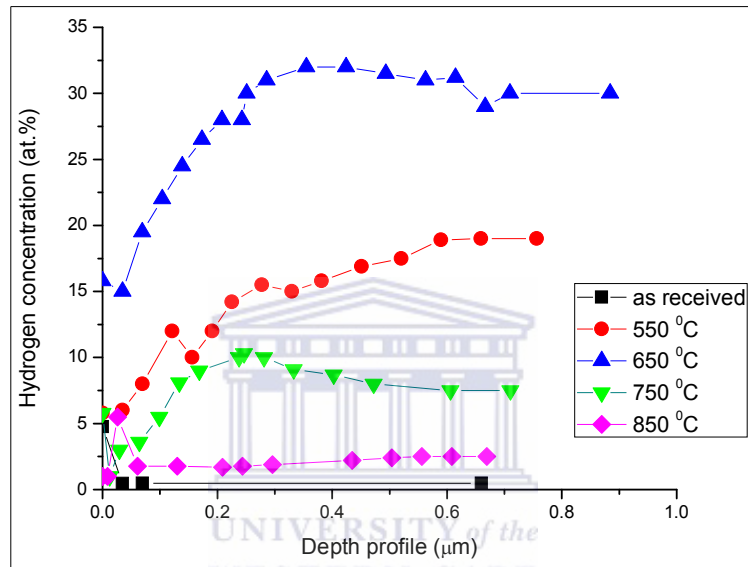
Figure 5-25: The depth profiles of hydrogen in Ti-6Al-4V alloy samples before and after hydrogenation at high temperatures.

The hydrogen atoms on the surface region occupied a depth of 0.01 µm after the hydrogenation process at these temperatures, 750 ˚C and 850 ˚C. Therefore, the absorption rate of hydrogen in Ti-6Al-4V alloy is high at 650 ˚C and low at 550, 750 and 850 ˚C temperatures. However, the penetration depth of the ions has increased to 0.71 and 0.67 µm into the samples hydrogenated at 750 ˚C and 850 ˚C respectively.

Table 5-9: The average concentration and depth of penetration of hydrogen in Ti-6Al-4V alloy.

Ti-6Al-4V alloy	Average concentration of hydrogen on the surface		Average hydrogen concentration in bulk material	
	(at. %)	(wt. %)	(at. %)	(wt. %)
as received	4.75	0.11	0.47	0.01
550 ˚C	5.80	0.14	14.85	0.39
650 ˚C	15.80	0.42	28.78	0.90
750 ˚C	5.80	0.14	7.73	0.18
850 ˚C	1.00	0.02	2.18	0.05

In brief, the sample of Ti-6Al-4V alloy which was hydrogenated at 650 ˚C under LP-LC-ST conditions has absorbed the most hydrogen on its surface and into the bulk material as compared to the samples hydrogenated at 550 ˚C, 750 ˚C and 850 ˚C temperatures. An average hydrogen concentration of 28.78 at. % was detected in the bulk material. It was also established that the penetration of He$^+$ ions into Ti-6Al-4V alloy is hydrogen content dependent with 0.88 µm maximum depth of penetration in the sample hydrogenated at 650 ˚C.

(v) Micro-hardness testing

The micro-hardness of Ti-6Al-4V samples with different hydrogen contents is shown in Figure 5-26. The graph illustrates the change in hardness of Ti-6Al-4V alloy when it is annealed at different temperatures and when it is hydrogenated at both room and high temperatures. It is observed that the hardness value of the alloy increases from 285 HV to 381 HV when it is heat treated at 550 ˚C. The change in hardness of the alloy decreases with an increase in annealing temperature to 348, 328 and 323 at 650, 750 and 850 ˚C as a result of the grain growth in the microstructure. Hydrogenation at room temperature for 1 hour

increases the hardness to 349 HV. A further absorption of hydrogen decreases the hardness of the alloy. The degree at which the hardness is affected is low at 3 hours of hydrogenation relative to 1 hour and 7 hours.
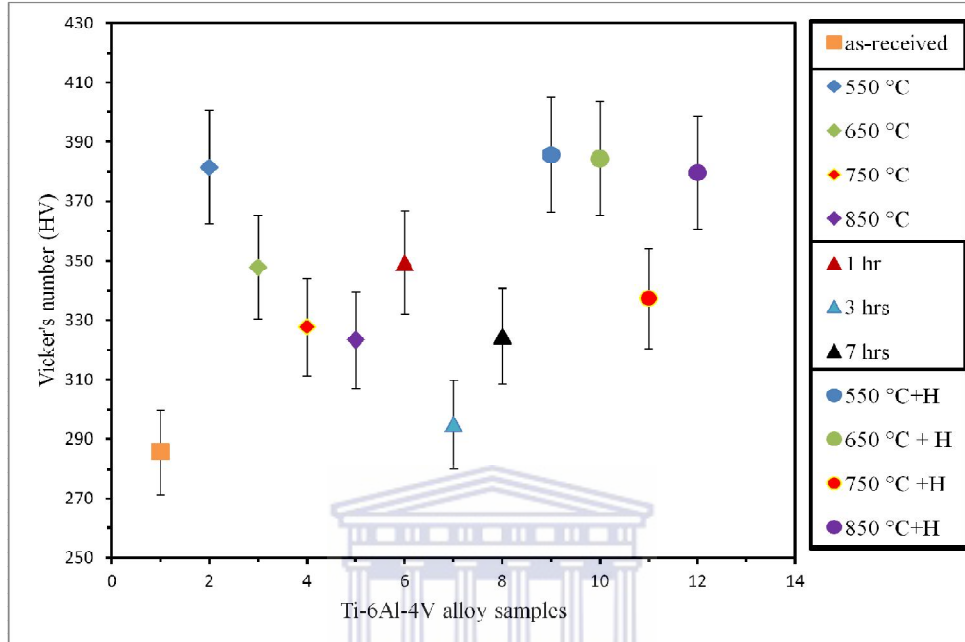
Figure 5-26: Hardness of Ti-6Al-4V alloy at different annealing temperatures and hydrogenation conditions.

The hardness of the alloy also increases when hydrogenation is conducted at high temperatures. The hardness values increase with the increase of hydrogen content in the samples as reported by *Zhao et al* [5.28]. Since the ß-phase absorbs more hydrogen than the α-phase in Ti-6Al-4V alloy, therefore hydrogenation increases the hardness for both α- and ß-phases but the increment is less in alpha than in beta phase. The influence mechanisms of hydrogenation on the microhardness of Ti6Al4V alloy is shown in Figure 5-27. According to the decohesion theory, the addition of hydrogen in titanium can weaken the binding force between titanium atoms because of its H^+ existence form in metals. The ion further enhances

the repulsive force of metal ion and weakens. This may result in the reduction of activation energy for Ti self-diffusion [5.23,5.29].
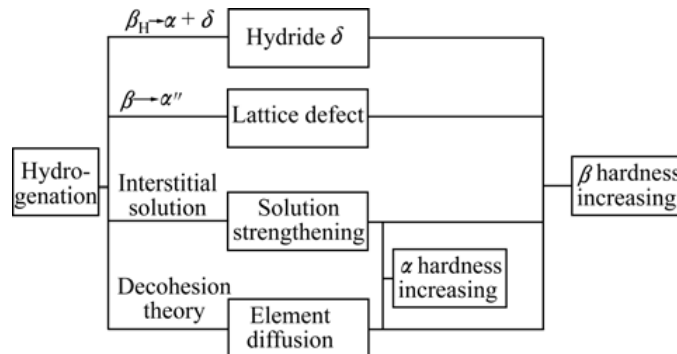
Figure 5-27: Influence mechanisms of hydrogenation on micro-hardness of Ti6Al4V alloy [5.28].

5.4.2 Discussions

The amount of hydrogen that can be absorbed by titanium was found to be pressure and temperature sensitive because according to *San-Martin et al.* [5.30], the amount decreases considerably when the hydrogen's partial pressure decreases with an increase in temperature. This, in combination with the high diffusivity of hydrogen in titanium, allows hydrogen to be almost completely removed (to a level less than 20 ppm) by vacuum annealing at 700 ˚C - 800 ˚C [5.31]. The absorption rate of hydrogen in Ti-6Al-4V alloy was found to be different to that of CP-Ti when the process is conducted in similar temperatures, pressure and time conditions. *Zhao et al.* [5.28] has studied the effects of hydrogenation on the Al and V alloying elements of Ti-6Al-4V alloy and revealed that hydrogen facilitates the increase of V concentration in the α-phase. *Hou et al.* [5.32] has also reported that the diffusion coefficient of Al is lower than that of V. It is known that V stabilises β- phase to lower temperatures hence, the solubility of the alloy to hydrogen is higher than that of CP-Ti.

Hydrogen was detected in all the samples including the as-received alloy by ERDA with the maximum found in the sample hydrogenated at room temperature for 1 hour. These findings show that the solubility of hydrogen in the alloy decreases with time (e.g. 3 and 7 hours). This is true considering the fact that at room temperature, the hydrogen is mostly absorbed in the α-phase of the Ti-6Al-4V alloy because the β-phase is soluble to hydrogen at elevated temperatures above 300 ˚C [5.30]. As a result of the hydrogen content, a hardening occurred. It was found that the hardness has increased more in the sample hydrogenated for 1 hour with more hydrogen content. This implies that the hardening of the Ti-6Al-4V alloy is hydrogen content dependent when the hydrogenation process is conducted at room temperature. The equiaxed (α+ß) dual phase structure was distorted due to the formation of elongated α-grains. The solid solution of hydrogen in α-phase causes distortion of the lattice which is the driving force of hydride formation. The distortion is a result of the excess hydrogen content which the α-lattice can no longer accommodate by maintaining its hcp structure [5.10]. However, the presence of hydrogen was not detected by XRD. This might imply that there were no hydrides formed yet or the hydride phases formed were below the detection limit since the diffractometer can only detect a phase with at least 0.2 wt. % of the sample [5.25]. Nevertheless, the Ti-6Al-4V alloy has the ability to store hydrogen at room temperature.

The study of the effects of annealing temperatures on the weight of the Ti-6Al-4V alloy conducted at 550 ˚C, 650 ˚C, 750 ˚C and 850 ˚C for 3 hours revealed that the weight difference is similar at all temperatures. It suggests that oxidation of Ti-6Al-4V alloy is not affected by annealing temperatures used in this study significantly.

The process of thermohydrogenation conducted in this study changed the microstructure of the Ti-6Al-4V alloy. The effect of thermohydrogen processing (THP) on the microstructure

and kinetics of the phase transformations in Ti-6Al-4V alloy was observed. Heating the system during hydrogenation affects the periodicity of the alloy by generating vacancies which will be occupied by hydrogen atoms [5.1]. The change of the microstructures show that temperature as the controlling factor in this case, is able to change the chemical potential in the alloy. Because the rate of absorption of hydrogen in the alloy changes with temperature and therefore, microstructure refinement depends on the hydrogen concentration and the corresponding phases formed [5.7,5.33]. Low nucleation and high growth rates of hydrides induced coarse microstructure with martensitic structure due to the presence of the alloying elements in Ti-6Al-4V alloy which stabilises the α-phase to higher temperatures i.e. aluminium, and the β-phase to lower temperatures e.g. vanadium [5.24]. According to the phase diagram of Ti-6Al-4V alloy, the β-transus temperature (T_β) can decrease from 1000 ˚C to 810 ˚C when the amount of hydrogen ranges from 0 - 30 at. % [5.10]. The presence of martensite in the microstructure was observed just above 650 ˚C hydrogenation temperatures. In comparison with the microstructure of this alloy annealed at the same temperature, hydrogen was able to decrease the martensite start temperature. This implies that cooling rate of the alloy increased with hydrogen content absorbed at these temperatures whereby fine needles were formed. Shan et al. [5.10] suggested that the formation of martensite indicate that the sample is conducted in a single phase β-region or above the β-transus temperature. Therefore, it can be concluded that the microstructure is dependent on its formation temperature and the hydrogen content. This is consistent with the investigation by *Shan et al* [5.10].

A summary of the hydrides detected in the hydrogenated samples is given in Table 5-7. The hydrides determined in this study appear to form at slightly different temperature range in comparison to the phase diagram in Figure 2-12 [5.26]. The mechanism of δ-hydride

formation in α-phase and β-phase is different at high temperatures and occurs as follows: $\rightarrow \alpha_H \rightarrow \alpha_H + \beta_H \rightarrow \beta_H \rightarrow \beta_H + \delta,$ and $\beta = \beta_H \rightarrow \beta_H + \delta$ which occurs only when the hydrogen content is above 0.5 wt. % [5.9]. An additional γ-TiH hydride was formed at 550 ˚C, 750 ˚C and 850 ˚C in which less hydrogen was absorbed as compared to the amount obtained at 650 ˚C. Therefore, this hydride is only stable at low hydrogen concentration absorbed at elevated temperatures. According to the phase diagram of Ti-6Al-4V-H, the α-phase is still present in the samples after the hydrogenation process is performed under these temperatures [5.26]. Contrary to the heat treatment process, thermo-hydrogenation process increases significantly the mass of samples particularly at 650 ˚C indicating that more hydrogen has been absorbed (results obtained by gravimetric method, 7.65wt. %). The less absorption occurrence of hydrogen at temperatures above 650 ˚C by Ti-6Al-4V alloy is due to the fact that the oxygen activity in the chamber increases with temperature causing the minor contamination of the hydrogen-argon mixture to facilitate significant oxygen absorption into the near surface of the samples and consequently retard the uptake of hydrogen [5.34]. Although the concentration values determined by ERDA technique are not directly comparable with those obtained from gravimetric measurements, there is a similar absorption trend. While ERDA showed the depth of hydrogen penetration on the surface region and in the bulk material, gravimetry measure the overall concentration of the absorbed hydrogen. Microstructure refinement has occurred due to the hydrogen-induced phase transformations. A significant increase in micro-hardness of Ti-6Al-4V alloy was detected at 550 ˚C and 650 ˚C temperatures due to the formation of hydrides. In fact, the solution of hydrogen in the β-phase is quite high as it was confirmed by *Sun et al.* [5.7,5.10] that a concentration of up to 50 at. % can be acquired at 600 ˚C which enhances the β-phase' plasticity. Hydrogen atoms cause lattice distortions that hinder dislocation motion while increasing the yield stress of the material. The degree of the strengthening effect decreases as

the martensite forms [5.7]. The presence of the martensite at higher temperatures (750 ˚C and 850 ˚C) leads to insignificant changes in comparison to that of the samples hydrogenated at 550 ˚C and 650 ˚C. The findings in this study are in agreement with the investigation conducted by *Sun et al* [5.7].

Furthermore, the investigation revealed that β- phase start softening when 0.5 wt. % of hydrogen is absorbed in the alloy [5.32]. The He^+ ions' depth of penetration was larger in the sample with higher hydrogen content implying that the volume fraction of the plastic β- phase has increased which correlates with the micro-hardness values of the alloy as shown in Figure 5-26. The growth of the β- phase indicate that a beta-transus temperature has been lowered to 650 ˚C temperature when 78.56 at. % of hydrogen was absorbed in the Ti-6Al-4V alloy [5.30].
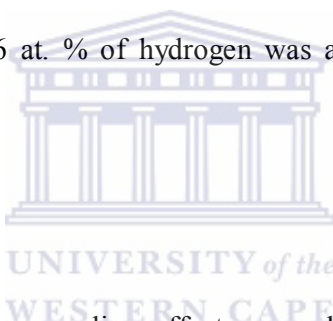
5.4.3 Conclusion

This study has investigated the annealing effects as well as the absorption capacity of hydrogen in Ti-6Al-4V alloy at room temperature and high temperatures under low pressure-low concentration-short charging time (LP-LC-ST) conditions. It is reasonable to assume that diffusivity will be influenced by temperature and time in that greater hydrogen absorption will occur at higher hydrogenation temperatures and shorter reaction intervals at room temperature. However, this is not the case. At room temperature, greater absorption occurred at short intervals whereas thermohydrogenation process was enhanced at 650 ˚C temperatures. Grain refinement, which increased the micro-hardness of the material, has occurred when annealing was performed on the alloy. The increase of the micro-hardness is high at 550 ˚C and 650 ˚C (approximately 380 HV) and decreases with an increase in temperature to 750 ˚C (337 HV). However, hardness value of 380 HV was measured after

hydrogenation at 850 ˚C. The study conducted at room temperature has revealed that hydrogen was absorbed in the material within 1 hour which subsequently distorted the grain boundaries of the α- phase. The micro-hardness of the alloy has increased as a result of the hydrogen but, the degree of increment is lower than when it is only annealed at elevated temperatures. Furthermore, when the alloy is exposed to hydrogen at short times, it absorbed the hydrogen more than when it is exposed for a long time because the solubility of hydrogen in the α-phase decreases with hydrogen content. Even though it was observed that absorption of hydrogen has occurred, there were no hydrides detected. It is probable due to the fact that the volume fraction of hydride phase present in the Ti-6Al-4V-H was low and below detection by XRD. Hydrides were detected in samples hydrogenated at elevated temperatures (550 - 850 ˚C). The different hydrides formed are: δ-TiH at 550 ˚C, γ-TiH at 550 ˚C, 750 ˚C and 850 ˚C, $TiH_{0.71}$ at 550 ˚C, 650 ˚C and 750 ˚C, $TiH_{1.92}$ at 750 ˚C, $TiH_{1.97}$ at 850 ˚C. The martensite formation temperature for Ti-6Al-4V alloy was lowered to just above 650 ˚C and needle-like structure was observed in the microstructure. In conclusion, the grain refinement and hardness increase of the Ti-6Al-4V alloy is a result of mutual effect of annealing temperature and hydrogen content.

5.5   References

[5.1] Q. Xu and A. Van der Ven, *Phys. Rev. B,* **76**, 064207 (2007).

[5.2] C.P. Liang and H.R. Gong, *Int. J. Hydrogen En.,* **35**, 3812-3816 (2010).

[5.3] F. Froes, *Int. J. Hydrogen En.,* **24**, 565-576 (1999).

[5.4] B. YUAN, C. LI, H. YU, and D. SUN, *Trans. Nonferrous Met. Soc.China,* **19**, s423-s428 (2009).

[5.5] J. Zhao, H. Ding, Y. Zhong, and C.S. Lee, *Int. J. Hydrogen En.,* **35**, 6448-6454 (2010).

[5.6] Y. Su, L. Wang, L. Luo, X. Jiang, J. Guo, and H. Fu, *Int. J. Hydrogen En.,* **34**, 8958-8963 (2009).

[5.7] Z. Sun, W. Zhou, and H. Hou, *Int. J. Hydrogen En.,* **34**, 1971-1976 (2009).

[5.8] H. Liu, J. Cao, P. He, and J.C. Feng, *Int. J. Hydrogen En.,* **34**, 1108-1113 (2009).

[5.9] H.J. Liu, L. Zhou, P. Liu, and Q.W. Liu, *Int. J. Hydrogen En.,* **34**, 9596-9602 (2009).

[5.10] D.B. Shan, Y.Y. Zong, T.F. Lu, and Y. Lv, *J. Alloys Compounds,* **427**, 229-234 (2007).

[5.11] H. Numakura and M. Koiwa, *Acta Metall.,* **32**, 1799-1807 (1984).

[5.12] W. Gao, W. Li, J. Zhou, and P.D. Hodgson, *J. Alloys Compounds,* **509**, 2523-2529 (2011).

[5.13] J. Zhao, H. Ding, Y. Zhong, and C.S. Lee, *Int. J. Hydrogen En.,* **35**, 6448-6454 (2010).

[5.14] Y.L. Kao, G.C. Tu, C.A. Huang, and T.T. Liu, *Mater. Sc. Eng.: A,* **398**, 93-98 (2005).

[5.15] K. Geels, *Metallographic and Materialographic Specimen Preparation, Light Microscopy, Image Analysis, and Hardness Testing,* ASTM International (2007).

[5.16] C.P. Liang and H.R. Gong, *Int. J. Hydrogen En.,* **35**, 11378-11386 (2010).

[5.17] N. Bozzolo, N. Dewobroto, T. Grosdidier, and F. Wagner, *Mater. Sc. Eng.: A,* **397**, 346-355 (2005).

[5.18] D. Setoyama, J. Matsunaga, H. Muta, M. Uno, and S. Yamanaka, *J. Alloys Compounds,* **385**, 156-159 (2004).

[5.19] R.J. Elias, H.L. Corso, and J.L. Gervasoni, *Int. J. Hydrogen En.,* **27**, 91-97 (2002).

[5.20] O.A. Kaibyshev, *J. Mater. Process. Technol.,* **117**, 300-306 (2001).

[5.21] D. Shih and H. Birnbaum, *Scripta metall.,* **20**, 1261-1264 (1986).

[5.22] H. Numakura, M. Koiwa, H. Asano, H. Murata, and F. Izumi, *Scr.Metall.,* **20**, 213-216 (1986).

[5.23] X.L. Han, Q. Wang, D.L. Sun, and H.X. Zhang, *Scr. Mater.,* **56**, 77-80 (2007).

[5.24] T. Wu and J. Wu, *Mater. Chem. Phys.,* **74**, 5-12 (2002).

[5.25] B.D. Cullity and S.R. Stock, *Elements of X-ray Diffraction,* Prentice Hall Upper Saddle River, NJ (2001).

[5.26] J. Qazi, J. Rahim, F. Fores, O. Senkov, and A. Genc, *Metall. Mater. Trans., A,* **32**, 2453-2463 (2001).

[5.27] J. Lu, J. Qin, W. Lu, Y. Chen, D. Zhang, and H. Hou, *Int. J. Hydrogen En.,* **34**, 9266-9273 (2009).

[5.28] J.W. Zhao, H. Ding, W.J. Zhao, X.F. Tian, H.L. Hou, and Y.Q. Wang, *Trans. Nonferrous Met. Soc. China,* **18**, 506-511 (2008).

[5.29] A.R. Troiano, *Trans. ASM,* **52**, 54-80 (1960).

[5.30] A. San-Martin and F. Manchester, *J. Phase Equilib.,* **8**, 30-42 (1987).

[5.31] J.I. Qazi, O.N. Senkov, J. Rahim, and F.H. Froes, *Mater. Sc. Eng., A,* **359**, 137-149 (2003).

[5.32] J. Lu, J. Qin, W. Lu, D. Zhang, H. Hou, and Z. Li, *Mater. Sc. Eng: A,* **500**, 1-7 (2009).

[5.33] H. Fujii, *Mater. Sc. Eng., A,* **243**, 103-108 (1998).

[5.34] L. Matthews and R. Knutsen, *J. S. Afr. Inst. Min. Metall.,* **111**, 155 (2011).

Chapter 6: .   Summary

The aim of this research was to study the effect of hydrogenation on two metal systems in order to compare their hydrogen storage capacity, and to investigate the changes in microstructure and mechanical properties caused by hydrogen absorption.

Two systems are investigated: (i) Pd-based and (ii) Ti-based system. Considering the Pd-based system, the research was performed on pure Pd, Pd-Pt alloys having different Pt content (2 at.%, 6 at.%, 10 at.% and 12 at.%) and Pd-Pt coated system where Pt layer was deposited on Pd substrate. A comparative study was conducted on commercially pure Ti (CP-Ti) and Ti-6Al-4V alloy.

The hydrogenation process was carried out under different conditions: (i) low pressure-low hydrogen gas concentration-short hydrogenation time (LP-LC-ST) and (ii) high pressure-high hydrogen gas concentration-long hydrogenation time (HP-HC-LT) conditions. Besides different time of exposure to hydrogen atmosphere, these processes differ in terms of hydrogen concentration present in gas environment (gas mixture with 15% hydrogen in LP-LC-ST, and pure hydrogen gas in HP-HC-LT conditions) and system pressure. The hydrogenation was performed under atmospheric pressure at LP-LC-ST conditions while the HP-HC-LT experiments were conducted under maximum pressure of 2000 mbar. In addition, the hydrogenation at elevated temperature was considered in LP-LC-ST conditions.

The effects of hydrogen on Pd- and Ti-based systems were investigated by several complementary techniques. The elastic recoil detection analysis (ERDA) was used to determine the hydrogen content absorbed in the metal systems and to determine its depth profile. The other technique, (IGA-intelligent gravimetric analyser), gave information on

sorption/desorption rate and weight changes as a function of hydrogen content. The effect of hydrogen and/or temperature on microstructure and coating morphology was investigated by optical and scanning electron microscope while X-ray diffraction was carried out for phase analysis. Considering the effect of hydrogenation on mechanical properties, the microhardness was measured by Vickers method.

A summary of the results is given in Table 1.

Table 1: Summary on Pd- and Ti-based systems

Metal system	Temperature	H gas (%)	Pressure (mbar)	Time (hour)	ERDA			Gravimetry		Hardness (HV)
					Near-surf. (wt.%)	Bulk (wt.%)	Depth (μm)	H $_{Sorb.}$ (wt.%)	H $_{Stored}$ (wt.%)	
Pd	received	-	-	-	0.29	0.02	0.38	-	-	-
	RT	15	1013	1	0.24	0.03	0.38	-	-	-
	RT	99.99	0.47-2000	33	0.54	0.04	0.38	0.67	0.60	-
Pd-Pt coat.	deposited				0.08	0.01	0.37	-	-	-
	550 °C	15	1013	3	0.11	0.01	0.37	-	-	-
	650 °C	15	1013	3	0.59	0.03	0.38	-	-	-
Pd-2at.% Pt	RT	99.99	0.47-2000	33	0.14	0.02	0.37	0.66	0.58	-
Pd-6at.% Pt	RT	99.99	0.47-2000	33	0.52	0.08	0.4	0.56	0.46	-
Pd-10at.% Pt	RT	99.99	0.47-2000	33	0.55	0.05	0.4	0.43	0.28	-
Pd-12at.% Pt	RT	99.99	0.47-2000	33	0.14	0.02	0.38	0.31	0.13	-
CP-Ti	received	-	-	-	0.3	0.02	0.74	-	-	166
	RT	15	1013	1	0.44	0.05	0.67	-	-	154
	RT	15	1013	3	0.25	0.02	0.67	-	-	144
	RT	15	1013	7	0.18	0.03	0.67	-	-	156
	550 °C	15	1013	3	0.18	0.8	0.85	-	1.88	247
	650 °C	15	1013	3	0.85	0.49	0.81	-	1.35	261
	750 °C	15	1013	3	0.08	0.13	0.69	-	0.84	262
	850 °C	15	1013	3	0.15	0.06	0.67	-	0.43	290
Ti-6Al-4V	received	-	-	-	0.11	0.01	0.66	-	-	285
	RT	15	1013	1	1.44	0.1	0.71	-	-	349
	RT	15	1013	3	0.22	0.03	0.68	-	-	295
	RT	15	1013	7	0.37	0.03	0.68	-	-	325
	550 °C	15	1013	3	0.14	0.39	0.88	-	1.90	386
	650 °C	15	1013	3	0.42	0.9	0.88	-	7.65	384
	750 °C	15	1013	3	0.14	0.18	0.71	-	0.50	337
	850 °C	15	1013	3	0.02	0.05	0.67	-	0.53	380

*Note that IGA was used for gravimetric measurements of Pd-systems while the mass difference in Ti-systems was determined by digital balance

1. Palladium and Palladium-based systems

1.1 Pure Palladium

▪ After hydrogenation performed at room temperature under LP-LC-ST conditions, the ERDA results show that the hydrogen concentration is significantly higher on the surface region than in bulk material (0.24 wt.% and 0.03 wt.% respectively). However, the HP-HC-LT conditions promoted more hydrogen absorption to occur particularly on the surface region (0.54 wt.%). The results show the presence of 0.04 wt.% of hydrogen in bulk material. On the other hand, the IGA results show that 0.67 wt.% of hydrogen was absorbed during hydrogenation. The total of 0.60 wt.% of hydrogen was remained in pure Pd after pressure release.

▪ The phase analysis results show the presence of $PdH_{0.64}$ hydrides after hydrogenation at room temperature for 1, 2 and 7 hours under LP-LC-ST conditions. The formation of hydrides was not detected at high temperature hydrogenation (550 ˚C and 650 ˚C for duration of 3 hours).
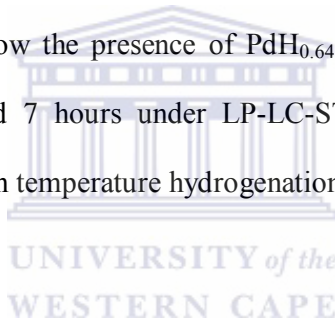
1.2 Pd-Pt coatings

▪ ERDA results of Pd-Pt coatings investigated in their deposited condition show 0.08 wt.% of hydrogen on the surface region and 0.01 wt.% in bulk material (deeper regions within coating layer). Hydrogenation at elevated temperatures show that significant increase in hydrogen concentration on the surface region occurs after annealing at 650 ˚C for 3 hours (0.59 wt.%).

▪ The $PdH_{0.71}$ hydrides were formed after hydrogenation at 550 ˚C and 650 ˚C for 3 hours.

▪ Scanning electron microscopy shows that the coating morphology changed as a consequence of high temperature hydrogenation performed at LP-LC-ST conditions.

Increased coating roughness and visible microstructural regions were created as a mutual effect of hydrogen and temperature.

1.3. Pd-based alloys

▪ The Pd-Pt alloys having different Pt content were investigated under HP-HC-LT conditions only due to restricted number of samples. The ERDA measurements gave "inconclusive" results since the measurements were performed after a long period of being hydrogenated. However, the IGA results show that the hydrogen capacity depends on Pt content; the higher Pt concentration, the smaller the hydrogen storage capacity. The highest hydrogen concentration of 0.66 wt. % was determined in the Pd-2 at. % Pt alloy. After pressure release, 0.54 wt.% of hydrogen was remained in alloy.

▪ The XRD results show formation of $PdH_{0.71}$ hydrides in Pd-10 at. % Pt alloy after 2 and 7 hours of treatment at room temperature under LP-LC-ST conditions.
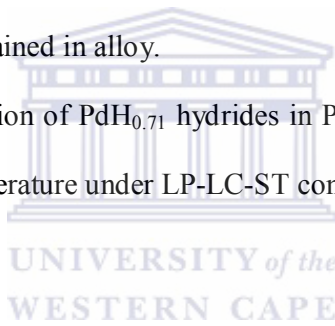
2. Ti and Ti-based systems

2.1 Commercially pure Titanium

▪ The content of hydrogen which remained in the sample hydrogenated for 1 hour at room temperature under LP-LC-ST conditions was higher than in samples hydrogenated for 3 and 7 hours with 0.44 wt. % on the surface region and 0.05 wt. % in the bulk material as determined by ERDA. The hydrogen concentration determined by ERDA (H concentration of 0.18 wt. % on the surface region and 0.8 wt % in bulk material) and digital balance (1.88 wt. %) showed that the sample hydrogenated at 550 ˚C has higher hydrogen content than the other samples hydrogenated at 650 ˚C, 750 ˚C and 850 ˚C.

▪ Optical microscopy of CP-Ti annealed at 550 ˚C, 650 ˚C, 750 ˚C and 850 ˚C temperatures for 3 hours show fully recrystalised α- grains with sizes increasing with temperature (30 µm

at 550 ˚C to 204 µm at 850 ˚C). The hydrogen content introduced at room temperature for different duration times under LP-LC-ST conditions caused recrystallisation of the α-grains to approximately 10 µm. The mutual effect of hydrogen and elevated temperatures on the microstructure of the CP-Ti conducted under LP-LC-ST conditions for durations of 3 hours formed hydrides. Martensitic structure formation occurred at temperatures above 550 ˚C.

▪ The phase analysis results indicate the presence of face centered cubic TiH_{2-x} hydrides in all samples hydrogenated at 550 ˚C, 650 ˚C, 750 ˚C and 850 ˚C and an additional tetragonal γ-TiH hydride was detected in the sample hydrogenated at 750 ˚C. Hydrides and β- phase were not detected in samples hydrogenated at room temperature for 1, 3 and 7 hours suggesting that either the presence of these phases is below the detection limit or that they are completely absent.

▪ The Vickers micro-hardness measurements show that due to elevated annealing temperatures (550 ˚C, 650 ˚C, 750 ˚C and 850 ˚C), hardness of CP-Ti decreases from HV = 166 in as-received to HV = 142 in the sample annealed at 850 ˚C for 3 hours. The presence of hydrogen in the CP-Ti system decreases the micro-hardness of the as-received material to HV = 142 after the hydrogenation process was conducted at room temperature for 7 hours. Micro-hardness of the as-received CP-Ti increases with temperature of hydrogenation from HV = 166 in as-received to HV = 290 at 850 ˚C.

2.2 Ti-6Al-4V alloy

▪ Hydrogen concentration of 1.44 wt. % in the near surface regions and 0.1 wt. % in the bulk of material was detected by ERDA in the Ti-6Al-4V sample hydrogenated at room temperature for 1 hour under LP-LC-ST conditions. It was observed that 650 ˚C temperatures of hydrogenation promote the absorption of hydrogen in Ti-6Al-4V alloy when the process is performed under LP-LC-ST conditions for 3 hours of exposure times whereby 7.65 wt. % of

hydrogen concentration was determined by digital balance measurements. Alternatively, ERDA technique detected 0.42 wt. % of hydrogen on the surface region and 0.9 wt. % in the bulk material.

▪ Optical microscopy show the distortion of α- grains after annealing of Ti-6Al-4V alloy at 550 ˚C, 650 ˚C, 750 ˚C and 850 ˚C temperatures for 3 hours and after hydrogenation at room temperature for 1, 3 and 7 hours performed under LP-LC-ST conditions. The formation of hydrides and martensitic structure make it difficult to observe the grains changes in the samples hydrogenated under LP-LC-ST conditions at 550 ˚C, 650 ˚C, 750 ˚C and 850 ˚C for 3 hours durations.

▪ The phase analysis results indicate that hydrides are not detected in the Ti-6Al-4V alloy when it is hydrogenated at room temperature for 1, 3 and 7 hours under LP-LC-ST conditions. At high temperatures of hydrogenation, the following hydrides were detected in samples hydrogenated at designated temperatures:

TiH_2, δ-TiH and $TiH_{0.71}$ at 550 ˚C; $TiH_{0.71}$ at 650 ˚C; TiH_2 and γ-TiH at 750 ˚C and, TiH_2 and δ-TiH at 850 ˚C.

▪ The micro-hardness measurements show a significant increase of hardness for the Ti-6Al-4V alloy after 3 hours of annealing at 550 ˚C, 650 ˚C, 750 ˚C and 850 ˚C temperatures. The presence of the hydrogen introduced at room temperature under LP-LC-ST conditions increases the hardness of the Ti-6Al-4V alloy. The effect of both hydrogen and high temperatures increases the hardness significantly